INVESTIGATING THE USE OF RUBBER TO ATTENUATE THE EFFECT OF BLAST LOAD APPLIED TO A SURROGATE LOWER LEG

By

Delmarie Ungerer

Thesis presented for the degree of Master of Science in Mechanical Engineering

In the special field of Impact Biomechanics

April 2008

ACKNOWLEDGEMENTS

The heart of all research conducted at or in conjunction with the Blast Impact and Survivability Research Unit (BISRU) revolves around saving the lives of people being exposed to various types of impact, which ranges from vehicle crashes to close range detonation of explosives. Completing a postgraduate degree in the midst of excellent academics and researchers with such a passion for life was a marvellous experience and privilege.

Professor Gerald Nurick supervised this study, providing much needed guidance and insight to maintain focus on and analyse the outcomes of this project. His patience and understanding manner is admired by all who have had the opportunity to work with him. Dr Steeve Chung Kim Yuen, Reuben Govender, Trevor Cloete and Annie van der Westhuizen were always willing to share their theoretical and practical knowledge and understanding of high strain rate impact as well as analysing the results of the blast tests performed during this study. Setting up the finite element model of the surrogate leg and conducting the finite element analyses of the various blast loading conditions would not have been possible without the incredible help of Victor Balden. Much appreciation is also shown towards Dr Steeve Chung Kim Yuen who assisted with the setup of the pendulum test rig in the blast laboratory and Reuben Govender who assisted with the setup and test procedure of the Split-Hopkinson Pressure Bar apparatus. Keith Balchin must also be thanked for sharing his vast experience gained in the engineering field as well as his enthusiasm; it served as great inspiration to many an engineering student, including myself.

The Department of Mechanical Engineering at UCT is supported by a great team of technical officers. Special dues need to be paid to Glen Newins and Horst Emrich who provided invaluable practical advice and manufactured the surrogate leg components and the test rig.

I am sincerely grateful to all the people who crossed my way and supported me in completing this study. A final thank you to UCT, Armscor and the National Research Foundation for the financial support provided in order to conduct this study.

PLAGIARISM DECLARATION

I, Delmarie Ungerer, declare that this dissertation is essentially my own work. It is being submitted in partial fulfillment of the requirements for the Masters of Science in Engineering degree at the University of Cape Town and has not been submitted in this or any other form for a degree at any other university.

Delmarie Ungerer
April 2008

ABSTRACT

Landmines are the epitome of the perfect soldier: always ready, never tiring. Landmines also do not choose their victims - it may very well be an armed and protected soldier or an innocent civilian who activates the detonator. As such, landmines have reached epidemic proportions in the Third World, affecting both combatants and civilians, whether they are on foot or in a vehicle. When stepping on an anti-personnel landmine, traumatic amputation of the foot, lower leg or upper leg is generally expected. However, an anti-vehicle landmine detonating underneath a vehicle can have equally as detrimental results, as the occupants of the vehicle are bound to sustain serious injuries to the lower extremities. These injuries can vary from being less life threatening to being fatal in some extreme cases. Anthropomorphic test devices have been developed and refined over the years to represent the occupant exposed to simulated landmine detonation and then to retrieve valuable technical information from the test data.

In the present investigation a simplified aluminium surrogate lower leg was designed, manufactured and subjected to axial blast testing. In addition, a rubber layer representing the sole of a standard army combat boot was placed below the foot model in a separate series of blast tests. The main factors investigated in this study were the effect of varying the amount and positioning of the explosives and the attenuation produced by including the rubber sole layer.

The blast tests were conducted using a horizontal ballistic pendulum, with the foot model placed axially in the pendulum. The disc shaped explosives of different mass was placed in the centre of the detonation plate and axially in line with the heel respectively to draw a comparison between the respective stresses induced in the lower leg. As expected, the stress recorded by the strain gauges placed on the lower leg was significantly higher when the explosives were positioned in line with the heel than when placed in the centre of the detonation plate.

The same series of blast tests were performed with the rubber sole being included in the test setup. Alternating the positioning of the explosives did not yield a significant difference in induced stress. Investigation of the blast attenuation provided by the rubber layer showed that the peak stress is mitigated by approximately 70%, which was much greater than expected.

An elementary analytical solution was performed as a preliminary validation of the experimental test results. Furthermore, a finite element model of the aluminium surrogate foot and the rubber layer was created and a numerical simulation of each blast test was executed. Material data for the aluminium and rubber obtained via Split-Hopkinson Pressure Bar testing

were employed to construct the material models used in the finite element model. The results from the numerical simulations compare well to the experimental test results for the blast loading conditions where the rubber layer was excluded from the test setup. In the case where the rubber layer was included in the testing, the trend and shape of the stress graphs obtained from the numerical simulation results agrees with the stress curves recorded during the actual blast tests. However, the peak stresses recorded during the experimental blast tests are found to be significantly higher than the peak stresses yielded by the numerical simulations.

Ultimately it was concluded that the blast testing performed during this study can be classified as "non-injurious", that detonating the explosives in line with the heel increases the peak stress experienced by the tibia, that placing a rubber layer underneath the foot provides a certain amount of blast attenuation and that the numerical modelling of the rubber requires more detailed attention.

TABLE OF CONTENTS

TABLE OF FIGURES

CHAPTER 2

CHAPTER 3

CHAPTER 4

CHAPTER 5

CHAPTER 6

CHAPTER 7

CHAPTER 8

TABLE OF TABLES

CHAPTER 6

CHAPTER 7

CHAPTER 8

NOMENCLATURE

Ottawa Treaty

Formally named the "Convention on the Prohibition of the Use, Stockpiling, Production and Transfer of Anti-Personnel Mines and on their Destruction". The Ottawa Treaty became binding international law on 1 March 1999 and it [1]:

- Prohibits the manufacture, trade and use of anti-personnel mines.
- Obliges countries to destroy stockpiles and clear their own territory.
- Urges governments to help poorer countries clear land and rehabilitate survivors.

Only anti-personnel mine are covered in the Ottawa Treaty. Anti-tank mines, mixed mines, remote controlled claymore mines, anti-handling devices (booby-traps) and other "static" explosive devices against persons are not covered within the treaty.

The countries that have joined the treaty are called States Parties. Each State Party is obliged to destroy their stockpiles mines within 4 years and to clear their mine-affected areas within 10 years[1]. States Parties are also obliged to give financial assistance for mine victims and mine clearance.

List of signatories (as of 18 September 2007) [2]:

Afghanistan, Albania, Algeria, Andorra, Angola, Antigua and Barbuda, Argentina, Australia, Austria, Bahamas, Bangladesh, Barbados, Belarus, Belgium, Belize, Benin, Bhutan, Bolivia, Bosnia and Herzegovina, Botswana, Brazil, Brunei Darussalam, Bulgaria, Burkina Faso, Burundi, Cambodia, Cameroon, Canada, Cape Verde, Central African Republic, Chad, Chile, Colombia, Comoros, Congo (Democratic Republic), Congo, Cook Islands, Costa Rica, Côte d'Ivoire, Croatia, Cyprus, Czech Republic, Denmark, Djibouti, Dominica, Dominican Republic, East Timor, Ecuador, El Salvador, Equatorial Guinea, Enitrea, Estonia, Ethiopia, Fiji, Former Yugoslav Republic of Macedonia, France, Gabon, Gambia, Germany, Ghana, Greece, Grenada, Guatemala, Guinea, Guinea-Bissau, Guyana, Haiti, Holy See, Honduras, Hungary, Iceland, Indonesia, Iraq, Ireland, Italy, Jamaica, Japan, Jordan, Kenya, Kribati, Kuwait, Latvia, Lesotho, Liberia, Liechtenstein, Lithuania, Luxembourg, Madagascar, Malawi, Malaysia, Maldives, Mali, Malta, Marshall Islands, Mauritania, Mauritius, Mexico, Moldova (Republic of), Monaco, Montenegro (Republic of), Mozambique, Namibia, Nauru, Netherlands, New Zealand, Nicaragua, Niger, Nigeria, Niue, Norway, Panama, Papua New Guinea, Paraguay, Peru, Philippines, Poland, Portugal, Qatar, Romania, Rwanda, Saint Kitts and Nevis, Saint Lucia,

Saint Vincent and the Grenadines, Samoa, San Marino, Sao Tome and Principe, Senegal, Serbia (Republic of), Seychelles, Sierra Leone, Slovakia, Slovenia, Solomon Islands, South Africa, Spain, Sudan, Suriname, Swaziland, Sweden, Switzerland, Tajikistan, Tanzania (United Republic of), Thailand, Togo, Trinidad and Tobago, Tunisia, Turkey, Turkmenistan, Uganda, United Kingdom, Uruguay, Vanuatu, Venezuela, Yemen, Zambia, Zimbabwe.

Countries that have not joined the Ottawa Treaty (as of 17 August 2007) [2]:

Armenia, Azerbaijan, Bahrain, Burma, China, Cuba, Egypt, Finland, Georgia, India, Iran, Israel, Kazakhstan, Korea (North), Korea (South), Kyrgyzstan, Laos, Lebanon, Libya, Micronesia, Mongolia, Morocco, Nepal, Oman, Pakistan, Palau, Russian Federation, Saudi Arabia, Singapore, Somalia, Sri Lanka, Syria, Tonga, Tuvalu, United Arab Emirates, United States of America, Uzbekistan, Vietnam, Yugoslavia.

Note that the United States of America is the only NATO country not to renounce antipersonnel landmines.

Anti-personnel mine (AP mine)

(Definition according to the Ottawa Treaty [2])

A mine designed to be exploded by the presence, proximity or contact of a person that will incapacitate, injure or kill one or more persons.

Anti-vehicular / Anti-tank mine (AV / AT mine)

(Definition according to the Ottawa Treaty [2])

A mine designed to be detonated by the presence, proximity or contact of a vehicle as opposed to a person, which is equipped with an anti-handling device. An anti-handling device means a device intended to protect a mine and which is part of, linked to, attached to or placed under the mine and which activates when an attempt is made to tamper with or otherwise intentionally disturb the mine.

NATO Task Group HFM-089/TG-024

This particular NATO Task Group was initiated with these chief goals in mind [3]:

- Investigate and review the various test methods currently in use for analysing protective footwear.
- Identify the benefits and limitations of the various test methods.
- Define testing guidelines that would ensure test results from different nations are meaningful and comparable.

Canadian Centre for Mine Action Technologies (CCMAT)

The CCMAT was established in 1998 to develop low cost, sustainable technologies for mine action and to work towards their successful deployment in the field[4]. This goal is accomplished through a comprehensive program of Research and Development, test and evaluation, and active communication with the user community. Funding for the CCMAT is provided through the Canadian Landmine Fund.

LIST OF ABBREVIATIONS

AIS	*Abbreviated Injury Scale*
AP	*Anti-personnel*
AT	*Anti-tank*
AV	*Anti-vehicle*
ATD	*Anthropomorphic test devices*
BFR	*Blast fragment resistant*
BISRU	*Blast Impact and Survivability Research Unit*
CLL	*Complex Lower Leg*
DSTO	*Defence Science and Technology Organisation*
EFP	*Explosively formed penetrator*
FEM	*Finite Element Model*
FSL	*Frangible Surrogate Leg*
H-III	*Hybrid-III*
HUMOS	*Human Model for Safety*
IABG	*Industrieanlagen-Betriebsgesellschaft (German engineering firm)*
IED	*Improvised explosive device*
LEAP	*Lower Extremity Assessment Program*
MTS	*Mine Trauma Score*
NATO	*North Atlantic Treaty Organisation*
NHTSA	*National Highway Traffic Safety Administration*
PMHS	*Post Mortem Human Surrogates*
PPE	*Personal protective equipment*
SC	*Shaped charge*
SHPB	*Split-Hopkinson Pressure Bar*
SIMon	*Simulated Injury Monitor*
SSL	*Simplified Surrogate Leg*
THUMS	*Total Human Model for Safety*
TNO	*Nederlandse Organisatie voor Toegepast Natuurwetenschappelijk Ondersoek (Netherlands Organisation for Applied Scientific Reseach)*
TROSS	*Test Rig for Occupant Safety System*

LIST OF SYMBOLS

I_0	*Impulse*
P	*Pressure*
W	*Charge mass*
ρ	*Density*
d, ϕ	*Diameter*
R	*Distance away from epicentre of the volume of the explosive*
P_S	*Overpressure*
Z	*Scale factor used to scale explosive mass w.r.t. overpressure distance*
σ_{11}	*Engineering stress in the 1,1 direction*
σ^e	*Quasi-static hyperelastic component of stress*
σ^v	*Dynamic rate-dependent viscoelastic component of stress*
λ	*Engineering stretch*
ε	*Engineering strain*
A_1, A_2, A_3, A_4, A_5	*Material parameters*
I_1, I_2	*1st and 2nd deviatoric strain invariants*
ε_i	*Strain in incident bar of SHPB setup*
ε_t	*Strain in output bar of SHPB setup*
ε_r	*Strain reflected by test specimen in SHPB setup*
E	*Modulus of Elasticity*
c_b	*Longitudinal wave speed in a specific material*
u	*Particle displacement*
u_1	*Displacement of front surface of SHPB test specimen*

u_2	Displacement of rear surface of SHPB test specimen
F_1	Force in incident pressure bar of SHPB setup
F_2	Force in output pressure bar of SHPB setup
A	Cross-sectional area of the pressure bar
A_S	Instantaneous cross-sectional area of the test specimen
U	Strain energy per unit of reference volume
U_{dev}	Deviatoric part of the strain energy potential
U_{vol}	Volumetric part of the strain energy potential
J	Total volume ratio
J_{el}	Elastic volume ratio
C_{10}, C_{01}, C_{11}	Temperature dependent material parameters
D_1	Temperature dependent material parameter
μ_i	Temperature dependent material parameter
α_i	Temperature dependent material parameter
$\bar{I}_1$, $\bar{I}_2$	1st and 2nd deviatoric strain invariant
$\bar{\lambda}_1, \bar{\lambda}_2, \bar{\lambda}_3$	Stretches in the 1, 2 and 3 directions
ν	Poisson's ratio

Chapter 1 - Introduction

1.1 SUBJECT OF THIS REPORT

This report concerns the investigation into the degree of attenuation provided by introducing a layer of rubber underneath an aluminium surrogate leg when exposed to axial blast impact.

1.2 BACKGROUND TO THE INVESTIGATION

Not only do anti-personnel (AP) landmines pose a serious threat to humanity, but anti-vehicle (AV) landmines present detrimental consequences as well. It is well understood that the landmine does not choose its victim, and as such the dangers of a hidden landmine extend from soldiers to peacekeepers and civilians alike.

Injuries sustained due to the detonation of AP and AV landmines differ in characteristics, as the injury mechanisms of the two types are inherently different:

- Detonation of AP landmines cause burn injuries due to the thermal effect at the centre of the blast, damage to the hollow organs caused by the intense overpressure wave originating from the blast, and ballistic injuries due to sharp fragments propelled radially outwards from the landmine[5]. The extent of these injuries is evaluated according to the Mine Trauma Score (MTS) system, which was generated during the Lower Extremity Assessment Program (LEAP) [6]. Depending on the size of the landmine, wearing civilian shoes or standard army combat boots do not provide sufficient protection against the effect of the landmine blast, which normally results in the traumatic amputation of a portion or the whole of the lower limb[7]. Trial testing using cadaver lower legs and frangible lower leg models has proved that wearing specifically designed landmine protective footwear may drastically decrease the degree of injury induced upon the lower extremities due to the detonation of an AP landmine[6].
- AV landmines on the other hand are designed to damage and immobilise vehicles. The occupants of a soft-skin vehicle exposed to an exploding landmine stand little chance of survival. As such, landmine protected vehicles are carefully designed and tested according to strict standards in order to ensure occupant safety during a landmine blast. Despite the excessive measures of protection provided by an armoured vehicle, the detonation of AV landmines is known to induce floor acceleration and velocity typically exceeding 100g and 12m/s respectively, which in turn causes injury to the

lower extremities of the occupants of the vehicle[8]. Floorboard intrusion is deemed to be the principle cause of lower leg injuries, ranging from less life threatening injuries (e.g. calcaneous, tibia and/or femur fracture), injuries with long term effects (e.g. traumatic amputation of one or both of the lower legs or on the upper legs) to fatal injuries[8]. Instrumented mechanical human surrogate models (such as the Hybrid-III dummy) are generally employed in the testing of landmine protected vehicles, allowing the forces and accelerations exerted upon the occupants to be measured and studied. Load limits predicting a 25% and 50% possibility of a moderate to severe injury occurring in the lower limb is assigned to each type of instrumented dummy[9].

Various test methods have been developed and successfully used to delineate blast related injuries in a controlled setting. These test methods comprise either a vertical setup (as used in the TROSS rig[8]) or a horizontal setup (e.g. the linear impactor used by Bir et al.[8] and the horizontal pendulum used by the Medical College of Wisconsin[10]). Notwithstanding, the axial impact test methods essentially operate on the same principle: Impact is applied axially in line with the tibial axis via an impactor plate that transmits the impact through the base of the foot of the surrogate leg.

The blast laboratory of the Blast Impact and Survivability Research Unit (**BISRU**) at the University of Cape Town has the facility to accommodate a horizontal ballistic pendulum to conduct blast tests on test specimens of different sorts. The ballistic pendulum operates on a similar principle as mentioned above; because the explosives placed against the detonation plate exerts impact on the surrogate foot by transmitting the impulse through the detonation plate, through the base of the surrogate foot and along the remainder of the leg. A project was therefore launched to develop, manufacture and test an economically viable surrogate lower leg which can be utilised for blast testing using the horizontal ballistic pendulum. The blast test results would thereafter be compared to existing results from previous successful blast test investigations to comment on the feasibility of the surrogate leg design. In addition to the original project outline, it was decided to investigate the effect on the stress wave passing through the surrogate leg when a layer of rubber, acting as a sole, is placed underneath the base of the foot.

1.3 OBJECTIVES OF THIS REPORT

The key objectives of this thesis are as follows:

- Based on the original surrogate foot designed as part of a previous undergraduate project, modify the ankle region to provide the surrogate lower leg with better biofidelic characteristics.

- Retrieve results from the blast tests which would illustrate the stress wave propagation through the modified lower leg model, using a horizontal ballistic pendulum rig specially constructed to accommodate the surrogate lower leg while providing axial sliding movement for the leg model.
- Construct a finite element model of the surrogate lower leg and retrieve results from the simulations of each of the different experimental blast tests. The numerical results are compared to the experimental results in order to validate the relevance and accuracy of the finite element model.
- Investigate the amount of attenuation provided by the rubber sole placed underneath the foot of the lower leg model. Use the numerical model to study the mechanism by which the rubber layer is perceived to provide attenuation to the stress transmitted to the surrogate leg.
- Compare the experimental results to the results provided by previous successful investigations. In doing so, the blast tests conducted in the present study can be categorised according to the level of injury estimated to be induced in the surrogate lower leg.

1.4 PLAN OF DEVELOPMENT OF THE REPORT

The report starts off with a Literature Review (Chapter 2) in which background into blast loading is provided, the human lower leg anatomy is briefly explained, and existing representations of the human lower leg, related test methods and injury criteria is discussed. The details regarding material characterisation of rubber-like materials using the Split Hopkinson Pressure Bar is also discussed in the Literature Review.

Chapter 3 details the material characterisation performed of the solid aluminium used to construct the foot and ankle complex, also of the rubber used to represent a sole underneath the base of the surrogate foot. Chapter 4 gives the experimental details and results of the blast tests performed with the rubber sole excluded from and included in the test setup, while changing the positioning of the explosives from the centre of the foot to being in line with the heel. The stress wave propagation along the lower leg is modelled analytically in Chapter 5. Details concerning the construction of the finite element model are provided in Chapter 6, as well as the results retrieved from the simulations.

The analytical, experimental and numerical results are summarised and compared in Chapter 7, after which coherent conclusions are drawn and documented in Chapter 8. Chapter 9 lists recommendations which are made in order to aid the future research into blast impact of the lower extremities conducted at BISRU.

Chapter 2 - Literature Survey

2.1 INTRODUCTION

Anti-personnel landmines in particular pose a significant threat to both military personnel and civilians of many countries throughout the world, as there are 110 million uncleared anti-personnel landmines around the world, scattered through more than 70 countries[11]. Clinical history shows that the foot, ankle and tibia are injured primarily during a landmine explosion[8;12]. Trauma to the lower extremities are however not limited to anti-personnel landmine explosions only. It is documented that occupants of a vehicle experiencing an anti-vehicle or anti-tank mine blast also exhibit primary injuries to the lower limbs, with the injuries ranging from fracture of the calcaneous to traumatic amputation of the upper legs[8]. As such, the assessment of protective equipment became of great importance. Although a vast variety of test protocols are currently in use, three basic approaches to blast testing can be defined according to the type of surrogate leg being used.

Surrogate legs can be divided into three main groups: mechanical, frangible and cadaver models of the human leg[13]. The selection of the appropriate test methodology is mainly determined by two factors. Firstly, the test procedure is dependent on the level of detail and information obtainable from the test. Secondly, the test method must be practical and able to be implemented by various users and countries with differing preferences and ethical regulations.

The NATO Task Group HFM-089/TG-024 categorised the test approaches such that simple mechanical legs are employed for screening, complex frangible leg models for proofing and human cadaver legs for validation purposes[13]. To simulate exposure to a landmine blast, all of these test approaches include explosive testing in a controlled environment.

Whether a mechanical, frangible or cadaver leg model is being used, every blast test procedure consists of the following basic elements:

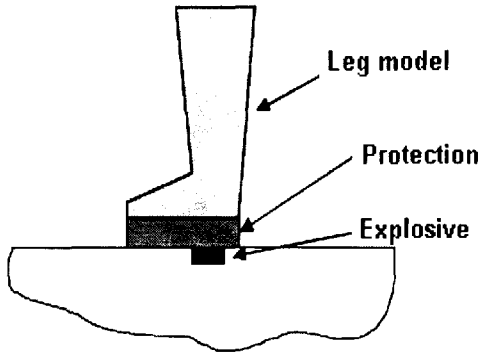

Figure 2.1– Schematic representation of typical test for protective footwear[13]

- Threat definition – Anti-personnel, anti-vehicle or anti-tank landmine.
- Representation of human body region – Whole body or singular limb being analysed.
- Representation of the protective wear
- Means of evaluating the effectiveness of the protection

This literature review discusses the threat definition, anatomy of the human ankle-foot complex, various surrogate leg models and the test protocols used when employing these leg models in blast testing. Injury criteria pertaining to mine blast effects and existing lower leg protective equipment is also overviewed. Thereafter the investigation of the stress versus strain behaviour of rubber materials is briefly duscussed and the theory behind material characterisation using the Split-Hopkinson Pressure Bar is explained.

2.2 THE BLAST EVENT

2.2.1 Defining an explosive material and an explosion

An explosion can be defined as the generation of a pressure wave of finite amplitude in air by a rapid release of energy[14], due to an explosive material being either chemically or energetically unstable. With a sudden expansion of the explosive material, heat and large pressure changes are produced upon initiation (which is typically accompanied by a flash and/or loud noise). This process is termed the explosion.

Chemical explosive materials are categorised according to their rate of decomposition[15]:

- A low explosive is typically a mixture of a combustible substance and an oxidant that decomposes rapidly (also known as deflagration). Deflagration occurs at rates varying from a few cm/s to approximately 400 m/s.
- A high explosive is a chemical compound which undergoes detonation that produces a shock-wave with a velocity ranging from 1000 m/s to 9000 m/s.

Plastic explosive is a specialised form of chemical explosive material which is soft and hand malleable and has the benefit of being usable over a wide range of temperature[15].

2.2.1.1 TNT (Trinitrotoluene)

TNT is a chemical compound which is 99% TNT and 1% DNT (Dinitroluene), and has an initial shock-wave velocity of 6800m/s to 6950m/s [16;17]. Crystalline and light yellow in colour, TNT is known as a useful explosive material that is safe to handle. TNT is the most common explosive for both military and industrial purposes, as its insensitivity to shock and friction reduces the risk of unexpected detonations. The low sensitivity also allows the compound to be melted and cast into casings.

2.2.1.2 RDX

RDX is a high explosive compound also known as Cyclonite, Hexagon and T4 [17;18]. RDX is white and crystalline in appearance, and as an explosive it is generally used mixed with other explosives and plasticizers. RDX is considered to be one of the most powerful and brisant of the military high explosives, boasting an initial shock-wave velocity of approximately 8500 m/s.

2.2.1.3 PE4

British Military plastic explosive is referred to as PE4 [19]. The explosive characteristics of PE4 are similar to that of C-4, the only difference between PE4 and C-4 being the type and proportion of plasticizer used. PE4 compound consists of 88% RDX and 12% plasticizer. The detonation velocity of PE4 is also approximately 8100 m/s.

2.2.1.4 C-4 (Composition C-4)

The term "composition" is used for any stable explosive. C-4 is a high explosive compound made up of 91% RDX and 9% non-explosive plasticizer, and detonates at approximately 8100 m/s [18]. The explosive output of C-4 is found to be roughly 1.4 times that of TNT. One of the main advantages of C-4 is that it can be easily moulded into any shape or form desired. Other advantages of using C-4 are its durability, reliability and safety, as it will only detonate when both heat and pressure is applied.

2.2.1.5 Plasticizer

The main functions of the plasticizer in explosives are[20]:

- Soften the explosives (make it more malleable).
- Increase the stability of the explosive by increasing the temperature at which it burns and/or the pressure at which it detonates.

2.2.2 Detonation and blast waves

When an explosive material is detonated, a stable chemical reaction rapidly propagates through the un-reacted portion of the explosive material which in turn causes a detonation wave that travels at supersonic speed. The detonation velocity varies for different explosive materials as the detonation velocity depends on the composition and density of the specific explosive material (information is provided in the above section). In the process of detonation the explosive material is converted into an extremely hot, dense and high pressure gas. The gas formed by the chemical reaction of the explosive material during detonation is the source of the strong blast waves in the air. The velocity of the blast wave is much slower than the velocity of the detonation wave[21].

2.2.3 Describing the blast load

The blast load is typically described by the nature of its pressure-time history. Referring to Figure 2.2 it is noticed that the blast load comprises an over-pressure region and an under-pressure region. Only the effect of the peak over-pressure is considered as it is much larger than the peak under-pressure.

The impulse of the blast load is represented by the area under the over-pressure portion of the pressure-time graph. Hence the impulse imparted by the blast load depends on the magnitude of the peak over-pressure, the duration of the over-pressure and the rate of decay.

$$I_o = \int_{t_a}^{t_a+T} P(t)dt \qquad \text{Eq. 2.1}$$

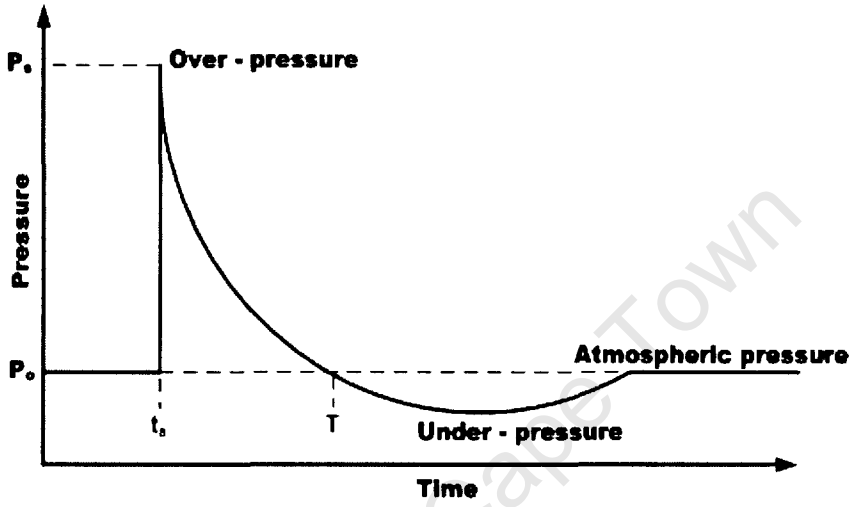

Figure 2.2 – Pressure-time history describing the blast load[22]

2.2.4 Scaling of blast overpressure waves

The blast overpressure wave decays exponentially with increasing distance from the explosive source, providing a safety standoff distance to be a possible solution in protective footwear[7]. The charge masses W_1 and W_2 consisting of the same explosive is calculated by the following equation, where ρ is the density of the particular explosive:

$$W_1 = \rho.\frac{\pi}{6}.d_1^{\,3} \qquad \text{Eq. 2.2}$$

$$W_2 = \rho.\frac{\pi}{6}.d_2^{\,3} \qquad \text{Eq. 2.3}$$

It is known that the explosive diameter d is directly proportional to the distance R away from the centre of the volume of explosive. As such, if the same overpressure P_s is to be produced by the two different charge masses, the ranges at which that specific overpressure is generated can be determined from the relationship given by Eq. 2.4 [14;23]:

$$\frac{R_1}{R_2} = \left(\frac{W_1}{W_2}\right)^{1/3} \qquad \text{Eq. 2.4}$$

The relationship given in Eq.2.4 yields a constant of proportionality Z which can be used as a scale factor.

$$Z = \frac{R_1}{W_1^{1/3}} = \frac{R_2}{W_2^{1/3}} \qquad \text{Eq. 2.5}$$

The expected peak overpressure P_S in the near field (P_S >10Bar) is demonstrated to be calculated by[24]:

$$P_S = \frac{6.7}{Z^3} + 1 \qquad \text{Eq. 2.6}$$

If the same charge mass is used, i.e. $W_1 = W_2$, the peak overpressure occurs at the same distance R_S. In order to determine the overpressure P_X experienced at a different range in the near field, the new scale factor Z_X is used with respect to the reference scale factor Z_S, as shown in Eq. 2.7 and illustrated in Figure 2.3.

$$\frac{Z_S}{Z_X} = \left(\frac{P_X - 1}{P_S - 1}\right)^{1/3}$$
$$\Rightarrow P_X = \left(\frac{Z_S}{Z_X}\right)^3 (P_S - 1) + 1 \qquad \text{Eq. 2.7}$$

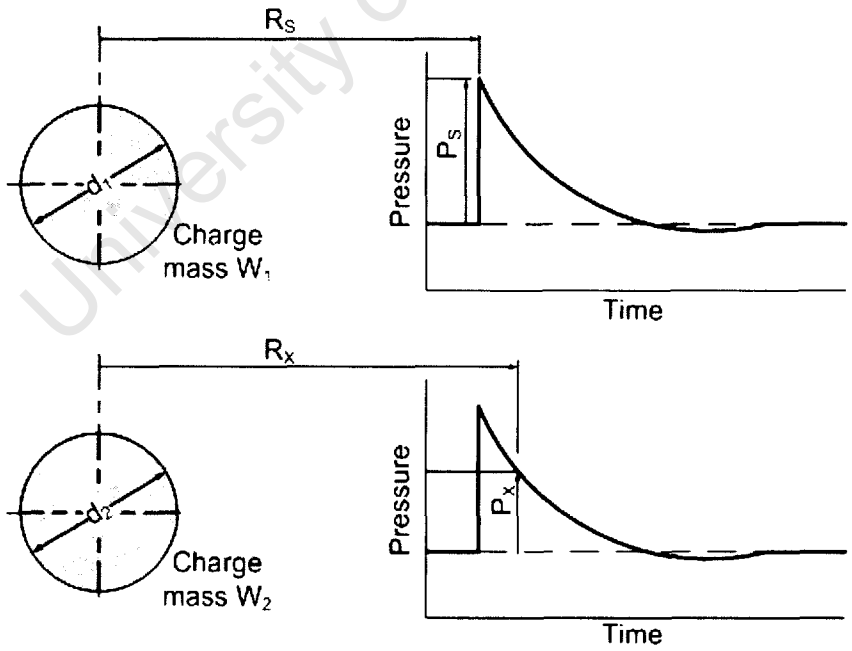

Figure 2.3 – Illustration of blast wave scaling

2.3 THREAT DEFINITION

In real landmines the amount of explosive may vary extensively and there always exists the possibility of deflagration instead of detonation of the explosives in the mine[13]. As such, the consistency of any real landmine may vary significantly in terms of explosive output, which makes the threat definition difficult to assess. Accessing real landmines to use as test devices is also made difficult after the Ottowa treaty limited the availability and transport of real mines[3;13]. Despite these setbacks, the types of landmines can be examined by using surrogate mines in an attempt to understand the expected threat.

Landmines are categorised according to their operational purpose and mechanism of injury[25]. According to operational purpose landmines are classified as anti-personnel and anti-tank landmines. Subsequently landmines can then be grouped according to their injury mechanism as either blast mines or fragmentation mines[13], as depicted in Figure 2.4.

Table 2.1 shows a few examples of anti-personnel and anti-tank landmines and the amount of explosives it comprises. The high explosive main-charges commonly used in mines are TNT, RDX, tetryl, picric acid, plastic explosive and nitromethane[17].

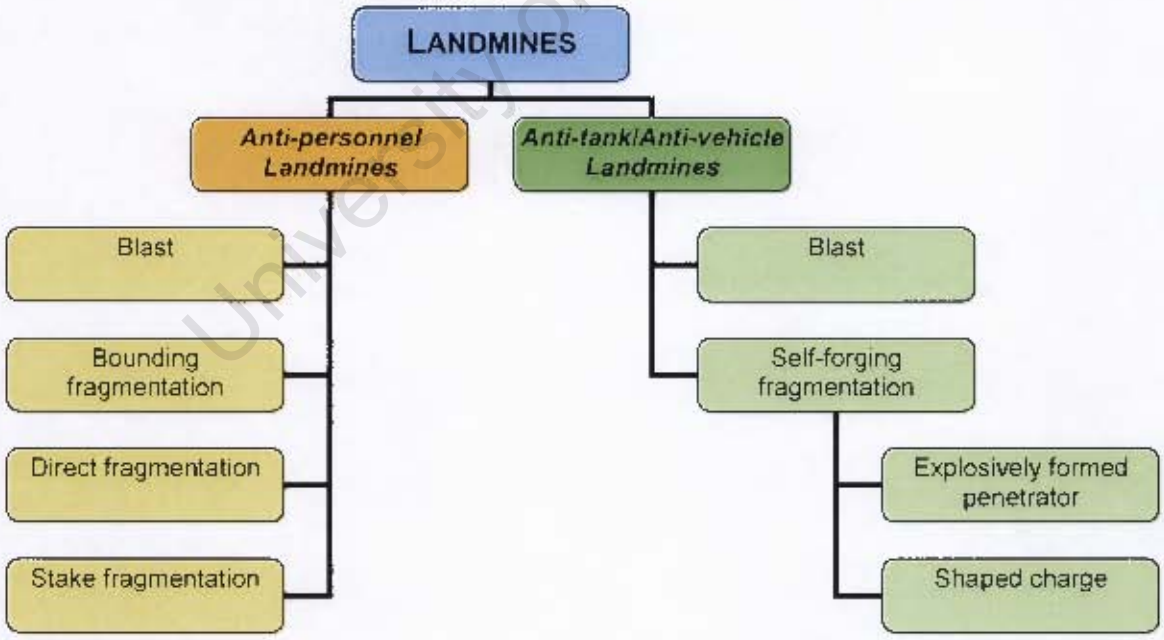

Figure 2.4 – Landmines categorised as anti-personnel and anti-tank landmines [26]

AP mine	Type	Explosives	Mass	AT mine	Type	Explosives	Mass
M14	blast	Tetryl	29 g	SB-81	blast	RDX/TNT	2.2 kg
PMA-3	blast	Tetryl	35 g	TM-72	shaped charge	RDX/TNT	2.5 kg
VS-50	blast	RDX	43 g	Mk-5	blast	TNT	3.7 kg
TS-50	blast	RDX	50 g	TMRP-6	blast	TNT	5.1 kg
MI DV 59	blast	TNT	70 g	TMA-4	blast	TNT	5.5 kg
PMR-2A	fragmentation	TNT	100 g	TC/6	blast	RDX/TNT	6.0 kg
PMA-2	blast	TNT	100 g	TMK-2	shaped charge	RDX/TNT	6.5 kg
PMA-1	blast	TNT	200 g	PM-60	blast	TNT	7.5 kg
PMN	blast	TNT	240 g	Mk-7	blast	TNT	8.9 kg
MON-50	fragmentation	RDX/TNT	700 g	M15	blast	RDX/TNT	10.3 kg

Table 2.1 – Examples of landmine types and the amount of explosives [17]

2.3.1 Anti-personnel landmines (APLs)

Anti-personnel mines are generally used in static mine fields along borders or as a manner of defence of strategic positions. APLs are however also deployed in small numbers or singularly to lay an ambush, protect a temporary base, protect equipment or evade pursuit.

Anti-personnel landmines generally contain 28 grams to 500 grams of explosives[27] and are typically buried under soil (at depths of 10mm – 40mm) or placed strategically on the surface (hidden by leaves or rocks). The APLs are activated by pressure which can be from a person stepping on them or a vehicle driving over them. Impulse resulting from the blast mine explosion is considerably influenced by the soil conditions, burial depth and explosive confinement. Generally deeper burial depth and soil with a higher moisture content and density will result in greater energy transfer from the landmine to the target[27].

2.3.1.1 Blast anti-personnel landmines

Blast APLs are the cheapest and most common form of landmine, which rely on the overpressure waves (or sonic shock waves) from the detonation of a high explosive to maim the victim, causing physical and psychological trauma[6]. Although blast APLs are designed to injure the victim, mines with larger charges can be lethal[6].

Figure 2.5 – AP landmine, French MI AP DV 59 [28]

An AP blast mine consists of four main components[27]:

- **Mine casing** – The casing houses and protects the components of the landmine. Early landmines had casings made of steel, but in order to prevent detection by electronic mine detectors most anti-personnel mines today are encased in plastic housings.
- **Pressure plate** – The pressure plate acts as a detonation mechanism that sets off the detonation charge. Generally a spring-loaded detonation mechanism strikes the detonator charge with a firing pin or an electric charge is passed through it to detonate the landmine.
- **Detonator charge** – The detonation charge consists of a highly sensitive explosive that would easily explode when an electric charge or sudden pressure is applied to it.
- **Main charge** – The main charge is a stable explosive that is detonated by the explosion of the detonator charge. TNT or tetryl is used in most AP blast mines, where a U.S. M-14 contains on average 31 grams of tetryl and in a Russian PMN anti-personnel landmine up to 200 grams of TNT is used.

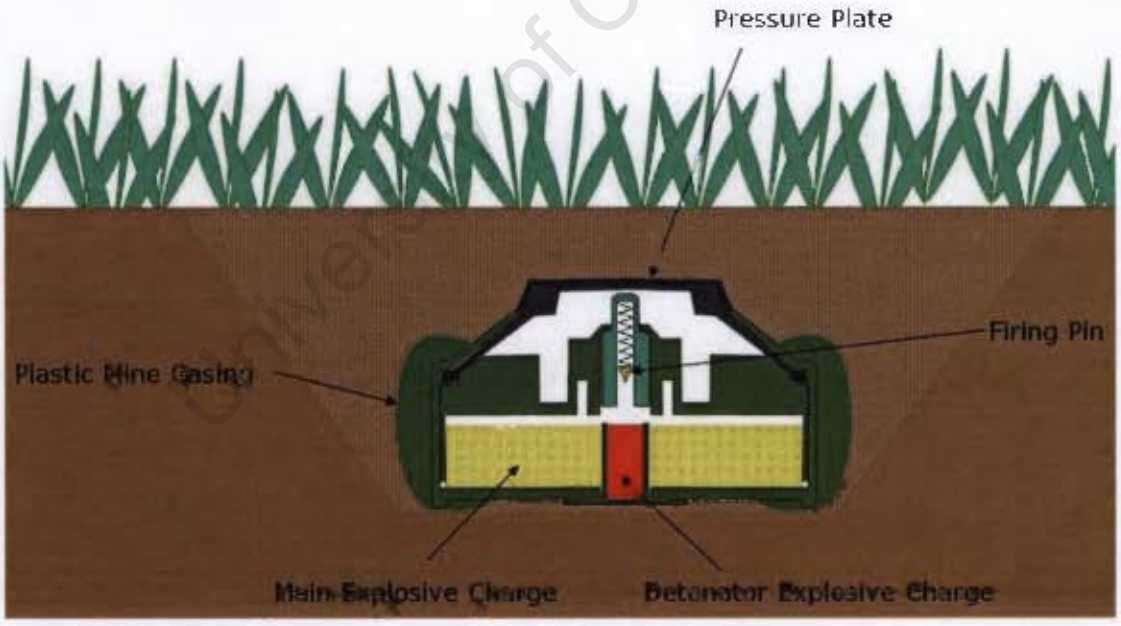

Figure 2.6 – Composition of a blast anti-personnel landmine [27]

2.3.1.2 *Fragmentation anti-personnel landmines*

Fragmentation mines are designed to spread shrapnel fragments, varying in shape, size, composition and initial velocity, to cause ballistic injuries[5]. The ultimate aim of the fragmentation APL is to kill the victim, maximising the mortality damage to the opposing forces[6]. Fragmentation APLs include stake mines, directional mines and bounding mines[27].

As the name suggests, stake mines are mounted on a stake at an appropriate height above the ground, camouflaged by vegetation or rubbish. The hollow cylindrical sleeve is filled with a small explosive charge and the sleeve is packed with fragments that will shoot out radially when the tripwire triggers the detonator.

Figure 2.7 – AP stake mounted mine, Yugoslav PMR-2A [27]

Directional mines are designed to spray fragments in a restricted arc. These mines are generally used to protect the combatants, by placing the mines such that the blast is directed towards the enemy.

Figure 2.8 – AP directional mine, Russian MON-50 [27]

A bounding mine is buried and when triggered, a lifting charge is detonated that throws the body of the mine up in the air where the main charge explodes and fragments are spread at waste level.

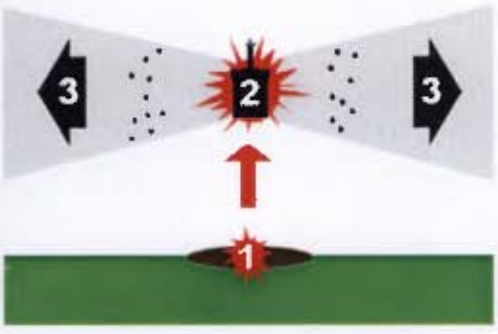

Figure 2.9 – AP bounding mine, USA "Bouncing Betty" [29]

2.3.1.3 *Injury mechanisms related to AP landmines*

Blast and fragmentation anti-personnel mines are designed with the intention of using two inherently different injury mechanisms to produce distinctly different types of injury to the victim, as explained in Table 2.2. Where a fragmentation mine causes ballistic injury to the victim by shooting fragments radially outward, a blast mine mainly employs the powerful overpressure shock wave to impart injury onto the victim[5]. However, Figure 2.10 shows how the type and probability of injury caused by the detonation of a blast AP mine changes as the victim's distance from the centre of the blast increases:

- **Thermal** effects are caused by the combustion of the explosives, which causes burn wounds to the body part(s) of the victim positioned at the epicentre of the detonating explosives.
- Detonation of the explosive material causes a detonation wave which travels at a supersonic speed and rapidly converts the explosive material into an extremely hot dense and high pressure gas, as such resulting in strong blast waves in the air. Therefore, the victim or the body regions of the victim situated further away from the epicentre of the blast would experience the intense **blast** overpressure wave. The periphery of the overpressure wave is relative to the size and mass of the explosive, as briefly discussed in Section 2.2.4. The blast overpressure wave mainly causes damage to the hollow organs and the blast wind created by the explosion can throw the victim against solid objects, causing blunt trauma.
- Fragments (of varying shape, size and composition) produced by the exploding landmine are propelled radially outwards, which causes **ballistic** injuries to the victim when the victim is positioned beyond the effect of the blast overpressure wave.

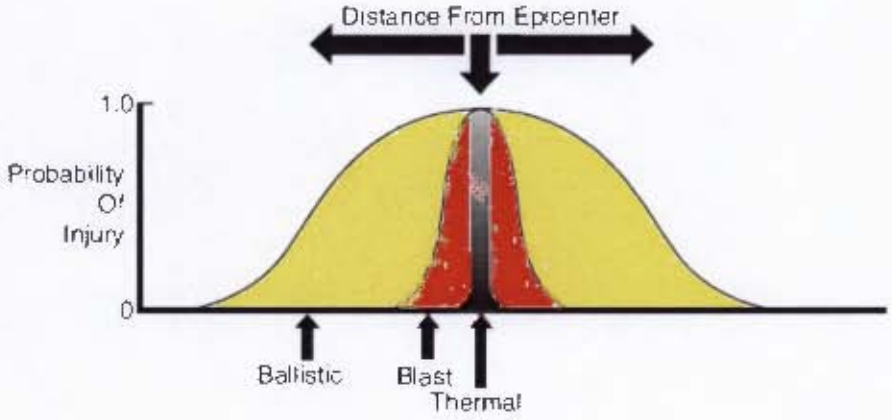

Figure 2.10 - Mechanisms of injury of blast mines [5]

Type of APL	***Blast APL***	***Fragmentation APL***	***Ref.***
Aim	*Injure victim*	*Kill victim*	*[6]*
Method	*Intense overpressure shock wave*	*Shoots fragments radially outwards*	*[5]*
Injury criteria	*Ears, lungs, gastrointestinal tract hollow organs*	*External ballistic injuries*	*[5]*

Table 2.2 – Comparison of blast and fragmentation APLs

2.3.2 Anti-tank/anti-vehicle landmines (AT/AV mines)

Anti-tank mines are specifically designed to immobilise or destroy tanks and armoured vehicles and were first improvised during the First World War as a counter measure against the first tanks introduced by the British[30]. AT mines evolved significantly from simply being a high explosive shell or mortar bomb buried with the fuse upright to the modern anti-tank mines used today.

Modern AT mines have plastic material casings to avoid easy detection and contain a much larger explosive charge (up to 10kg of explosives) than anti-personnel mines[30]. The explosives are more powerful and the detonation triggers are more sophisticated, enabling the explosives to be directed to either the tank tracks, anywhere on the tank body or the top or side of the vehicle. The detonator can be triggered by pressure or seismic effects caused by the vehicle, remote detonation or by using a combination of the triggering effects. AT landmines are generally buried under the ground surface to be exploded underneath the vehicle.

2.3.2.1 Self-forging fragmentation anti-vehicle landmines

Self-forging fragmentation AT/AV landmines employ two methods in order to damage, penetrate or destroy the target[26]. Either a shaped charge (SC) or an explosively formed penetrator (EFP) is used in these fragmentation mines.

A shaped charge (SC) is an explosive charge shaped in such a way as to focus the effect of the blast energy in order to penetrate armour[31]. Modern cone shaped explosive charges are metal-lined and the detonation of the explosives collapses the conical liner by force into a jet of metal. This metal jet can penetrate armour steel up to a depth of 10 times the diameter of the charge cone.

Figure 2.11 – Photograph of AT self-forging fragmentation landmine with shaped charge, Russian TMK-2 [26]

Explosively formed penetrator (EFP) charges (also known as explosively formed projectile) exploits the explosive's detonation wave to deform a plate or dish of ductile metal, such as copper, into a compact high-velocity missile[32]. This projectile's final shape is typically a ball or rod and is commonly termed the "slug". The slug is aimed and projected at the target at velocities reaching 2km/second, which makes an EFP much more effective over large standoff distances than a conventional shaped charge.

Figure 2.12 – Photograph of AT self-forging fragmentation landmine with explosively formed penetrator, Russian TMPR-6 [32]

2.3.2.2 *Blast anti-vehicle landmines*

Blast AT/AV landmines are essentially larger and more powerful versions of the AP blast mines and their composition and functionality are similar to AP blast mines. Blast mines usually contains 2kg – 10kg of explosives, TNT or RDX being the explosives most commonly used[33].

Figure 2.13 – Photograph of AT blast landmine, Italian TC/6 [33]

2.3.2.3 *"Off-route mines"*

However, not all anti-tank mines can be buried if the ground or surface is unsuitable. "Off-route mines" are useful in this case as they are designed to be effective when detonated next to the vehicle instead of underneath[30]. Off-route mines employ either a SC or EFP to focus the effect of the explosion such that the vehicle armour is penetrated. Although the term "off-route mine" refers to specifically manufactured AT mines, most improvised explosive devices (IEDs) are "home built" according to the same principles[32]. IEDs are proving to be the novel enemy of armoured vehicles, becoming increasingly popular in urban warfare.

Figure 2.14 – Photograph of a home built IED composed of an EFP [32]

2.3.2.4 *Injury mechanisms related to AV landmines*

During the event of an anti-vehicle landmine blast, it is possible for the average acceleration of a medium-sized armoured vehicle floor to exceed 100g and the velocity of the floor to exceed 12m/s [8]. Owing to such high accelerations of the vehicle, the occupants of the vehicle will subsequently be affected by the overpressure shock wave resulting from the explosion as well as the movement of the vehicle. Most common injuries are closed fractures of the upper extremities and especially the lower extremities[8], as depicted in Figure 2.15.

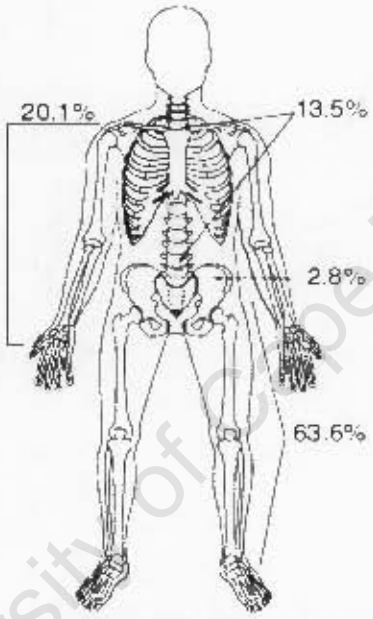

Figure 2.15 – Illustration of the distribution of fracture sites sustained by occupant of armoured vehicle that detonated a landmine [8]

Injuries sustained by occupants of an armoured vehicle during a mine blast are due to four main effects of the explosion, which is illustrated in Figure 2.16. The four effects created by the explosion underneath the vehicle include[8]:

- the blast overpressure,
- missiles from the landmine and fragments from the elastic deformation of the vehicle,
- translational blast injuries caused by the movement of the vehicle and the occupants
- toxic fumes released by combustion of Teflon coated interior of certain armoured vehicles.

The injuries imposed upon the occupants of an armoured vehicle experiencing a mine blast are classified according to the criteria given in Table 2.3.

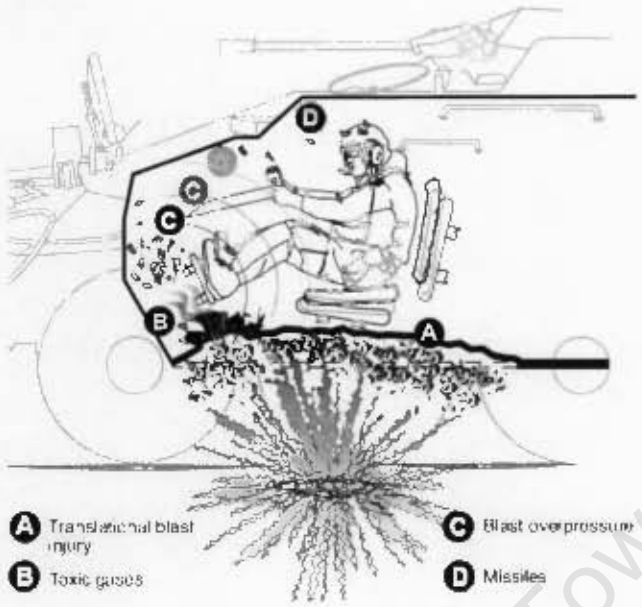

Figure 2.16 – Illustration of injuries sustained as a result of defeated armour [8]

Classification of injury	*Reason*	*Duration after detonation*	*Body regions affected*
Primary	*Blast overpressure wave / Shock wave*	*5 – 40 ms*	*Ears, lungs, hollow gastrointestinal organs*
Secondary	*Elastic deformation (missiles / projectiles)*	*10 – 35 ms*	*Skin penetration, blunt trauma to body*
Tertiary	*Vehicle & occupant movement*	*15 – 100 ms*	*Lower extremities, spine, neck and head*

Table 2.3 – Classification of injuries [8;26]

The nature of the injuries induced upon the occupants of an armoured vehicle subjected to a landmine blast is explained as follows[8;26]:

- **Primary injuries** are induced by the overpressure shock wave and impulse caused by the detonation of the explosives. Usually the injuries include rupture of the middle ear and damage to the lungs, trachea, larynx and abdominal cavity.
- **Secondary injuries** result from projectiles dispersed from the landmine itself. These projectiles may cause laceration or penetration of the skin and blunt trauma to the body.
- **Tertiary injuries** usually occur after the detonation of the landmine caused the vehicle to travel upwards and hit the ground at high velocity. The dramatic vehicle movement causes whole body movement and distinct impact of the occupants, which causes most damage to the body.

2.4 HUMAN LOWER LEG ANATOMY

The human foot and ankle consists of 26 bones, 33 joints, more than 100 muscles, tendons and ligaments and a vast network of blood vessels, nerves, skin and soft tissue[34]. These complex components are designed with the structural intent to provide the rest of the body with mobility, support and balance. The foot is flexible, yet resilient and able to sustain high pressure loads, whereas the ankle essentially acts as a shock absorber.

2.4.1 Foot bones

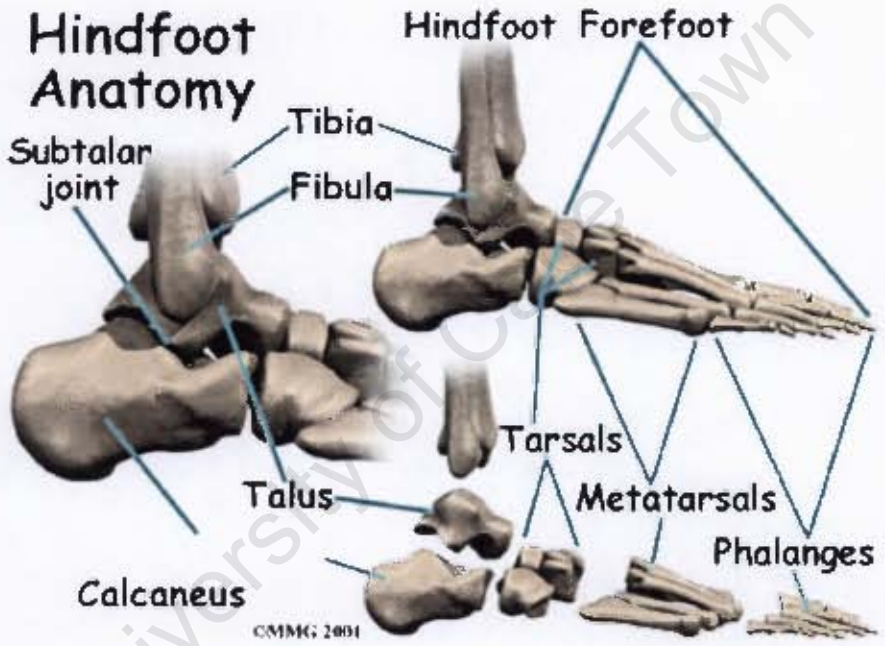

Figure 2.17 – Illustration of the anatomy of the human foot, showing the hindfoot and forefoot [34]

The structure of the foot can be divided into three main sections, the forefoot, midfoot and hindfoot[34]. The forefoot consists of the five toes (*phalanges*) which are connected to the long bones (*metatarsals*) at the ball of the foot. The midfoot is composed of five *tarsal* bones which locks and unlocks to support the foot under different types of load conditions. The hindfoot comprises of the ankle bone (*talus*) and the heel bone (*calcaneus*). The *calcaneus* connects to the *talus* at the subtalar joint, which allows the foot to flex inwards and outwards. Finally, the top of the *talus* is connected to the *tibia* and *fibula* (the two long bones of the lower leg) to work like a hinge, allowing upwards and downwards flexion of the foot.

The design of the ankle joint is similar to a *mortise and tenon* construction typically used by craftsmen to make structurally strong items[35]. In normal stance body weight is essentially distributed evenly between the hindfoot and forefoot, with the pressure being balanced on the heel and the ball of the foot.

Figure 2.18 – Illustration of the human ankle represented by mortise & tenon joint [35]

2.4.2 Foot tendons, ligaments and muscles

A collection of tendons, ligaments and muscles are arranged in the foot to hold the bones together while also enabling movement of the foot[34]. Ligaments attach bones to bones and tendons attach muscle to bone. The large Achilles tendon connects the calf muscle to the calcaneus and is the most important tendon for physical actions such as walking, running and jumping. Various other smaller tendons attach to the layers of muscle in the foot to support the foot arches and to allow movement of the ankle, foot and toes.

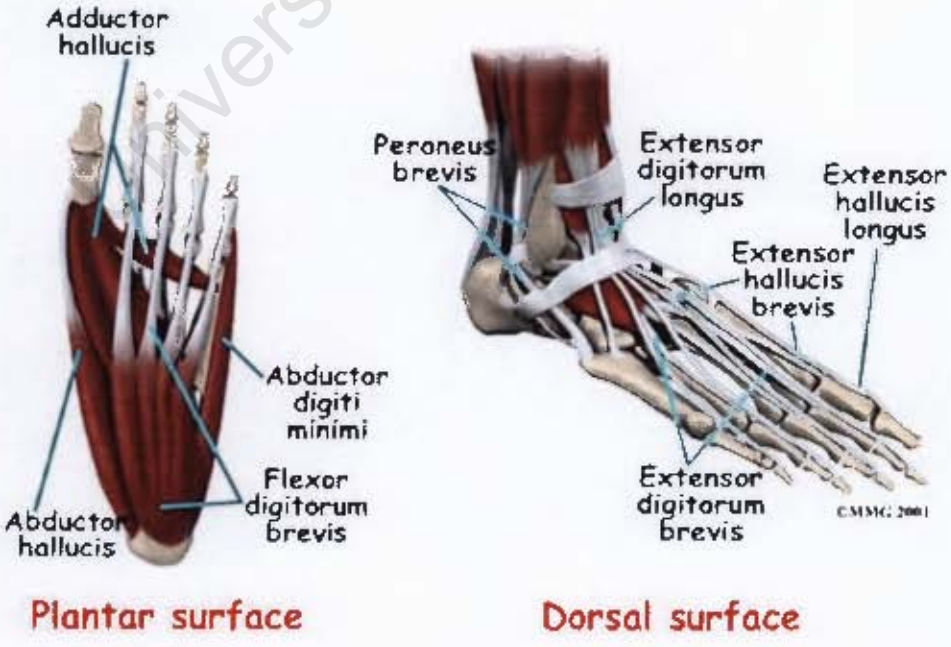

Figure 2.19 – Illustration of the muscles in the human foot [34]

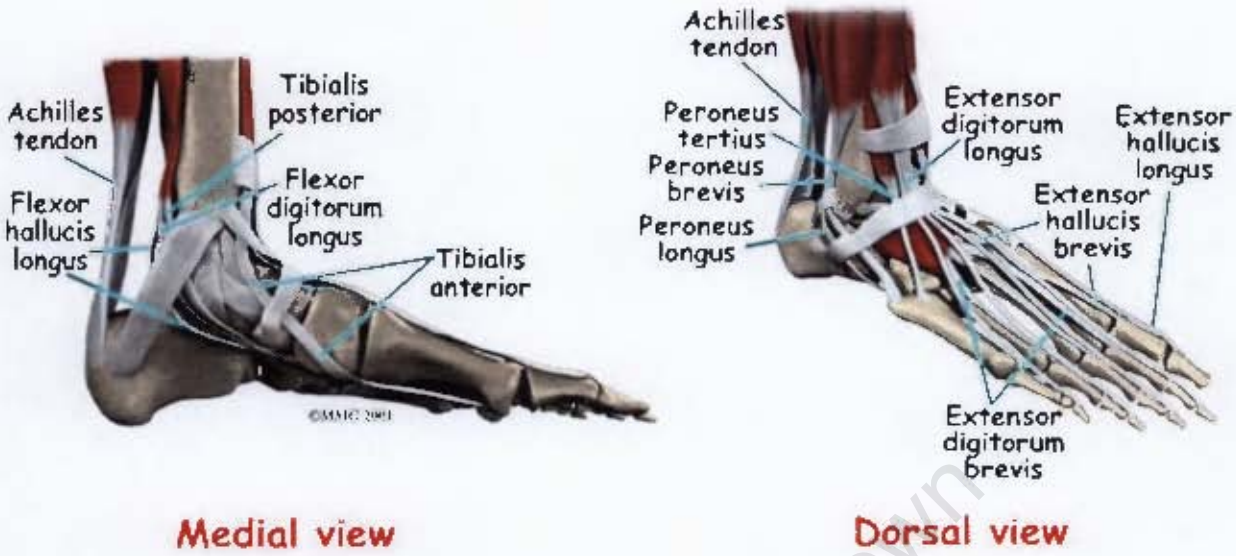

Figure 2.20 – Illustration of the tendons in the human foot [34]

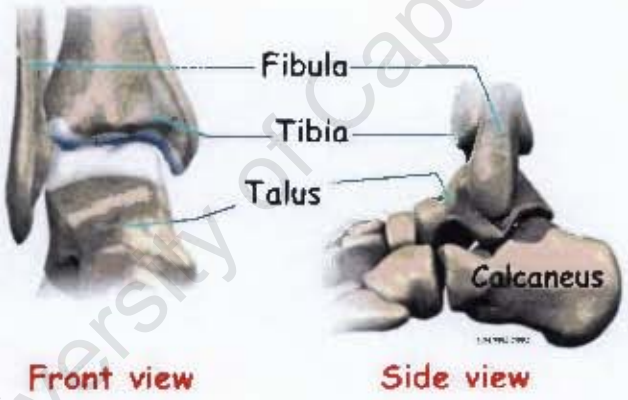

Figure 2.21 – Illustration of the bones comprising the human ankle [35]

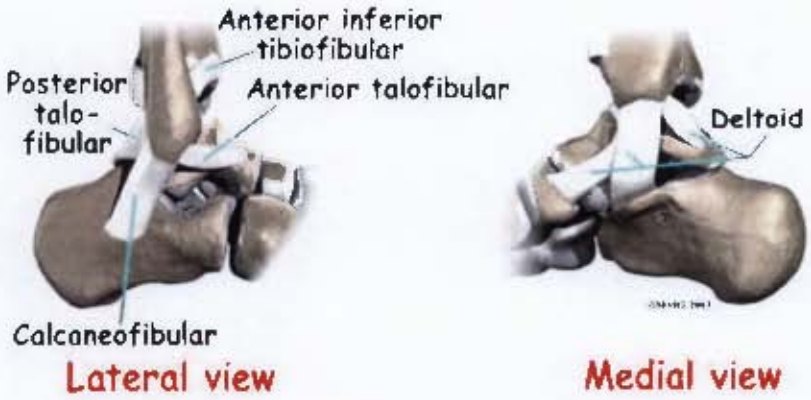

Figure 2.22 – Illustration of the ligaments present in the human ankle [35]

2.4.3 Movement of the foot

The human foot is capable of five main motions[34;35]:

- **Movement of the toes** – The metatarsal phalangeal joint forms the ball of the foot and also allows for movement of the toes. Numerous small muscles layered on the sole of the foot work together with the tendons around the toes to move the toes up and down.
- **Dorsiflexion** and **plantarflexion** – The strong muscles in the lower leg and the anterior tibial tendon allows the foot to be flexed upward (termed dorsiflexion) by approximately 30° and downwards (termed plantarflexion) by approximately 50°. Up and down flexion is made possible by the *talus* fitting in between the lower ends of the *tibia* and *fibula*, forming a hinge.
- **Eversion** and **inversion** – Two tendons run behind the outer bump of the ankle and attach to the outside of the foot, enabling the foot to be turned outwards by about 15° (termed eversion). The posterior tibial attaches the calf muscle to the underside of the foot, enabling the foot to turn inwards by about 20° (termed inversion). The talus connects to the calcaneus at the subtalar joint, allowing inversion and eversion of the foot.

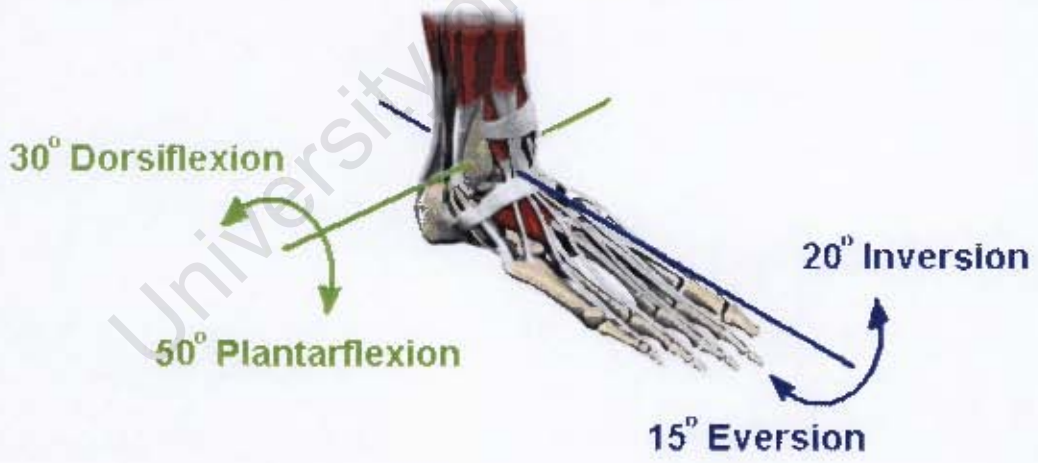

Figure 2.23 – Illustration of the planes of rotation of the human ankle joint

2.5 EXISTING REPRESENTATIONS OF THE HUMAN LOWER LEG AND TEST PROTOCOLS

Human data for mine loading conditions are not available, therefore experimental and numerical studies using different lower leg models aim towards improved confidence in mine protection research. In order to test and examine protective footwear effectively, it is necessary to have specific evaluation criteria[13]. Most importantly, the threat/protection combination together with the chosen test procedure used must relate to the expected medical outcomes or severity of injury. Whether the victim steps directly on an AP landmine or is seated inside a vehicle exposed to an AV/AT mine blast, the lower extremities are bound to experience primary injury during the landmine explosion. It is therefore essential that the test model employed must be able to evaluate the response in the lower leg.

Surrogate test models can be mechanical, frangible or cadaver models of the human body[13]. Mechanical models are reusable and used for initial testing, frangible models for more detailed analysis and human cadaver models are used to validate the results of the prior testing procedures. Each of these surrogate models has a specific test method to extract the desired information from the test.

2.5.1 Mechanical lower leg models

Mechanical legs are reusable test devices that primarily represent the dimensions and mass of the human leg[13]. Blast testing result in aggressive loading being imposed on the leg, therefore mechanical legs are generally constructed out of rugged materials, such as steel, to survive the explosive testing. Using reusable test devices is both cost effective and time efficient, making mechanical legs ideal for initial evaluation of protective footwear, vehicle occupant safety, etc.

Testing of protective footwear was initially performed by using mechanical legs, with this first kind of surrogate leg being used by the Netherlands, United Kingdom, United Stated of America and Canada in the 1990's [13]. These initial mechanical surrogate legs generally consisted of two metal tubes (representing the upper and lower leg) joined by a mechanical joint (the knee). Gelatine filled the space between the metal foot and the protection to represent the soft tissue of the human foot and lower leg. High-speed imaging was then used to assess the response of the mechanical leg. Figure 2.24 shows an illustration of one of the earliest mechanical legs designed by the Netherlands[13].

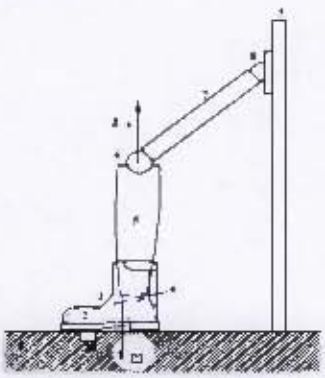

Figure 2.24 – Illustration of the Netherlands mechanical leg [13]

2.5.1.1 Canadian mechanical leg

The DRDC (Defence Research and Development Canada) mechanical leg is used by Canada as a screening tool and is constructed out of a combination of metallic and polymeric materials[13]. The tibia is represented by an aluminium tube and a urethane cast represents the foot and calf, allowing a combat boot to be fitted.

An explosive charge is buried at a certain depth or flush with the ground surface and detonated to simulate an AP landmine blast. The response of the DRDC leg is measured by strain gauges attached to the aluminium tube and accelerometers placed in the ankle unit.

Figure 2.25 – Photograph of the DRDC mechanical lower leg model [13]

2.5.1.2 Crash test dummies

Cadaver and animal testing were performed from as early as the late 1930's and yielded valuable information that was eventually used to construct the first representation of the human body in 1949 with the creation of "Sierra Sam" [36]. Sierra Sam was a mechanical test device designed to test aircraft ejection seats and pilot restraint harnesses, but ultimately paved the way of developing more humanlike anthropomorphic test devices (ATDs), such as the Hybrid series of crash test dummies. Although these ATDs are originally designed for automobile impact testing, the Hybrid-III dummy fitted with either the Denton lower leg or the Thor-Lx lower leg have widely been used in the evaluation of protective footwear and in assessing occupant loading in a vehicle subjected to an AV/AT mine blast[8].

- The **Denton lower leg** is shown in Figure 2.26, from which it can be seen that the tibia shaft is offset from the centres of the knee and ankle joint[37]. Dorsiflexion/plantarflexion and inversion/eversion motion originates from a single ball joint.
- The design of the **Thor-Lx lower leg** (also shown in Figure 2.26) is based on the latest biomechanical data, providing the leg model with more biofidelic characteristics[37]. The Thor-Lx has an element to simulate biofidelic axial load response in the tibia, the location of the dorsiflexion/plantarflexion and inversion/eversion joint centres of rotation is separated and an Achilles tendon is included to represent the muscle resistance to dorsiflexion. Internal and external rotation is also possible.

Denton lower leg ***Thor-Lx lower leg***

Figure 2.26 – Photographs of the Hybrid-III Denton and Thor-Lx lower legs [37;38]

The Test Rig for Occupant Safety System (TROSS) shown in Figure 2.27 is developed by IABG (Lichtenau, Germany) [8]. TROSS is one of the acclaimed systems used to study and analyse the response of the Denton and Thor-Lx lower legs subjected to AV landmine blast loading. The full Hybrid-III dummy, with both the H-III Denton and Thor-Lx lower legs attached, is seated on a seat that is fixed to the enclosure of the rig. The feet of the dummy rest on a footplate attached to the base plate under which an explosive charge is detonated. The floor structure is decoupled from the rest of the rig in order to eliminate shock effects on the rig enclosure and so seat motion would not affect the loading in the lower leg. A known relationship exists between the explosive charge used and a real AV landmine (2kg – 10kg TNT) detonated under a light armoured vehicle, therefore the loads induced upon the Hybrid-III dummy can be compared to what a human body would experience[8]. The response of the Hybrid-III Denton and Thor-Lx lower leg is monitored by accelerometers and load cells placed in strategic areas of the leg.

Figure 2.27 – Photographs of the Test Rig for Occupant Safety Systems (TROSS) showing the test setup of the Hybrid-III dummy [8]

Tibia force results obtained from AV landmine blast testing using the TROSS system and the Hybrid III surrogate ranged from 3709N (low severity test with a boot on the foot) to 10740N (high severity without a boot on the foot) [8]. A series of linear impact tests utilising the Hybrid III Denton lower leg and the Thor-Lx lower leg model were performed by Wayne State University[8] in an attempt to reproduce the TROSS test results. The Hybrid III surrogate was positioned according to Figure 2.28 to conduct the linear impact tests. Footplate displacement and the axial tibia force were the key parameters that needed to be matched to ensure the lower limb was being subjected to a similar impact.

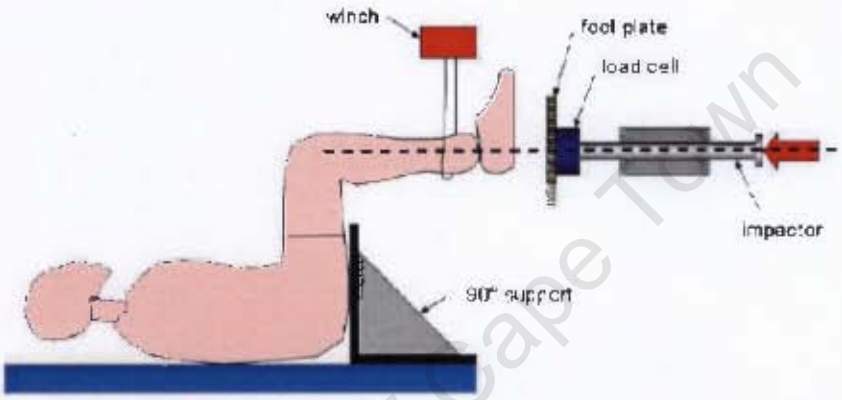

Figure 2.28 – Illustration of the positioning of surrogate for linear impact testing performed to compare to impact testing utilising the TROSS system [8]

Figure 2.29 and Figure 2.30 show the comparison of the data recorded during the TROSS tests and the linear axial impact tests. The first graph depicts the tibia force history recorded by the Hybrid-III lower leg (with boot) for the low severity tests and the second graph the tibia force history recorded by the Hybrid-III lower leg (with boot) for the high severity tests. The summary of the results from the tests using the linear impactor is displayed in Table 2.4.

		H-III Denton leg		*H-III Thor-Lx*	
Severity	***Avg impactor velocity***	Tibia force	Ankle force	Lower tibia force	Upper tibia force
Low (no boot)	*3.8m/s*	*6520 N*	*8905 N*	*2972 N*	*2414 N*
Low (with boot)	*3.8m/s*	*3833 N*	*4439 N*	*2504 N*	*2303 N*
Medium (no boot)	*4.7m/s*	*10017 N*	*13782 N*	*3845 N*	*2910 N*
Med (with boot)	*4.7m/s*	*6052 N*	*7576 N*	*3194 N*	*2601 N*
High (with boot)	*8.3m/s*	*9897 N*	*12165 N*	*5309 N*	*3706 N*

Table 2.4 – Results from the Hybrid III Denton and Thor-Lx testing with the linear impactor [8]

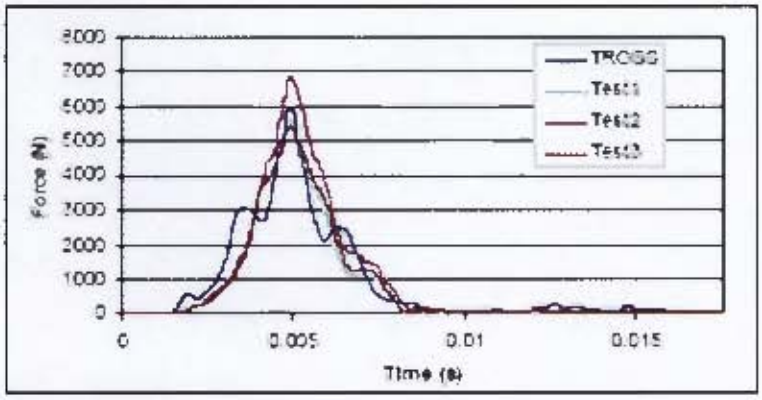

Figure 2.29 – Graph comparing linear impactor data with TROSS test data, low severity load [8]

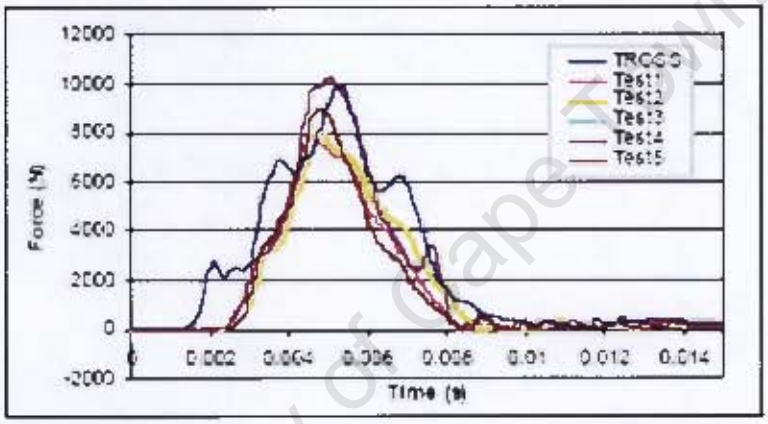

Figure 2.30 – Graph comparing linear impactor data with TROSS test data, high severity load [8]

The typical axial force experienced by a Hybrid III surrogate seated in a Canadian light-armoured vehicle subjected to an AV blast mine detonation is shown in Figure 2.31 below.

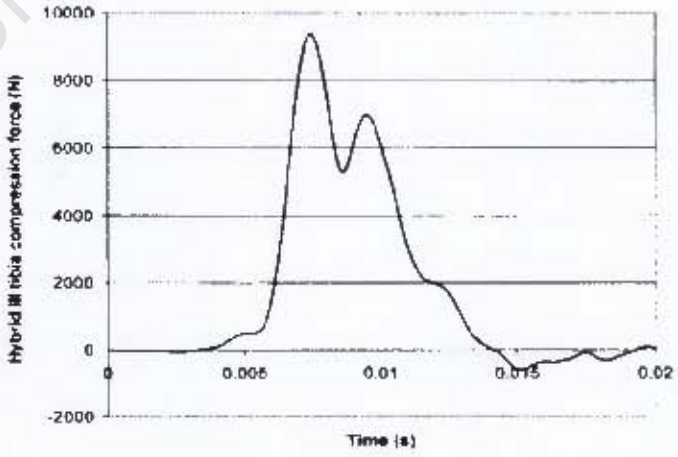

Figure 2.31 – Graph of the tibia force measured by H-III seated in light armoured vehicle during mine blast [39]

The Hybrid-III Denton leg has also been used in other test applications to test the effects of an AV landmine detonation. Canada employed the H-III Denton leg in conjunction with the Complex Lower Leg (a frangible lower leg model which is discussed later) in a series of tests using an air cannon and sled/rail system as the impact test device[39]. Compressed air is exhausted from the tank, pushing the piston (a rod placed inside the barrel of the air cannon) forwards against a sled. The sled then slides freely along the rail towards the target intended for impact. In order to position and secure the Denton leg a femur load cell simulator is fixed to the target table and the leg is inserted into the simulator.

2.5.2 Frangible lower legs

The term *frangible* means that the object is capable of being broken. This implies that a frangible leg model approximates the human leg geometry, material properties, bone fracture and tissue disruption[13]. Frangible leg models are designed specifically to perform similar to a human leg under the same loading conditions. Response of the frangible leg is monitored during testing using a combination of accelerometers, load cells, strain gauges and high-speed imaging. After testing is completed, "injuries" incurred upon the frangible leg can be examined using autopsy-based procedures.

2.5.2.1 Complex Lower Leg (CLL)

The CLL was originally developed to examine AP landmine injuries, but it was later also used to evaluate foot/ankle injuries induced upon occupants of an armoured vehicle experiencing an AV landmine blast[13;39]. The main objective of the design of the CLL was to select appropriate synthetic materials that can represent the bone and soft tissues of the human leg[13]. A single polymeric bone with suitable cross-sectional area and strength represents the tibia and fibula, and the foot and ankle complex incorporates a talus and calcaneous according to human geometry. The leg design also incorporates a nylon tendon, silicone rubber cartilage and heel pads, soft tissue and a latex skin layer. Although the CLL was designed to correspond to the geometry and material properties of the human lower leg, simplicity of the design was maintained to increase consistency between tests and reduce costs. Earlier versions of the CLL included instrumentation, but currently the CLL is examined using an autopsy-based procedure.

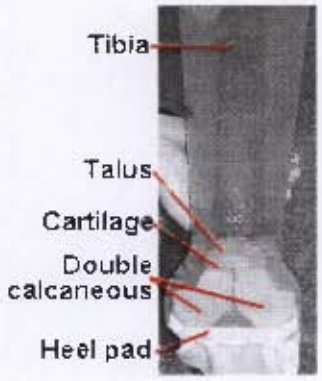

Figure 2.32 – Photograph of the Complex Lower Leg components [39]

Canadian researchers employed the sled/rail test rig (discussed in the Section 2.5.1) to simulate the impact produced by an AV mine blast on the floor of the vehicle[39]. High severity testing was performed by applying axial impact at a velocity of 5m/s to a rectangular steel plate at the base of the so-called heel pad of the CLL. Typical results of the high-velocity impact tests are shown in Figure 2.33 and Figure 2.34.

Figure 2.33 shows that calcaneous fracture occurred during two of the tests[39]. One test however produced talus fracture without calcaneous damage, which is unexpected in AP mine injuries. Overall, the injuries predicted by the CLL were not as severe and complex as the injuries documented to be sustained by PMHS (Post Mortem Human Surrogates) tests preformed under the same impact test conditions. This can be attributed to the fact that the CLL model is more resistant than the cadaver leg models and the biofidelity of the bone mechanical properties of the CLL need to be improved[39]. Figure 2.34 clearly shows the high stiffness of the Hybrid III leg compared to the more biofidelic CLL surrogate, which suggests that a tibia force of approximately 17kN and 10kN would induce significant fracture of the foot/ankle complex in the H-III leg and CLL respectively.

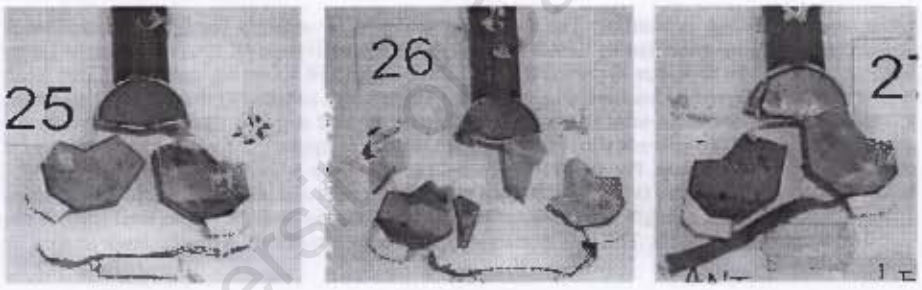

Figure 2.33 – Photographs of CLLs after high severity impact testing [39]

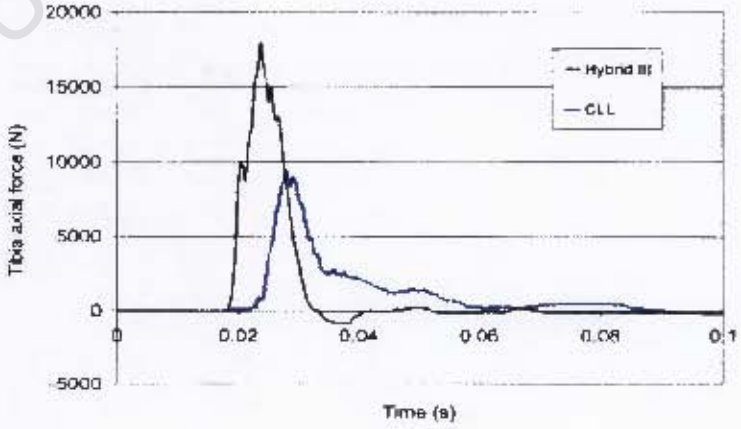

Figure 2.34 – Graph comparing Hybrid III and CLL tibia axial force results from high severity impact testing [39]

2.5.2.2 *Simplified Surrogate Leg (SSL)*

DRDC in Canada developed the SSL to evaluate landmine protection[13]. The SSL model was essentially the starting point for the evolution towards developing the Complex Lower Leg CLL. The SSL is a simplified representation of the human leg, consisting of a central bone structure to represent the tibia, fibula, calcaneous and talus. The soft tissues of the lower leg are represented by a concentric volume of gelatine that surrounds the bone structure. Reaction of the leg during testing is recorded by strain gauges on the bone, high-speed imaging and x-ray imaging.

Figure 2.35 – Photograph of Simplified Lower Leg [13]

2.5.2.3 *Frangible Surrogate Leg (FSL)*

The Defence Science and Technology Organisation (DSTO) in Australia developed the FSL which is an exact representation of the 50th percentile Australian male leg[13]. All the major bones, tendons and muscles are included in the surrogate model. The bones are manufactured from mineralised plastic, the muscles from ballistic gelatine, the tendons from elastic materials and the skin is simulated with a heavy nylon mesh that is melted into the outer layer of the gelatine.

Figure 2.36 – Photographs of DSTO Frangible Surrogate Leg, showing the accurate bone structure and joints fitted with strain gauges, and the bones enclosed in gelatine [12]

The Canadian Centre for Mine Action Technologies (CCMAT) started the Lower Extremity Assessment Program (LEAP) to evaluate and categorise the effectiveness of existing mine-protective footwear and to document the process of the injury to the lower leg during a landmine

blast[12]. To date the LEAP data has formed the most complete dataset pertaining to injury to the lower extremities. Cadavers were used in LEAP, which were very difficult to work with, as this type of tests could only be performed at specialised institutions within strict legal and ethical borders. Some sort of replacement leg model that would still produce results similar to that of the cadavers was needed; therefore a number of FSLs were bought and tested by CCMAT[4;12]. As such, the ethical constraints were eliminated, as well as the need for medical staff and special facilities.

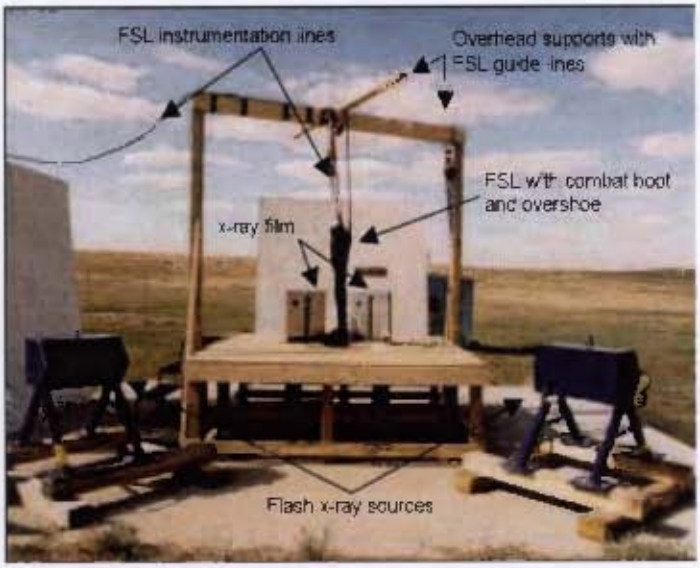

Figure 2.37 – Photograph showing the experimental setup for FSL blast tests [12]

Testing of protective footwear using the FSL is performed according to the test setup shown in Figure 2.37. Essentially the surrogate leg supports its own weight, and a sand box is placed underneath the leg. The landmine is placed directly below the heel of the leg and buried at a specific depth or flush with the surface. After each test, the area needs to be combed to retrieve the pieces of the boot and FSL fragments. Strain gauges, load cells and accelerometers are used to analyse the response of the leg during blast testing and the trauma to the leg is thereafter inspected by a surgeon using an autopsy-based procedure.

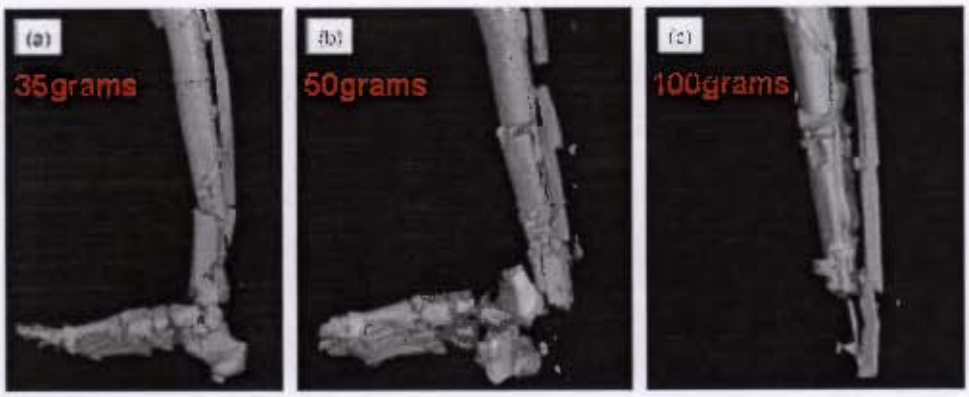

Figure 2.38 – X-ray images showing the internal damages to the FSL with boot/overshoe combination for the (a) PMA-3, (b) 50g C4 and (c) PMA-2 [12]

The injuries shown in Figure 2.38 are experienced by the FSL after being exposed to 3 different AP landmine detonations. The pictures in Figure 2.38 are specific to a series of tests conducted to evaluate the protection provided by wearing a standard boot and overshoe during a landmine blast[12]. The graphs provided in Figure 2.39 shows a good correlation exists between the results obtained from the FSL tests with the LEAP test results, indicating that the FSL can be used as a practical tool to analyse the performance of a human leg experiencing an AP landmine blast[12].

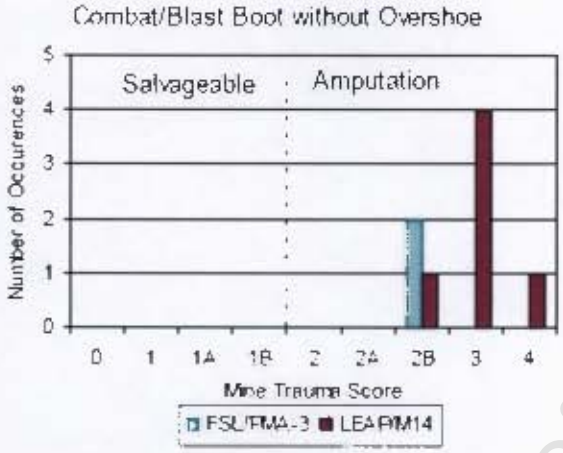

(a) Results for tests using M14/PMA-3 mines

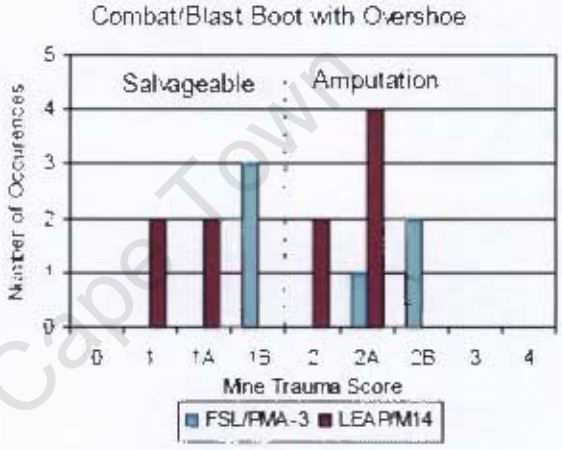

(b) Results for tests using M14/PMA-3 mines

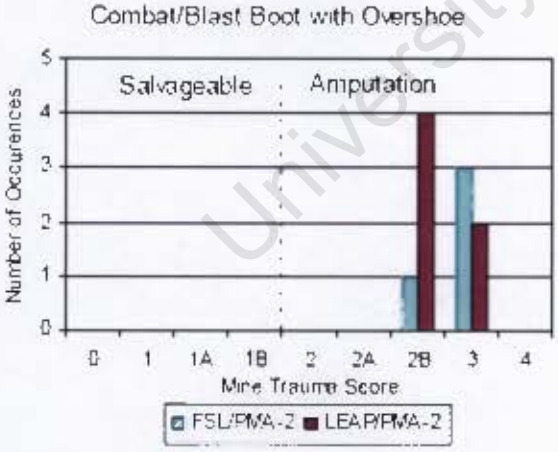

(c) Results for tests using PMA-2 mines

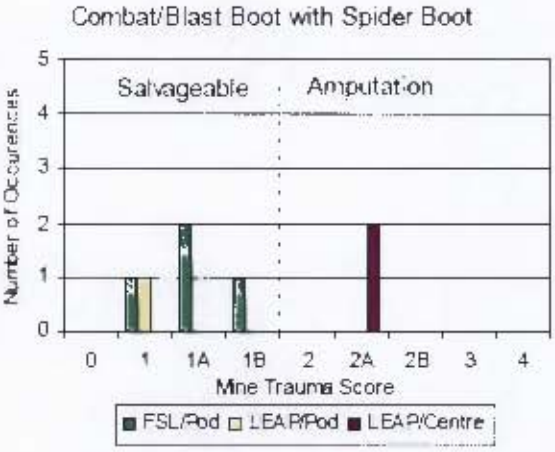

(d) Results for tests using PMA-2/PMN mines

Figure 2.39 – FSL vs. LEAP test results for using different combinations of protective footwear against AP landmine blast [12]

2.5.3 Cadaver lower legs

Commercial production of automobiles began in the 1890s, making the automobile part of daily life but on the other hand causing the number of motor vehicle deaths to become a serious issue. Cadaver testing started in the late 1930s at Detroit's Wayne State University to collect data about the effects of high-speed collisions on the human body[36]. The first biological test devices were human cadavers that were subjected to rudimentary test procedures, such as steel ball bearings being dropped on skulls and bodies being dropped down unused elevator shafts onto steel plates[36].

Blast testing using human cadavers to document the effects of a landmine explosion on the human body effectively only started in the late 1990s with the institution of the LEAP program[6]. Biological test devices include isolated human lower limbs and also whole body cadavers. Using cadaver models proves to be particularly successful in evaluating protective footwear, as the geometry and material properties are superb representations of the living human[13]. Mechanical properties of the bone and soft tissue might differ slightly though from the living human due to the age or presence of pre-existing diseases in the donor.

2.5.3.1 *Whole body human cadaver model*

Ethical constraints, availability and the ability to test with full body human cadaver models generally hamper testing of this nature. However, in the United States of America a number of full body human cadaver tests was carried out in the Lower Extremity Assessment Program (LEAP) with successful results[13]. Usually the cadavers are received in the "fresh frozen" state after which they are thawed, instrumented and tested in a suitable time period in order to preserve the mechanical and material properties of the various human tissues. The response of the human cadaver is monitored by strain gauges in the knee and ankle regions, and a load cell in the tibia. The instrumentation of the cadaver is illustrated in Figure 2.40. After testing, the trauma caused by the mine blast can be assessed through an autopsy.

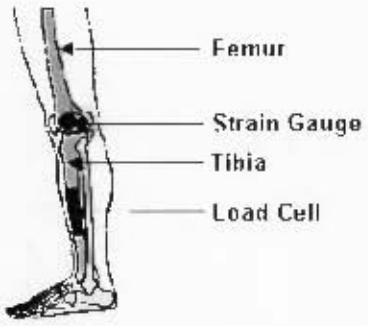

Figure 2.40 – Illustration showing instrumentation of the full body human cadaver model [13]

2.5.3.2 *Isolated human lower leg model*

Researchers from the United Kingdom assessed footwear protection concepts by using amputated human lower legs, the amputations being either above or below-knee due to peripheral vascular disease[13]. Using isolated lower limb cadavers instead of full body human cadavers ensure the mechanical properties of the bone and soft tissues have not degraded due to age; and handling of the specimens are much easier. The lower limb cadavers are mounted at or close to the knee joint for testing, and an autopsy procedure are used after the testing to examine the injuries.

Axial impact tests on cadaver lower limbs and the Hybrid-III dummy lower leg were also conducted at the Medical College of Wisconsin[10]. The main objective of the study was to determine the dynamic stiffness and damping properties of the human cadaver lower leg and the H-III dummy leg, as well as to characterise the axial force response ratio between the cadaver legs and the H-III leg. The leg specimen was attached to a mini-sled that was free to slide on a rail after being impacted by a pendulum, as shown in Figure 2.41. The pendulum impacted the plantar surface of the foot with velocities ranging from 2.2 m/s – 5.6m/s. In order to record the accelerations and forces at the plantar surface of the foot and the proximal leg, load cells and accelerometers were attached to the pendulum and the mini sled.

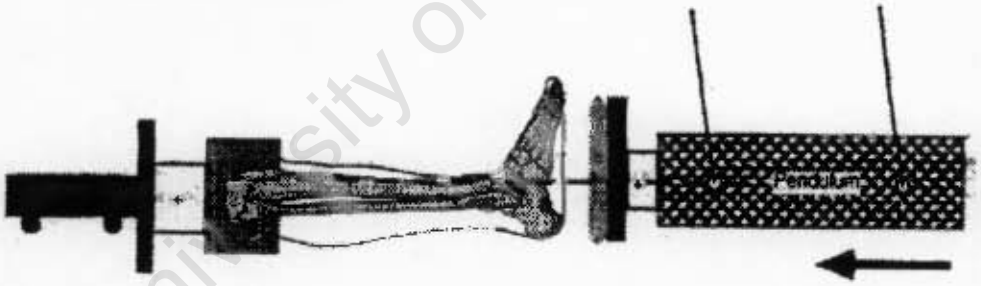

Figure 2.41 – Illustration of setup for the axial impact tests at the Medical College of Wisconsin[10]

The velocity and impact energy was kept the same in each of the comparative tests. The graph in Figure 2.42 shows that the H-III dummy lower leg experienced higher force at the proximal end than the cadaver lower leg during each of the tests[10]. As the mass difference between the H-III leg and the cadaver leg is minimal (the H-III leg weighing 11.2kg and the cadaver leg 11.5kg), the results therefore clearly imply that the dynamic stiffness and damping properties of the cadaver and dummy leg differ greatly[10].

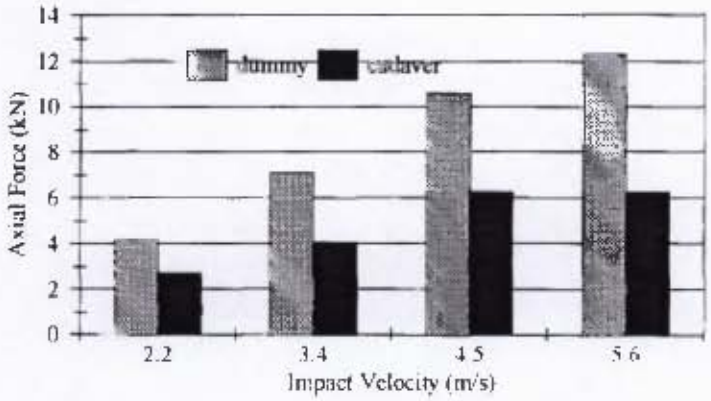

Figure 2.42 – Graph comparing human cadaver and H-III dummy responses under similar impact conditions [10]

Wayne State University used human cadaver lower leg specimens and conducted axial impact tests in a similar way to establish human response corridors[8]. All the lower limbs were cut roughly 7 inches above the knee at the femur, a load cell was implanted approximately midshaft and the cadaver leg specimen was fixed into a device specially designed to fit onto the Hybrid-III dummy[8]. The test apparatus setup employed is shown in Figure 2.28. The results obtained from the Hybrid III and Thor-Lx lower leg surrogates subjected to the same test conditions were then compared to the human response corridors. The graphs shown in Figure 2.43 and Figure 2.44 illustrate that the Thor-Lx leg model produces a better biofidelic response to axial impact than the Hybrid III leg model.

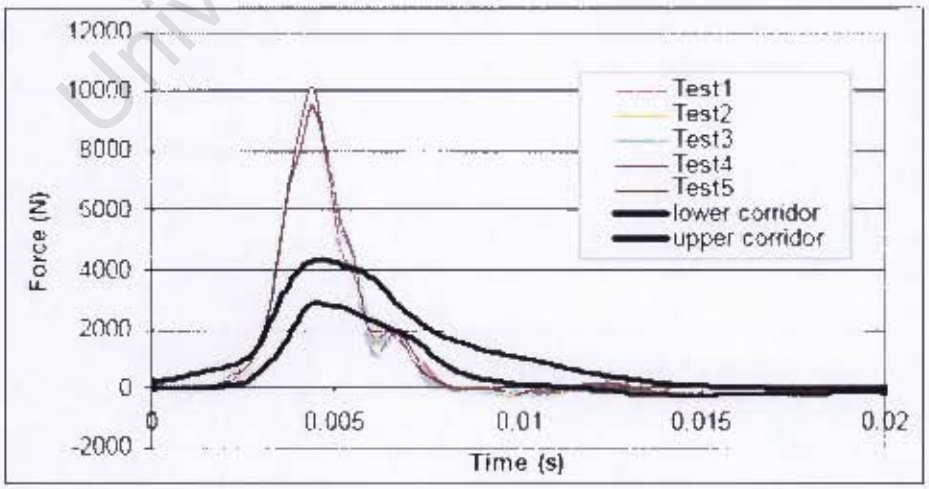

Figure 2.43 – Graph comparing force-time histories of Hybrid III lower leg surrogate to human response corridors [8]

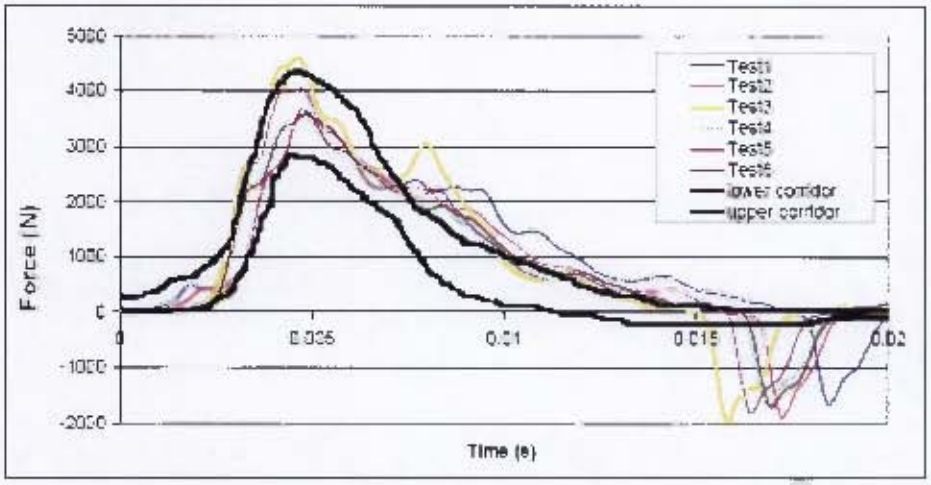

Figure 2.44 – Graph comparing force-time histories of Thor-Lx lower leg surrogate to human response corridors [8]

2.5.4 Numerical representation of lower leg

The mine blast essentially consists of two events following close after one another; the detonation of the explosives and the resulting interaction of the pressure wave with the human leg[13]. Experimental testing is vital in the assessment and development of landmine protective wear. However, developing protective wear purely by experimental means can be costly and time consuming, and measuring the detailed response of the complex structures (such as the leg and protective footwear) during an explosive event is very difficult.

Extensive effort is currently being put into validating numerical models of the human body response to high loads over short time periods with real life data. Ultimately, numerical modelling aims at providing a cost and time effective tool for the assessment of mine protection and trauma to the human body exposed to mine blast. An example of the analytical value of utilising numerical modelling to study the effects of a landmine blast is shown in Figure 2.45.

- Part (a) illustrates the sequence of events caused by the detonation of an actual AP landmine under the foot of a person.
- Part (b) shows results of a numerical simulation of an SSL model experiencing an AP landmine blast with the time frames correlating to that of the real landmine blast event.
- Part (c) shows photographs taken from the high speed video footage of an SSL model exposed to the detonation of a landmine. It is generally expected that high speed video footage of the blast event would provide helpful information, but as Figure 2.45 shows, the view might be obscured during critical fractions of time[40].

Correlation of the results retrieved from the numerical blast simulation to the physical results obtained from the blast tests performed using human cadavers and surrogate leg models is of utmost importance to ensure the accurate analysis of the physics and effects of the blast event.

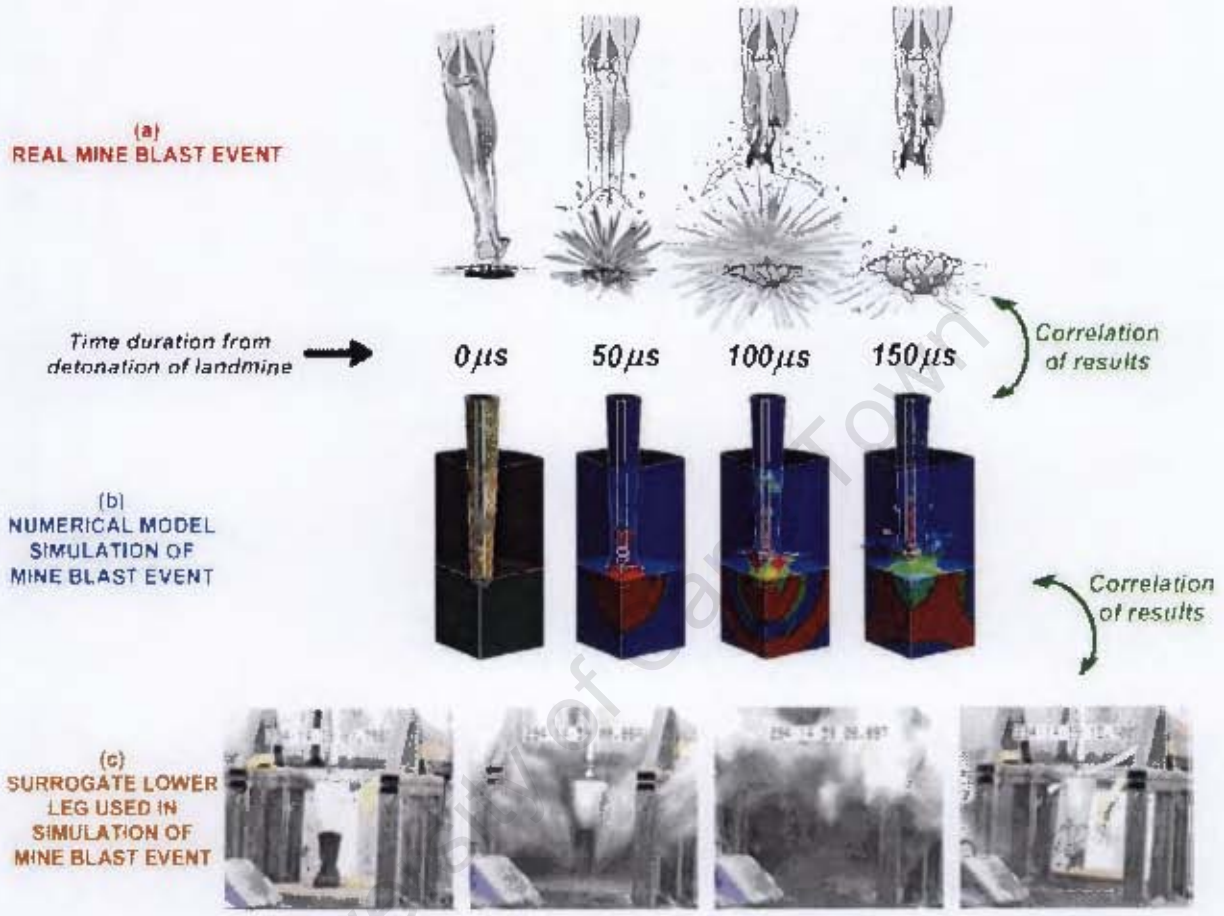

Figure 2.45 – Correlation of actual mine blast response[5] with a numerical model[40] and the high speed video of the blast and resulting injury to the SSL model[40]

Figure 2.46 – Photograph of TROSS test setup and Madymo simulation setup [8]

One of the commercially available simulation codes used to assess occupant response in a vehicle subjected to crash loading is Madymo, which is a TNO Automotive engineering software tool[41]. Madymo is a multi-body computational code that is based on the Hybrid III surrogate fitted with the Denton leg[41]. The data retrieved from the AV landmine blast tests conducted using the TROSS (as discussed in Section 2.5.1) were used to validate the Madymo Hybrid III Denton leg model for axial impact caused by an AV mine detonation.

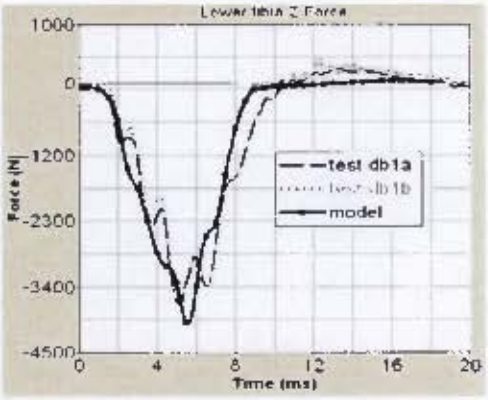

(a) Results for low severity AV mine test

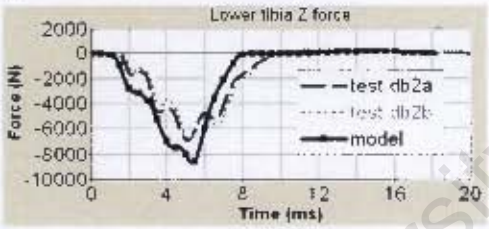

(b) Results for medium severity AV mine test

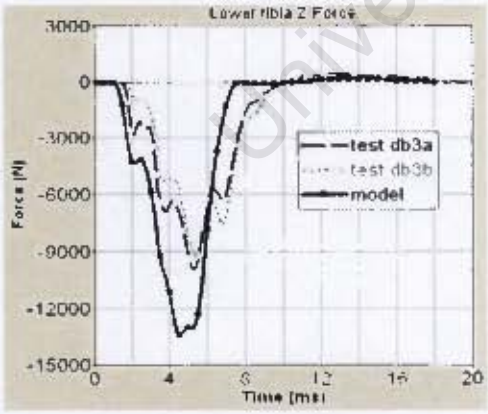

(c) Results for high severity AV mine test

The Madymo Hybrid III 50th percentile male dummy with Denton leg model was placed in a simplified model of the TROSS, as shown in Figure 2.46 [42]. The data from the medium severity test with the dummy wearing boots were used as the base for the validation. The vertical acceleration experienced by the foot and tibia and the compressive load in the tibia were considered as the main parameters to compare the experimental data to the data obtained from the Madymo simulations.

Figure 2.47 shows the comparison of the results from the low, medium and high severity TROSS tests and Madymo simulations (with the Denton leg wearing a boot) [42]. The results clearly indicate the increase in induced loads due to the increase of blast load. Varying the contact friction between the foot and the footplate proved to be insignificant, but varying the contact damping showed that employing low damping at the foot yields the best results. The increased effects of contact damping at higher loading conditions are evident from the results (Figure 2.47 (c)), as the difference in tibia forces increases from low severity to high severity testing.

Figure 2.47 – Graphs comparing the TROSS and Madymo results for AV mine detonation [42]

Human computational impact simulation codes are also available. such as:

- SIMon (Simulated Injury Monitor) developed by NHTSA (National Highway Traffic Safety Administration), which is designed to aide new advanced mechanical surrogates and interpret the enriched experimental output data obtained from the tests[41].
- THUMS (Total Human Model for Safety) developed and tested by the Toyota Research Company, which is a relatively detailed model that is based on Toyota research and models created by Wayne State University[41].
- Madymo human models, which consist of various combinations of detailed multi-body and finite element segments[41].

An international attempt is however being made to standardise the methodology for modelling the human body for impact biomechanics and vehicle occupant safety, in the form of the HUMOS project[41]. The aim is not to create specific numerical models, but rather to build a data base which contains characteristics, properties, guidelines and rules regarding geometry acquisition, the meshing process, material property assignment and validation of the human body segments. A first definition of a finite element model of the human body (known as the H-Model) in a seated driving position has been developed. which was put into practice with the Madymo dynamic crash code, amongst others[41]. Details of the lower extremity models are shown below in Figure 2.48 and Figure 2.49.

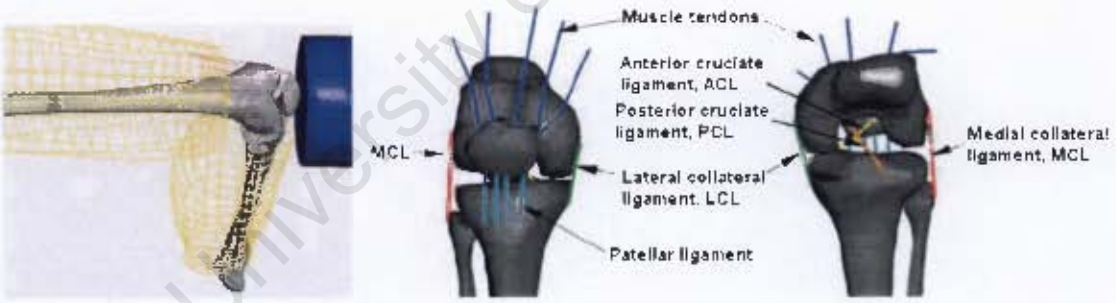

Figure 2.48 – Illustrations of the knee joint and ligaments used in the HUMOS model [41]

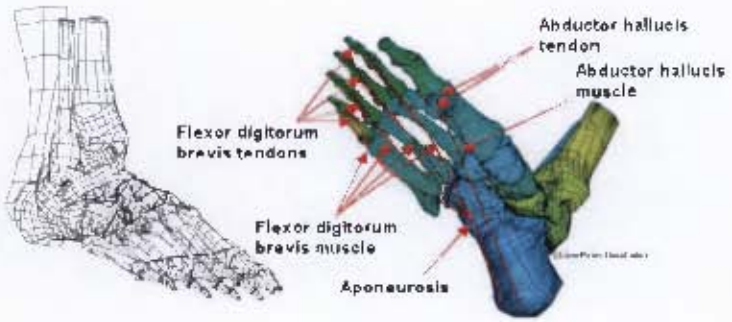

Figure 2.49 – Illustrations of the foot and ankle model used in the HUMOS model [41]

2.6 LANDMINE PROTECTIVE FOOTWEAR

Although personal protective equipment (PPE) is not available to all soldiers and civilians finding themselves in a mine-threat area, deminers responsible for the clearance of landmines require protection in the case of accidental detonation of the explosive ordnance. After the first AP landmines were used during the early 1900's, soldiers tried to devise their own protective footwear by using materials such as lumber and rope[7]. A 6-inch sabot attachment for the combat boots was developed in the early 1950s by the U.S. Marine Corps, after which the U.S. Army developed and assessed protective shanks in the 1960s[7].

Design of mine protective footwear has developed significantly since then, with the effectiveness being highly advertised by the manufacturers. Testing however showed that none of these specially designed boots are capable of preventing severe injury to the lower leg but that they can provide a reduction in injury severity, especially with smaller explosive charges[7].

Mine protective footwear strategies are categorised according to their safety mechanism, although none of the boots strictly utilises only one independent method[7]. The safety techniques employed in the boot designs are intended to:

- Deflect the blast away from the limb in contact with the landmine; e.g. Wellco® Blast Boot alone.
- Reduce the blast by using either certain materials that will decrease the energy transmitted by the blast through the change in their physical state or by the destruction of the boot itself; e.g. Wellco® Over Boot.
- Create a standoff distance between the limb and the mine blast by either elevation or off-axis detonation; e.g. BFR boot and the Med-Eng Spider Boot™.

Examples of various mine protective footwear are discussed in limited detail in the next section.

2.6.1 Standard Army Combat Boot

The standard combat boots issued to the infantry is not designed to provide any protection against AP landmine blasts[7:43]. Therefore, when 21 gram C-4 (equivalent to 28 gram PE4) is detonated underneath a standard combat boot, the result will be a severely injured lower limb as shown in Figure 2.50.

Figure 2.50 – Photograph of the effect of 21 gram C-4 detonated under a standard army combat boot [43]

2.6.2 Wellco® Blast Boot

Sandwiched between the specially shaped polyurethane outer sole and the multi-layer Kevlar innersole is a wedge of metallic honeycomb attenuator, as shown in Figure 2.51 [43]. Blast tests conducted on aluminium-honey comb-aluminium sandwich specimens proved that the maximum deflection induced upon the rear aluminium surface (in this case the rear surface would be the top surface in contact with the insole and the honey comb) is greatly reduced due to the energy absorbing properties of the honey comb (refer to Section 2.8 of this report). The layered sole composition of the Wellco® Blast Boot therefore directs the blast away from the leg and absorbs energy from the blast, helping to minimise the effects of an AP landmine explosion.

Figure 2.51 – Photographs of Wellco® Blast Boot, showing detail of the protective sole [43]

Wellco® conducted several test at the U.S. Army Aberdeen Test Centre[43]. The surrogate landmines used during testing contained 21 gram of C-4 (equivalent to 28 gram PE4). Notice that the blast attenuator absorbed most of the energy and the rest of the sole is still intact.

Figure 2.52 – Photograph of Wellco® Blast Boot after 21 gram C-4 was detonated under the heel [43]

2.6.3 Wellco® Over Boot

The Over Boot shown in Figure 2.53 is designed to be worn over a standard army combat boot or over the Blast Boot for maximum protection[7;43]. The polyurethane sole is fused directly to the Nylon-Kevlar upper and rubber studs are imbedded in the sole bottom to create a vented and cleated surface. Two layers of stainless steel covers an aluminium honeycomb attenuator that is sandwiched between the outer sole and multi-layer Kevlar inner sole. The Over Boot is designed to create deflection and attenuation of the landmine blast and create additional standoff distance from the blast.

Figure 2.53 – Photograph showing the Wellco® Over Boot [43]

The same tests that were performed on the Wellco® Blast Boot were performed on the Wellco® Over Boot[43]. The Over Boot was used in combination with a standard army combat boot and also with the Blast Boot. The results in Figure 2.54 showed that the attenuator absorbed most of the blast energy, leaving the standard combat boot and the Blast Boot virtually undamaged. However, as the amount of explosives increase, the Blast Boot and Blast Boot-Over Boot combination does not prevent internal fractures or traumatic amputation (Figure 2.55) [12].

Figure 2.54 – Photographs of blast test results of the Standard Army Combat Boot/Over Boot combination and the Wellco® Blast Boot/Over Boot combination [43]

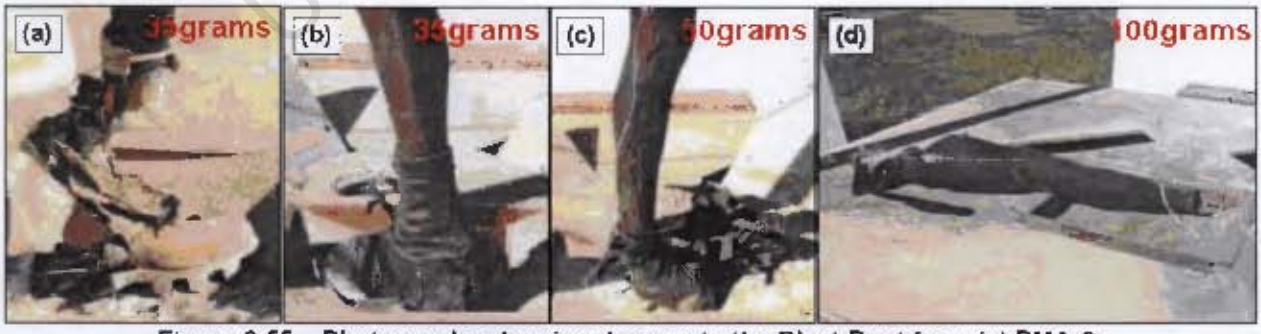

Figure 2.55 – Photographs showing damage to the Blast Boot from (a) PMA-3; and the Blast Boot-Over Boot combination from (b) PMA-3 (c) 50 gram C4 (d) PMA-2 [12]

2.6.4 BFR-40 protective combat boot

The Blast and Fragment Resistant (BFR) protective combat boot has a unique protective sole system which is based on specially woven fabric bonded together with specifically designed sole and heel plates and a heel plug (shown below in Figure 2.56) [44]. The materials help to provide a certain amount of protection against blast temperatures generated by an AP landmine explosion. The safety features of the BFR boot also incorporate an intermediate protection system in the upper lining of the boot.

Figure 2.56 – Photographs of the BFR protective combat boot, showing the construction of the heel [44]

The BFR boots were tested by the Royal Military College of Science in the United Kingdom against different explosive charge sizes representing different AP landmines[44]. Explosives were independently detonated underneath the ball and heel of the foot. The tests showed that although wearing the BFR protective boots were not uniformly successful, the BFR boots mitigate the blast injuries to such an extent that even though soft tissue and skeletal damage still occur, the integrity of the lower limb might be maintained. It is therefore concluded that the BFR protective boot do provide considerable protection against hot gas streams, high-velocity fragments and debris resulting from the explosion.

Figure 2.57 – Photographs of the testing of the BFR protective boot against an AP landmine detonation [44]

2.6.5 Med-Eng Spider Boot™

The blast overpressure wave generated by the detonation of explosives is known to decay exponentially with increasing distance from the explosive source (discussed in Section 2.2.4). The Spider Boot illustrated in Figure 2.58 utilises the advantages of creating a stand-off distance in the boot design[7;45]. The Spider Boot consists of a platform mounted to a nominal height of 144mm on a deflector shell and two forward and two rear protruding legs, each ending in a rubber pod. The blast wave and fragments are vented away from the foot via the fragment resistant shell through the front and rear protruding pods. Most of the residual energy is also absorbed through the sacrificial materials on the underside of the Spider Boot.

The Spider Boot is designed to be worn with regular footwear, and the design is such that it permits demining operations over a diversity of terrain.

Figure 2.58 – Illustration showing the anatomy of the Med-Eng Spider Boot™ [45]

Blast tests to evaluate the Spider Boot were performed at Defence Research Establishment Suffield[45]. The photographs in Figure 2.59 show that the two front pods were broken and the front end of the Spider Boot was damaged after the detonation of the PMA-1 under the right front leg, but the standard combat boot was undamaged. Figure 2.60 shows similar results after the PMA-3 was detonated under the rear right leg of the Spider Boot. The two rear pods were severed, but the combat boot sustained no damage.

Figure 2.59 – Photographs of PMA-1 AP mine (200 gram TNT) under the front right pod of the Spider Boot, showing pre-detonation and post-detonation [45]

Figure 2.60 - Photographs of PMA-3 AP mine (35 gram Tetryl) under the rear right pod of the Spider Boot, showing pre-detonation and post-detonation [45]

2.6.6 Comparison of protective footwear

The graph in Figure 2.61 shows the effect of charge mass on the resultant acceleration experienced at the ankle of the surrogate leg while each of the abovementioned protective footwear was worn[45]. The results provided are relative to a blast protective boot which is based on a standard military combat boot fitted with an enhanced sole.

The resulting acceleration for a detonation under the rear right pod (RRP) of the Spider Boot proves to be higher than the acceleration experienced by the detonation of the same amount of explosives under the front right pod (FRP) of the Spider Boot. The Spider Boot results therefore emphasise that a target closer to the detonation experiences higher blast loading.

The test results indicates the following percentage differences in the ankle acceleration experienced due to the detonation of 25g C4 while wearing the various blast protective boots[45]:

- Detonations under the front and rear pods of the Spider Boot while wearing a regular army combat boot reduced ankle acceleration by >90%.
- Detonation under the heel of the Blast Boot with Overboot (2cm overburden) reduced ankle acceleration by >30%.
- Detonation under the heel of the Blast Boot with Overboot (no overburden) reduced ankle acceleration by ≈40%.
- Detonation under the heel while wearing only the Blast Boot increased the ankle acceleration by >60%.

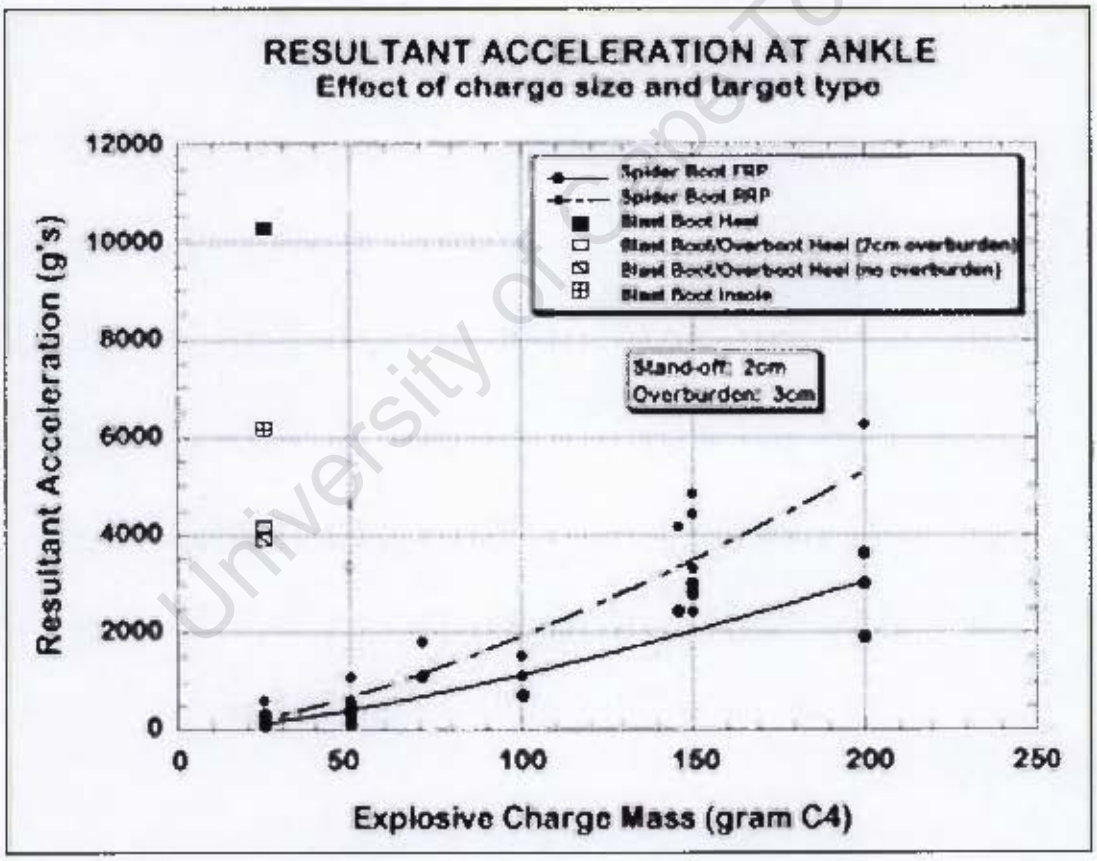

Figure 2.61 – Graph showing resultant accelerations at the ankle of the surrogate leg with different foot protection systems [45]

2.7 INJURY CRITERIA

Currently there exists no universally accepted injury classification and coding system among any known databases[46]. The majority of the injury classification schemes focus on the description, severity and mechanism of the injury. The most established and widely used scheme is the AIS, which is an anatomical scoring system where the scores are assigned in terms of "threat to life" associated with a single injury[46]. As such the AIS scores do not represent a comprehensive measure of severity where the combined effects of multiple injuries on one person are taken into account. To score the overall injury severity of a single injured person, the Injury Severity Score and the Maximum AIS (both systems are derivatives of the AIS) are used[46].

The AIS classifies the injury according to the body region, the type of and specific anatomic structure, details of the wound and the severity of the injury[46]. A numerical identifier is assigned to each category, while the severity of the specific injury is ranked on a 6-point scale (given in Table 2.5). The 7th digit is provided to code "Unknown".

Injury	*AIS Score*
1	*Minor*
2	*Moderate*
3	*Serious*
4	*Severe*
5	*Critical*
6	*Not survivable*
7	*Unknown*

Table 2.5 – Table of Abbreviated Injury Scale scores [46]

2.7.1 Mechanical test devices

Evaluating impact effects on the critical regions of the lower extremities produced criteria which help to indicate when fatal injury would occur due to severe loading conditions. Kuppa et al.[37] proposed injury criteria and limits for the 50th percentile male at 25% and 50% probability of experiencing AIS2+ injuries. The injury criteria attempt to assign a load limit which could induce moderate to serious injuries to the specific anatomic structure. The load limits related to the lower extremity anatomic structures are presented in Table 2.6.

The criteria and performance limits of the Hybrid III Denton and Thor-Lx lower leg surrogates are also given in Table 2.6, as these two lower leg models have been successfully utilised in extensive automotive crash and blast load impact testing. The injury criteria shown below in Table 2.6 are mainly intended for assessing lower extremity injuries experienced by an occupant in a vehicle subjected to a landmine blast.

		50th percentile male[37]		***Denton[37]***	***Thor-Lx[47]***
Body region	Injury criteria	25% prob	50% prob	Threshold	Threshold
Hip/femur/knee	*Axial femur force*	*9040 N*	*11150 N*	*9070 N*	*9040 N*
Knee ligament	*Knee/fibula shear*	*~*	*15 mm*	*15 mm*	*15 mm*
Tibia plateau	*Upper tibia axial force*	*5600 N*	*7000 N*	*8000 N*	*5600 N*
Tibial/fibula shaft	*(Revised) Tibia index, (R)TI*	*0.91*	*1.16*	*1.0*	*0.91*
Ankle/midfoot/ calcaneous	*Lower tibia axial force*	*5200 N*	*6800 N*	*8000 N*	*5200 N*
Ankle/malleolus	*Dorsiflexion*	*~*	*60Nm/35deg*	*~*	*35deg*
	Inversion/eversion	*~*	*40Nm/35deg*	*~*	*35deg*

Table 2.6 – Table of injury criteria related to human surrogate impact testing

2.7.2 Cadaver and FSL test devices

The LEAP tests performed by CCMAT were used to generate the Mine Trauma Score (MTS) to classify the lower leg injury caused by a mine blast[6]. After each blast test was performed, the cadaver leg was inspected by surgeons using an autopsy procedure to record the extent and type of damage induced upon the lower leg.

The MTS system is similar to the AIS system in the sense that the severity of an individual injury is scored using numerical identifiers. The MTS employs a nine score system, where the number from 0 to 4 describes the level of amputation required and the letter A or B indicates the level of soft tissue contamination[6]. The MTS score system is provided in Table 2.7.

- A closed injury (using numbers 1 or 2 without a letter) does not violate the skin and pose a minimal risk of infection, although internal bone fractures might be present.
- An open contained injury (denoted by letter A) is any injury where the skin is lacerated or torn, but contamination from external debris has been minimised because the inner footwear was not breached.
- An open contaminated injury (denoted by letter B) is when the footwear was breached, the skin is violated and contamination by external debris is visible.

MTS Score	Contamination level	Injury assessment
0	Minimal	No major surgery required
1	Closed	Salvageable limb
1A	Open contained	
1B	Open contaminated	
2	Closed	Below knee amputation
2A	Open contained	
2B	Open contaminated	
3	Open contaminated	Below or above knee amputation
4	Open contaminated	Above knee amputation

Table 2.7 – Table with definitions of the Mine Trauma Score for the lower extremity [6]

The chief objective of the MTS system is to assess lower leg injuries related to the direct blast impact of an AP landmine. The LEAP tests used three levels of explosive content to represent blast AP landmines: small (M-14, 29 gram), medium (PMA-2, 100 gram) and large (PMN, 240 gram). A general range of footwear was tested, including unprotected footwear (an improvised sandal, standard US Army Combat Boot), mine-protected boots (Wellco® Blast Boot, BFR-40 boot) and boot supplements (Wellco® Over Boot, Med-Eng Spider Boot™). The MTS grading of the various LEAP tests are documented in Table 2.8.

	Range of MTS scores obtained for AP landmine blast		
Footwear	M-14 (29 g)	PMA-2 (100 g)	PMN (240 g)
Combat Boot alone	3 - 4	Not tested	3
Sandal	2B	Not tested	4
Blast Boot alone	2B	Not tested	Not tested
BFR boot alone	2B - 3	Not tested	Not tested
Over Boot combinations	1 – 2A	2B - 3	2A – 3
Spider Boot combinations	Not tested	2A	1 – 2A

Table 2.8 – MTS results of LEAP tests with different footwear [6]

2.8 ATTENUATION PROPERTIES OF METALLIC HONEY COMB

The results of blast impact tests performed on metallic honey comb specimens to investigate the blast attenuation properties of honey comb are presented in Figure 2.62 [48]. The difference between having the honey comb section sandwiched between two 1.6mm mild steel layers and using the honey comb layer independently were assessed. The graph in Figure 2.62 shows that the maximum deflection experienced by the rear surface of the specimen during a high applied impulse is reduced by employing the *mild steel - aluminium honey comb - mild steel* sandwich setup. The attenuating effect of the metallic honey comb is therefore an ideal safety mechanism to be utilised in the design of blast protective boots.

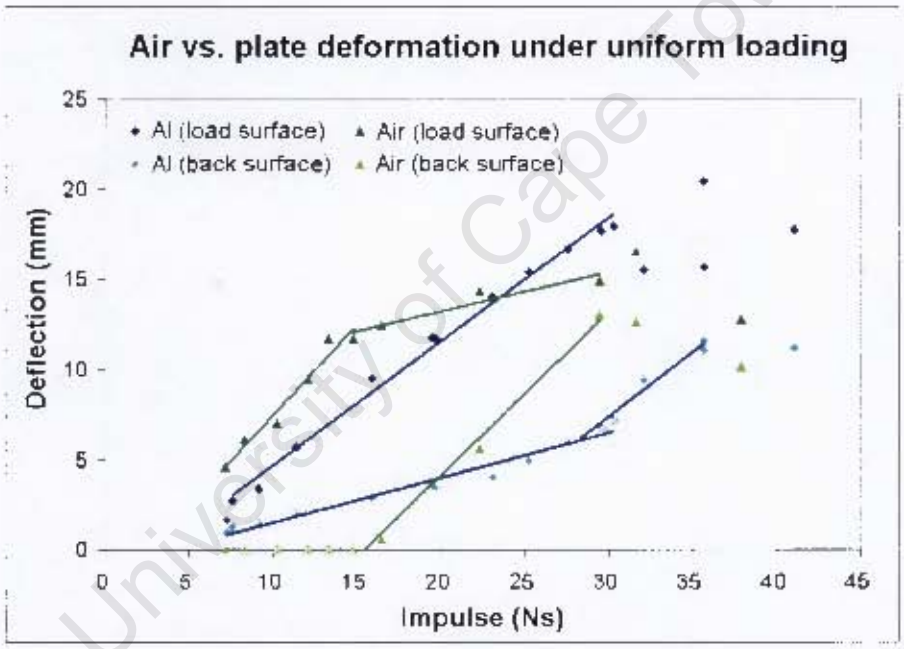

Figure 2.62 – Graph showing attenuation effects of honey comb against blast load [48]

2.9 UNIAXIAL COMPRESSION STRESS VERSUS STRAIN BEHAVIOUR OF RUBBER-LIKE MATERIALS

Figure 2.63 shows the range of strain rates of interest to material scientists and the associated test methods used to obtain the particular strain rate. The research of this thesis is focused on the effect of blast loading, which falls in the $10^3 s^{-1}$ to $10^4 s^{-1}$ strain rate range, and using the SHPB has become the standard test method for dynamic material characterisation[49]. Quasi-static material testing using conventional cross-head machines are also performed in order to generate material data over a broad spectrum of strain rates.

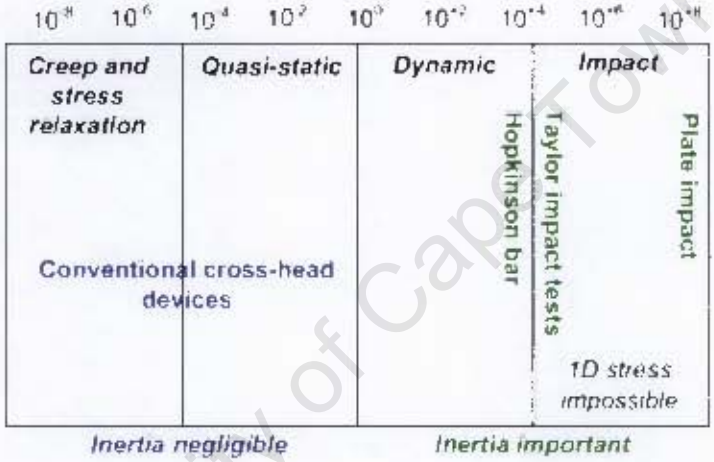

Figure 2.63 – Test techniques developed to obtain specific strain rate regimes [49]

Experimental investigation of the mechanical stress-strain response of low impedance materials such as natural rubber, polyethelene and plastics date back to the pioneering studies of Kolsky[50] and his contempories[50]. As with high impedance metallic and non-metallic materials, the response of low impedance materials are studied at various strain rates and temperatures. However for the present investigation, the effect of the strain rate on the mechanical properties of rubber is of more importance as the material characterisation of rubber will be conducted.

Mobility of the polymer chain on atomic and macroscopic scale is the reason for the visco-elastic nature of amorphous rubbers. The inherent strain rate sensitivity of rubbers is strongly related to its microstructure, as the strain rate sensitivity is a sign of the time required for these polymer chains to reorientate themselves[51]. Low strain rates give the chains ample time to reorientate themselves, whereas high strain rates limit deformation of the chains to bending and stretching of the chemical bonds. These properties of rubber materials are the cause for little

change being noticed in the mechanical behaviour when experiencing strain rates in the range of 10^{-3} to $10^{-1}s^{-1}$, but the Young's modulus becoming more sensitive and increasing by a factor of 8 when the strain rate is increased to $3x10^{3}s^{-1}$ [51].

2.9.1 *Low and medium strain rate test results*

Uniaxial low and medium strain rate testing is generally performed using a hydraulic or screw driven testing machine. Low strain rate testing is done by compressing the specimen at a rate of approximately $0.001s^{-1}$ to $1.0s^{-1}$, while medium strain rate testing allows the specimen to be compressed at a rate of approximately $50s^{-1}$. A static hyperelastic constitutive equation can be used to represent the behaviour of rubber under quasi-static deformation[52]:

$$\sigma_{11} = 2\lambda(1-\lambda^{-3})\{A_1\lambda - A_2 - A_3[I_1 - 3 + \lambda(I_2 - 3)]\} \quad \text{Eq. 2.8}$$

where the relationship between engineering stretch λ and strain ε_{11} in the direction of the applied load is $\lambda = 1 + \varepsilon_{11}$ [52]. A least squares method were used to fit the data obtained from compression tests done on specimens of SHA30 (soft rubber) and SHA70 (stiff rubber) at $0.001s^{-1}$ strain rate to the hyperelastic formulation (Eq. 2.8) in order to solve for the A_1, A_2 and A_3 parameters. Comparing the experimental data with the analytical results proves good correlation, as shown in Figure 2.64. More experimental and analytical results of rubber in quasi-static compression (where a visco-hyperelastic formulation is employed) are given in Figure 2.65 and Figure 2.66.

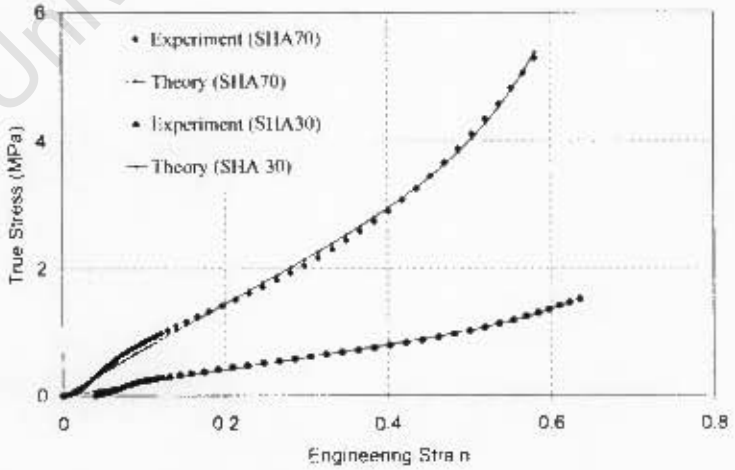

Figure 2.64 – Graph comparing the hyperelastic rubber material model to data from quasi-static material testing of SHA30 and SHA70 performed at $0.001s^{-1}$ [52]

2.9.2 High strain rate test results

High strain rate testing of materials are generally conducted utilising the SHPB to achieve dynamic strain rates of up to approximately $5x10^3$ [49]. The main purpose of the SHPB is to deform the specimen between two bars excited above their resonance, the bars staying elastic while the specimen is subjected to large strains. The theoretical details required to perform material characterisation using the SHPB are given in Section 2.10.

Dynamic testing of rubber and like materials using the SHPB shows that the specimens effectively return to the same geometric state after unloading and that the residual strains are insignificant, indicating that the stress-strain behaviour of the rubber specimen can readily be described by a visco-hyperelastic material model[52]. Visco-hyperelasticity stems from combining the characteristics of quasi-static hyperelasticity (σ^e) and dynamic rate-dependent viscoelasticity (σ^v), resulting in the expression below[52]:

$$\sigma_{11} = \sigma_{11}^{e} + \lambda^2 \int_0^t \lambda\left[A_4 + A_5(I_2 - 3)\right]\exp\left(-\frac{t-\tau}{A_6}\right)\dot{\lambda}\,d\tau + \frac{1}{2}\lambda^{-1}\int_0^t \lambda^{-2}\left[A_4 + A_5(I_2 - 3)\right]\exp\left(-\frac{t-\tau}{A_6}\right)\dot{\lambda}\,d\tau \qquad \text{Eq. 2.9}$$

where σ_{11}^{e} is equal to Eq. 2.8 and $\dot{\lambda} = \dot{\varepsilon}_{11}$. Data obtained from uniaxial dynamic compression SHPB tests performed on SHA30 and SHA70 rubber specimens were used to determine the A_4, A_5 and A_6 parameters via a least-squares fit[52]. Good correlation between the experimental high-strain rate data from the SHA30 and SHA70 rubber specimens and the analytical results is evident from Figure 2.65 and Figure 2.66.

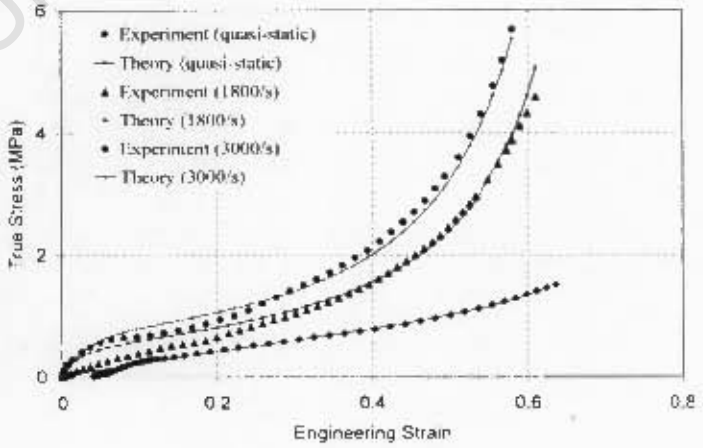

Figure 2.65 – Graph comparing the visco-hyperelastic material model to dynamic strain rate data from SHPB testing of SHA30 rubber [52]

Various material models representing the mechanical behaviour of rubber-like materials exist which can be used in the numerical simulation of the response of rubber. Quasi-static response are generally modelled by employing material laws such as those developed by Mooney and Rivlin as well as Ogden[53]. The Ogden material model describes a broad spectrum of strain hardening characteristics, but the Mooney-Rivlin model is unsuitable for simulating responses that entails strong strain hardening characteristics[51]. However, during high-strain rate activity, the inherent strain rate dependence of rubber materials becomes noticeable. It also has to be taken into account if the strain rate varies according to the location, especially during impact simulations[53]. In order to compensate for this type of characteristic behaviour of rubber material, viscous terms need to be introduced to generalise the Ogden material model, resulting in a large amount of parameters that need to be identified for the specific material[53].

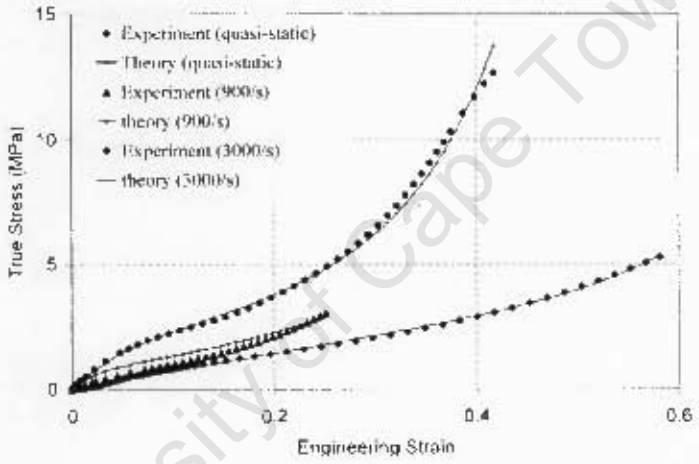

Figure 2.66 – Graph comparing the visco-hyperelastic material model to dynamic strain rate data from SHPB testing of SHA70 rubber [52]

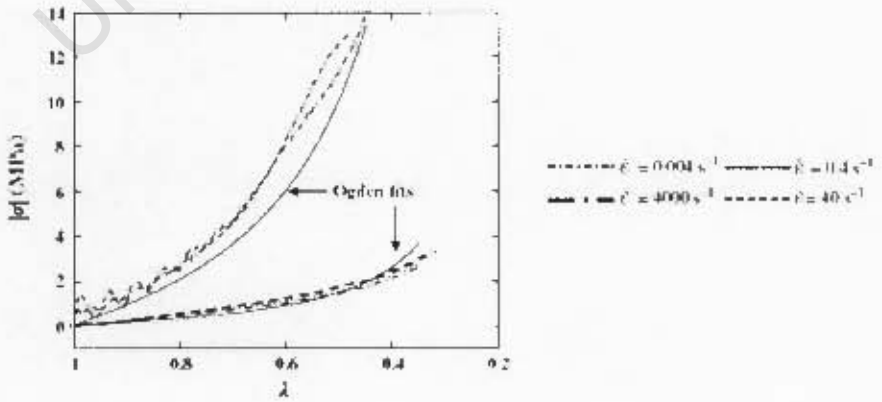

Figure 2.67 – Graph comparing the experimental stress-strain data of B452 silicone rubber to numerical results using the Ogden rubber material model [49]

2.10 Material Characterisation using the Split-Hopkinson Pressure Bar

In circumstances where materials are exposed to sudden impacts, it is required to discern how the material properties depend on the rate at which strain is applied. Knowing the material properties of engineering materials at high loading rates is therefore of great importance, since these characteristics will determine the mechanical behaviour of the material in question.

Mechanical properties of materials are generally measured by conducting load tests in compression, tension or torsion[54]. Various testing methods exist that can be used to achieve constant loading rates for limited plastic strains, therefore producing a constant engineering strain rate. Testing at strain rates of above 200 s^{-1} however requires a more unconventional technique where stress-wave propagation is induced in the specimen by direct or indirect projectile driven impact[54]. The Split-Hopkinson Pressure Bar is the most widely used technique, as it is able to achieve the highest uniform uniaxial compressive stress loading of a specimen at nominally constant strain rates of the order of 10^3 s^{-1} [54].

2.10.1 Principles of the Split-Hopkinson Pressure Bar

The dynamic stress-strain behaviour of materials experiencing strain rates up to $2x10^4$ s^{-1} can readily be determined in a single test by using the conventional compression Hopkinson bar method. The basic components that a compression Hopkinson bar test setup consist of is shown in Figure 2.68.

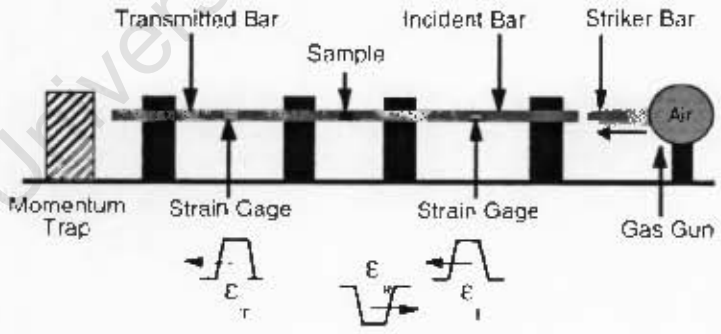

Figure 2.68 – Schematic representation of a compression Split-Hopkinson Pressure Bar [54]

The material specimen is sandwiched between the input (incident) and the output (transmitted) bar. Both these bars are elastic so that the displacement measured in the bars can be used to determine the stress-strain conditions at each end of the specimen[54]. A stress wave is commonly generated by propelling a striker bar, consisting of the same material and diameter as the pressure bars, to impact the free end of the input bar. The length

of the striker bar and the impact velocity will determine the strain rate and total strain within the specimen.

Impacting the input bar causes a longitudinal compressive stress wave in this bar, referred to as ε_i. When the input wave reaches the bar-specimen interface, a portion of the pulse is reflected, denoted by ε_r. The remainder of the pulse passes through the test specimen and enters the output bar, such that the pulse is now referred to as ε_t. The input and output stress wave signals are represented by compressive load pulses and the reflected stress wave is a tensile load pulse. Strain gauges positioned along the length of the two pressure bars capture the magnitude and duration of these three elastic pulses. An example of the load pulses recorded by the strain gauges during a Split-Hopkinson Pressure Bar test of a 304 stainless steel specimen is shown below in Figure 2.69.

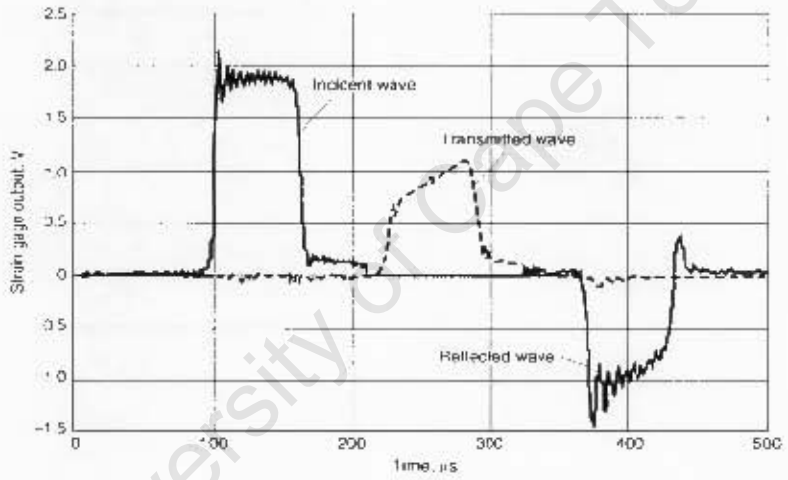

Figure 2.69 – Graph of strain gauge data showing the compressive input and output load pulses and the tensile reflected pulse [54]

2.10.2 Theory of the Split-Hopkinson Pressure Bar

The stress-strain behaviour of the test specimen can be determined by applying the principles of one-dimensional elastic-wave propagation through the pressure bars[54]. The displacements and/or stresses experienced at any point along the system can be found by measuring the elastic wave at the point of interest, x, as it transmits through the bar. Basic wave theory yields the wave equation; where $c_b = \sqrt{E/\rho}$ is the longitudinal wave speed in the pressure bars, u is the displacement and t the time:

$$\frac{\partial^2 u}{\partial x^2} = \frac{1}{c_b^2}\frac{\partial^2 u}{\partial t^2} \qquad \text{Eq. 2.10}$$

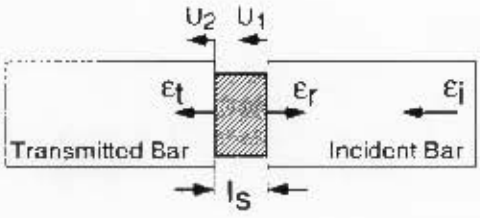

Figure 2.70 – Schematic detailed view of the input bar-specimen-output bar region [54]

The subscripts 1 and 2 indicates the input and output bar ends of the specimen, therefore the displacements of the ends of the specimen are given as u_1 and u_2. The strains experienced by the bars are denoted as ε_i (input strain), ε_r (reflected strain) and ε_t (output strain).

Considering the input bar and using elementary wave theory, the wave equation given in Eq. 2.10 can be written as:

$$\begin{aligned} u &= f(x - c_b t) + g(x + c_b t) \\ &= u_i + u_r \end{aligned} \qquad \text{Eq. 2.11}$$

where function f describes the input wave shape, function g describes the reflected wave shape and c_b is the longitudinal wave speed in the pressure bars.

It is known that 1-dimensional strain is given by:

$$\varepsilon = \partial u / \partial x \qquad \text{Eq. 2.12}$$

Therefore differentiating Eq. 2.11 with respect to x allows the strain in the input bar to be written as:

$$\begin{aligned} \varepsilon &= f' + g' \\ &= \varepsilon_i + \varepsilon_r \end{aligned} \qquad \text{Eq. 2.13}$$

Differentiating Eq. 2.11 with respect to time and using Eq. 2.13 gives the velocities at the input bar-specimen interface, $\dot{u}_1$, and the output bar-specimen interface, $\dot{u}_2$:

$$\dot{u}_1 = c_b(-\varepsilon_i + \varepsilon_r) \qquad \text{Eq. 2.14}$$

$$\dot{u}_2 = -c_b \varepsilon_t \qquad \text{Eq. 2.15}$$

The strain rate in the test specimen can then be related to the velocities experienced by each end of the specimen, $\dot{u}_1$ and $\dot{u}_2$,and the instantaneous length of the specimen, l_s , by:

$$\dot{\varepsilon} = \frac{(\dot{u}_1 - \dot{u}_2)}{l_s} \quad \text{Eq. 2.16}$$

The force in the input bar, F_1 , and the output bar, F_2 , are:

$$F_1 = AE(\varepsilon_i + \varepsilon_r) \quad \text{Eq. 2.17}$$

$$F_2 = AE\varepsilon_t \quad \text{Eq. 2.18}$$

where A is the cross-sectional area of the pressure bar and E is the Young's (elastic) modulus of the bars.

The true stress experienced by the test specimen is calculated from the transmitted force measured from the strain gauge signal, F_2 , divided by the instantaneous cross-sectional area, A_s , over which it acts:

$$\sigma(t) = \frac{AE\varepsilon_t}{A_s} \quad \text{Eq. 2.19}$$

2.10.3Determining the stress-strain behaviour of the test specimen

In order to employ the SHPB equations to relate the strain gage measurement of the pressure bars to the stress-strain behaviour of the test specimen, the specimen needs to deform uniformly[54]. The stress-state equilibrium of the specimen can be verified by comparing the 1-wave and 2-wave stress-strain response.

The 1-wave stress analysis represents the stress conditions at the specimen-output bar interface. In the waveform retrieved from the 1-wave stress analysis the back stress in the specimen is directly proportional to the strain in the output bar (calculated from Eq. 2.18). On the other hand, the 2-wave stress analysis represents the conditions at the incident bar-specimen interface. In this latter stress analysis the front stress in the specimen is directly proportional to the sum of the strain in the input bar and the reflected strain (calculated from Eq. 2.17). Figure 2.71 shows an example of the 1-wave and 2-wave stress curves obtained from a SHPB test of a 304 stainless steel specimen.

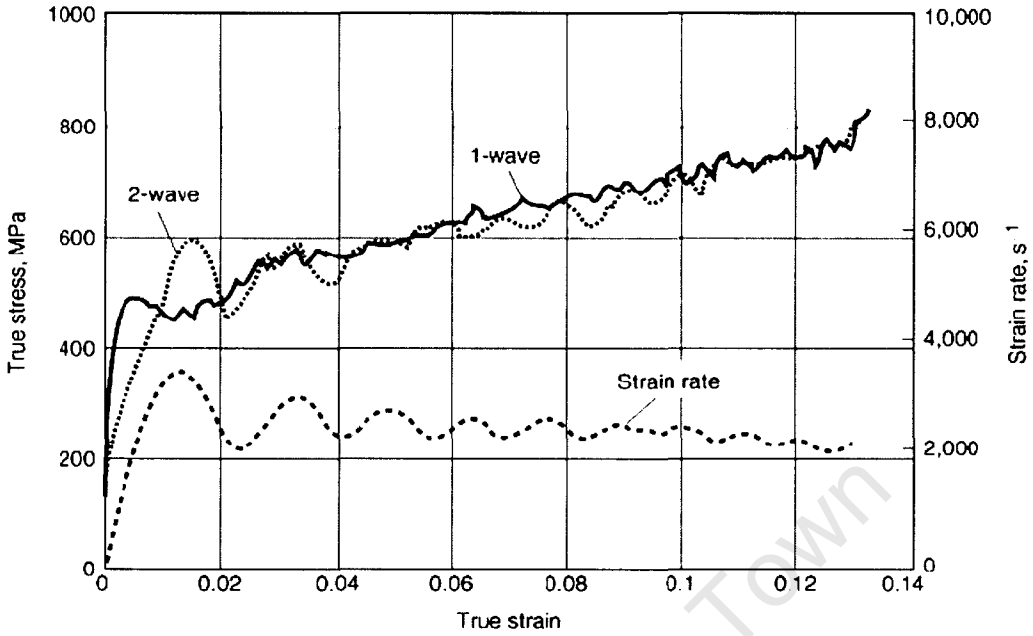

Figure 2.71 – Graph of stress-strain response showing the 1-wave and 2-wave stress curves [54]

When the 2-wave stress oscillates equally above and below the 1-wave stress, it shows that the front and back specimen faces exhibits similar stress response, verifying that the stress state is uniform throughout the specimen[54]. However, when the 2-wave stress diverges and exceeds the 1-wave stress, it indicates that the specimen does not experience stress equilibrium.

2.10.4SHPB testing of rubber

Measuring the mechanical response of rubber-like materials is challenging due to the characteristic low elastic impedance and flow strength of such materials[55]. When using traditional steel pressure bars in the SHPB setup, the wave impedance of the rubber specimen is much lower than that of the steel pressure bars. The wave impedance mismatch results in the transmission of a very weak pressure pulse, making it difficult and sometimes impossible to resolve the transmitted pulse of the rubber. It has become more popular to use pressure bars with a lower elastic modulus, as it increases the signal-to-noise level of the strain gauges in order to efficiently aid dynamic testing of low-strength materials, provided that the yield strength of the pressure bars are adequately higher than that of the specimen material[55].

2.10.4.1 Pressure bar materials

Table 2.9 provides the wave impedance properties of pressure bar materials most commonly used in the SHPB setup.

Bar material	***Elastic modulus GPa***	***Wave impedance (ρC_0) km.g/s.cm^3***	***Impedance relative to steel***
Steel	*212*	*40.8*	*1.00*
Ti-6Al-4V	*115*	*22.8*	*0.56*
Aluminium	*90*	*13.5*	*0.33*
Magnesium	*45*	*8.6*	*0.21*
Polymethyl methacrylate (PMMA)	*4*	*2.2*	*0.05*

Table 2.9 – Material properties of bar materials used in SHPB testing [55]

From Table 2.9 it is obvious that using polymeric material pressure bars is ideal for the SHPB testing of soft material specimens as the impedance difference is very small compared to that of the rubber specimen, enabling the transmitted pulse to be sufficiently large for measurement[52]. However, before the pressure bar material is decided upon, the roll that the pressure bars play in the "classic" SHPB material analysis must be understood. As the theory is based on utilising metallic bars (which generally displays a linear elastic response when loaded in the elastic regime), classic SHPB analysis relies on the wave propagation being undistorted such that the locally measured strain pulse would also describe the stress wave and particle velocity at various points along the pressure bar[54]. Polymeric materials on the other hand do not display ideal linear elastic characteristics, as the wave amplitude gradually decreases due to attenuation and the shape of the associated waveform becomes distorted as the wave travels down the pressure bar[55]. As such, the measured strain pulse would not represent the stress wave or particle velocity at another point along the pressure bar and complex manipulation of the data is required to extract the stress-strain behaviour of the specimen. The behaviour of polymeric bars is also very sensitive to temperature changes, creating the extra need to control the entire bar system and specimen temperature to within a few degrees when performing the SHPB testing[55].

Titanium (Ti), aluminium (Al) and magnesium (Mg) bars are low impedance metallic bars that are increasingly being utilised in the dynamic material testing of low wave-speed material specimens. The main advantage of using any of these low impedance metallic bars is that the classic linear-elastic SHPB theory can be applied and no data reduction assumptions or rules are required to analyse the stresses and strains in the test specimen[55].

Another technique employed to increase the signal to noise measured during SHPB testing of low wave-speed materials is to use a hollow high-strength aluminium alloy output (transmitted) pressure bar together with a pulse shaper to increase the input pulse rise time and filter out high-frequency components of the input stress wave at the same time[55].

It must be noted though that although low-impedance pressure bars can improve the data acquisitioning through SHPB testing of the stress-strain material properties of low-strength solids, certain classes of soft materials cannot be analysed using traditional SHPB testing. The theory of SHPB data analysis relies on the assumption of one-dimensional wave propagation in the pressure bars and the specimen, therefore the specimen material is required to conserve its volume during deformation[55].

2.10.4.2 Specimen size

The successful analysis of the high strain rate response of low impedance material specimens during SHPB testing greatly depends on the size and thickness of the specimen to guarantee a uniform stress state, which will ensure the data to be accurate and repeatable[55]. Kolsky[50] originally demonstrated the importance of using thin rubber specimens in order to allow the specimen to reach a state of uniform uniaxial stress in a shorter time period. Also, because rubber is rather compliant and allows a very weak pulse to be transmitted, thin specimens need to be used else the original assumption that pressure on both surfaces of the specimen is reasonably the same can no longer be valid[50;55].

Figure 2.72 clearly shows the effect of the specimen size on the stress-strain data retrieved from the SHPB test. It is noticed that the specimens with an aspect ratio of 1 to 1 display the most scattered and oscillatory ringup as well as the quickest falloff in stress after the maximum stress state was attained[55]. The specimens with the 0.5 aspect ratio however display significantly lower ringing amplitude and clearly show when the yield strength is reached. It is also proven that using specimen aspect ratios of as low as 0.25 may reduce wave attenuation while controlling frictional effects[55].

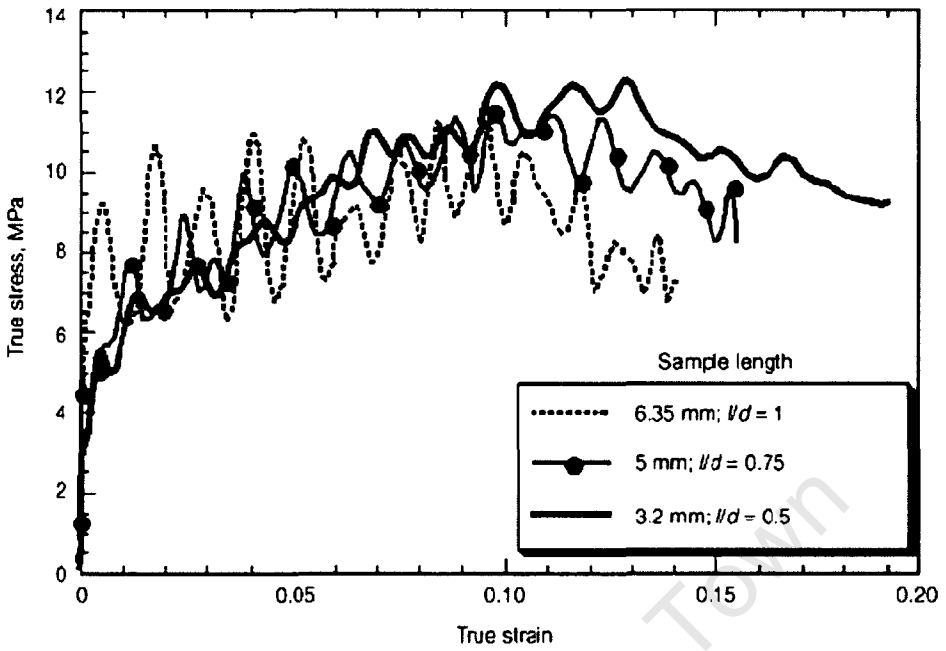

Figure 2.72 – Graph showing the stress-strain response of 6.35mm diameter Adiprene L100 specimens as a function of specimen length compressed at high strain rate ($2500s^{-1}$) [55]

The dynamic testing of rubber-like materials using the SHPB technique is deemed valid when the input and output strain data measured from the pressure bars shows a stress-state equilibrium and when the strain rate achieved during the test was constant[55]. The conditions for a uniform stress-state were explained in Section 2.10.3.

Chapter 3 - Material Characterisation

3.1 INTRODUCTION

The present investigation examines the attenuation provided by a rubber layer placed underneath the foot of a surrogate lower leg exposed to blast impact. The entire leg model is created from Al6000 series solid aluminium, the tibia is represented by a tube of Al6063-T6 aluminium and the rubber layer is taken from the rubber outer sole of a standard army combat boot. The design of the leg model and rubber sole is described in Chapter 5. It is required to construct a finite element model of the surrogate leg and the blast test setup, which entails not only accurate geometric modelling of the components, but also accurate material properties being assigned to the various components.

When materials are used in an application where they are expected to withstand sudden impacts, it is important to understand how the rate at which the strain is applied affects the material properties, as these material characteristics will ultimately determine the mechanical behaviour of the specific material. Equally as important is the correct modelling of these material characteristics, because applying the material properties correctly or incorrectly can greatly affect the accuracy of the numerical simulation and the results obtained from it.

In essence, proper material characterisation and application of the various materials forms the backbone of constructing a good finite element model, ensuring accurate results to be retrieved from the numerical analysis.

Seeing that a standard issue Al6063-T6 aluminium tube is used for the tibia of the lower leg model, the relevant and necessary material properties are known. However, as it is unclear which specific series of solid aluminium is used to construct the foot and ankle, the material properties required to create the numerical model of the foot and ankle is not known either. It is also not known which type of rubber the boot sole consist of. This section of the report therefore describes and discusses the techniques used to acquire the material properties of the solid aluminium and the rubber.

3.2 ALUMINIUM

The Elastic modulus of the aluminium used to construct the foot and ankle complex was not known, and although the material properties of the aluminium tube used for the tibia is known, the density and Elastic modulus of the solid aluminium parts could not be assumed to be the same. A wave speed test using a cylindrical bar of the same grade aluminium as the solid pieces of aluminium is performed to determine the Elastic modulus experimentally.

3.2.1 Wave speed test apparatus setup

The Hopkinson Pressure Bar is used to record the wave speed of the aluminium bar. The 1.6m long cylindrical aluminium bar is strain gauged to measure the stress wave propagation in the bar and is placed in the position of the incident bar according to the setup shown in Figure 3.1. An aluminium striker bar is then launched via the gun barrel of the gas gun, impacting the aluminium bar to send a pulse through the aluminium bar. Effectively, the time the pulse takes to transmit from the strain gauge to the rear end of the bar and reflect back to the strain gauge, will determine the wave speed of the aluminium. The wave form of one of the pulses retrieved from the tests is shown in Figure 3.2.

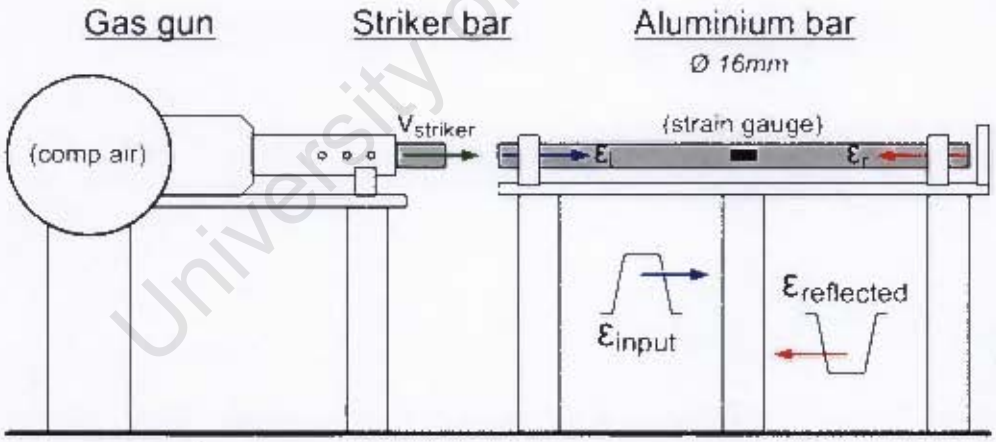

Figure 3.1 – Test apparatus setup for wave speed tests of aluminium bar

3.2.2 Determining the Elastic Modulus of the aluminium bar

Theory states that the wave speed of a material is determined by the time that a sound wave takes to travel a certain distance through the material[56]. The wave speed of a material however is also dependent on the Elastic modulus and the density of the particular material[50;56]. These two relationships describing the wave speed, c, are written as:

$$c = \Delta s / \Delta t \qquad \text{Eq. 3.1}$$

$$c = \sqrt{E / \rho} \qquad \text{Eq. 3.2}$$

The wave speed of the aluminium bar is determined to be 5136.7m/s by considering the time the pulse takes to travel past and reflect back to the strain gauge placed on the aluminium bar. Also, the aluminium bar is found to have a density of 2709.7kg/m^3. Following from Eq. 3.2 the Elastic modulus of the aluminium bar is calculated to be 71.5GPa.

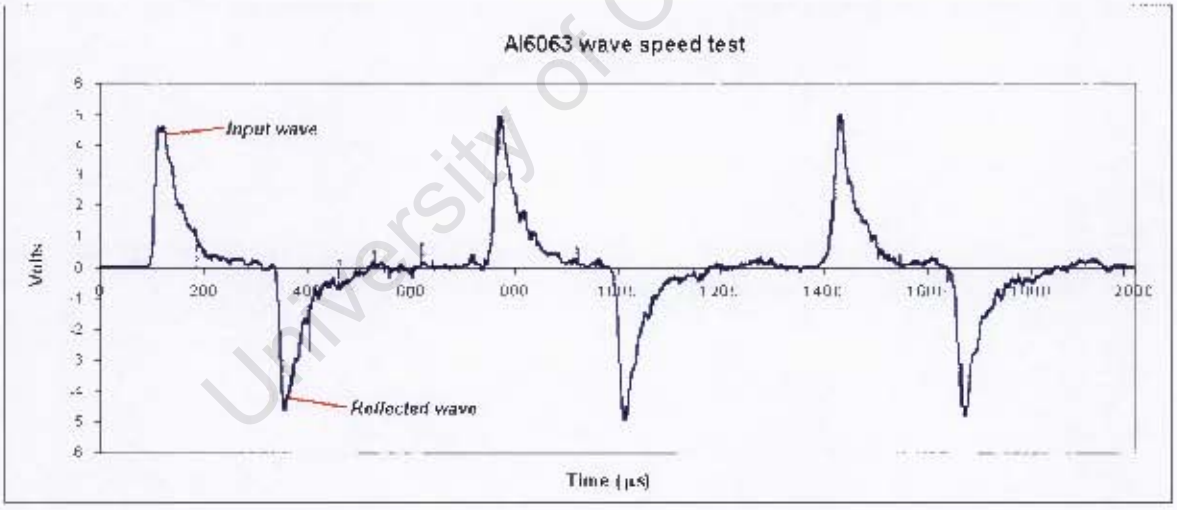

Figure 3.2 – Strain gauge data to determine wave speed of Al6063 aluminium bar

3.3 RUBBER

Uniaxial compression tests are performed on disk shaped rubber specimens cut from the soles of a pair of standard issue army combat boots. The rubber test samples are tested at strain rates ranging from $0.004s^{-1}$ to $4000s^{-1}$. Low to medium strain rate tests (10^{-3} to $10^{1}s^{-1}$) is generally conducted on conventional mechanical test machines, while using a split-Hopkinson pressure bar (SHPB) is an accepted test method used to determine the mechanical response of an engineering material at high strain rates (10^{3} to $10^{4}s^{-1}$).

3.3.1 Quasi-static (low strain rate) experiments

A Zwick hydraulic testing machine is utilised for the quasi-static uniaxial compression tests. Circular cylindrical rubber specimens of 13mm diameter and 9mm length are used to perform compression tests at strain rates of $0.004s^{-1}$, $0.04s^{-1}$ and $0.2s^{-1}$. For each test the rubber sample is placed on the bottom platen, after which the bottom platen is raised until the top surface of the specimen touches the top platen of the machine. The bottom platen is then raised at a constant speed to produce the desired strain rate in the rubber specimen, and stopped when the required specimen deflection of 4mm is reached. In order to achieve a strain rate of $0.004s^{-1}$, the bottom platen is raised at a cross-head speed of $2.16mm.s^{-1}$. A cross-head speed of $21.6mm.s^{-1}$ and $108mm.s^{-1}$ is used to produce a strain rate of $0.04s^{-1}$ and $0.2s^{-1}$ respectively. Three tests at each of the aforementioned strain rates are conducted and the results of the stress-strain response are shown below in Figure 3.3.

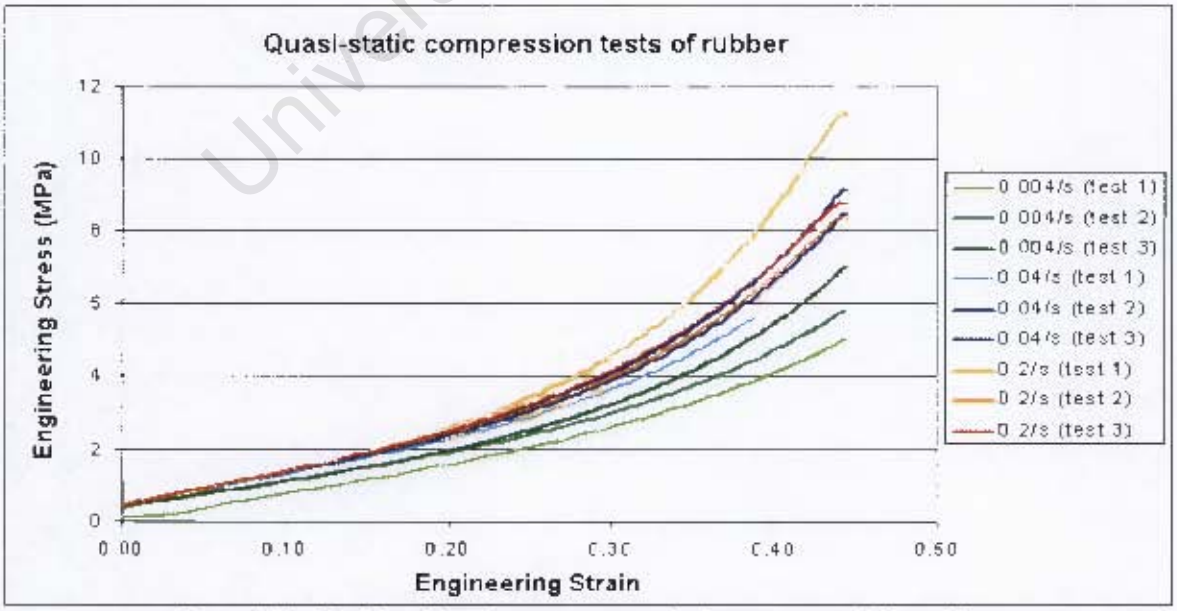

Figure 3.3 – Engineering stress versus strain response of the rubber

3.3.2 Dynamic (high strain rate) experiments

3.3.2.1 Test apparatus setup and procedure

The SHPB test apparatus used for the material characterisation of the rubber sole specimens is of conventional design, where a compressed air gas gun is used to propel the striker bar along a gun barrel onto the pressure bars. The diagrammatic representation of the SHPB test setup is depicted below in Figure 3.4.

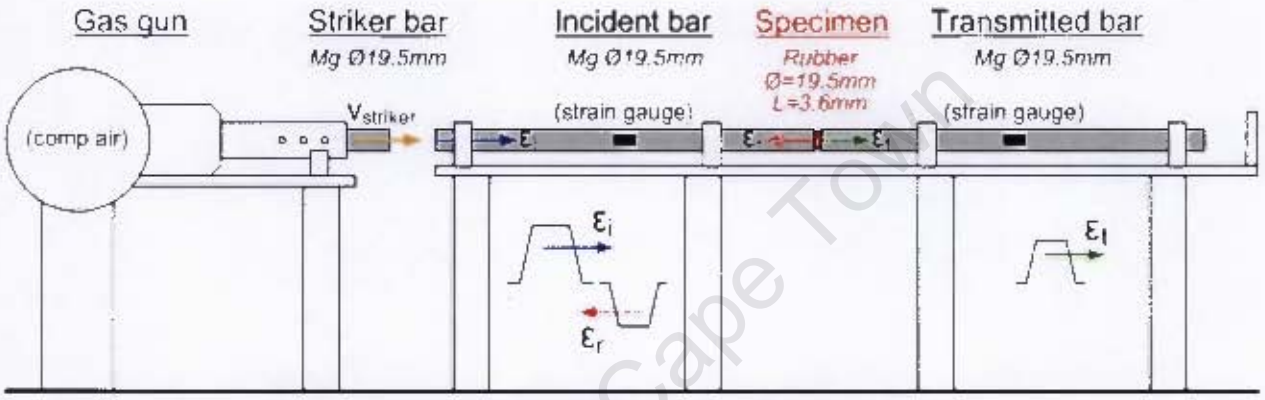

Figure 3.4 – SHPB setup

Steel or aluminium pressure bars are usually used, but research has shown that if the wave impedance of the test specimen is much lower than that of the pressure bars, the magnitude of the transmitted pulse can be weak[55]. Accurately determining the high strain rate uniaxial stress mechanical response of polymeric materials using an SHPB therefore poses to be very challenging. As such, it has become popular to use increasingly lower impedance metallic pressure bars (e.g. titanium, aluminium and magnesium) to attain higher resolution signals from the output bar, also eliminating the need for additional data reduction techniques[55].

Magnesium (ZK60A) extruded 19.5mm rods are used for the input and output pressure bars in the SHPB setup. The magnesium bars were age hardened to attain the following the material properties:

- The density, ρ, is calculated to be 1.82g/cm^3.
- The magnesium bars are determined to have an Elastic modulus of 44.87GPa by conducting a wave speed test.
- Tensile testing of magnesium specimens of the same set of magnesium rods revealed a tensile yield stress of 337.65MPa.

The striker bars used to apply impact and the bars used for the input and output bars in the SHPB test setup are from the same set of age hardened magnesium rods. The lengths and corresponding masses of the magnesium striker bars employed in the material testing of the rubber are given in Table 3.1. It is desirable to generate a square input pulse with a high rise time and a long duration[54]. Using the shorter striker bars (Striker 1, 2 and 3) result in the recorded input pulse having a short duration, as is displayed by the strain gauge recordings shown in Figure 3.5. Striker 4 however produced a long square input pulse which can be seen in Figure 3.7 and Figure 3.9.

Striker ID	*Length*	*Mass*
Striker 1	*50 mm*	*27.31 g*
Striker 2	*125 mm*	*67.75 g*
Striker 3	*250 mm*	*136.80 g*
Striker 4	*500 mm*	*273.70 g*

Table 3.1 – Table of magnesium striker bar length and mass

The gas gun is operated at 0.08–0.14MPa, generating striker bar velocities in the range of $4m.s^{-1}$ - $6m.s^{-1}$. When the striker bar impacts the front end of the input bar, an elastic compressive stress wave is sent through the input bar. The displacement of the input bar subsequently causes the specimen, which is sandwich between the input and output bar, to be compressed. The specimen transmits a portion of the compressive stress wave while the remaining fraction of the pulse is reflected back through the input bar in the form of a tensile stress wave. Readings of the strain experienced by the input and output bars are recorded by strain gauges located halfway along each of the bars.

3.3.2.2 Specimen size

Polymeric materials typically have low longitudinal sound speeds, complicating SHPB testing of such specimens because a dramatic impedance mismatch exist between the specimen and the bars. In turn, this mismatch of the mechanical impedance makes it difficult to achieve a uniform stress state in a polymeric test specimen. Research has shown that in order to reach stress equilibrium in a short time at lower strain levels during SHPB testing of the high strain rate response of polymeric materials, an l/d aspect ratio of 0.5 and a lower striker bar velocity need to be used[55]. Gray et al.[55] also proved that thin specimens with aspect ratios of 0.5 and 0.25 are able to minimise the wave attenuation, control friction

constraints at the specimen-pressure bar interfaces, as well as ensure that the stresses at the interfaces can still be assumed to be essentially the same.

The stress-strain response of rubber test samples with aspect ratios of 0.5, 0.27, 0.2 and 0.175 are analysed in the material characterisation process. The length and diameter dimensions related to the various aspect ratios of the rubber specimens are tabulated in Table 3.2. SHPB testing of the rubber specimens with an l/d ratio of 0.5 demonstrated transmission of a negligible amount of the stress wave, therefore it was decided to pursue more acceptable results employing specimens with lower aspect ratios.

Figure 3.5 and Figure 3.8 illustrate the effect of the specimen aspect ratio on the transmission of the stress wave. Rubber specimens with an aspect ratio of 0.27 transmit a weak stress wave, whereas rubber specimens with an aspect ratio of 0.2 prove to be more successful in transmitting a pulse. Analysing the signal to noise ratio of the applicable signal is also important, as a higher signal to noise ratio generally ensures a more clear and satisfactory signal. Figure 3.6 and Figure 3.8 show the maximum signal value with respect to the amplitude of the signal noise of the transmitted signals from the tests performed using specimen aspect ratios of 0.27 and 0.2 respectively. The signal to noise ratio of the transmitted signal obtained by using a specimen aspect ratio of 0.27 is 3.91, whereas using a lower aspect ratio of 0.2 increased the signal to noise ratio to 10.56.

Ultimately it was decided to use rubber specimens with an aspect ratio of 0.175 since an acceptable transmitted stress pulse is produced and the signal to noise ratio is increased to 13.30. The circular cylindrical specimens used to perform the material characterisation tests are of length 3.5mm and diameter 19.5mm.

Aspect ratio	*Length (mm)*	*Diameter (mm)*	*Signal to noise ratio*
0.5	*6.5*	*13*	*~*
0.27	*3.5*	*13*	*3.91*
0.2	*4.0*	*19.5*	*10.56*
0.175	*3.5*	*19.5*	*13.30*

Table 3.2 – Table of various rubber specimen aspect ratios

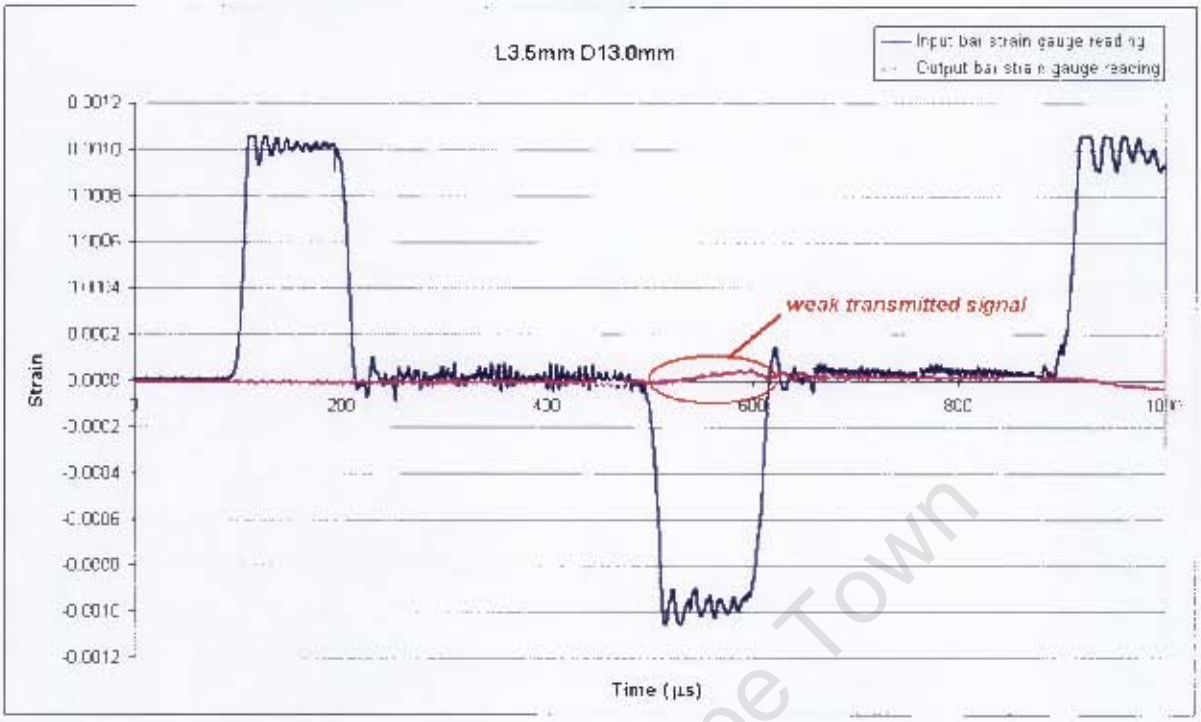

Figure 3.5 – Graph of SHPB strain gauge reading of rubber specimen with aspect ratio of 0.27 (length 3.5mm, diameter 13.0mm)

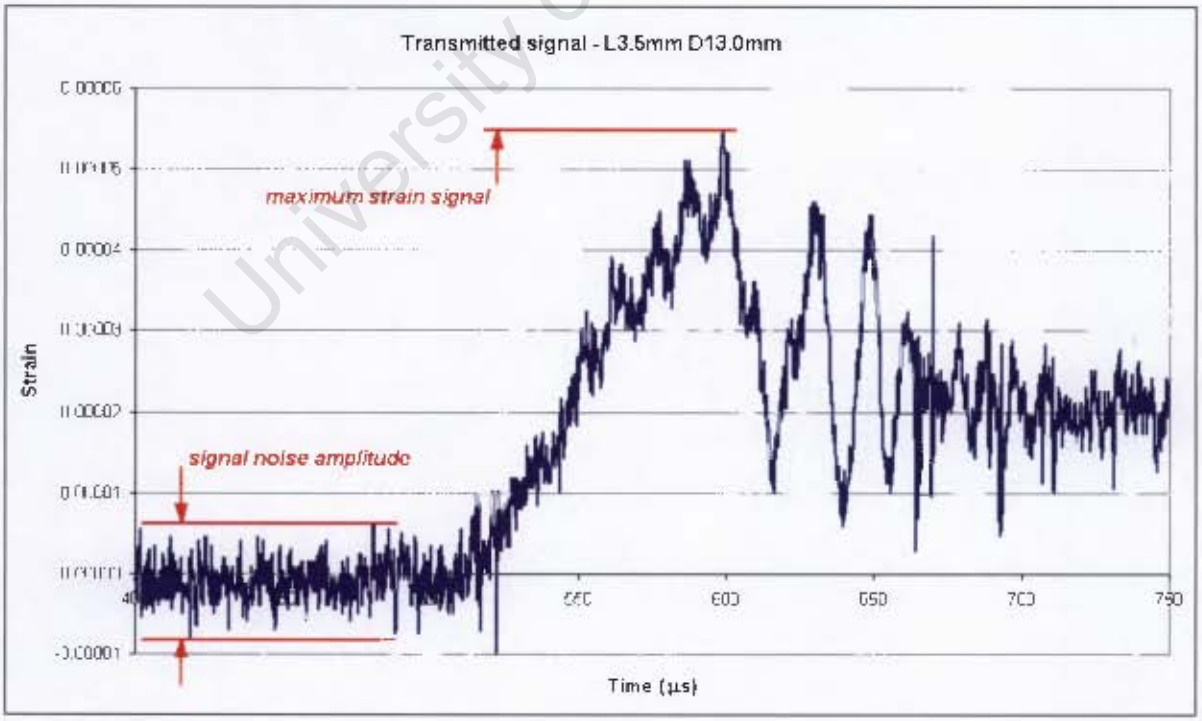

Figure 3.6 – Graph displaying signal to noise ratio of transmitted signal for SHPB testing of rubber specimen with aspect ratio 0.27

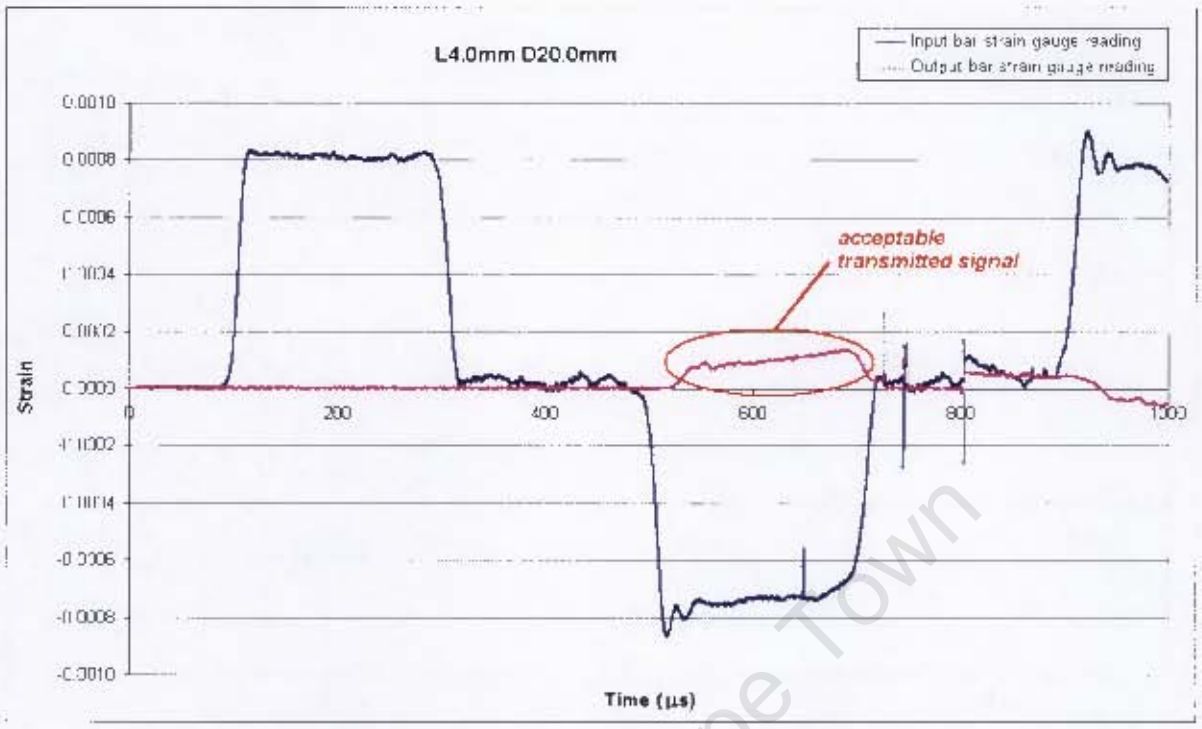

Figure 3.7 - Graph of SHPB strain gauge reading of rubber specimen with aspect ratio of 0.2 (length 4.0mm, diameter 20.0mm)

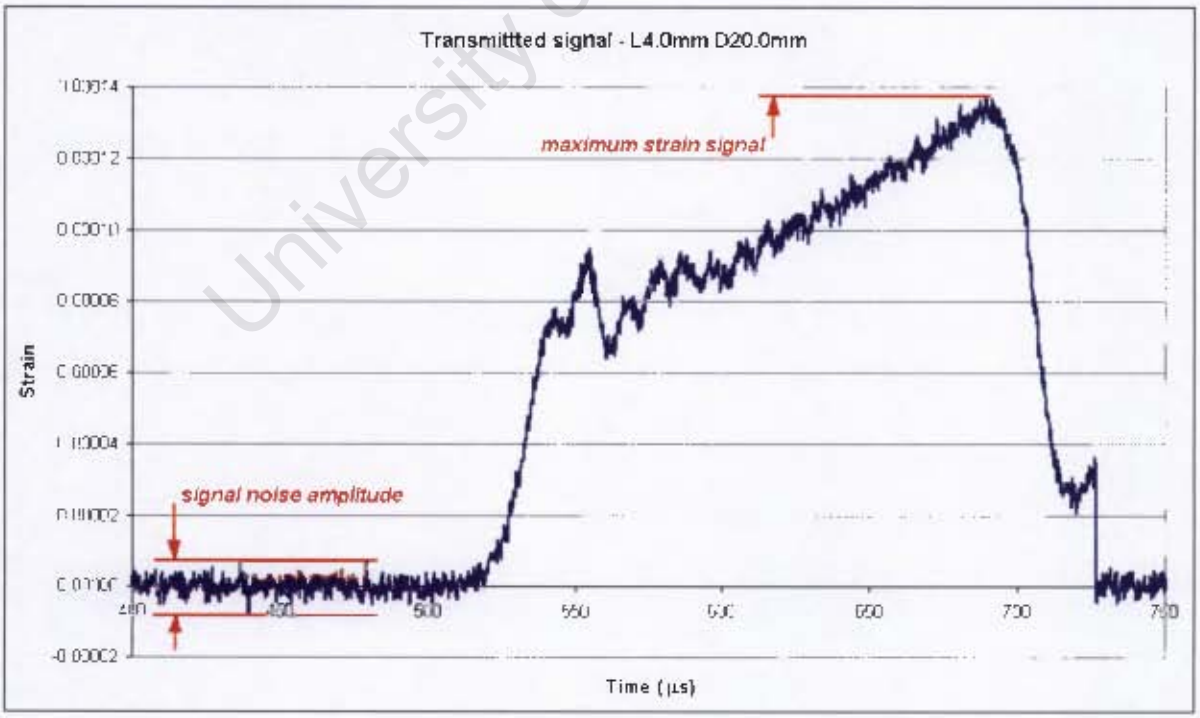

Figure 3.8 - Graph displaying signal to noise ratio of transmitted signal for SHPB testing of rubber specimen with aspect ratio 0.2

3.3.2.3 Interpretation of the SHPB strain data

Dispersion correction of the recorded input, output and reflected strain gauge readings are performed prior to being manipulated according to the SHPB theory given in the Literature Survey (Section 2.10). The results of the dispersion correction of the raw signals shown in Figure 3.9 are displayed in Figure 3.10.

It is known that the true stress experienced by the test specimen is determined from the transmitted force measured from the output strain signal divided by the instantaneous area of the specimen[54] (according to Eq. 2.9). The true stress experienced by the rubber specimen is represented in Figure 3.11 by the "1-stress" wave. The range of SHPB tests conducted covers strain rate conditions ranging from 1750/s to 2500/s. The stress-strain response of the rubber specimens experiencing strain rates of 1750/s, 2200/s and 2500/s in compression is compared in Figure 3.12.

The uniformity of the stress state throughout the specimen is checked by comparing the 1-wave stress to the 2-wave stress, as the 1-wave stress and 2-wave stress represent the stress state at the front and back surfaces of the specimen respectively[54;55]. Figure 3.11 shows the dispersion corrected stress vs. strain data from the SHPB test that produced an approximate strain rate of 2500/s in the rubber specimen. It can be seen that the stress state is in equilibrium only up to approximately 0.16 strain, after which the 2-wave diverges dramatically from the 1-wave but converges again before the specimen surfaces loses contact with the pressure bars. The impact manages to induce maximum compression of approximately 0.38 strain in the rubber specimen.

The dispersion corrected stress vs. strain data retrieved from the SHPB tests which produced 1750/s and 2200/s strain rates respectively in the rubber specimens are provided in Appendix A. For both of these tests the specimen is seen to exit the state of equilibrium earlier than the 2500/s strain rate test. During the SHPB test which produced a 1750/s strain rate equilibrium is maintained only up to 0.09 strain and compression of 0.09 strain is reached in the rubber specimen. Test data from the 2200/s strain rate testing showed that the specimen is in equilibrium only up to 0.075 strain and that the impact produced 0.075 strain in the specimen.

Considering all the facts mentioned above, it is clear that the data from the 2500/s strain rate test is the most suitable to employ in the creation of the rubber material model when constructing the finite element model of the rubber sole layer.

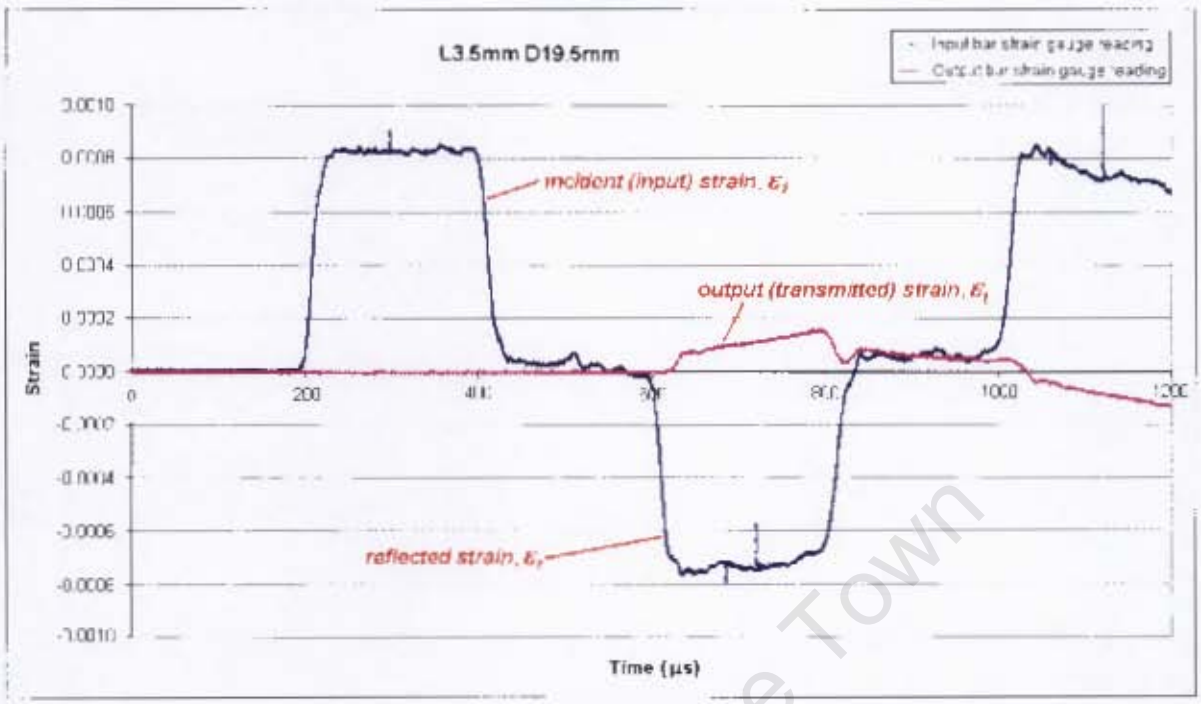

Figure 3.9 - Graph of the strain gauge readings from SHPB testing of rubber specimen with aspect ratio of 0.175 (length 3.5mm, diameter 19.5mm) tested at 2500/s strain rate

Figure 3.10 – Graph showing dispersion corrected strain data from SHPB testing of rubber specimen at 2500/s strain rate

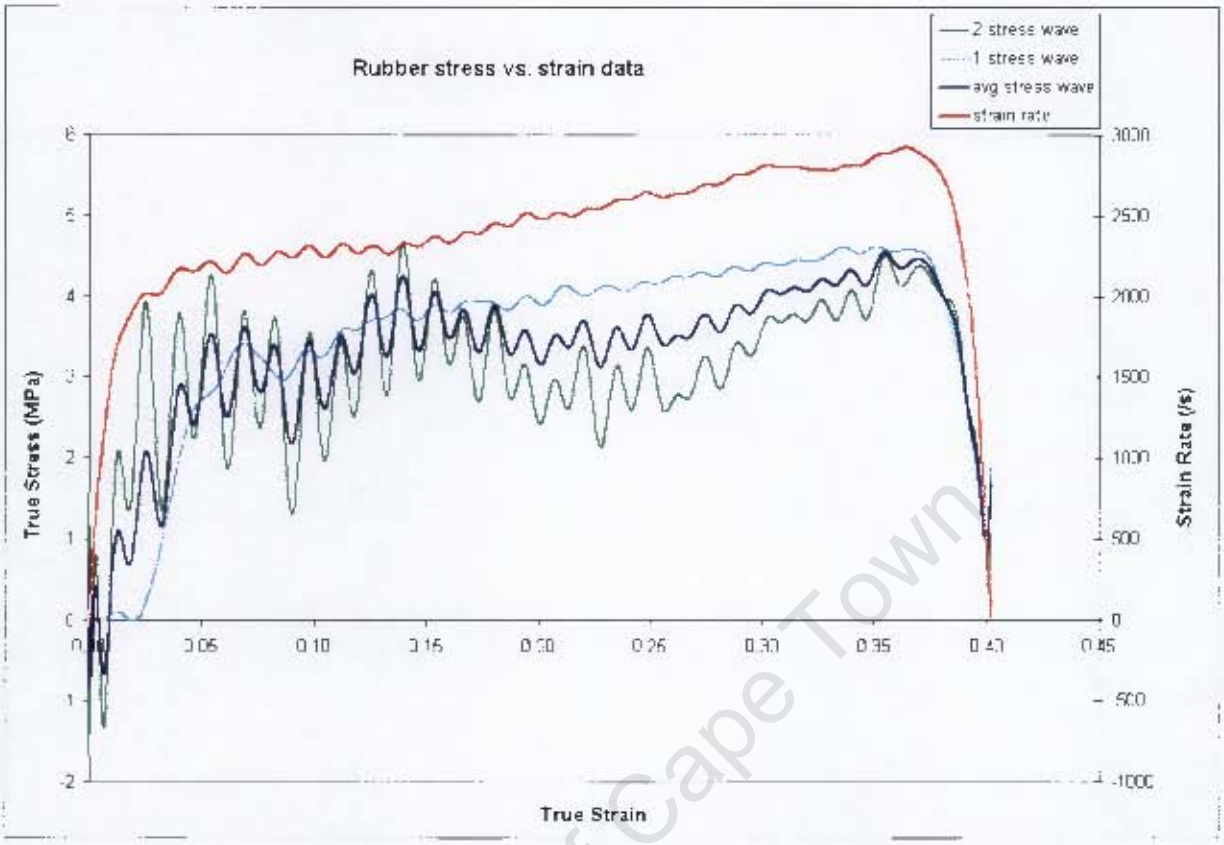

Figure 3.11 – Graph displaying the stress vs. strain results obtained for the rubber specimen, and the strain rate at which the SHPB testing is performed

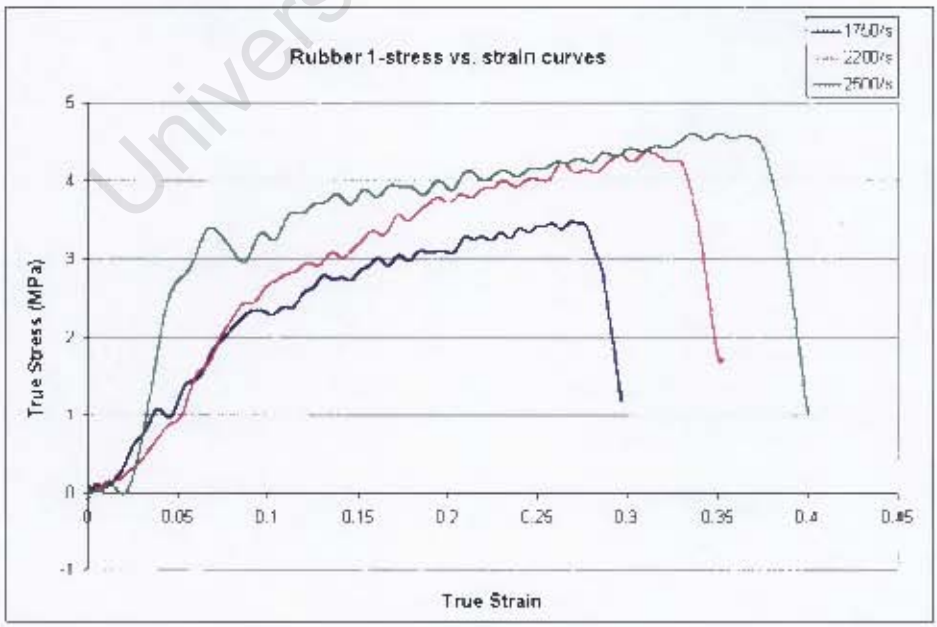

Figure 3.12 – Graph comparing the 1-stress vs. strain data of the rubber for strain rates of 1750/s, 2200/s and 2500/

Chapter 4 - Experimental Details

4.1 INTRODUCTION

The purpose of a mechanical surrogate leg is to measure the physical forces applied on the lower leg as a result of particular loading conditions[13]. In the case of blast loading, employing a mechanical lower leg model is desirable for initial evaluation of the blast effects on the leg as well as the foot protection used. Using a surrogate leg for mine blast testing provides a relatively inexpensive method to measure the load experienced by the lower leg while the surrogate leg can also be used for multiple tests if the explosive charge is limited.

The main structure of a mechanical leg model usually consists of metal components, which is instrumented according to what loading effects are to be analysed[13]:

- Strain gauges are used to measure tension, compression and/or bending of the leg, serving as an indication of the possibility of bone fracture due to blast-induced flailing.
- Accelerometers are used to measure the shock transmitted to the leg, indicating the chance that the bones in the leg will shatter.
- A linear transducer placed at the top of the test rig is used to measure the vertical movement and the energy transmitted to the leg.

Given the vertical loading conditions induced by the mine blast, injuries are most commonly seen to the calcaneous and lower portion of the tibia and fibula[8]. As such, special attention is given to the design of the calcaneous and ankle area of the lower leg model.

This chapter contains the details pertaining to the blast loading experiments of a simplified mechanical lower leg model. The horizontal ballistic pendulum is utilised to accommodate the instrumented leg model in order to perform the blast loading. Disc shaped plastic explosives is used to transmit the blast load onto the lower leg. Using the horizontal ballistic pendulum enables the impulse transmitted to the leg model to be measured. The aim of the experiments is to investigate the attenuation effect of a rubber sole on the load experienced by the lower leg model during the blast event.

4.2 DESIGN OF THE EXPERIMENTAL FOOT-ANKLE MODEL

The mechanical lower leg model is a simplified version of a human foot, of which the design is based on an existing foot model designed and tested as part of an undergraduate project[57]. X-rays were taken of the human foot and imported into a drawing program (AutoCAD) in order to acquire the relevant measurements needed to design the foot and ankle complex[57]. The X-ray images portraying the dimensions are displayed in Figure 4.1.

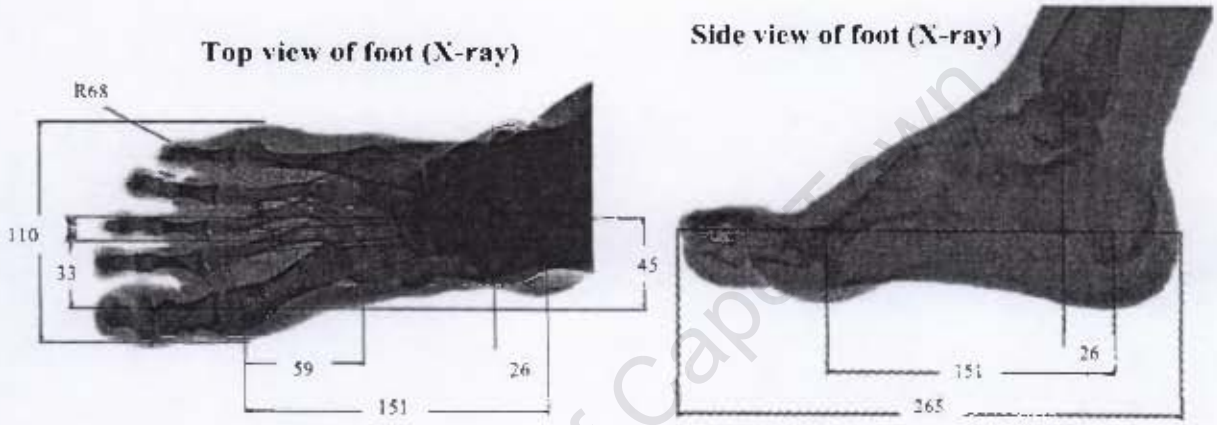

Figure 4.1 – X-rays of the top and side view of the human foot, dimensions in mm [57]

The design of the foot model allows the impact to be applied through the pressure points of the foot: at the bottom of the *calcaneous* (heel) and the front end of the *metatarsals*[57].

Figure 4.2 – Illustration of the pressure points of the foot

A photograph of the assembled foot-ankle-tibia model is shown in Figure 4.3. The final model used to obtain experimental data consists of four fundamental sections:

- The foot
- The ankle complex, comprising of four parts
- The tibia
- A rubber representation of a boot sole

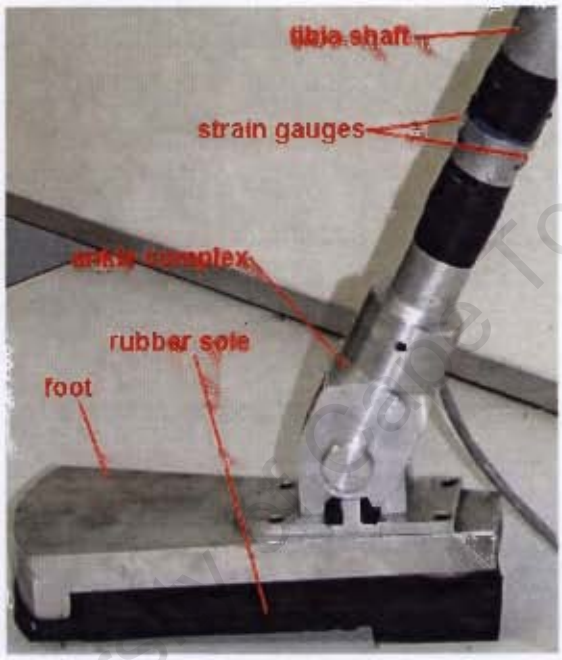

Figure 4.3 – Photograph of the assembled foot model featuring the rubber sole

4.2.1 The foot

The foot is machined from a solid aluminium plate, the aluminium being of the Al6000 range. The "bridge" of the foot is modelled as a flat section connecting the *metatarsals* to the *calcaneous*, with the *metatarsals* being represented by an arc and the *calcaneous* as a hemisphere at the rear of the foot.

4.2.2 The ankle

The design of the ankle complex resembles the essential functional features of the human ankle. Firstly the human ankle represents a mortise and tenon joint (shown in Figure 2.18) and secondly only dorsiflexion and plantarflexion of the ankle is important in the current investigation. As such, the ankle is model is represented purely by a hinge which is limited to allow 30° dorsiflexion and 40° plantarflexion. The bottom part of the hinge models the *talus*

and the top part of the hinge models the *tibia* and *fibula* as a connected segment. These two parts (machined from the solid aluminium) hinges around a pin (machined from the solid aluminium). The pin runs inside a brass bush and the inner walls of the bottom and top parts of the hinge are separated by two Teflon washers.

(a) Bottom view of foot showing calcaneous and metatarsals

(b) Ankle hinge of model compared with human ankle

(c) Flexion limits of ankle

Figure 4.4 – Details of foot and ankle design

4.2.3 The tibia

The tibia is an aluminium (Al6063-T6) tube which has a 25mm and 22mm outer and inner diameter respectively. The tube is 500mm long to provide sufficient time for the strain gauges to record a satisfactory reflected signal. The tube is mounted into a 25mm diameter recess made in the top part of the ankle hinge and is fixed in position by a small pin.

4.2.4 Rubber sole

A pair of standard army combat boots was sacrificed for the noble sake of research. The ideal setup would have been to utilise the combat boot as is during the blast testing. However, constructing a numerical model involves generating material models that will accurately represent the material properties related to the parts used in the numerical model. Taking the combat boot apart reveals the combat boot sole to consist of an inner sole, a cardboard-like mid-layer, a short metal strip that shapes the sole from the heel into the mid-foot section, nails holding the heel section together and finally the external rubber sole and thickened heel. Material properties and the relevant interaction between all the boot sole components therefore need to be established in order to ensure the accuracy of the numerical model. As such, including the complete boot model in the numerical simulation of the blast tests introduces complexities that are beyond the scope of this project.

It is therefore decided to only use the external rubber layer to serve as an attenuator during the blast tests. The shape of the rubber sole is based on the shape of the foot as viewed from above. The sole consists of a flat 9mm thick piece of rubber (taken from the army combat boot) and a double layered rubber section at the rear end to represent the heel of the boot.

4.2.5 Muscles, tendons and ligaments

A blast event occurs in a matter of approximately 2ms – 8ms [8], which does not render enough time for the muscles supporting the lower extremities (such as the calf muscle) to react to the impact[47]. Therefore the calf muscle is assumed to be passive during the blast event and that reaction of the Achilles tendon is not activated. The passive state of the Achilles tendon increases the dorsiflexion stiffness and superimposes axial force on the tibia, as noticed in the response of a human lower leg[47]. In order to maintain simplicity and eliminate as many unknowns in the model of the lower leg, the Achilles tendon was not included in the present model of the lower leg.

Figure 4.5 – Effect of calf muscle and Achilles tendon on lower leg response to axial impact [47]

4.3 INSTRUMENTATION OF THE EXPERIMENTAL LEG MODEL

Strain gauges certified for use on aluminium are used to record the strain experienced by the tibia during the blast event. Two strain gauges are placed just above the ankle hinge 60mm upwards on the aluminium tube, one on the front surface and one on the back surface of the tube (shown in Figure 4.6 (a)).

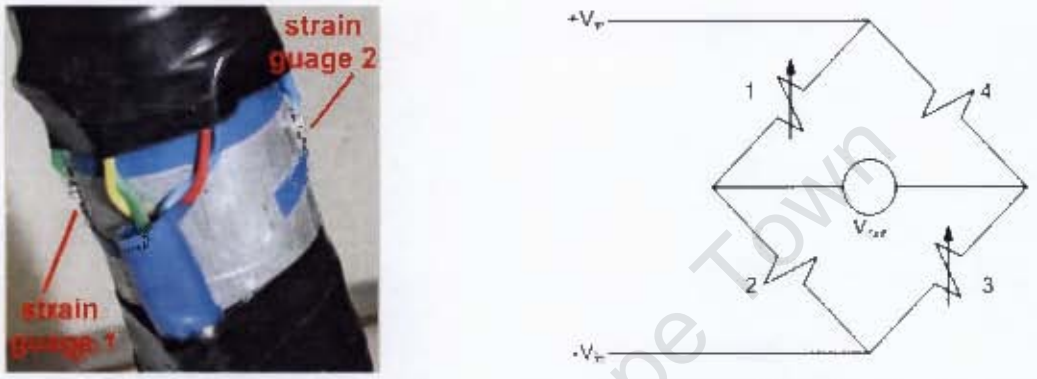

(a) Position of strain gauges on tibia shaft (b) Half bridge configuration of strain gauge

Figure 4.6 – Instrumentation of tibia shaft using strain gauges

4.3.1 Strain gauge configuration

The application of a specific strain gauge depends on the particular bridge configuration and unbalanced modes in the strain gauge design. Three bridge configurations exists[58]:

- The **quarter bridge** is employed where axial strain or tension in a uniaxial stress field are to be measured. In this arrangement only one arm is unbalanced.
- In the **half bridge** configuration, two of the arms are unbalanced. When two opposite arms are unbalanced, the strain gauge is used to measure axial strain, tension or compression in a uniaxial stress field. On the other hand, if two adjacent arms are unbalanced, the strain gauge is used to measure pure bending with one arm in tension and the other arm in equal compression. Figure 4.6 (b) shows the wiring diagram of the half bridge configuration.
- All four arms are unbalanced in the **full bridge** configuration, where two opposite arms are in tension and the other pair is in compression. This configuration is employed to measure bending, torsion and shear.

4.3.2 Output conversion of strain gauge signals

In the present investigation it is desired to obtain the stress-time history recorded by the strain gauges; however the output of the strain gauges is in voltage (V). The voltage output of the strain gauges can be converted into stress (σ) by the following equation[58]:

$$\sigma = E\varepsilon_m \quad \text{Eq. 4.1}$$

where the strain ε_m is:

$$\varepsilon_m = \frac{4V_{out}}{ABFV_{in}} \quad \text{Eq. 4.2}$$

Substituting Eq. 5.2 into Eq. 5.1 renders:

$$\sigma = \frac{4EV_{out}}{ABFV_{in}} \quad \text{Eq. 4.3}$$

This yields the theoretical K factor by which the output voltage needs to be multiplied in order to obtain the experimental stress output:

$$K = \frac{4E}{ABFV_{in}} \quad \text{Eq. 4.4}$$

The theoretical K factor is calculated to be 12.759.

Variable	Property	Value
E	*Young's modulus of material on which strain gauge is placed*	*68.9 GPa*
A	*Amplification*	*1000*
F	*Strain gauge factor for Aluminium*	*2.16*
B	*Bridge factor*	*2*
V_{in}	*Bridge excitation voltage*	*5*
V_{out}	*Test results output voltage*	*From test*

Table 4.1 – Variables necessary to convert strain gauge voltage to stress

4.4 THE BALLISTIC PENDULUM

4.4.1 The test rig

Blast testing on the foot model is performed using a horizontal ballistic pendulum. The test rig built to accommodate the surrogate lower leg during the blast testing is based on an existing template of a horizontal ballistic pendulum. The rig assembly consists of a 25mm mild steel detonation plate, a 20mm mild steel backing plate and two 20mm machined mild steel plates used to position the lower leg model. The four rig plates are held squarely in place by four angle bars and four flat bars. The two positioning plates are constructed out of four parts that are machined to form five holes; one hole is machined off-centre to align the tibia shaft, four holes to align the four silver steel Hopkinson bars and all five holes are fitted with a Teflon bush to reduce friction. The Hopkinson bars are bolted to the detonation plate and the ends of the bars are not to touch the backing plate prior to the detonation of the explosives. A 3mm rubber mat is glued to the backing plate to act as a buffer if the Hopkinson bars impact the backing plate during the blast event. The base of the foot is placed flush with the detonation plate before detonating the explosives to ensure maximum transmission of the impulse generated by the blast event. The position of the foot is such that the centre of the detonation plate is aligned with the midpoint between the pressure points (the *metatarsals* and the *calcaneous*) of the foot. The rig design and positioning of the foot is shown in Figure 4.7.

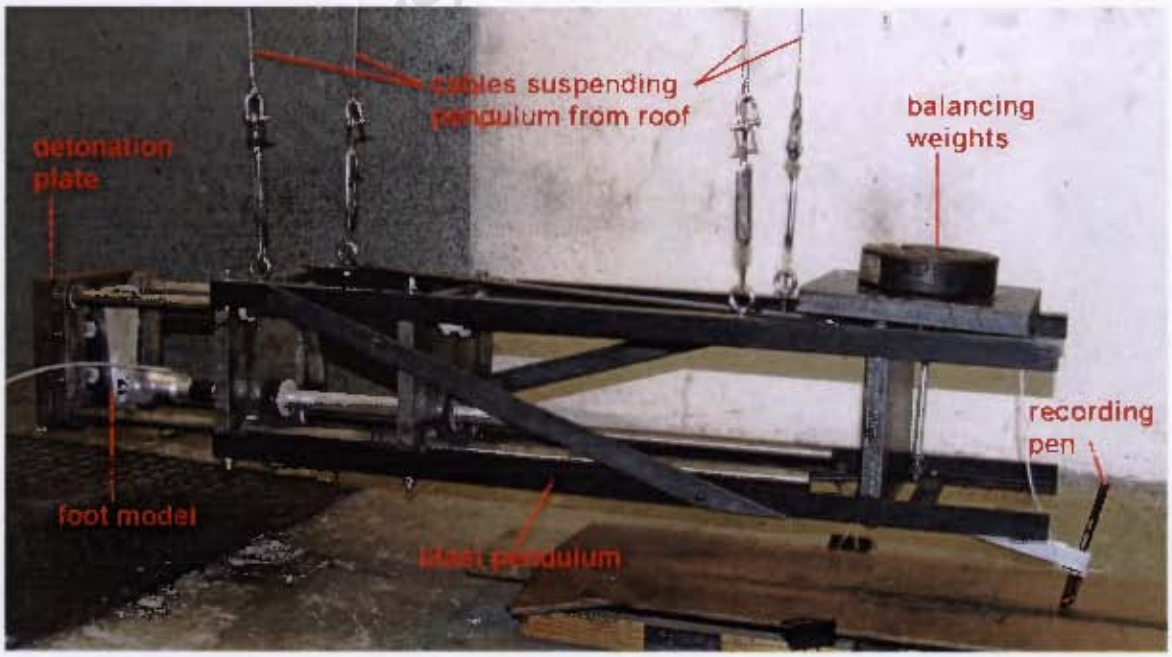

Figure 4.7 – Photograph of the horizontal ballistic pendulum and foot model setup

4.4.2 The test apparatus setup

The horizontal ballistic pendulum is suspended by four cables from the ceiling of the blast laboratory. Each of the cables has an adjustable screw which is used to level the pendulum vertically and horizontally. Balancing of the pendulum is also aided with the addition of weights at the rear end of the pendulum. A well-balanced pendulum is important in order for:

- the four cables to carry approximately an equal amount of weight;
- the impulse from the blast event to act through the centroid of the pendulum;
- the pendulum to swing along its axis without any rotation.

The horizontal displacement of the pendulum is recorded on a piece of tracing paper by a marker pen that is attached to the bottom of the rear end of the pendulum. The impulse transmitted through the system during each blast test can then be calculated by using the relevant measured displacement.

4.4.3 Horizontal ballistic pendulum theory and equations

Figure 4.8 shows an illustration of the ballistic pendulum and the geometric relationships associated with the theory.

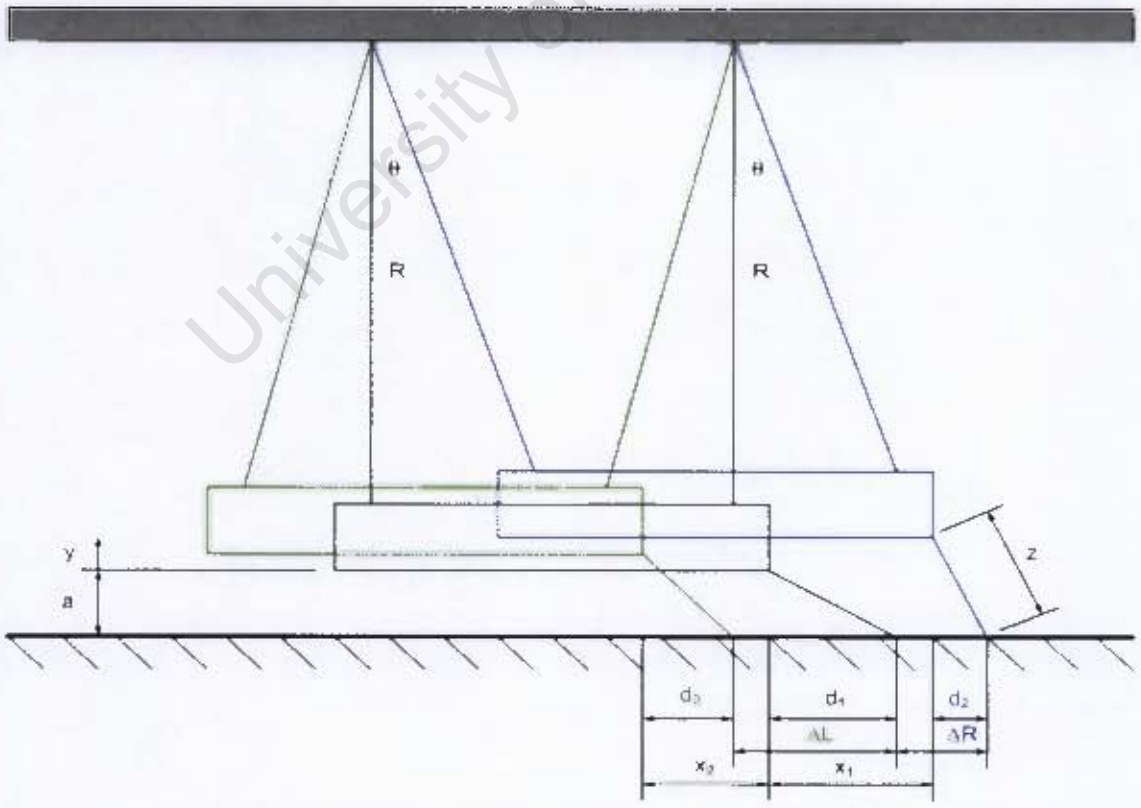

Figure 4.8 – Diagrammatic representation of the horizontal ballistic pendulum

The amplitude recorded by the pen on the tracing paper underneath the ballistic pendulum is directly proportional to the impulse applied to the lower leg positioned in the pendulum. This relationship is shown by applying the linearised equation of motion of the pendulum. While assuming viscous damping of the system, the linearised equation of motion of the ballistic pendulum is given by:

$$\ddot{x} + 2\beta\dot{x} + \omega_n^2 x = 0 \qquad \text{Eq. 4.5}$$

where:

$$\beta = C/2M \qquad \text{Eq. 4.6}$$

$$\omega_n = 2\pi/T \qquad \text{Eq. 4.7}$$

where:

β = damping constant

C = damping coefficient

M = total mass of the entire pendulum (the rig, test specimen, balancing weights and the explosive charge)

T = natural period of the pendulum motion

The solution to the linearised equation of motion (Eq. 4.5) is given by:

$$x = \frac{(e^{-\beta.t})\dot{x}_0 \, Sin\omega_d t}{\omega_d} \qquad \text{Eq. 4.8}$$

where:

$\dot{x}_0$ = initial velocity of the pendulum, and:

$$\omega_d = \sqrt{\omega_n^2 - \beta^2} \qquad \text{Eq. 4.9}$$

If x_1 is the horizontal displacement at $t = T/4$ and x_2 is the horizontal displacement at $t = 3T/4$, substitution into Eq. 4.8 yields the following relationships:

$$x_1 = \frac{\dot{x}_0 T e^{\frac{-\beta T}{4}}}{2\pi} \qquad \text{Eq. 4.10}$$

$$x_2 = \frac{\dot{x}_0 T e^{\frac{-3\beta T}{4}}}{2\pi} \qquad \text{Eq. 4.11}$$

Dividing x_1 by x_2:

$$\frac{x_1}{x_2} = e^{\frac{\beta . T}{2}} \qquad \text{Eq. 4.12}$$

yields the damping constant:

$$\beta = \frac{2}{T} \ln\left(\frac{x_1}{x_2}\right) \qquad \text{Eq. 4.13}$$

Substitution and simplification of Eq. 4.10 – Eq. 4.13 renders the following relationship for the initial velocity of the ballistic pendulum:

$$\dot{x}_0 = \frac{2\pi}{T} x_1 e^{\frac{\beta T}{4}} \qquad \text{Eq. 4.14}$$

The average time it takes for the ballistic pendulum to complete a number of oscillations is used to obtain the natural period T of the pendulum.

x_1 (forward displacement) and x_2 (backward displacement) of the ballistic pendulum motion are determined by using the amplitude of the pen recordings marked on the tracing paper. However it is noted that the pendulum moves in a circular arc, and therefore the displacement recorded by the marker pen on the tracing paper will not be the same as the actual horizontal displacement of the pendulum. It is important to take this discrepancy in account in order to determine the true displacements x_1 and x_2. The true displacement of the horizontal ballistic pendulum is determined by the following approach.

From Figure 4.8, the horizontal displacement from the end of the stationary pendulum to the tip of the marker pen is written as:

$$d_1 = \sqrt{z^2 - a^2} \qquad \text{Eq. 4.15}$$

and at maximum amplitude of the oscillation the horizontal distance from the end of the pendulum to the tip of the pen decreased, and is written as:

$$d_2 = \sqrt{z^2 - (a+y)^2} \qquad \text{Eq. 4.16}$$

Since the angle θ remains very small during the experiment, it can be assumed that:

$$x_1 = R.\theta; \qquad y \approx \frac{R\theta^2}{2}$$

which yields the vertical displacement:

$$y = \frac{x_1^2}{2R} \qquad \text{Eq. 4.17}$$

Inspection of the diagram presented in Figure 4.8 shows that the displacements x_1 and x_2 can be written as:

$$x_1 = \Delta R + d_1 - d_2 \qquad \text{Eq. 4.18}$$

$$x_2 = \Delta L - d_1 + d_2 \qquad \text{Eq. 4.19}$$

Substituting for d_1 and d_2 in Eq. 4.18 and Eq. 4.19 gives the true forward and backward displacements of the ballistic pendulum:

$$x_1 = \Delta R + \sqrt{z^2 - a^2} - \sqrt{z^2 - \left[a + \frac{x_1^2}{2R}\right]^2} \qquad \text{Eq. 4.20}$$

$$x_2 = \Delta L - \sqrt{z^2 - a^2} + \sqrt{z^2 - \left[a + \frac{x_1^2}{2R}\right]^2} \qquad \text{Eq. 4.21}$$

The displacements x_1 and x_2 calculated in Eq. 4.20 and Eq. 4.21 is used to determine the value of β, which enables the initial velocity of the pendulum to be calcualted from Eq. 4.14. The impulse imparted onto the lower leg is calculated by:

$$I = M\,\dot{x}_0 \qquad \text{Eq. 4.22}$$

4.5 EXPLOSIVES

4.5.1 Setup of the explosives

The type of explosive used to provide the blast loading on the lower leg model is plastic explosives, PE4. The PE4 is shaped into a 20mm diameter disc and is placed onto a circular polystyrene piece which is 110mm in diameter and 12mm thick. The polystyrene piece including the explosives is in turn positioned on the detonation plate, as shown in Figure 4.9. Creating a stand-off distance between the explosives and the detonation plate helps to prevent pitting of the mild steel detonation plate.

The total mass of the explosives consists of the charge mass that ultimately produces the impulse plus the one gram explosives which is used to attach the detonator to the main charge. The series of total charge masses used in the present investigation is 6g, 7g and 8g PE4. The charge mass is limited so as not to exceed the yield stress of the aluminium tube (representing the tibia of the lower leg model) during the blast loading.

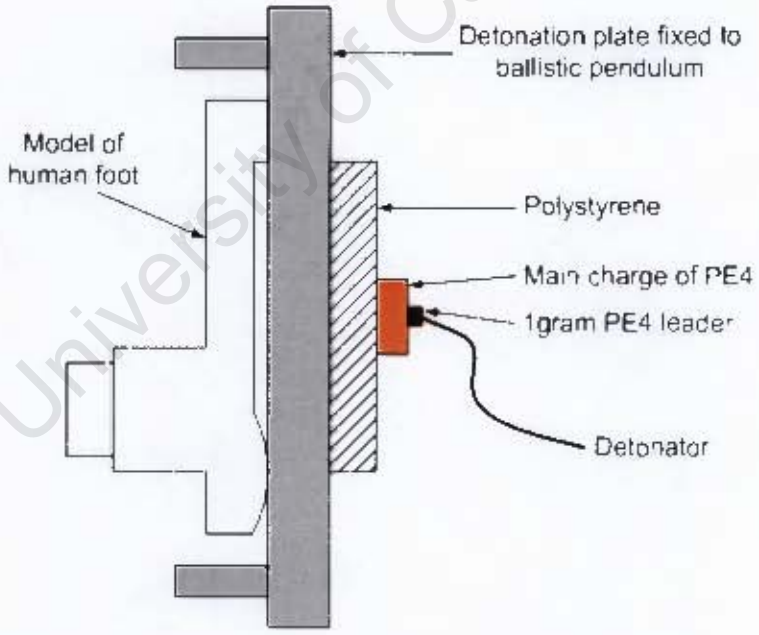

Figure 4.9 – Illustration of the setup of the explosives to perform blast test

4.5.2 Burn and impulse duration

Burn duration of the explosive is dependent on the burn speed (velocity of detonation) of the particular explosive and the charge radius, as illustrated in Fig. 4.10. The impulse duration is taken to be effectively equal to the duration over which the resulting impulse is transmitted to the blast test specimen.

The burn duration T_{burn} of the plastic explosive is approximated by:

$$T_{burn} = \frac{D_{charge}}{2 \times V_{burn}} \qquad \text{Eq. 4.23}$$

The explosive charge diameter D_{charge} is chosen to be 20mm for all the blast tests. PE4 has a detonation velocity V_{burn} of approximately 8200m/s and a density of 1.6g/cm^3 [13;15]. The burn duration is therefore calculated to be in the range of 1.2μs.

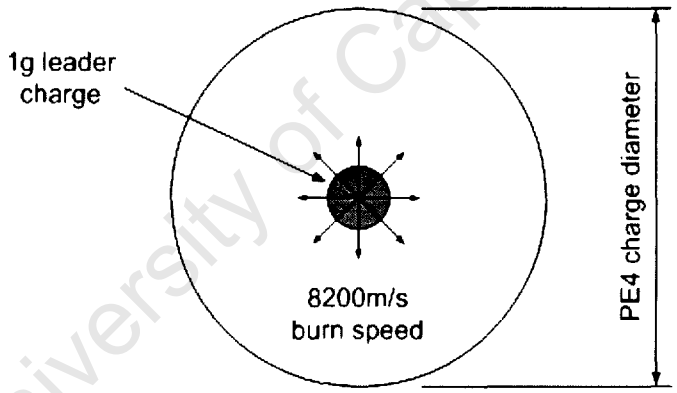

Figure 4.10 – Illustration of explosive detonation velocity

4.5.3 Blast loading scenarios

In performing the series of blast tests, the variation in the load experienced by the lower leg model is investigated when placing the explosives at different impact positions. The explosive charges are positioned in the centre of the detonation plate during one portion of the tests and the remainder of the blast tests is performed with the explosives placed in line with the heel of the foot model.

The effect on the load experienced by the lower leg model by introducing a rubber sole as blast attenuator is also investigated. For the second part of the series of blast tests the two loading conditions (explosives in the centre and in line with the heel) are repeated, the only difference being the inclusion of an elementary representation of a rubber sole.

Figure 4.11 illustrates the four different blast loading conditions and the amount of explosive charges used with each setup.

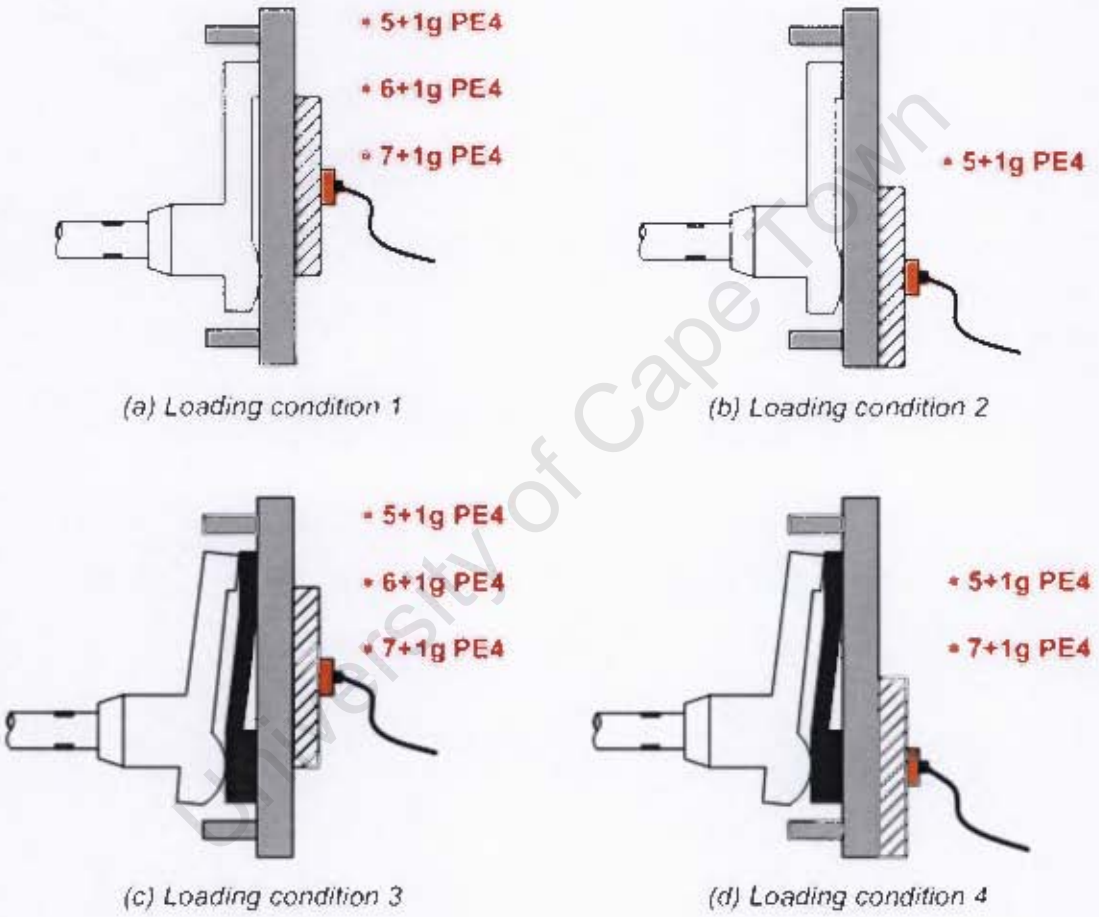

(a) Loading condition 1 *(b) Loading condition 2*

(c) Loading condition 3 *(d) Loading condition 4*

Figure 4.11 – Illustration of the four blast loading conditions

4.5.4 Relationship between the impulse, force and pressure induced by the detonation

The manner in which the load is applied to the detonation plate can be viewed in two different ways:

- The first method is to apply a uniform load over the surface area in contact with the detonating explosives. The pressure applied to the detonation plate is in this case represented by a square stress pulse.
- The second method is to apply a non-uniform load which decreases in magnitude at a certain rate outwards from the centre of the detonated explosives. The pressure applied to the detonation plate is defined as a peak pressure corresponding to the position of the explosives, with the pressure decaying radially outwards towards the edges of the detonation plate.

The results using either of the two load applications should however be reasonably the same, as long as the impulse and the duration (Δt) over which the load is applied is the same for both applications. The load duration Δt is assumed to be equal to the burn duration T_{burn}. The impulse generated by the detonation of the explosives is determined by applying the theory explained in Section 5.4.3. The force induced by the impulse is related by:

$$I = \int_0^t Force.dt$$
$$\therefore Force = I/\Delta t \qquad \text{Eq. 4.24}$$

Given that:

$$Pressure = \frac{Force}{Area} \qquad \text{Eq. 4.25}$$

the uniform pressure applied would be calculated by:

$$Pressure = \frac{I}{\Delta t \times Area} \qquad \text{Eq. 4.26}$$

4.6 RESULTS FROM THE EXPERIMENTAL BLAST TESTS

4.6.1 Test schedule

Table 4.2 shows the test schedule of the blast test performed on the lower leg model in which the horizontal ballistic pendulum is employed. The characteristics of the pendulum setup and the data measured from the pendulum marker pen after each test is also provided. The calculated true displacement, damping constant and initial velocity of the pendulum is given, as well as the resulting impulse. The full set of blast test information is provided in Appendix B.

	RUBBER SOLE OMITTED				RUBBER SOLE INCLUDED				
Charge mass (g)	**5+1g**	**6+1g**	**7+1g**	**5+1g**	**5+1g**	**6+1g**	**7+1g**	**5+1g**	**7+1g**
Number of tests performed	2	1	1	2	3	2	1	1	1
Name of test analysed	DU_090107c	DU_110107b	DU_110107c	DU_110107a	DU_150107c	DU_150107h	DU_150107f	DU_150107a	DU_150107e
Explosive position	centre	centre	centre	heel	centre	centre	centre	heel	heel
Charge diameter (m)	0.02	0.02	0.02	0.02	0.02	0.02	0.02	0.02	0.02
Charge area (m^2)	0.000314159	0.000314159	0.000314159	0.000314159	0.000314159	0.000314159	0.000314159	0.000314159	0.000314159
Burn velocity (m/s)	8200	8200	8200	8200	8200	8200	8200	8200	8200
Period (s)	3.6	3.6	3.6	3.6	3.6	3.6	3.6	3.6	3.6
z (m)	0.19	0.19	0.19	0.19	0.19	0.19	0.19	0.19	0.19
a (m)	0.06	0.06	0.06	0.06	0.06	0.06	0.06	0.06	0.06
R	2.93	2.93	2.93	2.93	2.93	2.93	2.93	2.93	2.93
ΔT (μs)	1.22	1.22	1.22	1.22	1.22	1.22	1.22	1.22	1.22
Pendulum mass (kg)	71.5	71.5	71.5	71.5	71.5	71.5	71.5	71.5	71.5
ΔR (m)	0.0605	0.07	0.071	0.062	0.06	0.0675	0.072	0.06	0.068
ΔL (m)	0.06	0.069	0.07	0.062	0.06	0.064	0.071	0.0585	0.0695
X1 (m)	0.0607	0.0702	0.0712	0.0622	0.0602	0.0677	0.0722	0.0602	0.0682
X2 (m)	0.0597	0.0687	0.0697	0.0617	0.0597	0.0637	0.0707	0.0582	0.0692
β	0.0084	0.0124	0.0124	0.0039	0.0038	0.0339	0.0123	0.0179	-0.0078
V_2 (m/s)	0.1067	0.1240	0.1258	0.1089	0.1054	0.1219	0.1275	0.1067	0.1183
Impulse (Ns)	**7.6338**	**8.8694**	**8.9962**	**7.7920**	**7.5389**	**8.7185**	**9.1231**	**7.6352**	**8.4588**
Force (MN)	6.2597	7.2729	7.3769	6.3894	6.1819	7.1492	7.4809	6.2609	6.9362

Table 4.2 - Table of the blast test schedule, ballistic pendulum measurements and calculated results

4.6.2 Stress-time results obtained during the experimental blast tests

For the purpose of studying the general behaviour of the stress propagating through the lower section of the tibia, only the results for the blast tests performed using 5+1g PE4 is discussed in this section of the report. Comparison of the three different analyses (analytical, experimental and numerical) is also based on comparing the results obtained using 5+1g explosives. All of the stress-time results recorded while performing the series of experimental blast tests are however provided in Appendix B.

4.6.2.1 Blast loading performed excluding the rubber sole

The stress-time results obtained from the data recorded by the strain gauges are shown in Figure 4.12 and Figure 4.13. The initial portion of the graphs is mostly taken up by signal noise due to the interference caused by the electrical signal being sent through the detonator. As the stress wave is also only expected to propagate through the strain gauges from roughly 40μs at the earliest, it is decided to present only the section of the graph that is of significance to the investigation.

Two of the tests performed while detonating 5+1g explosives in the centre of the foot model are presented in Figure 4.12. The maximum stress recorded for the two tests is 16.8MPa and 20.3MPa respectively. A 9.6% standard deviation exists between these two tests, indicating acceptably good repeatability of the series of experimental blast tests. A curious event is noticed in the second test (DU_110107a), namely the unexpected peak occurring at approximately 120μs. Even though it is possible that this sudden peak in the stress may purely be due to signal noise, earlier research has pointed out that applying an impact load in the centre of the foot model would cause a second peak in the stress results[8]. The numerical analysis will however be scrutinised for an explanation.

Figure 4.13 shows the stress-time results obtained during two blast tests which were performed by detonating 5+1g explosives axially in line with the calcaneous of the foot model. A maximum stress of 27.7MPa and 32.7MPa is recorded for the respective two blast tests. Once again an acceptable standard deviation of 8.2% exists between the two maximum stress results.

The shape of the stress-time graphs obtained for blast loading performed excluding the rubber sole is as predicted in the analytical solution (Section 4), i.e. elongated with the peak stress fading off gently. The time domain predicted in the analytical solution for blast loading at the heel is also similar. However, the time domain for blast loading in the centre of the foot is notably extended. The finer details of these stress results are discussed later in this section of the report.

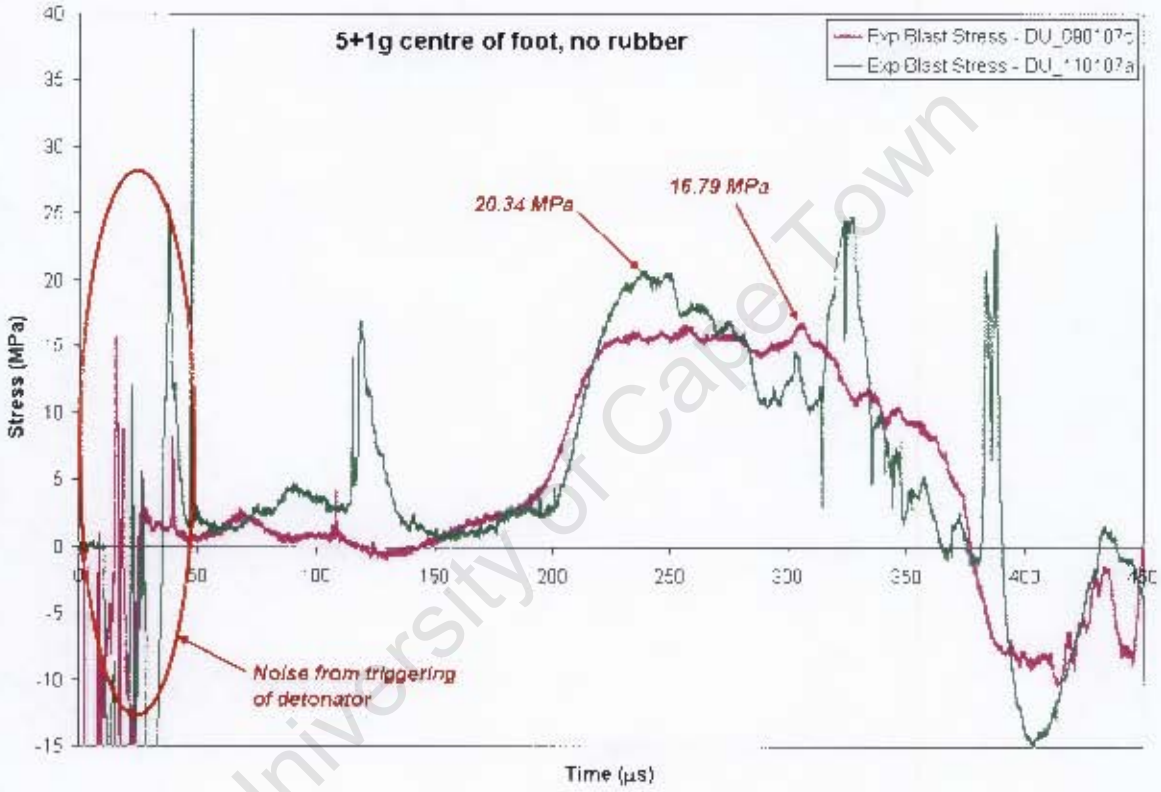

Figure 4.12 – Graph of blast test results for 5+1g PE4 placed in the centre of the foot model, excluding the rubber sole

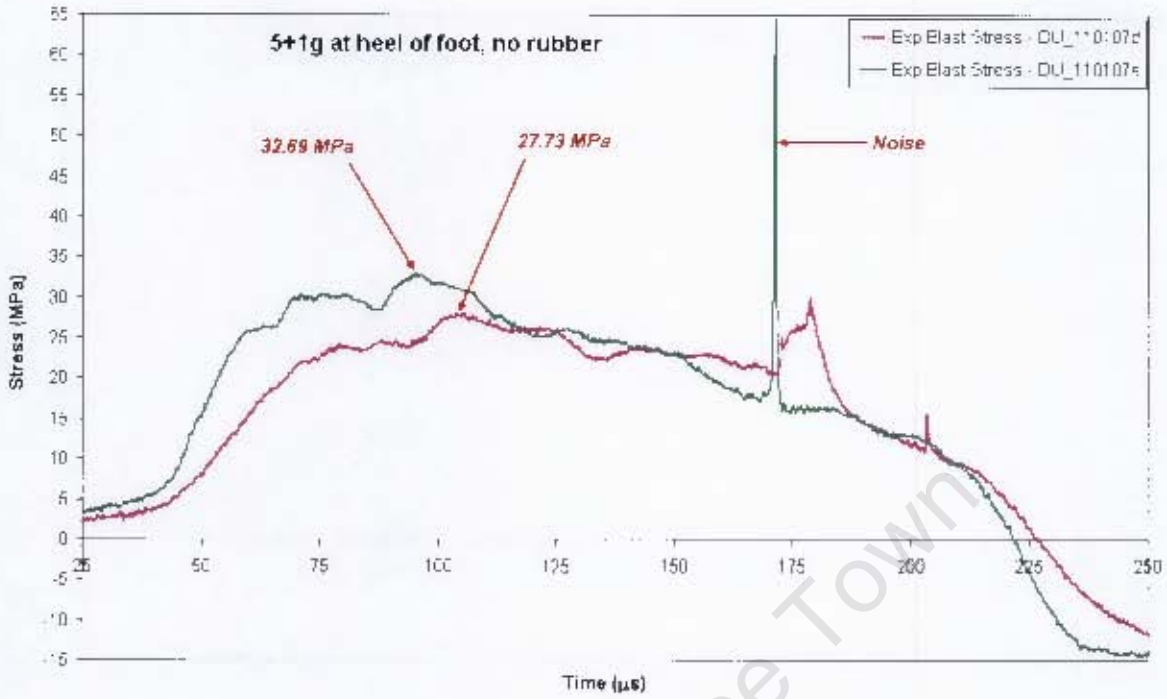

Figure 4.13 - Graph of blast test results for 5+1g PE4 placed in line with the heel of the foot model, excluding the rubber sole

4.6.2.2 Blast loading performed including the rubber sole

Figure 4.14 shows the stress-time results obtained when 5+1g explosives are detonated in the centre of the foot with the rubber sole included in the test setup. Two distinct peaks in the stress signal are observed. The first peak stress of 4.2MPa occurs in the time span estimated in the analytical solution (Chapter 4) which the compressive stress wave is expected to take to propagate through the foot and tibia. The second peak stress of 5.4MPa occurs after approximately twice the time span as the first, implying that a second compressive stress wave propagating through the foot model caused an exaggeration in the maximum stress. Maximum stress values of 4.8MPa and 5.2MPa are recorded for the first peaks and 8.6MPa and 12.3MPa are recorded for the second peaks occurring during the other two centre blast tests. The magnitude of the initial peak stresses differs by roughly 3.9%, whereas the maximum stress values of the second peaks differs by a standard deviation of 17.7%.

The stress-time graph for the blast test performed with 5+1g explosives being detonated in line with the heel with the rubber sole included in the setup is given in Figure 4.15. The maximum stress found for this blast test setup is 6.6MPa.

The shape of the stress-time graphs obtained for the blast tests where the rubber sole is included is as predicted by the analytical solution, i.e. the graph is characterised by a peak stress of short duration.

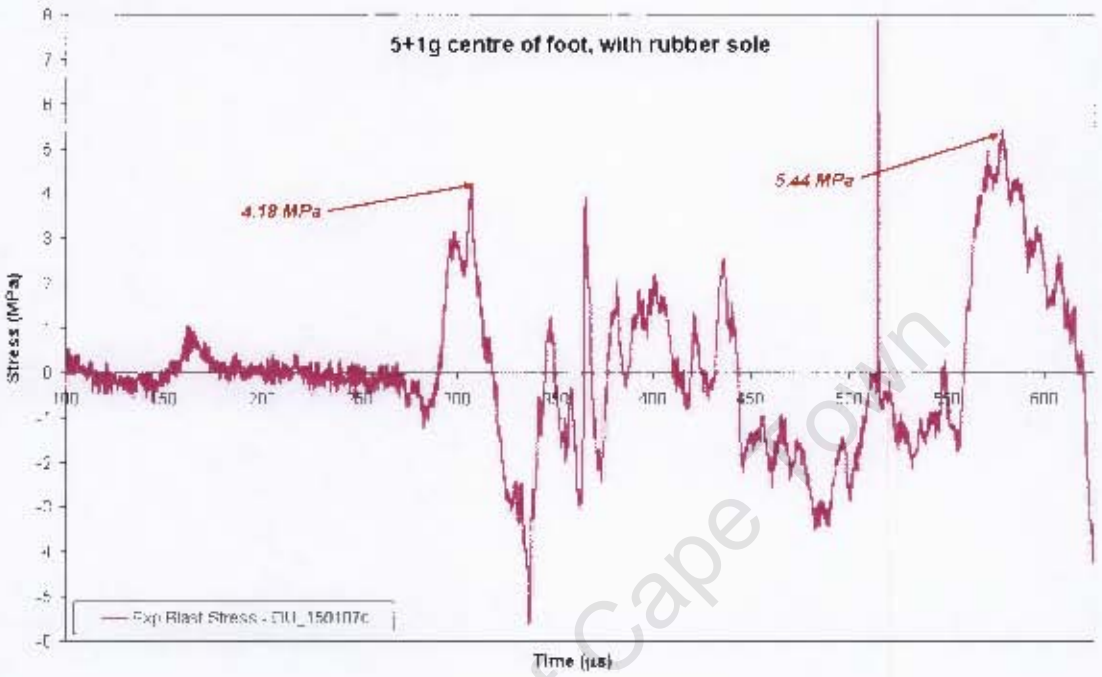

Figure 4.14 - Graph of blast test results for 5+1g PE4 placed in the centre of the foot model, including the rubber sole

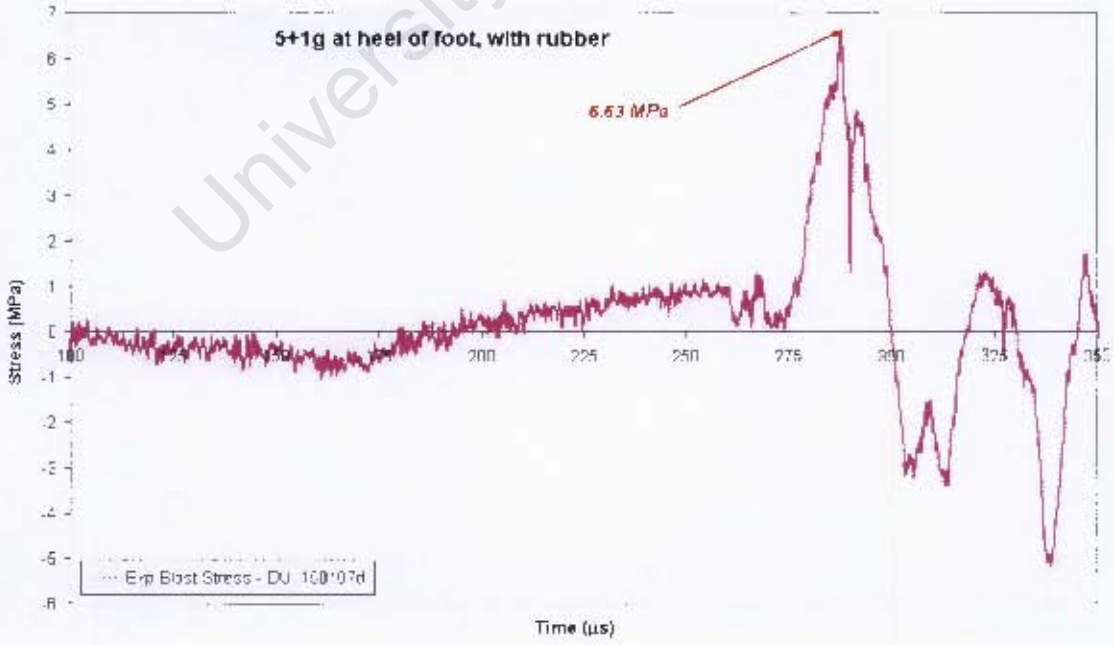

Figure 4.15 - Graph of blast test results for 5+1g PE4 placed at the heel of the foot model, including the rubber sole

4.6.3 Investigating the effect of blast loading position

The positioning of the blast load is naturally expected to affect mainly two aspects of the stress-time results:

- The magnitude of the maximum stress transmitted through the strain gauges placed on the tibia is affected, because the impact load applied in line with the calcaneous of the foot model is expected to induce a higher stress in the tibia than when the load is applied in the centre of the foot model.
- The time at which the stress starts to rise sharply while approaching the maximum stress value is also affected. This is due to the stress wave needing less time to propagate directly through the calcaneous and the ankle complex to reach the strain gauges on the tibia. When the impact load is applied in the centre, the stress wave needs to travel further via the detonation plate, calcaneous and metatarsals before reaching the strain gauges.

4.6.3.1 *Impact load applied excluding the rubber sole*

The stress-time comparison between applying the blast load in the centre with respect to applying the blast load in line with the calcaneous of the foot model is shown in Figure 4.16. A maximum stress of 16.8MPa is induced during the centre blast load and 27.7MPa during the heel blast. Comparing these maximum stress values yields a 65% increase in stress if the impact load position is moved from the centre of the foot to the heel of the foot. A 61% increase in stress is observed when the test results from test DU_110107a (centre blast, 20.34MPa) and test DU_110107e (heel blast, 32.69MPa) is compared. The time delay for the onset of reaching the peak stress for an impact in the centre is approximately 80μs with respect to impact applied in line with the calcaneous.

4.6.3.2 *Impact load applied including the rubber sole*

Figure 4.17 shows the comparison between the stress-time results obtained for centre and heel blast loading conditions where the rubber sole is included in the test setup. Blast loading in the centre of the foot model results in a maximum stress of 5.4MPa recorded by the strain gauges, whereas blast loading at the heel of the foot induced a maximum stress of 6.6MPa in the tibia. Comparing these results shows that blast loading at the heel results in a 22% increase in maximum stress experienced by the lower region of the tibia than for blast loading applied in the centre of the foot model. An approximate 275μs delay in onset of reaching the peak stress is observed for centre impact with respect to heel impact.

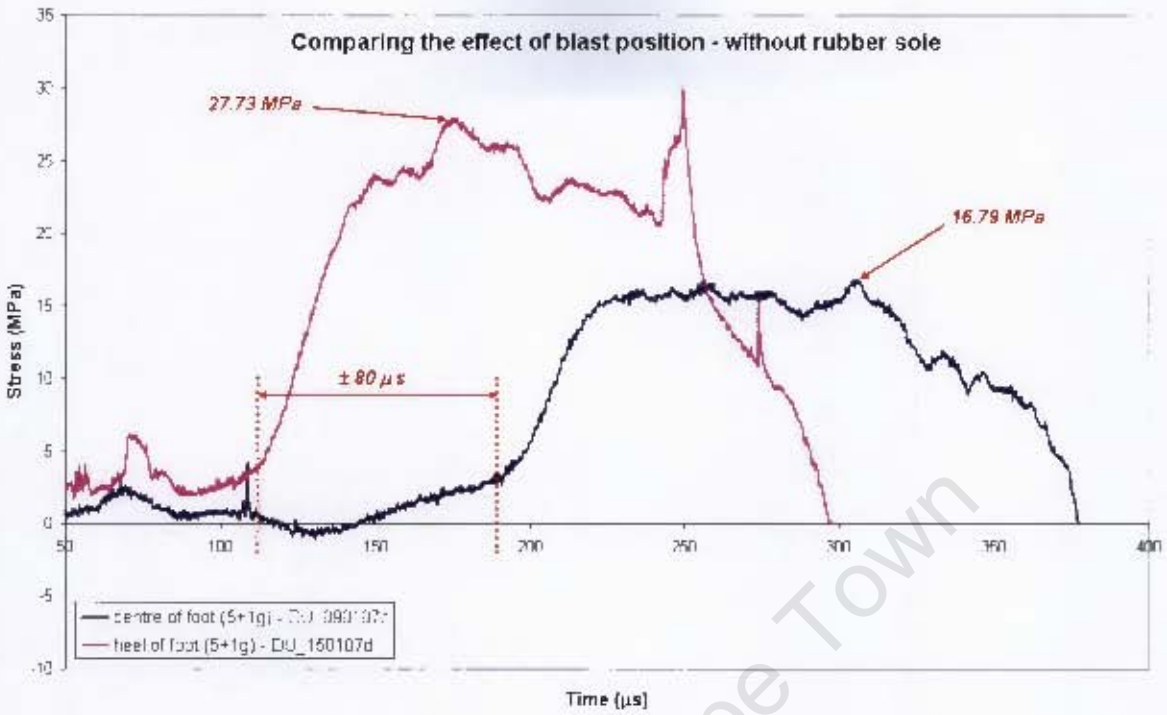

Figure 4.16 – Graph comparing the effects of blast loading in the centre of the foot vs. at the heel of the foot, excluding rubber sole

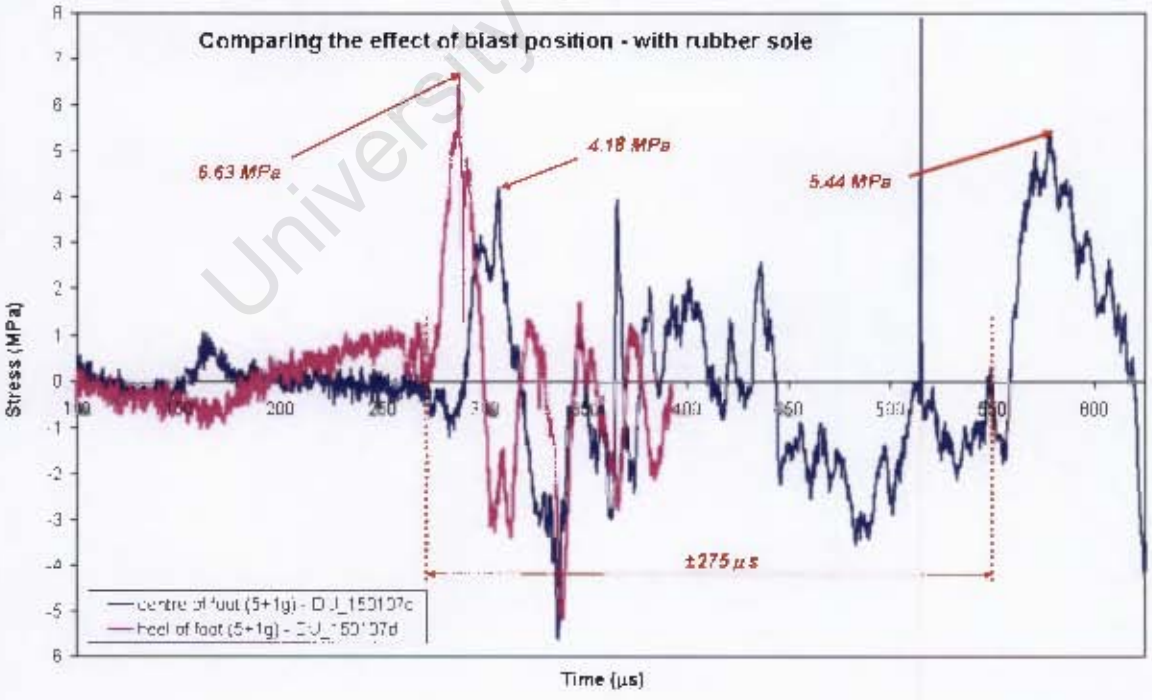

Figure 4.17 - Graph comparing the effects of blast loading in the centre of the foot vs. at the heel of the foot, including rubber sole

4.6.4 Investigating the attenuation effect of including the rubber sole

The degree of attenuation supplied by including the rubber sole layer in the test setup is evaluated in terms of the amount of stress transmitted to the strain gauges. A delay in the transmission of stress as a result of the dissipative nature of rubber material (energy dissipated by the rubber material) is also expected to be observed in the stress-time results.

4.6.4.1 Blast loading in the centre of the foot model

A collection of results obtained from the various blast tests performed with the explosives placed in the centre of the test setup is presented in Figure 4.18. Including the rubber layer in the blast tests performed using 5+1g explosives decreased the maximum stress experienced by the tibia by 68%. For the blast tests performed using 6+1g and 7+1g explosives, an attenuation of 76% and 55% respectively is observed in the stress recorded by the strain gauges. Introducing the layer of rubber is noticed to cause a time delay of 90μs in the onset of reaching the initial maximum stress and approximately 340μs in reaching the second peak stress.

4.6.4.2 Blast loading at the heel of the foot

Results from the blast tests performed with the explosives placed axially in line with the calcaneous of the foot model is given in Figure 4.19. In order not to induce plasticity in the Aluminium (Al6063-T6) tube used to represent the tibia, it was decided not to continue heel blast testing using more than 5+1g PE4 when the rubber sole is excluded. However when the rubber sole is included in the test setup, the rubber proved to provide enough attenuation to increase the amount of explosives used to 7+1g. Unfortunately blast loading using 7+1g explosives generated an unexpected maximum stress of 3.8MPa which is lower than the maximum stress of 6.6MPa generated by the blast loading performed using 5+1g explosives. As such, the opportunity to draw a comprehensive comparison between the results produced by different impact loading conditions is lost. Nevertheless, the attenuation provided by the rubber layer is observed to be approximately 76%. Including the rubber layer in the test setup is noticed to create a time delay of 170μs in the onset of reaching the maximum stress.

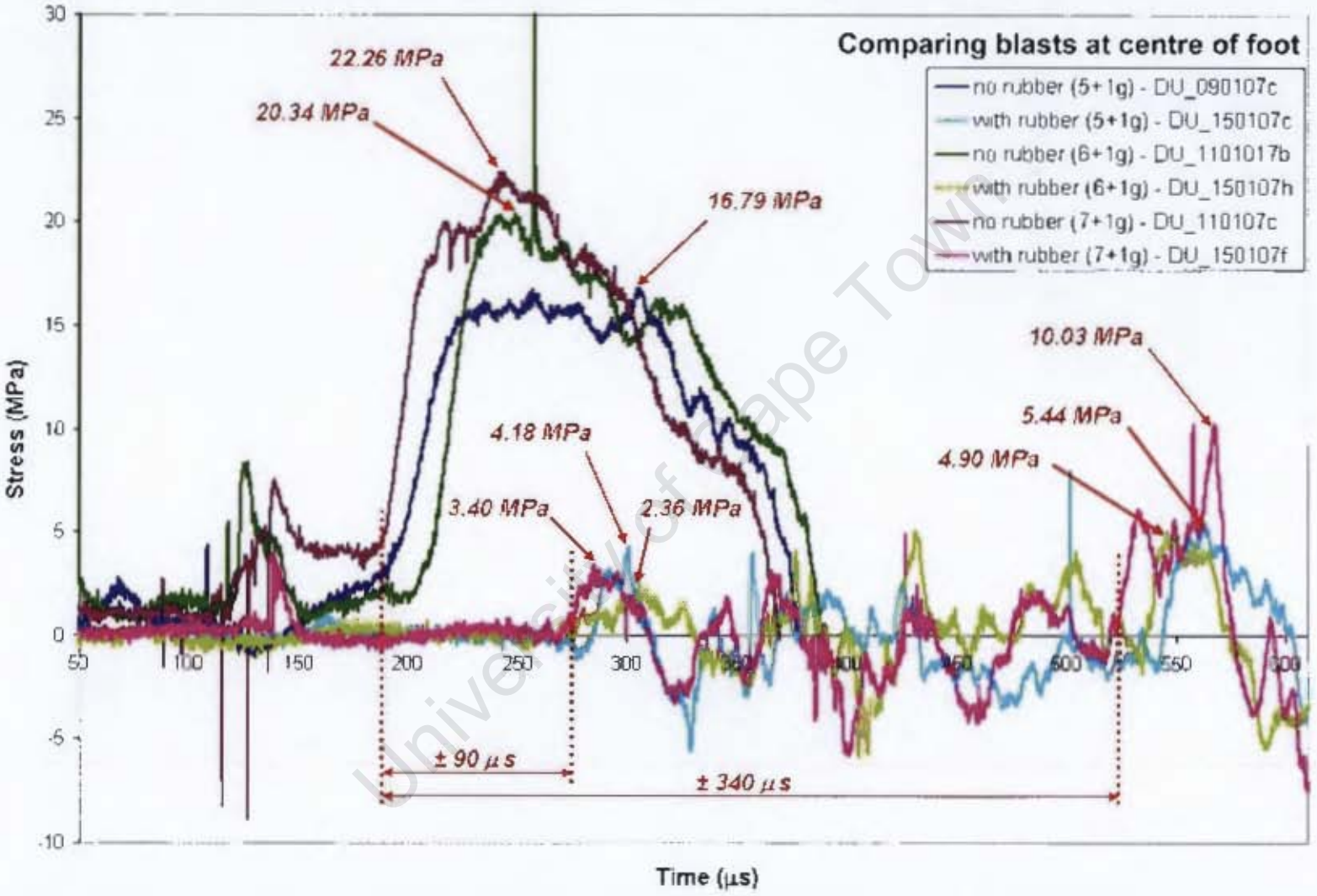

Figure 4.18 – Graph comparing results when excluding and including the rubber sole for blast loading in the centre of the foot

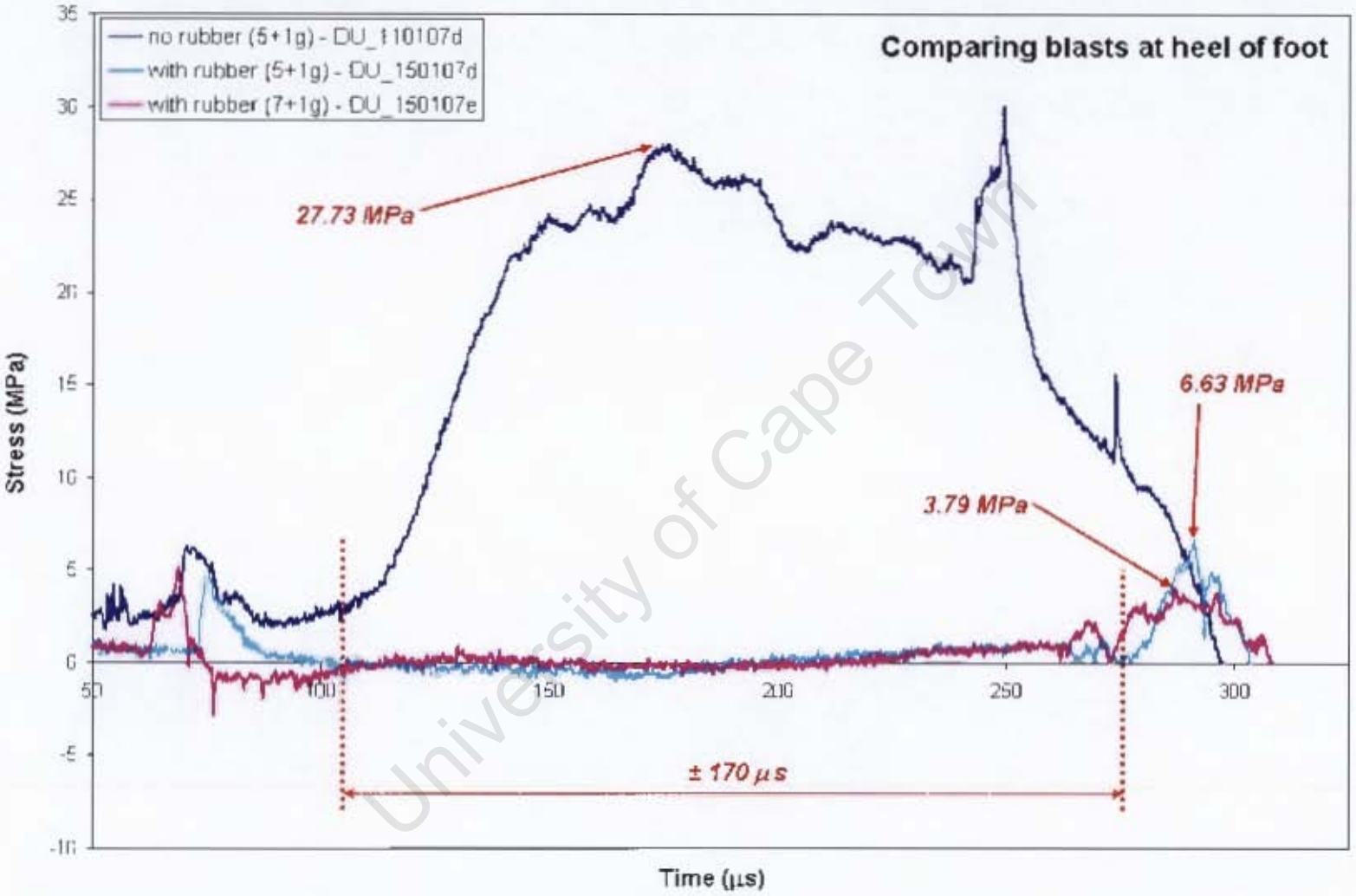

Figure 4.19 - Graph comparing results when excluding and including the rubber sole for blast loading at the heel of the foot

4.6.5 Comparison of results from all loading conditions

In order to readily compare the effect produced by blast loading using a certain amount of explosives positioned in the centre or at the heel of the foot surrogate and excluding or including a rubber layer, Table 4.3 is constructed. The values given in Table 4.3 represent the percentage by which the stress results from the yellow section differ with respect to the blue section. For example: the stress resulting from 5+1g (no rubber, centre blast) is 17% less than the stress resulting from 6+1g (no rubber, centre blast); whereas the stress resulting from 7+1g (no rubber, centre blast) is 33% higher than the stress resulting from 5+1g (no rubber, centre blast).

The cells of Table 4.3 marked in green and red indicates the comparison in the blast impact scenarios which represent the opposite corners of the scale. The green cell shows that the stress resulting from a blast load in the centre of the foot when the rubber sole is included results in 82% less stress experienced by the lower tibia than during a blast load applied at the heel of the foot model when the rubber sole is not included in the test setup. The red cell simply shows the opposite, i.e. that a blast load at the heel of the foot excluding the rubber layer results in a 466% higher stress than during a blast load applied in the centre of the foot when the rubber layer is included.

				CENTRE BLAST						HEEL BLAST		
				No rubber			With rubber			No rubber	With rubber	
			Charge mass	5+1g	6+1g	7+1g	5+1g	6+1g	7+1g	5+1g	5+1g	7+1g
		Charge mass	Stress (MPa)	16.8	20.3	22.3	5.4	4.9	10.0	27.7	6.6	3.8
CENTRE BLAST	No rubber	5+1g	16.8	0	-17	-25	+209	+243	+67	-39	+153	+343
		6+1g	20.3	+21	0	-9	+274	+315	+103	-27	+207	+437
		7+1g	22.3	+33	+9	0	+309	+354	+122	-20	+236	+487
	With rubber	5+1g	5.4	-68	-73	-76	0	+11	-46	-80	-18	-44
		6+1g	4.9	-71	-76	-78	-10	0	-51	-82	-26	-29
		7+1g	10.0	-40	-51	-55	+84	+105	0	-64	+51	+165
HEEL BLAST	No rubber	5+1g	27.7	+65	+36	+25	+410	+466	+176	0	+318	+632
	With rubber	5+1g	6.6	-61	-67	-70	+22	+35	-34	-76	0	+75
		7+1g	3.8	-77	-81	-83	-30	-23	-62	-86	-43	0

Table 4.3 – Table documenting the percentage difference between the stress results

Chapter 5 - Analytical Model of Stress Wave Propagation

5.1 INTRODUCTION

This section of the report describes the attempt to model analytically the stress-wave propagation through the foot. The system is essentially represented as a series of "bars" in full contact with each other, each bar of its own particular cross-sectional area.

The first part of the impact loading is performed using only the aluminium foot model. Aluminium and mild steel are linear elastic solid materials, therefore the basic equations for linear elasticity can be used to analyse the stress-wave propagation.

The second part of the impact loading introduces a rubber layer wedged between the detonation plate and the base of the aluminium foot model. However, rubber is not a linear elastic material, which implies that the constitutive equations for linear elasticity cannot be used to derive the stress-wave propagation through the rubber "bars" in the analytical model. A hyperelastic strain energy potential is incorporated to analyse the stress-wave propagation through the rubber material.

It is important to remember that the results from this analysis serves to indicate the estimated stress propagation through the foot model components (from the base of the detonation plate up to the top of the tibia) and not the stress propagation through the strain gauges. The graphs representing the stress propagation is however still plotted with respect to time and not distance, as it takes a specific time for the stress to travel through each component. The point at which the stress passes through the strain gauges is indicated on each graph so that the peak stress values obtained from the experimental blast tests and the numerical simulations can eventually be compared and validated (see Chapter 7).

5.2 ONE-DIMENSIONAL STRESS WAVE PROPAGATION

5.2.1 Linear elastic solid material

The theory of one-dimensional stress wave propagation in uniform bars is used to obtain the analytical solution to the impact loading problem under investigation. The analysis is based on the set of constitutive equations for a linear elastic solid material in which a relationship between stress and strain is constructed[59]. Considering a Cartesian coordinate system, for $i, j = 1,2,3$, the constitutive equations of linear elasticity are[59]:

$$\frac{\partial T_{ji}}{\partial x_j} + \rho b_i = \rho a_i \qquad \text{Eq. 5.1}$$

$$T_{ij} = \frac{E_Y}{1+\nu}\left[E_{ij} + \left(\frac{\nu}{1-2\nu}\right)E_{kk}\delta_{ij}\right] \qquad \text{Eq. 5.2}$$

$$E_{ij} = \frac{1}{E_Y}\left[(1+\nu)T_{ij} - \nu T_{kk}\delta_{ij}\right] \qquad \text{Eq. 5.3}$$

T_{ji} = Cauchy stress component in the j direction, acting on the plane with an outward normal in the i direction

E_{ij} = strain component in the i direction, acting on the plane with an outward normal in the j direction

T_{kk} = $T_{11} + T_{22} + T_{33}$

E_{kk} = $E_{11} + E_{22} + E_{33}$

x_j = position in the j direction

b_i = body force acting in the i direction

a_i = particle acceleration in the i direction

ρ = density of the material

E_Y = Modulus of elasticity (Young's Modulus) of the material

ν = Poisson's ratio of the material

δ_{ij} = Kronecker delta, which is defined by $\delta_{ij} = \begin{cases} 1 & if \quad i = j \\ 0 & if \quad i \neq j \end{cases}$

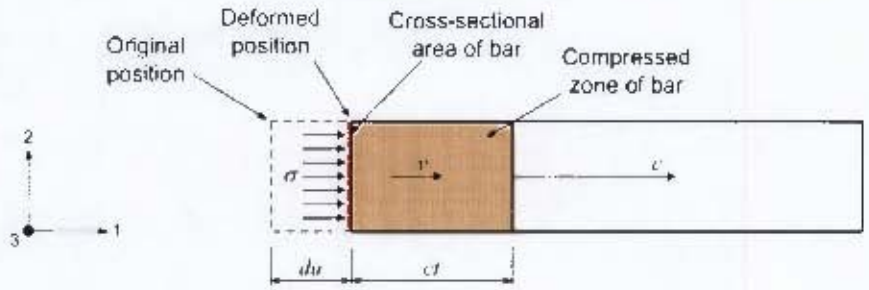

Figure 5.1 – Illustration of one-dimensional impact loading of a uniform bar [56]

In order to analyse the one-dimensional stress wave propagation, a long slender bar of specific density, ρ, and Elastic Modulus, E_Y, is considered, of which the impact loading is illustrated in Figure 5.1. When a stress is rapidly applied to the one end of the bar, a compressive stress wave is set up which propagates along the length of the bar. If the presence of body forces is neglected, Cauchy's equation of motion given in Eq. 5.1 becomes[59]:

$$\frac{\partial T_{11}}{\partial x_1} = \rho \frac{\partial^2 u_1}{\partial t^2} \qquad \text{Eq. 5.4}$$

From Eq. 5.2 and Eq. 5.3, considering a one-dimensional case:

$$T_{11} = E_Y . E_{11} \Rightarrow \frac{\partial T_{11}}{\partial x_1} = E_Y \frac{\partial E_{11}}{\partial x_1} = E_Y \frac{\partial^2 u_1}{\partial x_1^2} \qquad \text{Eq. 5.5}$$

Equating Eq. 5.4 and Eq. 5.5 yields the wave equation, where c is the wave speed. The wave speed is a material property which represents the velocity at which a stress wave travels along the bar[59]:

$$\frac{\partial^2 u_1}{\partial t^2} = c^2 \frac{\partial^2 u_1}{\partial x_1^2} \qquad \Rightarrow \qquad c = \sqrt{\frac{E_Y}{\rho}} \qquad \text{Eq. 5.6}$$

Referring to the impact loading illustrated in Figure 5.1, at a specific time t, the momentum is equal to the impulse transferred via the impact[56]:

$$m_{bar} \times v_{particle} = F_{applied} \times t$$
$$(\rho_{bar} A_{bar} ct) v_{particle} = (\sigma_{applied} A_{bar}) t$$

As such, the stress due to the impact is:

$$\sigma = \rho_{bar} c v_{particle} \qquad \text{Eq. 5.7}$$

Knowing that the density and the wave speed are material constants, it is implied that the stress experienced by the bar is directly proportional to the change in particle velocity in the bar[56]. The wave speed and particle velocity are in the same direction (and therefore have the same sign) for a compressive stress wave, while the opposite is true for a tensile stress wave.

In the case of the impact of two uniform bars of the same material but with different cross-sectional areas, the following assumptions are made[56]:

- Full contact is made over the entire contact area of the smaller bar.
- The two bars remain in total contact during the duration of the impact, implying that the overall particle velocity at the two contact surfaces is the vector sum of the particle velocities at the input and output interfaces[56]:

$$v_{total} = v_{in} + v_{out} = \frac{\sigma_{in}}{c\rho} + \frac{\sigma_{out}}{c\rho} \quad \text{Eq. 5.8}$$

The forces at the interface are in equilibrium, therefore:

$$\sigma_{in} A_{in} = \sigma_{out} A_{out} \quad \text{Eq. 5.9}$$

Rearrangement of Eq. 5.8 and Eq. 5.9 enables the stresses in each bar to be written in terms of the particle velocity at the interface and the ratio of the cross-sectional areas of the two bars[56]:

$$\sigma_{in} = \frac{A_{out}}{A_{in} + A_{out}} \rho c v_{total}$$

$$\sigma_{out} = \frac{A_{in}}{A_{out} + A_{in}} \rho c v_{total} \quad \text{Eq. 5.10}$$

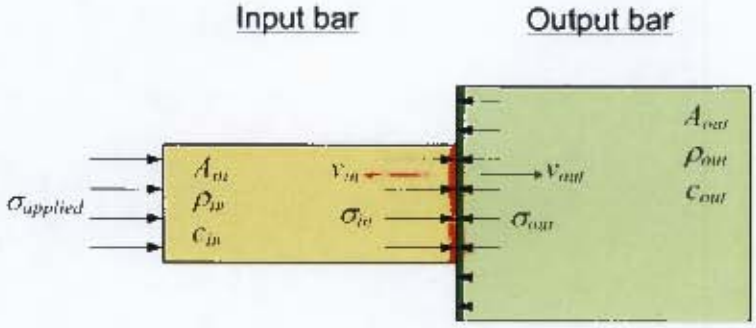

Figure 5.2 – Illustration of one-dimensional impact of two uniform bars

5.2.2 Hyperelastic incompressible solid material

It is a well-known fact that the mechanical behaviour of rubber is rate dependent[52;60]. Hyperelasticity is commonly used to model the mechanical behaviour of rubber-like materials, as rubber is an ideally elastic material which possesses isotropic and nonlinear material properties[60]. Hyperelastic behaviour is described by a strain energy potential, which relates the strain energy stored at a certain point in the material to the strain experienced at that point in the material. Various mathematical strain energy models exist which can be used to model the hyperelasticity, of which the polynomial model (and other derived models such as the Neo-Hookean, Mooney-Rivlin and Yeoh models) is the most popular strain energy function generally utilised[60]. The polynomial strain model for the strain energy function is[60]:

$$U = \underbrace{\sum_{i+j=1}^{N} C_{ij}\left(\bar{I}_1 - 3\right)^i \left(\bar{I}_2 - 3\right)^j}_{\text{Deviatoric part}} + \underbrace{\sum_{i=1}^{N} \frac{1}{D_i}(J_{el} - 1)^{2i}}_{\text{Volumetric part}} \qquad \text{Eq. 5.11}$$

It has been found that using a polynomial strain energy function with three terms in the resulting polynomial series is sufficient to create an adequate stress-strain fit of the available test data[52]. It is also reasonable to assume that rubber-like materials are incompressible, which means the volumetric part of the strain energy function may be ignored[52;60]. This results in the polynomial strain energy function to be written as[52]:

$$U = C_{10}\left(\bar{I}_1 - 3\right) + C_{01}\left(\bar{I}_2 - 3\right) + C_{11}\left(\bar{I}_1 - 3\right)\left(\bar{I}_2 - 3\right) \qquad \text{Eq. 5.12}$$

where C_{10}, C_{01} and C_{11} are material parameters determined by using available one-dimensional test data.

During uniaxial loading of a specimen, λ indicates the stretch in the loading direction. The stretches in the principle directions and the resulting first and second deviatoric strain invariants are[52;61]:

$$\lambda_1 = \lambda \qquad \bar{I}_1 = \lambda^2 + 2\lambda^{-1}$$
$$\lambda_2 = \lambda_3 = \lambda^{-1/2} \qquad \bar{I}_2 = \lambda^{-2} + 2\lambda$$

The engineering strain ε_{11} in the direction of the uniaxially applied load is related to the stretch λ by the equation $\lambda = 1 + \varepsilon_{11}$ [52;61].

In order to determine the nominal stress-strain relationship of the hyperelastic material, the principle of virtual work is applied. The change in potential energy is related to the change in stretch, which yields the stress σ_{11} that is acting on the particle in the uniaxial loading direction[61]:

$$\begin{aligned} T &= \frac{\partial U}{\partial \lambda} \\ &= \frac{\partial U}{\partial \bar{I}_1}\frac{\partial \bar{I}_1}{\partial \lambda} + \frac{\partial U}{\partial \bar{I}_2}\frac{\partial \bar{I}_2}{\partial \lambda} \\ &= 2\left(1-\lambda^{-3}\right)\left[\lambda\frac{\partial U}{\partial \bar{I}_1} + \frac{\partial U}{\partial \bar{I}_2}\right] \\ \sigma_{11} &= 2\left(1-\lambda^{-3}\right)\left[C_{10}\lambda + C_{01} + C_{11}\left(\bar{I}_1 - 3 + \lambda\left(\bar{I}_2 - 3\right)\right)\right] \end{aligned} \qquad \text{Eq. 5.13}$$

The experimental stress-strain data obtained from the SHPB testing of the rubber specimens for dynamic compression at a strain rate of 2500s^{-1} (as provided in Section 3.3.2 of this thesis) is used to ascertain the material parameters C_{10}, C_{01} and C_{11}. A simple linear least-squares fit is employed to match the empirical data to the existing experimental data. The values for the three material parameters are calculated to be:

$$\begin{aligned} C_{10} &= 71.6\,MPa \\ C_{01} &= -61.8\,MPa \\ C_{11} &= -85.2\,MPa \end{aligned}$$

The nominal stress-strain relationship of the rubber used in this investigation experiencing dynamic compression at a strain rate of 2500s^{-1} is therefore given by:

$$\sigma_{11} = 2\left(1-\lambda^{-3}\right)\left[(71.637\times10^6)\lambda - (61.876\times10^6) - 85.238\times10^6.\left(\bar{I}_1 - 3 + \lambda\left(\bar{I}_2 - 3\right)\right)\right]$$

Eq. 5.14

Following the strain energy potential theory, if the amount of strain induced upon the hyperelastic material at a specific strain rate is known, the stress transmitted by the hyperelastic material can readily be determined.

5.3 ANALYTICAL MODEL OF THE BLAST LOADING OF THE FOOT MODEL, EXCLUDING THE RUBBER SOLE

The blast loading test setup of the ballistic pendulum and foot model is analytically represented by a series of uniform "bars" of varying cross-sectional area. The one-dimensional stress wave propagation theory relating to linear elastic materials is employed to obtain the stress-time curve which indicates the approximated maximum stress experienced by the various interfaces as the stress pulse travels through the foot. The estimated stress-time plot for each loading condition (in the centre of the foot and at the heel) is determined for blast loading using 5+1g explosives.

As this is a simple first order approximation, a few important aspects and assumptions that are made need to be pointed out:

- Full contact is assumed to exist over the total contact surface of the bar with the smaller cross-sectional area.
- A state of force equilibrium is assumed at each contact interface; as such Eq. 5.9 applies.
- The stress pulse applied to the system is taken to be a square planar stress wave that propagates without change in amplitude from the front end to the rear end of each bar.
- The stress pulse applied to the front surface of each bar is assumed to travel at a constant wave speed specific to the material of each particular bar.
- Even though the density of the detonation plate (mild steel, ρ=7800 kg/m^3) differs to that of the aluminium used to construct the foot model (Al6000 range, ρ=2710 kg/m^3), Eq. 5.9 indicates that only the stress experienced by one of the contact surfaces and the ratio of the areas of the two bars need to be known in order to determine the stress experienced by the second contact surface. The magnitude of the planar stress pulse applied to the front surface of the detonation plate is known, and the rear surface of the detonation plate is assumed to be subjected to the same magnitude of stress. The stress experienced by the surface in contact with the rear surface of the detonation plate can therefore be easily calculated using Eq. 5.9. The same principle is applied to each of the interfaces in order to determine the stress experienced by the contact surfaces.
- The impact loading problem is solved by means of a purely one-dimensional model. The stress distribution over the impact surface is therefore not taken into account, and the stress applied to the front surface of each bar is modelled as a uniformly distributed load acting over the total cross-sectional area of each bar.

The wave speed of the aluminium used to construct the foot and ankle model was determined in Section 3.2 to be 5137 m/s. Knowing that mild steel has a Young's Modulus of 207 GPa and a density of 7800 kg/m^3, the wave speed for mild steel is calculated using Eq. 5.6 to be 5152 m/s. The shock wave caused by the detonation of the explosives is assumed to travel via two paths, pass through the strain gauges and then at the end of the aluminium tube reflect back through the strain gauges. With the distances between each interface and the wave speed of the material of the particular "bar" being known, the time it will take for the stress wave to travel from interface to interface can be estimated by:

$$t = s/c \qquad \text{Eq. 5.15}$$

5.3.1 Blast loading in the centre of the foot

Figure 5.3 illustrates the two paths along which the stress wave caused by the blast loading is assumed to travel, as well as the various interfaces the stress wave encounters. The approximate distance from the detonating explosives to the strain gauges is 279mm via Path 1 and 441mm via Path 2. It will therefore take the stress wave an estimated 54μs via Path 1 and a longer 86μs via Path 2 to reach the strain gauges after the detonation of the explosives. It will be a further approximately 165μs before the reflection of the shock wave passes through the strain gauges again.

As explained earlier, the components of the system is considered to be uniform bars with the contact surfaces in full contact. Table 5.1 documents the characteristics pertaining each of the "bar" components:

- the given area is the area of the surface in contact with the neighbouring components;
- the distance provided is the length of the component (i.e. the distance the stress wave travels from the first to the second surface of the component);
- the time provided is the total time the stress wave has taken to propagate to the second surface of the particular component;
- ultimately the stress experienced by the contact surfaces of the particular component is produced.

Although the pressure caused by the detonation of the explosives is actually decaying radially outwards at a certain rate from the centre of the detonation (explained in Section 2.2.4), it is deemed sufficient for this first order analysis to represent the applied pressure as a uniformly distributed stress acting over the total area of the detonation plate. In performing the blast tests, the impulse induced by the detonation of 5+1g PE4 is calculated to be in the order of 7.7Ns. According to the equations discussed in Section 4.5.4, the force applied to the

system is therefore approximately 6.3MN, which in turn yields the magnitude of the uniform stress applied to the detonation plate to be 157.5MPa.

The magnitude of the stress acting on the surfaces of each interface as the stress wave travels along the system is presented in a tabular fashion in Figure 5.4 and Figure 5.5. Figure 5.4 shows the dramatic difference in the amount of stress experienced by the calcaneous surface (in contact with the detonation plate) with respect to the stress experienced by the metatarsal surface (in contact with the detonation plate). In reality the calcaneous surface is a point in contact with the surface of the detonation plate. In order to employ the theory of stress propagation through uniform bars, the calcaneous surface is approximated to be a circular surface of diameter 1.2mm. As such, the calcaneous contact surface is estimated to experience a stress of 4195MPa and the metatarsal contact surface only 2.7MPa.

A closer look is taken in Figure 5.5 at the stress behaviour in the ankle complex and the tibia. The stress flow through the contact interfaces of the ankle components is clearly shown by a short series of stress variations, with the stress peaking at 10.6MPa at the contact surfaces of the ankle hinge pin. The stress wave reaches the ankle region approximately 30μs later via Path 2, as the detour via the metatarsals increases the distance travelled by the stress wave. Finally, a maximum average stress of 36MPa is determined to transmit along the tibia. The maximum average stress displays a stress "plateau" which lasts roughly 147μs.

		PATH 1			PATH 2		
Name assigned to each "bar"	Area	Distance	Time	Stress	Distance	Time	Stress
	(m^2)	(m)	(μs)	(MPa)	(m)	(μs)	(MPa)
Detonation plate	0.04000	0.106	20.63	**157.5**	0.106	20.63	**157.5**
Calcaneous	$9.8x10^{-7}$	0.01	22.58	**4194.7**	~	~	~
Metatarsals	0.0015	~	~	~	0.01	22.58	**2.7**
Foot bridge	0.011	0.015	25.50	**0.36**	0.177	57.03	**0.36**
Hinge bottom	0.001	0.025	30.36	**4**	0.025	61.90	**4**
Hinge pin	0.000377	0.006	31.53	**10.6**	0.006	63.07	**10.6**
Hinge top	0.00048	0.017	34.84	**8.3**	0.017	66.38	**8.3**
Tibia base	0.0016	0.02	38.74	**2.5**	0.02	70.27	**2.5**
Strain gauges	0.000111	0.08	54.31	**36**	0.08	85.85	**36**
End of tibia	0.000111	0.42	136.07	**36**	0.42	167.61	**36**
Strain gauges	0.000111	0.42	217.84	**36**	0.42	249.37	**36**

Table 5.1 – Table of stress propagation through the foot model, rubber sole excluded (blast loading in centre of foot)

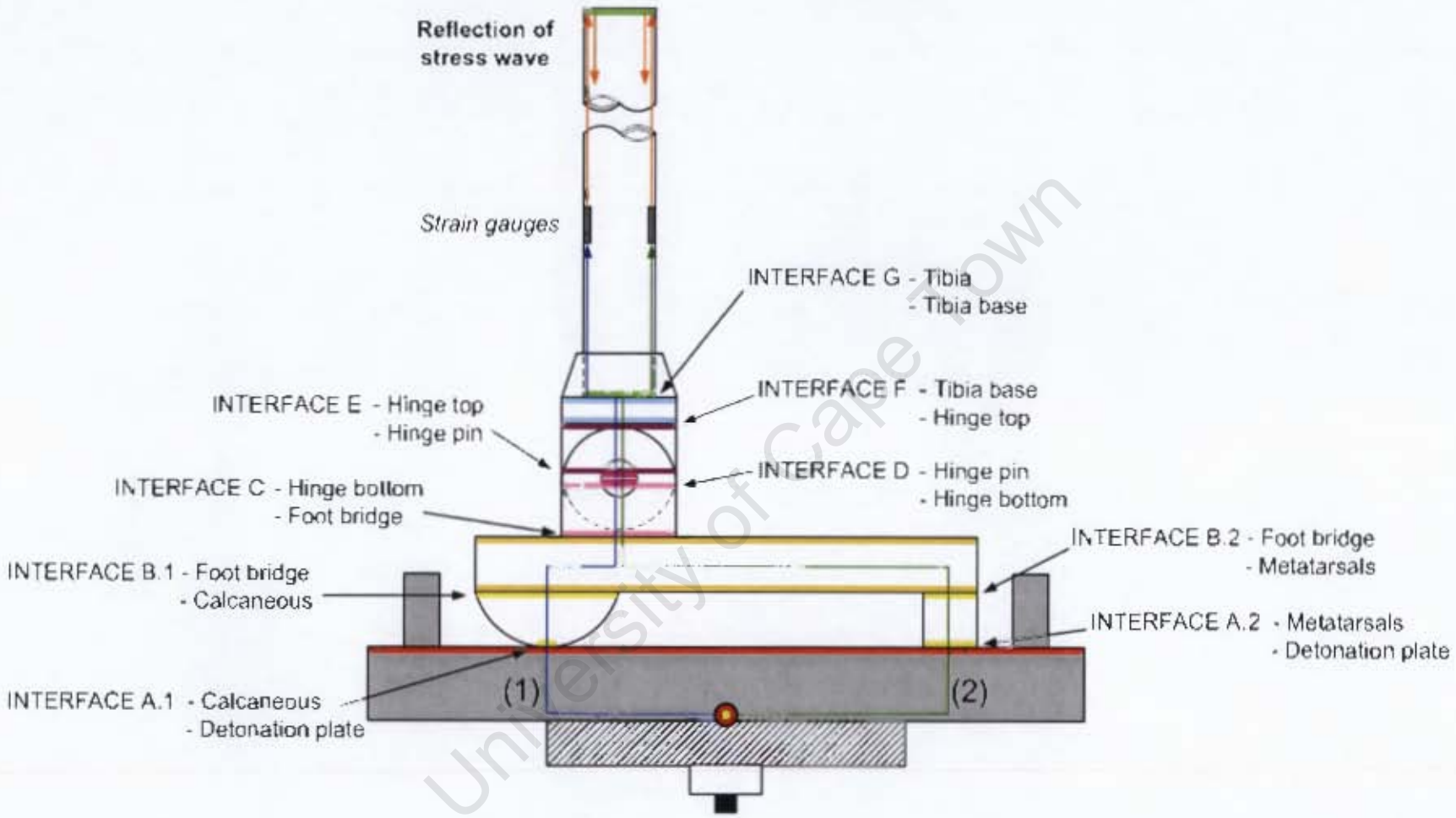

Figure 5.3 – Diagram indicating Path 1 and Path 2 of stress wave propagation for blast loading in the centre of the foot, excluding rubber sole

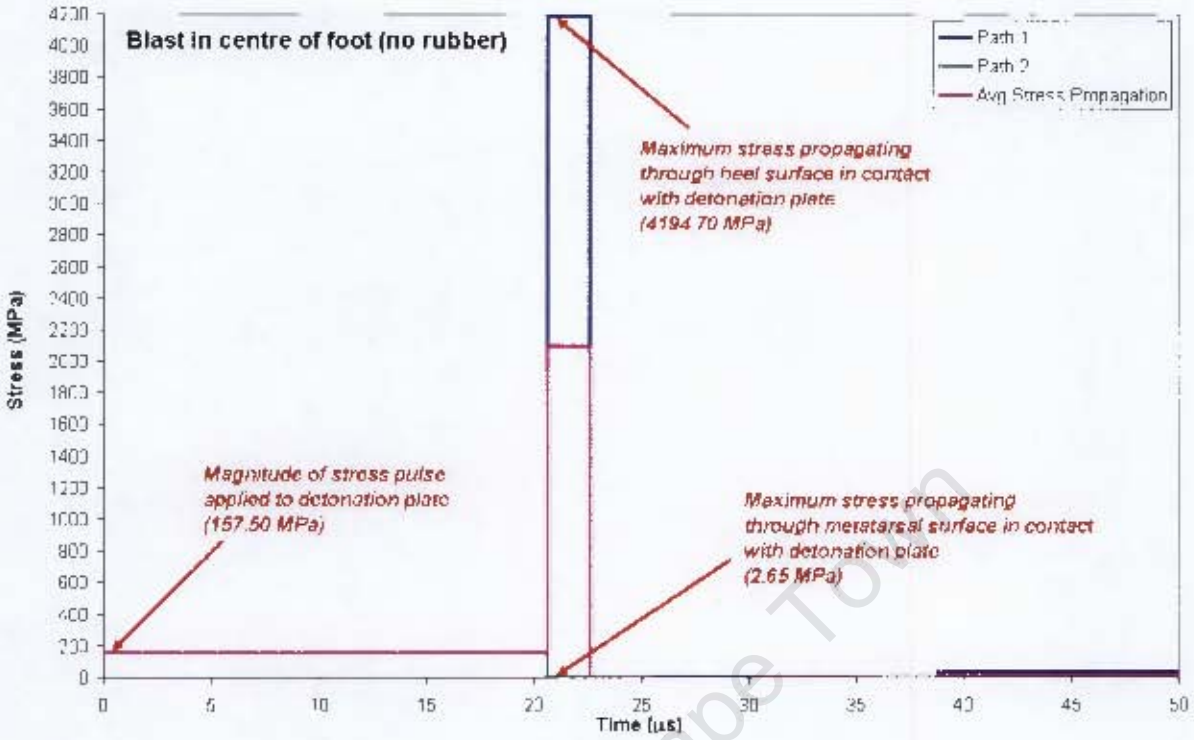

Figure 5.4 - Graph showing analytical prediction for maximum stress experienced by calcaneous and metatarsal contact surfaces during blast loading in centre of the foot model, excluding the rubber sole

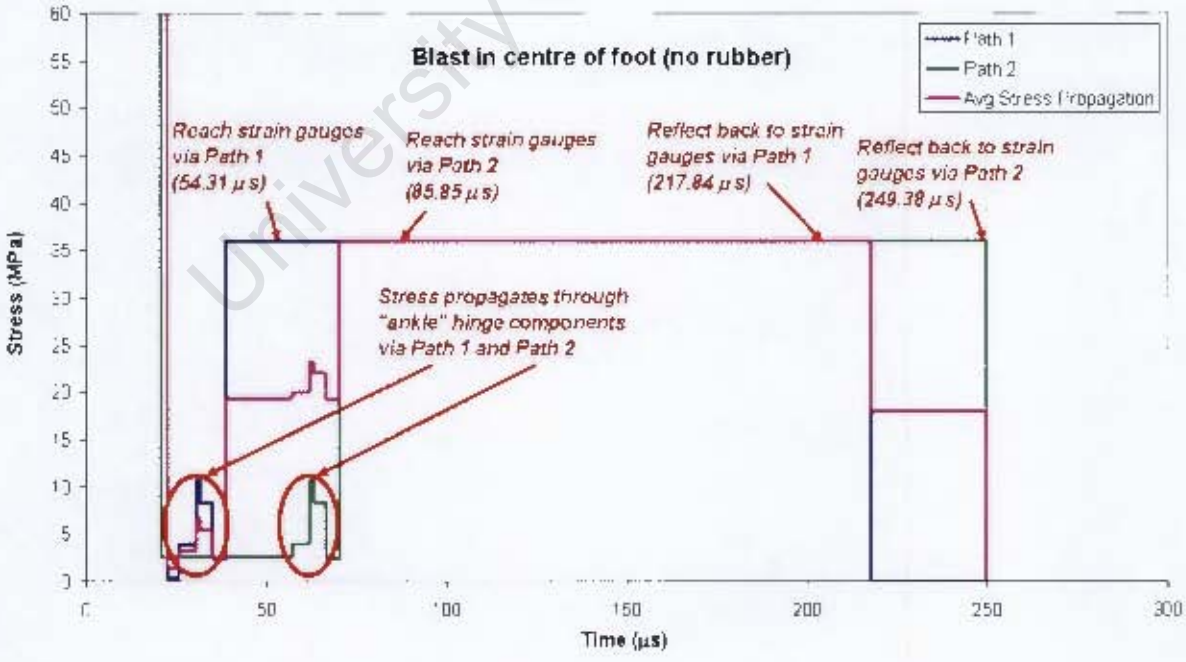

Figure 5.5 – Graph showing analytical prediction for stress propagation during blast loading in centre of the foot model, excluding the rubber sole

5.3.2 Blast loading at the heel of the foot

Figure 5.6 illustrates the two paths the stress wave is assumed to travel. The setup is similar, only in this case the detonated explosive responsible for the impact load is positioned at the heel of the foot model. As such, the distances of Path 1 and Path 2 differ to the distances relating to the centre impact loading condition. Following the detonation of the explosives, the stress wave travels an approximate distance of 198mm in 39μs along Path 1 to reach the strain gauges, and roughly 522mm in 102μs along Path 2 before reaching the strain gauges. Once again the stress wave transmits along the tibia and reflects back to the strain gauges in 165μs.

The results documented in Table 5.2 are similar to the results shown in Table 5.1. The impulse transmitted during the heel blast loading conditions is of the same magnitude as what is calculated for the centre blast loading conditions. As such, the uniform stress acting over the surface of the detonation plate is also 158MPa. The position of impact is however moved from the centre of the setup to be axially in line with the calcaneous of the foot model, which alters the distance travelled by the stress wave through the detonation plate via Path 1 and Path 2. Therefore the time related to the stress propagation through the series of interfaces along Path 1 and Path 2 differs significantly, which is also clearly seen in Figure 5.7 and Figure 5.8.

It is observed in Figure 5.7 that the maximum stress transmitted to the calcaneous and metatarsal contact surfaces is the same as for the centre impact loading position. This is due to the assumption that the stress wave is planar and does not change in amplitude as it travels along the uniform bar. However, the stress wave reaches the metatarsal contact surface roughly 30μs later than the calcaneous contact surface.

Figure 5.8 also demonstrates the time lag in stress transmission via Path 2 relative to Path 1. The stress wave travelling along Path 2 reaches the ankle region 63μs later than the stress wave travelling along Path 1. The stress flow through the ankle hinge components is again clearly identifiable by the short series of stress variation, with a peak stress of 10.6MPa experienced by the contact surfaces of the hinge pin.

The maximum average stress propagating along the tibia is found to be 36MPa, although the duration of the "plateau" of the maximum average stress for the heel impact loading condition is only 116μs compared to the duration of 147μs observed in the centre impact loading condition.

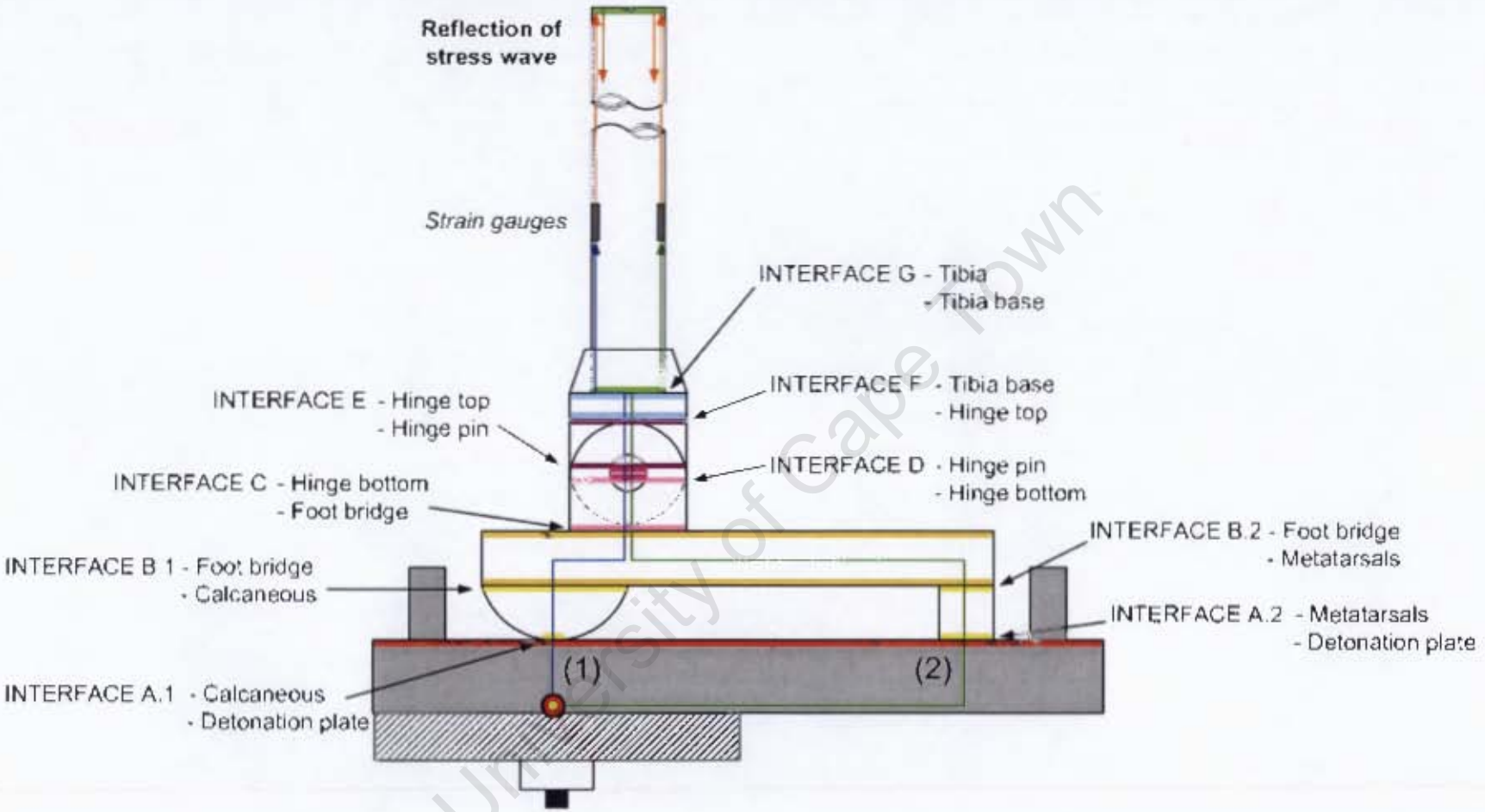

Figure 5.6 - Diagram indicating Path 1 and Path 2 of stress wave propagation for blast loading at the heel of the foot, excluding rubber sole

		PATH 1			PATH 2		
Name assigned to each "bar"	Area	Distance	Time	Stress	Distance	Time	Stress
	(m^2)	(m)	(μs)	(MPa)	(m)	(μs)	(MPa)
Detonation plate	0.04000	0.025	4.86	**158**	0.187	36.40	**158**
Calcaneous	$9.8x10^{-7}$	0.01	6.81	**4195**	~	~	~
Metatarsals	0.0015	~	~	~	0.01	38.35	**2.7**
Foot bridge	0.011	0.015	9.73	**0.36**	0.177	72.80	**0.36**
Hinge bottom	0.001	0.025	14.60	**4**	0.025	77.67	**4**
Hinge pin	0.000377	0.006	15.76	**10.6**	0.006	78.84	**10.6**
Hinge top	0.00048	0.017	19.07	**8.3**	0.017	82.15	**8.3**
Tibia base	0.0016	0.02	22.97	**2.5**	0.02	86.04	**2.5**
Strain gauges	0.000111	0.08	38.54	**36**	0.08	101.62	**36**
End of tibia	0.000111	0.42	120.30	**36**	0.42	183.38	**36**
Strain gauges	0.000111	0.42	202.07	**36**	0.42	265.14	**36**

Table 5.2 - Table of stress propagation through the foot model, rubber sole excluded (blast loading at heel of foot)

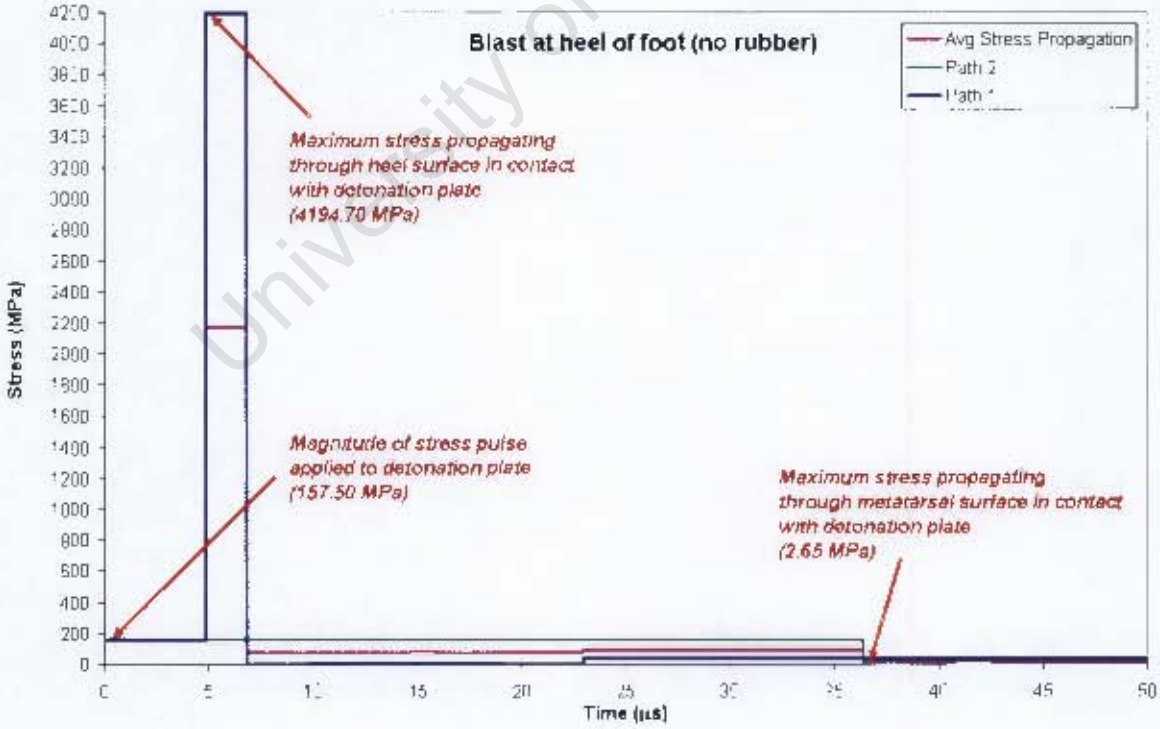

Figure 5.7 - Graph showing analytical prediction for maximum stress experienced by calcaneous and metatarsal contact surfaces during blast loading at the heel of the foot model, excluding the rubber sole

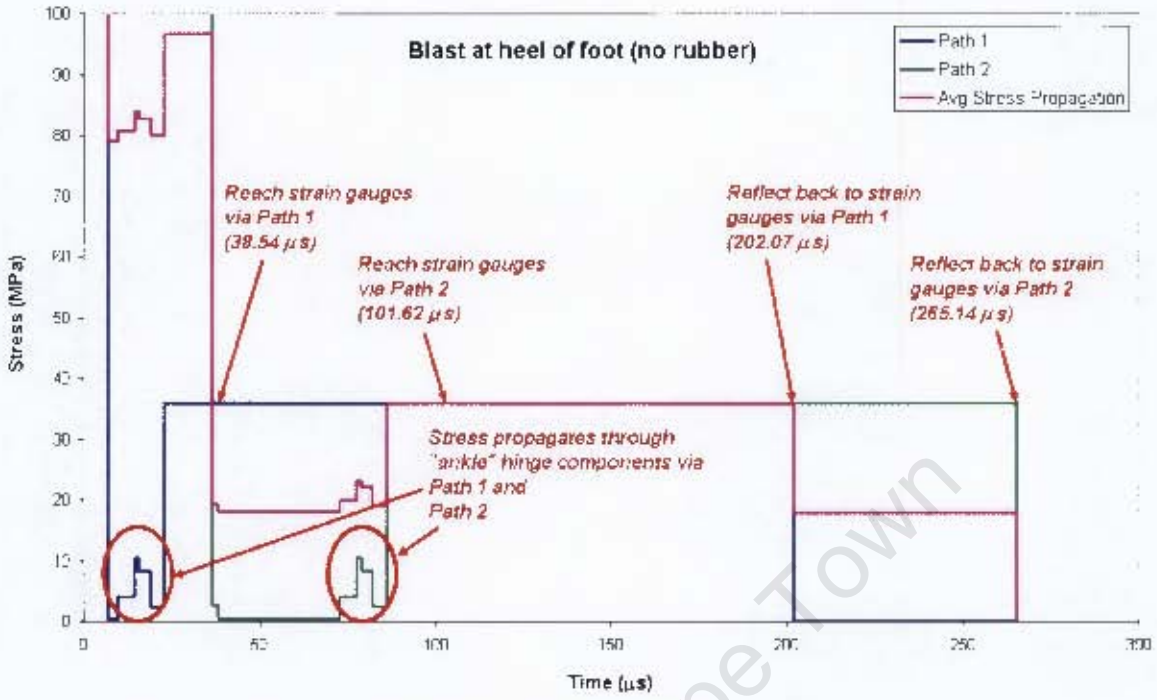

Figure 5.8 - Graph showing analytical prediction for stress propagation during blast loading at the heel of the foot model, excluding the rubber sole

5.4 ANALYTICAL MODEL OF THE BLAST LOADING OF THE FOOT MODEL, INCLUDING THE RUBBER SOLE AS ATTENUATOR

In the second section of the blast testing a layer of rubber is wedged between the detonation plate and the base of the aluminium foot to investigate the blast attenuation attributes. The rubber attenuator is introduced in the analytical model as a "bar" component of non-linear elastic material, characterised by a hyperelastic material model.

The one-dimensional stress wave propagation theory relating to linear elastic materials is applied to the detonation plate, where the induced stress wave is assumed to propagate as a planar stress pulse with a wave velocity of 5152 m/s through the mild steel detonation plate, until it encounters the first surface of the rubber layer. After reaching the first rubber surface, some of the stress is dissipated due to the release of energy as the stress wave travels through the thickness of the rubber component. The strain energy potential theory relating to the behaviour of hyperelastic materials is therefore employed to estimate the amount of stress transmitted by the rubber layer due to the impact loading. Equation 5.14 yields the stress-strain relationship particular to the rubber undergoing compression at a $2500s^{-1}$ strain rate. The wave speed of rubber is taken to be approximately 1500m/s [62]. Knowing the wave velocity of the rubber, the time it takes for the stress wave to transmit through the thickness of the rubber layer can be determined. In turn the strain (and therefore the stretch) induced upon the rubber in that transmitting time can be calculated. The stretch value is used in Equation 5.14 to determine the stress transmitted by the layer of rubber. Stress wave propagation along the remaining series of aluminium components is once again analysed according to the linear elastic theory of stress wave propagation, with the wave velocity of the aluminium being 5137m/s.

An important aspect to take note of is the paths along which the stress wave is assumed to travel. As for the analyses performed on the impact loading without the rubber layer, the stress wave travels along two distinct paths (Path 1 via the calcaneous and Path 2 via the metatarsals of the foot model). However, in the situation including the rubber layer, the stress wave is assumed to split a second time along each path when the rubber sole is reached. Path 1 separates in the heel of the rubber sole, travels along the mid-section of the sole, exits through the toe section, transmits along the metatarsals and unites at the bottom surface of the hinge component. Path 2 diverts in the toe section of the rubber sole, travels along the mid-section of the sole, exits through the heel surface of the rubber sole, transmits trough the calcaneous of the foot model and reconnects also at the bottom surface of the hinge. The second separation of the stress path is clearly illustrated in Figure 5.11 and Figure 5.14.

5.4.1 Blast loading in the centre of the foot

Figure 5.9 illustrates the two paths and their respective diversions along which the stress wave is expected to travel. The sequence of contact interfaces encountered along these paths is also indicated.

The stress wave induced by the impact loading is expected to travel approximately 66μs along the 297mm of Path 1.1 to reach the strain gauges, and roughly 208μs to transmit along the 624mm of Path 1.2. The stress wave will travel the 450mm of Path 2.1 in roughly 92μs before reaching the strain gauges, and more or less 170μs to propagate along the 453mm of Path 2.2. The duration of the stress propagation along Path 1.2 and Path 2.2 differs substantially with respect to Path 1.1 and Path 2.1 due to the "detour" of Path 1.2 and Path 2.2 through the mid-section of the rubber sole. The wave speed of rubber is much lower than the wave speed of mild steel or aluminium, increasing the duration of the stress wave propagation. As for the previous loading scenarios, it will take a further 165μs for the stress wave to transmit along the tibia and reflect back to the strain gauges.

Table 5.3 details the propagation of the stress wave as it encounters the various interfaces associated with Path 1.1, Path 1.2, Path 2.1 and Path 2.2. From Table 4.3 and Figure 5.10 it is observed that an estimated 2MPa is transmitted through the rubber heel when the stress wave follows Path 1.1, inducing a maximum stress of 3716MPa upon the contact surface of the calcaneous. It is further noticed that an estimated 0.9MPa is transmitted through the toe section of the rubber sole when the stress wave follows Path 2.1, causing the metatarsals to experience a maximum stress of 2.3MPa.

Similar to the analytical results of the loading conditions excluding the rubber sole, the distinctive short step-like stress propagation occurring through the interfaces of the ankle hinge is clearly noticeable in Figure 5.11. The only difference is that when the rubber sole is introduced in the analysis, a second pair of short step-like stress propagations is observed, which occurs due to the delayed stress wave transmission along Path 1.2 and Path 2.2. The maximum stress experienced by the pin is 9.4MPa and is caused by the stress wave travelling along Path 1.1.

It is found that the tibia feels a maximum stress of 31.9MPa which is induced by the stress wave propagating down Path 1.1. However, the maximum average stress transmitted along the tibia is 21.3MPa and it peaks between 190μs and 230μs.

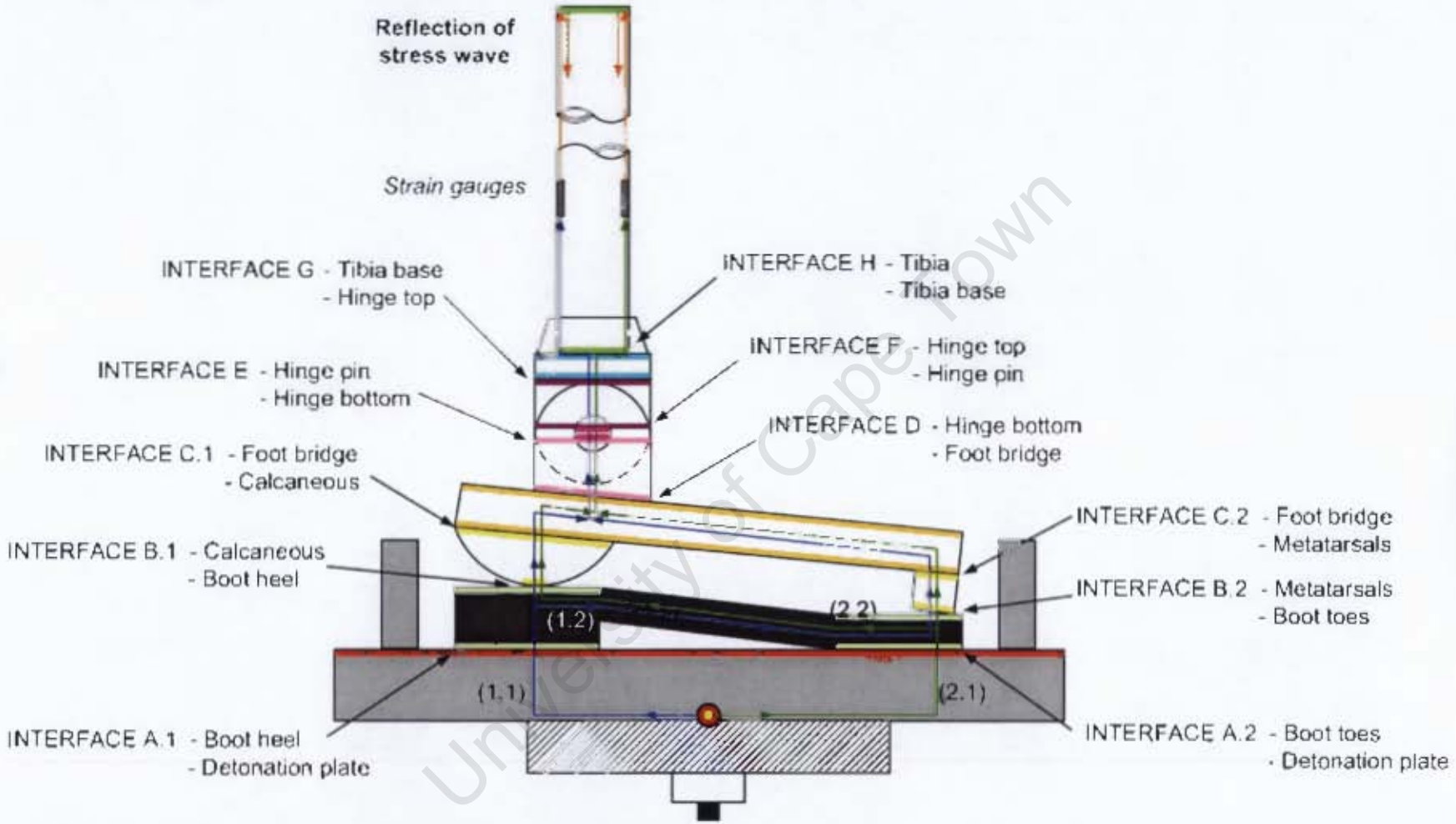

Figure 5.9 - Diagram indicating Path 1.1 & Path 1.2 and Path 2.1 & Path 2.2 of stress wave propagation for blast loading in the centre of the foot, including rubber sole

Name assigned to each "bar"		Area	PATH 1.1			PATH 1.2			PATH 2.1			PATH 2.2		
			Dist.	Time	Stress	Dist.	Time	Stress	Dist.	Time	Stress	Dist.	Time	Stress
		(m^2)	(m)	(μs)	(MPa)	(m)	(μs)	(MPa)	(m)	(μs)	(MPa)	(m)	(μs)	(MPa)
Detonation plate		0.04000	0.106	20.63	**157.5**	0.106	20.63	**157.5**	0.106	20.63	**157.5**	0.106	20.63	**157.5**
Boot Heel	Surface 1	0.00182	0.018	32.63	**770.6**	0.183	142.63	**770.6**	–	–	–	0.174	136.63	–
	Surface 2				**1.9**			–			–			**0.46**
Boot Toes	Surface 1	0.003635	–	–	–			–	0.009	26.63	**385**			**385**
	Surface 2				–			**0.46**			**0.94**			–
Calcaneous		$9.8x10^{-7}$	0.01	34.58	**3716**	–	–	–	–	–	–	0.01	138.58	**870.2**
Metatarsals		0.0015	–	–	–	0.01	144.58	**1.1**	0.01	28.58	**2.3**	–	–	–
Foot bridge		0.011	0.015	37.50	**0.32**	0.177	179.03	**0.15**	0.177	63.03	**0.31**	0.015	141.50	**0.08**
Hinge bottom		0.001	0.025	42.36	**3.5**	0.025	183.90	**1.7**	0.025	67.90	**3.4**	0.025	146.36	**0.83**
Hinge pin		0.000377	0.006	43.53	**9.4**	0.006	185.07	**4.4**	0.006	69.07	**9.0**	0.006	147.53	**2.2**
Hinge top		0.00048	0.017	46.84	**7.4**	0.017	188.38	**3.5**	0.017	72.38	**7.1**	0.017	150.84	**1.7**
Tibia base		0.0016	0.02	50.74	**2.2**	0.02	192.27	**1.0**	0.02	76.27	**2.1**	0.02	154.74	**0.52**
Strain gauges		0.000111	0.08	66.31	**31.9**	0.08	207.85	**14.9**	0.08	91.85	**30.8**	0.08	170.31	**7.5**
End of tibia		0.000111	0.42	148.07	**31.9**	0.42	289.61	**14.9**	0.42	173.61	**30.8**	0.42	252.07	**7.5**
Strain gauges		0.000111	0.42	229.84	**31.9**	0.42	371.37	**14.9**	0.42	255.37	**30.8**	0.42	333.84	**7.5**

Table 5.3 - Table of stress propagation through the foot model, rubber sole included (blast loading in centre of foot)

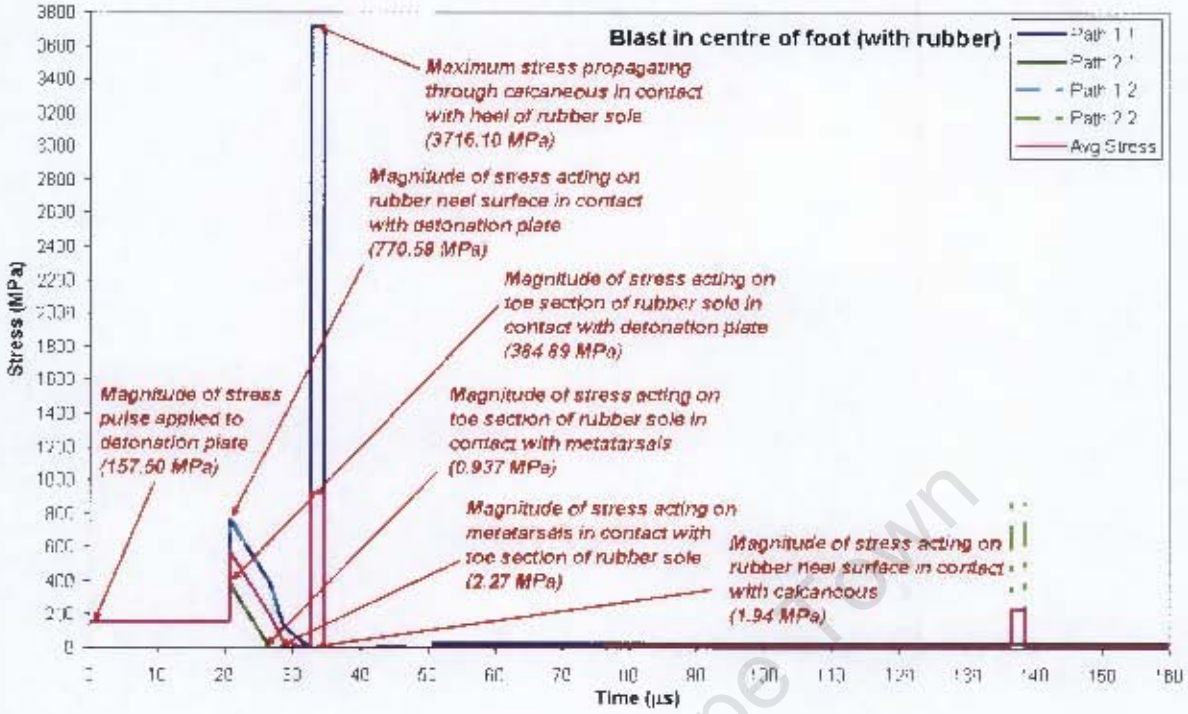

Figure 5.10 - Graph showing analytical prediction for maximum stress experienced by calcaneous and metatarsal contact surfaces during blast loading in the centre of the foot model, including the rubber sole

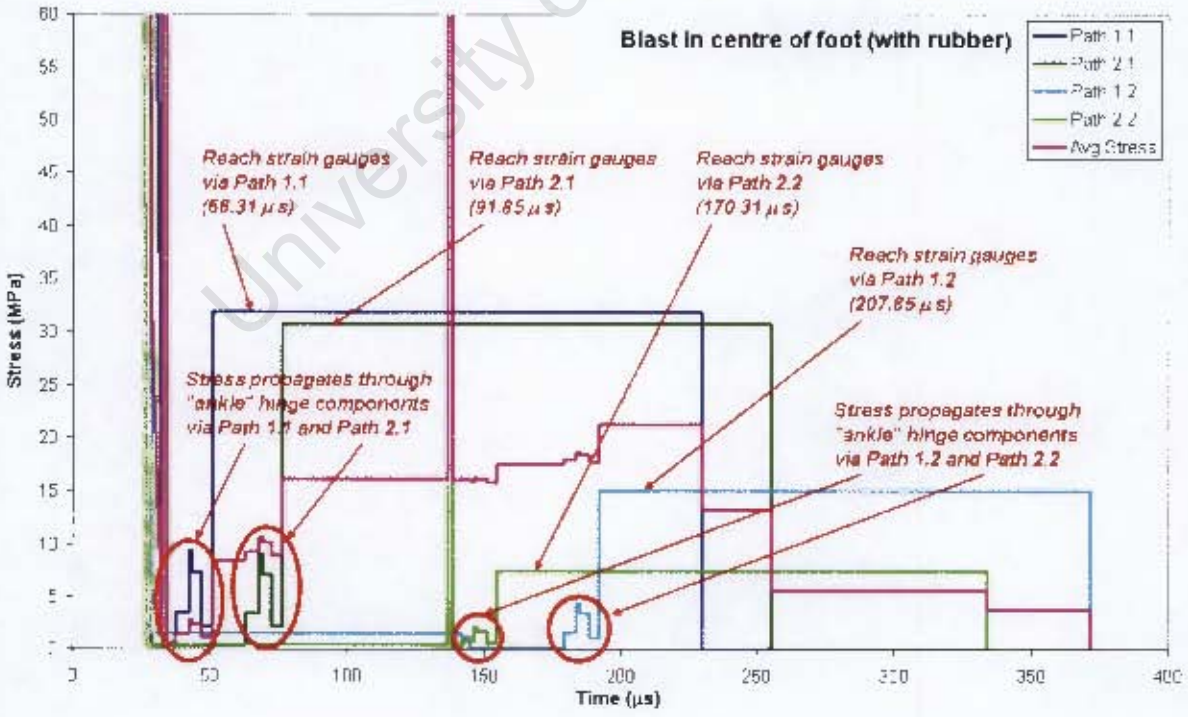

Figure 5.11 - Graph showing analytical prediction for stress propagation during blast loading in the centre of the foot model, including the rubber sole

5.4.2 Blast loading at the heel of the foot

The propagation paths and their relevant series of contact interfaces along which the stress wave is expected to transmit is demonstrated in Figure 5.12.

The stress wave induced by the impact loading is expected to travel the 216mm of Path 1.1 in approximately 51μs before reaching the strain gauges, and the 543mm of Path 1.2 in more or less 192μs. The stress wave is expected to travel approximately 108μs along the 531mm of Path 2.1 to reach the strain gauges, and about 186μs to propagate along the 534mm of Path 2.2. As for the previous loading scenarios, it will take a further 165μs for the stress wave to transmit along the tibia and reflect back to the strain gauges.

The results of the stress wave propagation through the range of contact surfaces associated with Path 1.1, Path 1.2, Path 2.1 and Path 2.2 are documented in Table 5.4. Table 5.4 and Figure 5.13 shows that the stress wave induces the same magnitude of maximum stress in the contact surface of the calcaneous (3716MPa) and the metatarsals (2.3MPa) after 1.9MPa and 0.94MPa is respectively transmitted through the heel and toe section of the rubber sole layer. However, because the impact loading position is at the heel, the stress wave travelling along Path 2.1 takes approximately 26μs longer before transmitting through the metatarsal surface.

Considering the graph shown in Figure 5.14, it is noticed that the stress wave reaches the ankle region 57μs later if travelling via Path 2.1 than Path 1.1. Interesting to note is that the stress wave travelling along Path 1.2 and Path 2.2 reaches the ankle region at approximately the same time (168μs via Path 1.2 and 162μs via Path 2.2). This is unlike the results found for the centre impact loading condition where the stress wave following Path 1.2 and Path 2.2 reaches the ankle region at 184μs and 146μs respectively. Once again, the maximum stress induced upon the ankle hinge pin is 9.4MPa.

A maximum stress of 31.9MPa generated in the tibia by the stress wave propagating along Path 1.1, although the maximum average stress felt by the tibia is 21.3MPa which peaks between 176μs and 214μs.

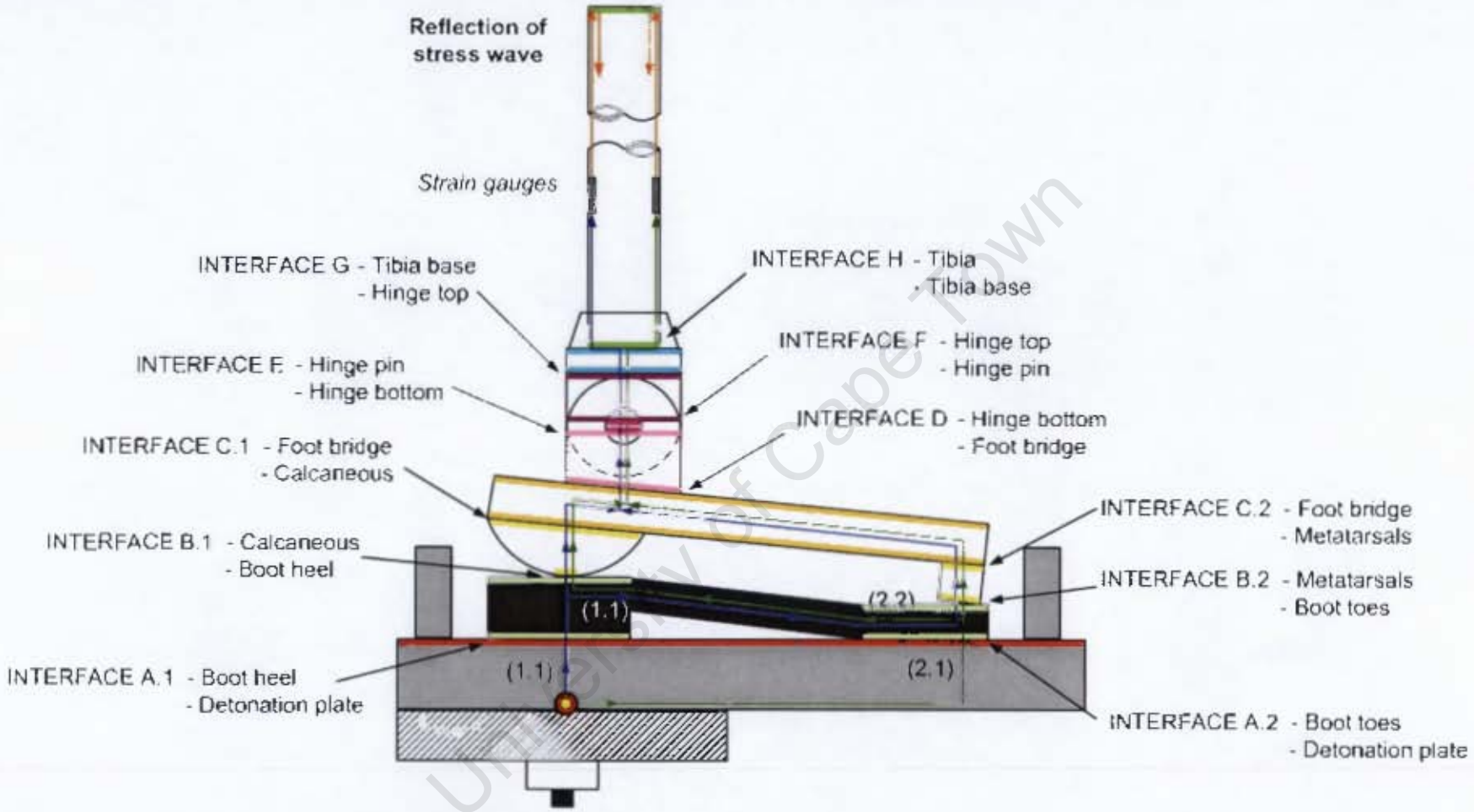

Figure 5.12 - Diagram indicating Path 1.1 & Path 1.2 and Path 2.1 & Path 2.2 of stress wave propagation for blast loading at the heel of the foot, including rubber sole

Name assigned to each "bar"		Area	PATH 1.1			PATH 1.2			PATH 2.1			PATH 2.2		
			Dist.	Time	Stress	Dist.	Time	Stress	Dist.	Time	Stress	Dist.	Time	Stress
		(m^2)	(m)	(μs)	(MPa)	(m)	(μs)	(MPa)	(m)	(μs)	(MPa)	(m)	(μs)	(MPa)
Detonation plate		0.04000	0.025	4.86	157.5	0.025	4.86	157.5	0.187	36.40	157.5	0.187	36.40	157.5
Boot Heel	Surface 1	0.00182	0.018	16.86	770.6	0.183	126.86	770.6	~	~	~	0.174	152.40	~
	Surface 2				1.9			~			~			0.46
Boot Toes	Surface 1	0.003635	~	~	~			~	0.009	42.40	384.9			384.9
	Surface 2				~			0.46			0.94			~
Calcaneous		$9.8x10^{-7}$	0.01	18.81	3716	~	~	~	~	~	~	0.01	154.35	870.2
Metatarsals		0.0015	~	~	~	0.01	128.81	1.1	0.01	44.35	2.3	~	~	~
Foot bridge		0.011	0.015	21.73	0.32	0.177	163.27	0.15	0.177	78.81	0.31	0.015	157.27	0.08
Hinge bottom		0.001	0.025	26.60	3.5	0.025	168.13	1.7	0.025	83.67	3.4	0.025	162.13	0.83
Hinge pin		0.000377	0.006	27.76	9.4	0.006	169.30	4.4	0.006	84.84	9.0	0.006	163.30	2.2
Hinge top		0.00048	0.017	31.07	7.4	0.017	172.61	3.5	0.017	88.15	7.1	0.017	166.61	1.7
Tibia base		0.0016	0.02	34.97	2.2	0.02	176.50	1.0	0.02	92.04	2.1	0.02	170.50	0.52
Strain gauges		0.000111	0.08	50.54	31.9	0.08	192.08	14.9	0.08	107.62	30.8	0.08	186.08	7.5
End of tibia		0.000111	0.42	132.30	31.9	0.42	273.84	14.9	0.42	189.38	30.8	0.42	267.84	7.5
Strain gauges		0.000111	0.42	214.07	31.9	0.42	355.60	14.9	0.42	271.14	30.8	0.42	349.61	7.5

Table 5.4 - Table of stress propagation through the foot model, rubber sole included (blast loading at heel of foot)

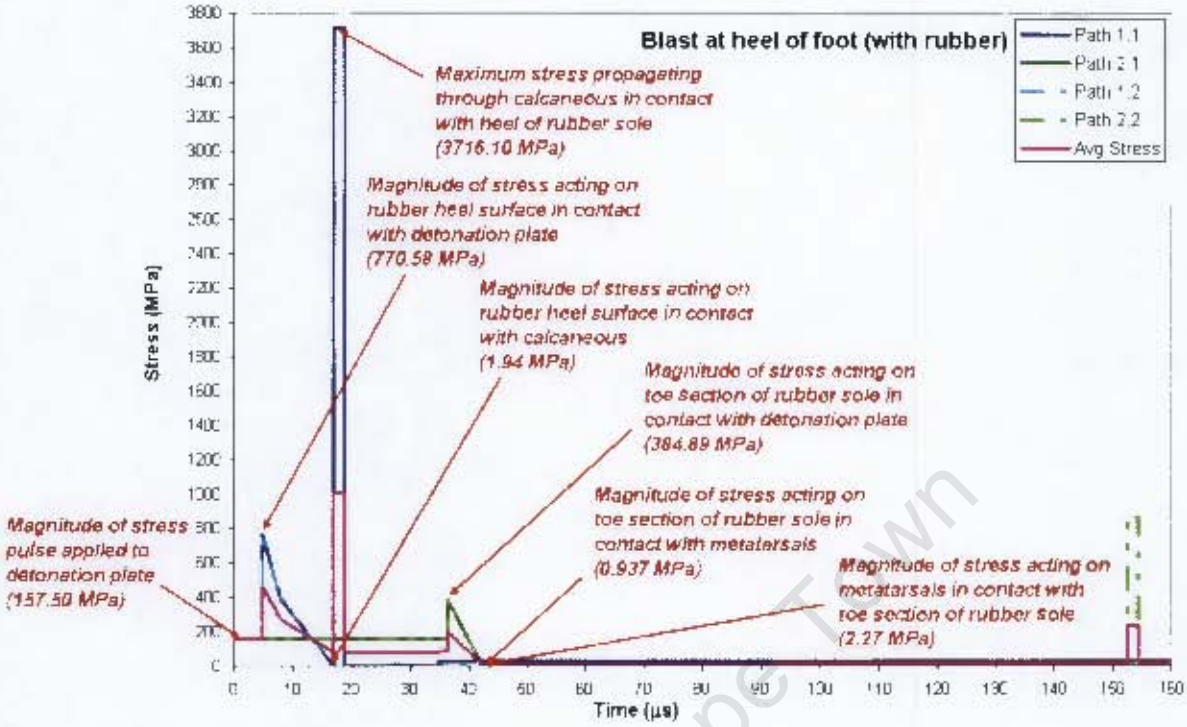

Figure 5.13 - Graph showing analytical prediction for maximum stress experienced by calcaneous and metatarsal contact surfaces during blast loading at the heel of the foot model, including the rubber sole

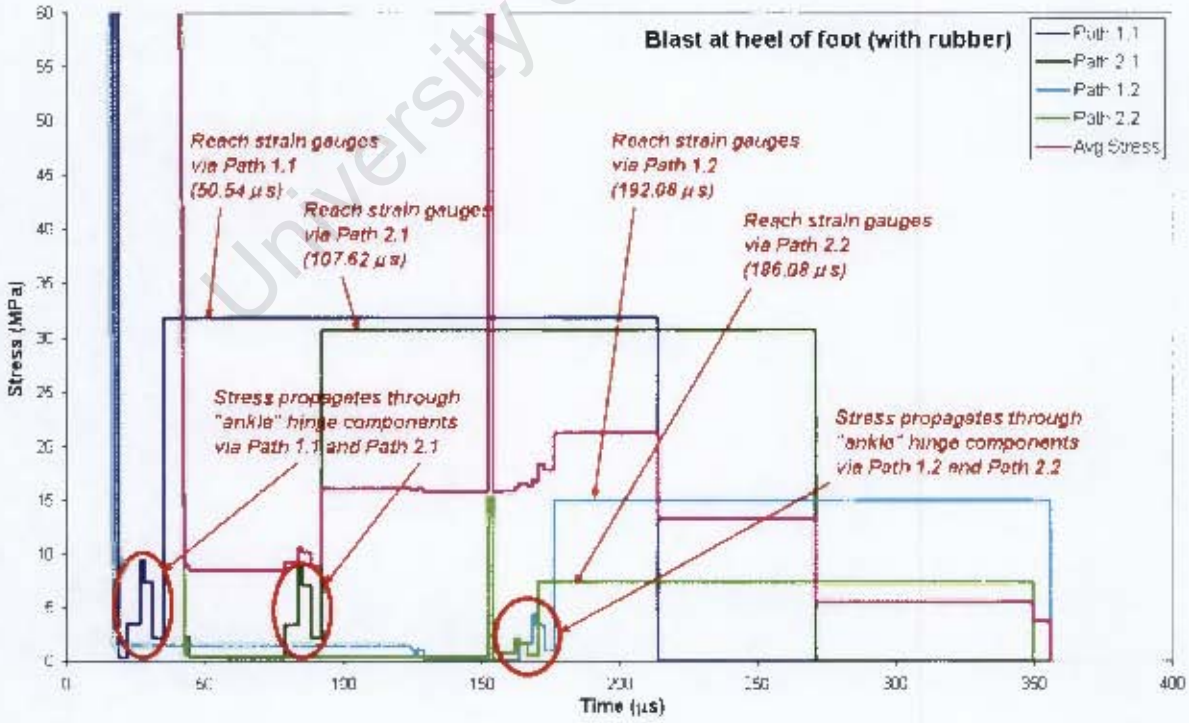

Figure 5.14 - Graph showing analytical prediction for stress propagation during blast loading at the heel of the foot model, including the rubber sole

5.5 DISCUSSION OF ANALYTICAL RESULTS

5.5.1 Maximum stress

The maximum stress acting on the surfaces of each component is calculated to be of the same magnitude when the centre and heel impact loading conditions are analysed, although the time at which the maximum stress is initially experienced by the component differs according to the choice of loading condition. The magnitude of the maximum stress is therefore only influenced by the presence of the rubber sole layer. The results provided in Table 5.5 indicates that including the rubber sole layer is expected to reduce the maximum stress experienced by the calcaneous, ankle hinge pin and tibia by approximately 11%. The stress acting on the metatarsals is shown to be reduced by 15%.

		EXCLUDING RUBBER SOLE			INCLUDING RUBBER SOLE		
Impact load position			Centre	Heel		Centre	Heel
Component		Stress (MPa)	Time (μs)	Time (μs)	Stress (MPa)	Time (μs)	Time (μs)
Rubber heel	Surf 1	~	~	~	770.6	20.63	4.86
	Surf 2	~	~	~	1.9	32.63	16.86
Rubber toes	Surf 1	~	~	~	384.9	20.63	36.40
	Surf 2	~	~	~	0.94	26.63	42.40
Calcaneous		4194.7	20.63	4.86	3716	32.63	16.86
Metatarsals		2.7	20.63	36.40	2.3	26.63	42.40
Ankle hinge pin		10.6	30.36	14.60	9.4	42.36	26.60
Tibia (strain gauges)		36	54.31	38.54	31.9	66.31	50.54

Table 5.5 – Table listing the time at which maximum stress initially occurs in critical components

5.5.2 Average stress

The strain gauges are placed on the front surface (in the direction of the metatarsals) and on the back surface (in the direction of the calcaneous) of the aluminium tube. The strain gauge signal obtained from the blast experiments is the average of the stress recorded by the two strain gauges; hence the average stress results obtained from the analytical model is of significant importance.

Table 5.6 provides the magnitude of the maximum average stress propagating along the tibia as well as the duration (the "plateau" duration) of the maximum average stress in the tube. The average stress "plateau" duration is easily observed in Figure 5.15. The results indicate that the presence of the rubber sole is expected to reduce the maximum average stress in the tibia from 36MPa to 21.3MPa, which is an attenuation of approximately 41%. It is also noticed that the "plateau" duration is much shorter for impact loading when the rubber sole is included than when the rubber layer is excluded, serving as an indication of the expected shape of the graphs obtained for the experimental and numerical stress-time results. The stress-time graph for the blast loading without the rubber sole is therefore expected to be of a more elongated shape, whereas the stress-time graph for the blast loading with the rubber is expected to have a shorter more definite peak in maximum stress.

Impact loading condition		Avg Stress (MPa)	Start – Finish of "plateau" (duration)
Excluding rubber sole	**Centre impact**	*36*	*70μs – 218μs (148μs)*
	Heel impact		*86μs – 202μs (116μs)*
Including rubber sole	**Centre impact**	*21.26*	*193μs – 230μs (37μs)*
	Heel impact		*177μs – 214μs (37μs)*

Table 5.6 – Table detailing the maximum average stress transmitted in the tibia

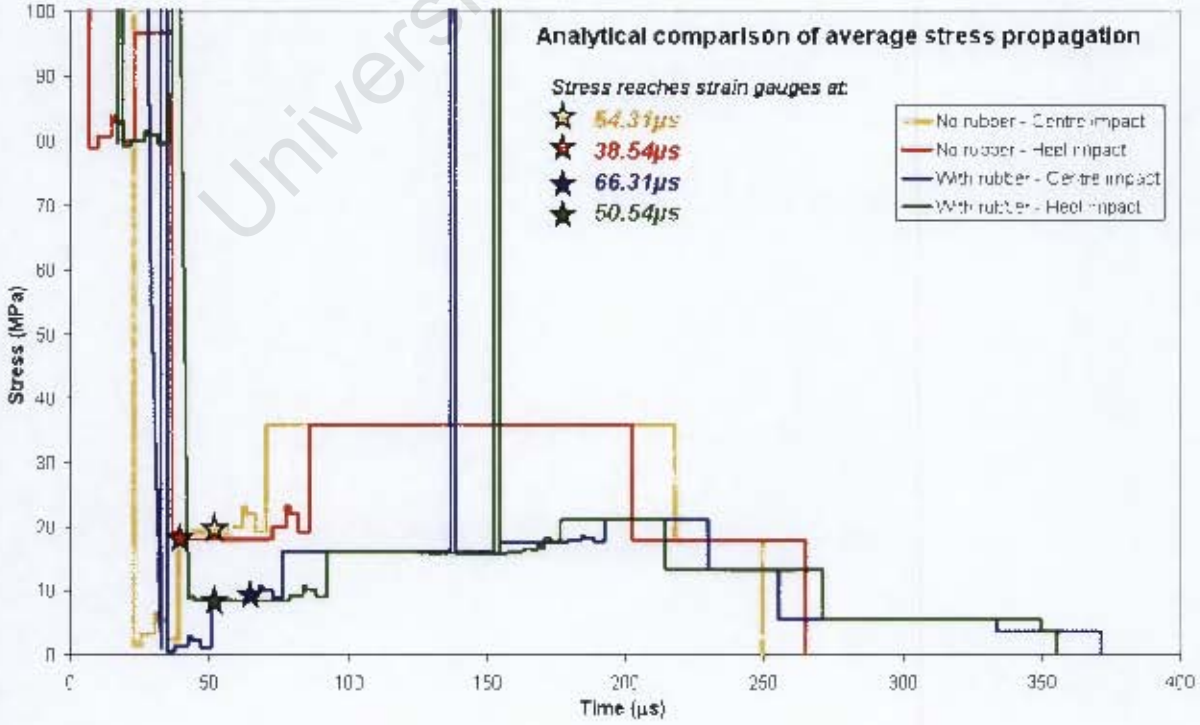

Figure 5.15 – Graph showing the average stress "plateau" experienced by the tibia during the four loading conditions, also the time at which the stress reaches the strain gauges in the tibia

Although the strain gauges will only start to record stress values from approximately 38μs onwards and therefore not the stress experienced by the rubber sole surfaces, calcaneous or metatarsals, it is of interest to note from Table 5.7 and Figure 5.16 that the introduction of a rubber sole is expected to reduce the maximum average stress experienced by the calcaneous by approximately 54%.

	Excluding rubber sole	*Including rubber sole*
Impact loading condition	Avg Stress (MPa)	Avg Stress (MPa)
Centre impact loading	*2090*	*930*
Heel impact loading	*2176*	*1008*

Table 5.7 – Table comparing the maximum average stress experienced by the calcaneous for loading conditions where the rubber sole is excluded and included

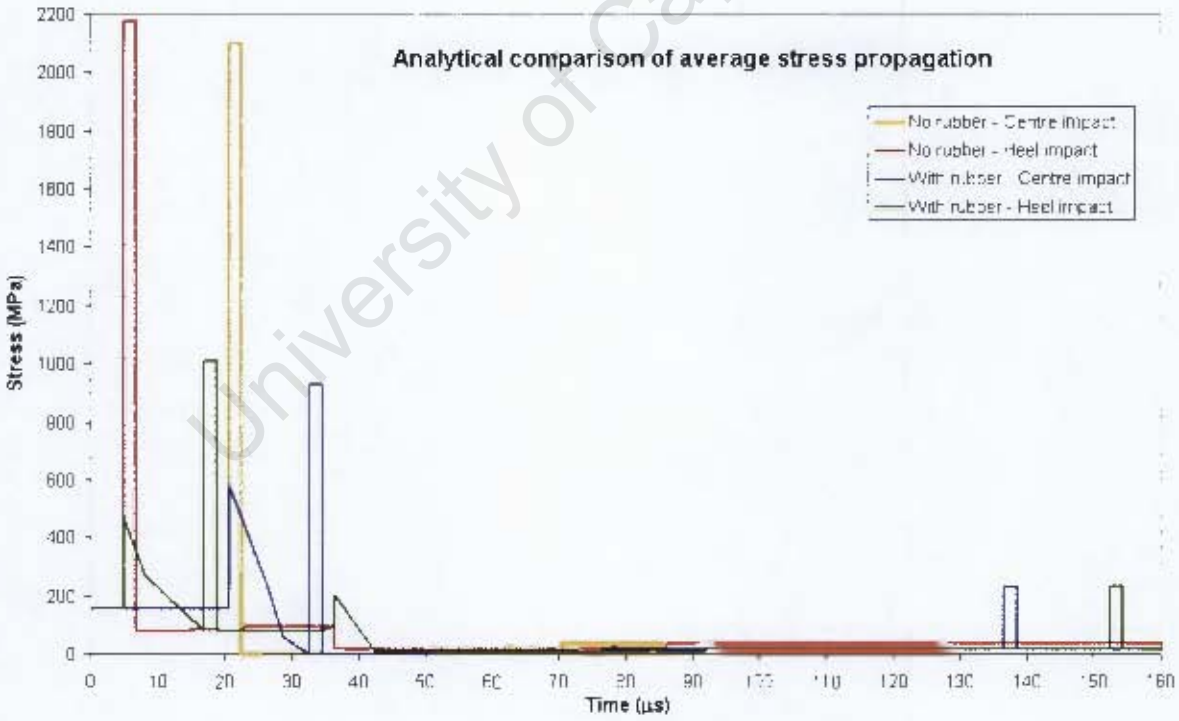

Figure 5.16 – Graph showing the analytical results of the average stress experienced during the initial 160μs for the four loading conditions

Chapter 6 - Numerical Foot-Ankle Model

6.1 INTRODUCTION

The Finite Element Method is an approximate numerical technique used to determine the solution of a physical system. The physical system is described by an underlying mathematical governing equation to which physical properties, geometry, loading and boundary conditions are assigned. The governing equation is solved in order to obtain the desired results. Finite element modelling has become a powerful tool in the investigation and understanding of both static and dynamic problems, as intricate details of the physical system can be studied, which is generally difficult to do by performing practical experimentation only.

The finite element software package used to perform the numerical analyses of the experimental blast tests is ABAQUS [63]. A finite element model of each of the two experimental test setups is constructed, the first model with the rubber sole excluded and the second model with the rubber sole included in the test setup. The various loading conditions are then simulated according to the experiments performed in the blast test schedule (provided in Section 5.6.1).

This chapter details the construction of the numerical model of the horizontal ballistic pendulum and foot model test setup. It will be noted that in order to minimise the runtime and size of the simulations, the whole ballistic pendulum is not modelled, but only the detonation plate and the Teflon alignment bushes. Applying the correct boundary conditions to the detonation plate and alignment bushes inherently reproduces the behaviour of the pendulum. The interactions between the parts and the material properties relevant to the components used in the test setup is provided, with special attention being given to the material model used to simulate the behaviour of the rubber sole.

Finally the results retrieved from the finite element simulations carried out for each loading condition, where the rubber sole is excluded and included, is presented and discussed.

6.2 DESIGN AND MESHING OF THE INDIVIDUAL PARTS

6.2.1 Assembly of the numerical model

Table 6.1 lists the parts and their sub-components that the numerical model consists of, along with the relevant material properties. Figure 6.1 shows views of the two finite element models used in the ABAQUS simulations of the experimental blast tests.

Numerical model part	*Model component*	*Material*
Foot	*Foot*	*Solid Aluminium*
Ankle	*Bottom hinge component*	*Solid Aluminium*
	Top hinge component	*Solid Aluminium*
	Hinge pin	*Solid Aluminium*
	Hinge pin bush	*Brass*
	Inner Teflon bushes	*Teflon*
Tibia	*Tibia*	*6063-T6 Aluminium tube*
	Tibia connecting pin	*Steel*
Alignment bush	*Alignment bush*	*Teflon*
Boot sole	*Boot sole*	*Rubber*
Detonation plate	*Detonation plate*	*Mild steel*

Table 6.1 – Table of components comprising the numerical model

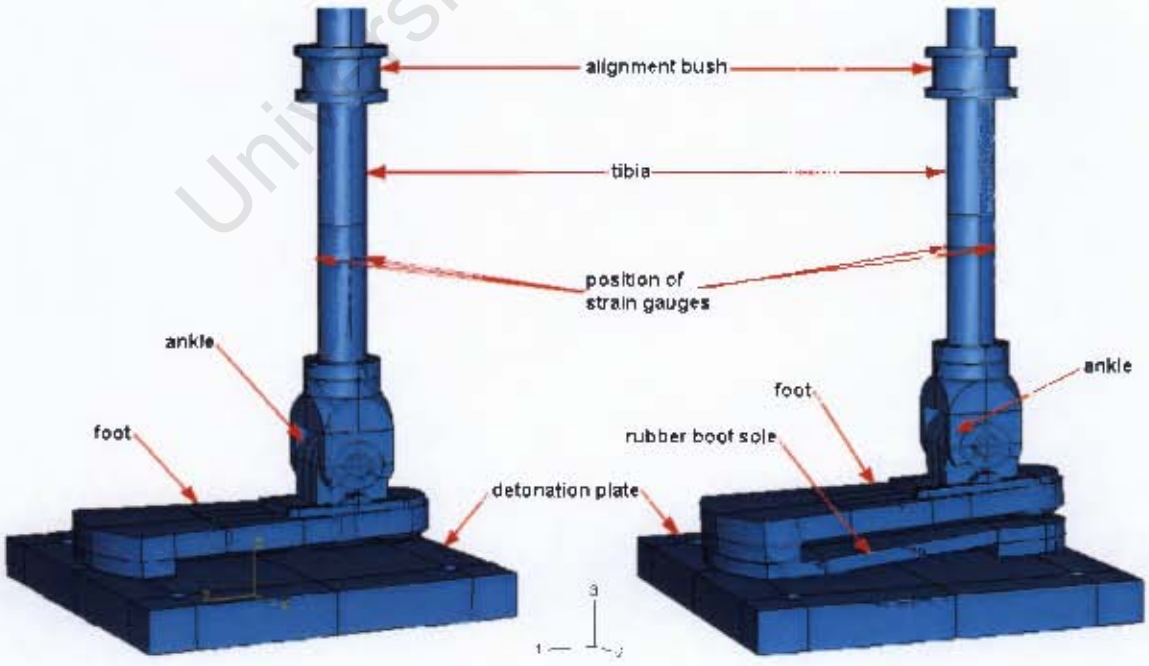

Figure 6.1 – Assembly of the two numerical models

6.2.2 Foot

The numerical model of the foot is adapted from the physical foot component used in the blast testing. There are two differences between the experimental and the finite element foot component:

- In the experimental model the edges of the metatarsal arc are chamfered. The edges of the numerical foot model are not chamfered in order to simplify meshing of the component.
- The four holes for the four screws fixing the bottom component of the hinge to the foot are omitted from the numerical model of the foot, although the surfaces of where the holes would have been are identified in the numerical model.

Figure 6.2(a – b) shows how the numerical foot model is partitioned in order to achieve the desired mesh which contains a total of 8186 C3D8R and C3D6 elements.

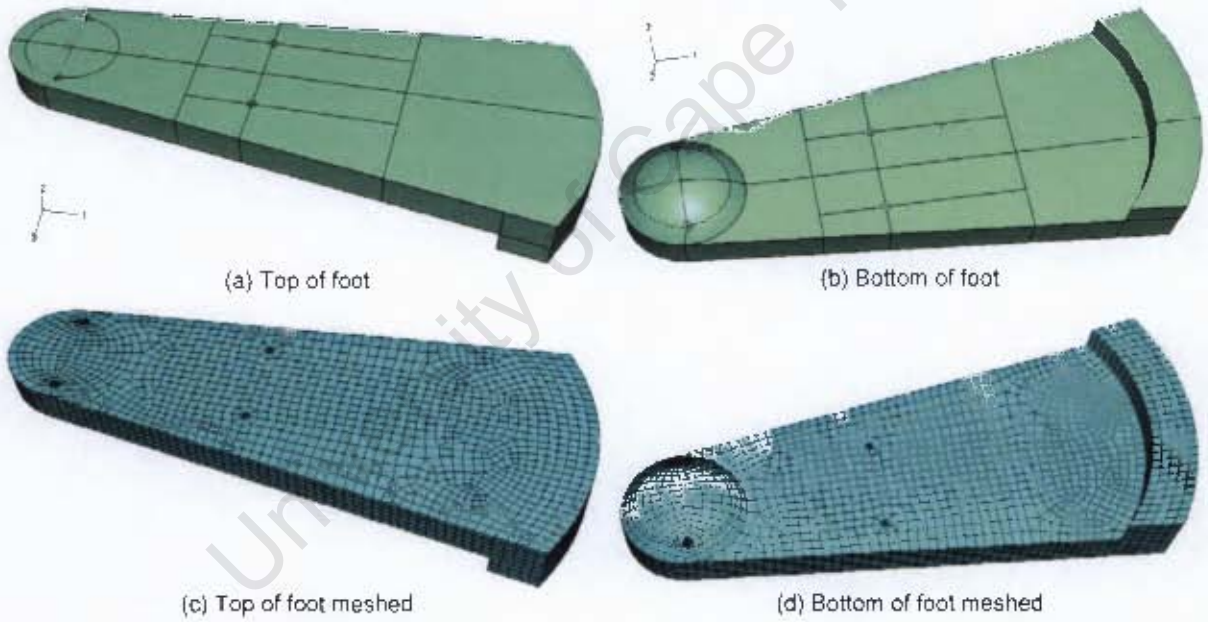

(a) Top of foot (b) Bottom of foot

(c) Top of foot meshed (d) Bottom of foot meshed

Figure 6.2 – Design of the foot

6.2.3 Ankle

Figure 6.4 shows that the finite element model of the ankle consists of three primary components; the bottom and top sections of the hinge and the hinge pin. The brass bush is included in the bottom and top part models as a section to which the material properties of brass is assigned. Incorporation of the two Teflon spacers in the model of the top part of the hinge is also done by giving the material properties of Teflon to the two specifically assigned sections. The inclusion of the brass bushes and the Teflon spacers are shown in Figure 6.3.

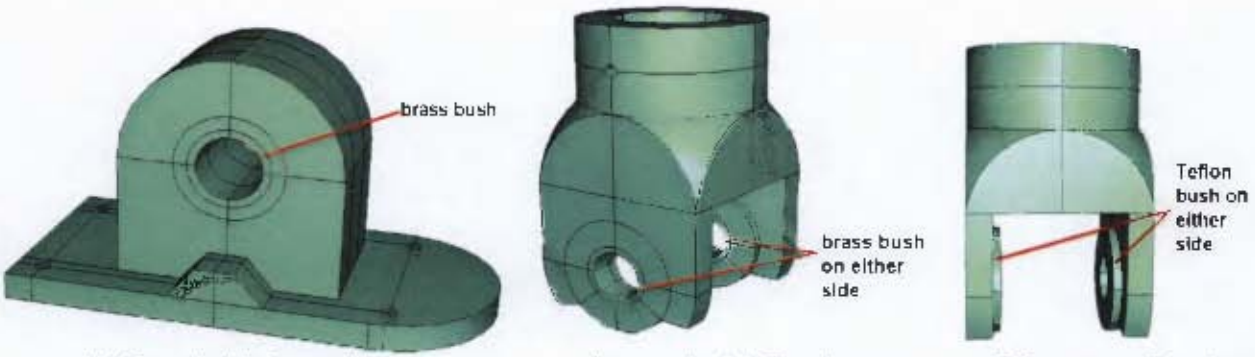

(a) Brass bush in Bottom hinge (b) Brass bush in Top hinge (c) Teflon bush in Top hinge

Figure 6.3 – Inclusion of the sub-components in the numerical model of the ankle parts

Partitioning of these three parts to obtain the optimum element mesh is shown in Figure 6.4(a – f). The bottom part of the hinge consists of 90882 C3D8R elements, the top part of the hinge has a total of 7283 C3D8R and C3D4 elements, and the pin has 5832 C3D8R elements.

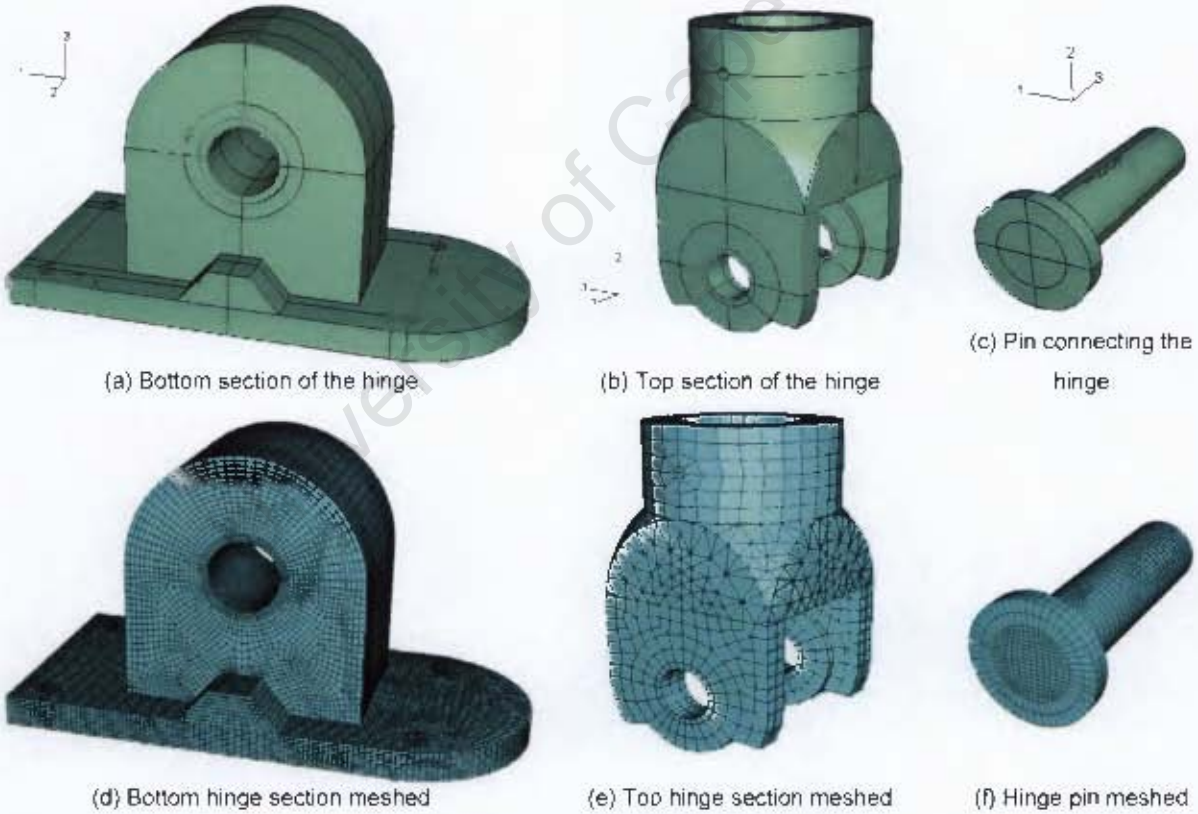

(a) Bottom section of the hinge (b) Top section of the hinge (c) Pin connecting the hinge

(d) Bottom hinge section meshed (e) Top hinge section meshed (f) Hinge pin meshed

Figure 6.4 – Design of the ankle

6.2.4 Tibia

The numerical model of the tube and the pin connecting the tube to the hinge is the same as the physical parts. The tube is meshed to contain 22256 C3D8R elements and the pin 1920 C3D8R elements.

(a) Tibia

(b) Pin connecting tibia to the top section of the hinge

(c) Tibia meshed

(d) Tibia pin meshed

Figure 6.5 – Design of the tibia

6.2.5 Blast pendulum alignment bushes

The bushes employed in the blast pendulum rig to guide the movement of the physical foot model are also included in the numerical model. The numerical model of the alignment bushes is partitioned in order to obtain the mesh containing 1480 C3D8R elements as shown in Figure 6.6.

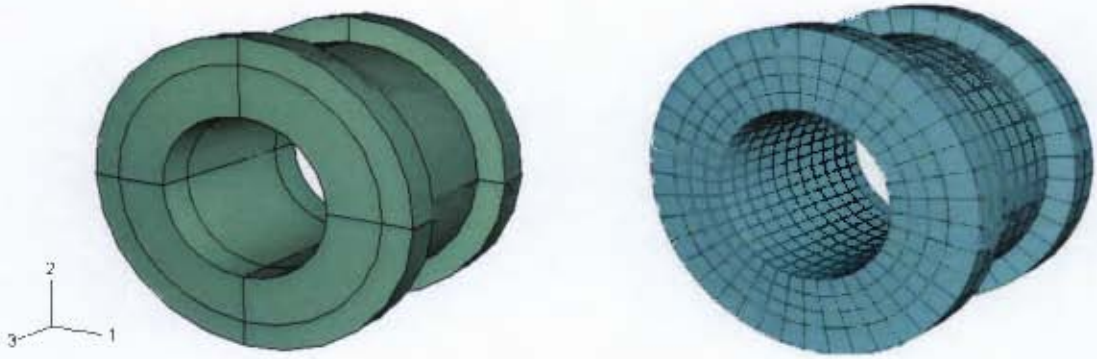

(a) Alignment bush

(b) Alignment bush meshed

Figure 6.6 – Design of the bushes aligning the tibia in the ballistic pendulum rig

6.2.6 Boot sole

The physical boot sole used in the blast tests is cut according to the profile of the top view of the foot, but is not moulded or machined to have a specific shape when viewed from the side. Two different configurations for the design and placement of the numerical rubber sole model were therefore considered, as the precise shape and contact conditions between the foot, sole and detonation plate is not known.

Initially the first configuration (shown in Figure 6.7(a)) was used in the numerical model, but inadequate numerical results were obtained as the simulation showed that negligible stress were transmitted through the rubber contact surfaces. Using the second configuration (Figure 6.7(b)) resulted in more realistic stress transmission through the rubber contact surfaces. The comparison between the stress results obtained for when the first and second rubber sole configurations are used is presented in Section 6.10.1.1 in Figure 6.18 and Figure 6.19.

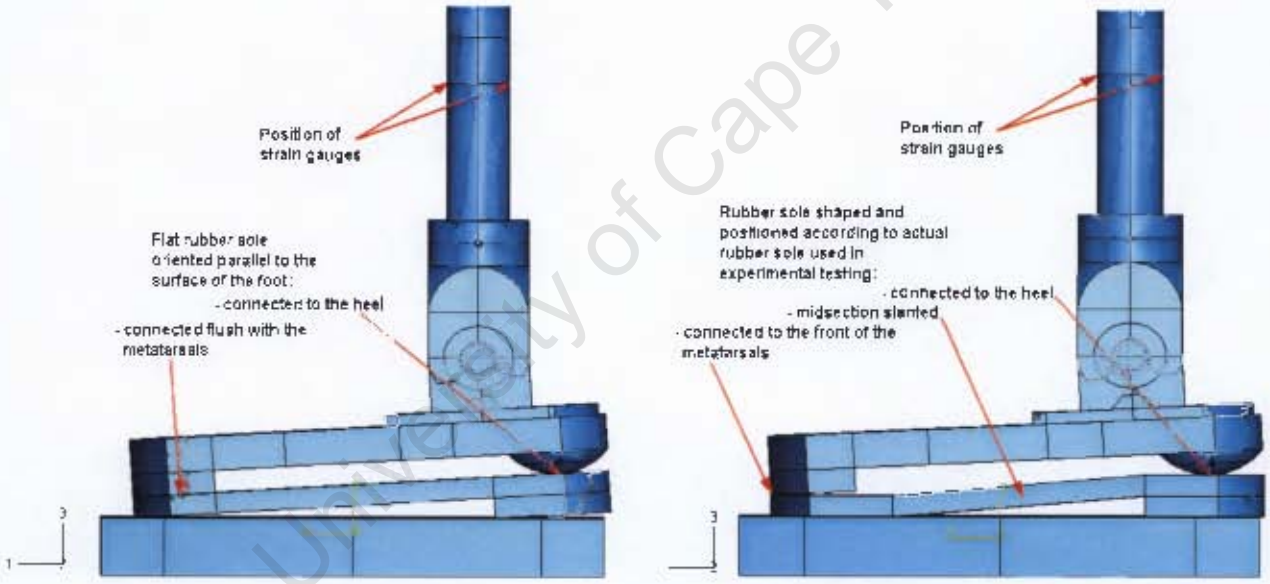

(a) Rubber boot sole configuration 1 (b) Rubber boot sole configuration 2

Figure 6.7 – Design and positioning of the rubber boot sole

The numerical model of the rubber sole is displayed in Figure 6.8 and consists of 9160 C3D8R elements. It must be noted that the finite element model is not an exact representation of the rubber sole utilised in the blast tests. The experimental sole is made of the rubber layer from a standard army combat boot sole which was separated from the rest of the boot and cut according to the desired shape. Shallow grooves are present underneath the sole, the thickness of the rubber layer is not constant and the curve of the sole (viewed from the side) is not specifically defined. The bottom surface of the numerical model of the sole however has

no grooves, the thickness of the layer is a constant 9mm and the sole has a defined curved shape when viewed from the side. Also, the heel section in the finite element model is a solid piece, whereas the heel in the experimental sole consists of a smaller second layer of rubber glued onto the top rubber layer.

(a) Boot sole

(b) Boot sole meshed

Figure 6.8 – Design of the rubber boot sole

6.2.7 *Detonation plate*

The detonation plate is modelled according the plate used during the blast tests. The finite element model consists of a total of 7780 C3D8R elements.

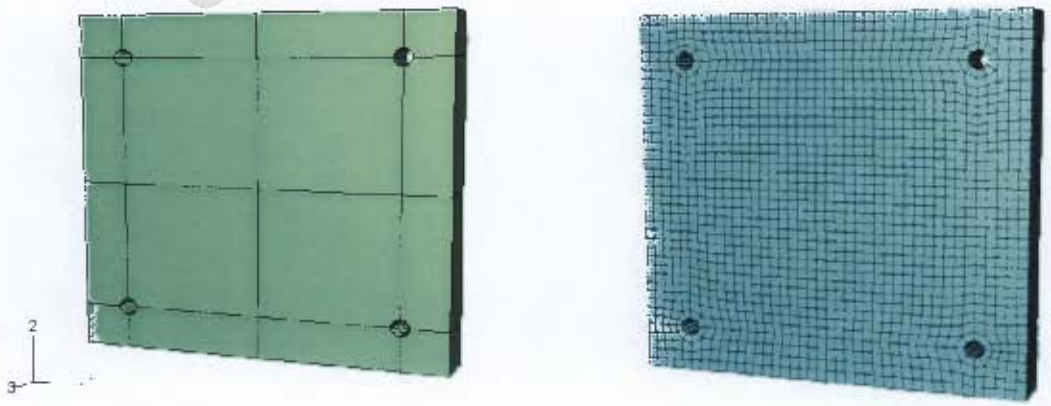

(a) Detonation plate (b) Detonation plate meshed

Figure 6.9 – Design of the detonation plate

6.3 ELEMENTS USED TO CONSTRUCT THE NUMERICAL MODEL

Stress/displacement solid (continuum) elements in ABAQUS and large deformations are expected[64].

- **C3D8R** *(HEXAHEDRAL)*
  - 1st order 8-node linear brick element, reduced integration with hourglass control
  - 1st order hexahedral solid elements provide constant volumetric strain throughout the element, which ultimately prevents "mesh locking" when the material response reaches an almost incompressible state.
  - Reduced integration essentially employs a lower-order integration to construct the element stiffness. Using reduced integration also reduces the running time to complete the numerical analysis.
  - Hourglassing is generally a problem encountered in stress/displacement analyses when 1st order reduced integration elements are used. The elements have a singular integration point, making it possible for the elements to distort in such a way that the strains calculated at that point are all zero, which in turn may result in the uncontrolled distortion of the mesh. Although hourglass control is included in the 1st order reduced integration elements, these elements should preferably be employed in a sufficiently fine mesh.

Hexahedral "brick" element

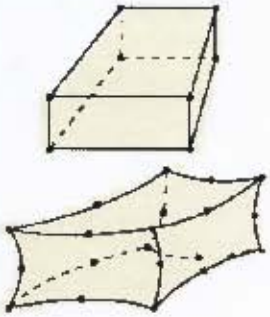

Figure 6.10 – Illustration of the structure of a hexahedral ("brick") element [65]

- **C3D6** *(TRIANGULAR)*
  - 1st order 6-node linear triangular prism element
  - The use of 1st order triangular solid elements are generally not recommended in stress analysis simulations as the tetrahedral solid elements are excessively stiff and display slow convergence. The incorporation of tetrahedral elements could however not be avoided in the present numerical model. As such, the mesh was refined to a considerable extent in order to achieve satisfactory results.

Triangular "prism" element

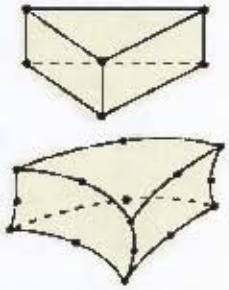

Figure 6.11 – Illustration of the structure of a triangular ("wedge") element [65]

6.4 MATERIAL PROPERTIES

Each of the parts in the model is assigned material properties corresponding to those of the parts used in the experimental foot model. The effect of the blast event did not induce plasticity in any of the parts during the experiments, therefore a plasticity model such as the Johnson-Cook model is not included in any of the material models employed in the finite element representation of the foot and rubber sole.

The material properties used to construct the various material models are given in Table 6.2. The Young's modulus, density and Poisson's ratio of all the materials except the rubber were either taken from a material catalogue or experimentally determined. The material model for rubber is however constructed by using stress-strain data obtained from SHPB tests, density which is calculated and a Poisson's ratio which is determined by trial and error.

Material	*Property*	*Value*	*Reference*
Mild steel	*Young's Modulus, E* (GPa)	*207*	*[66]*
	Density, ρ (kg/m^3)	*7800*	*[66]*
	Poisson's ratio, ν	*0.3*	*[66]*
6063-T6 Aluminium tube	*Young's Modulus, E* (GPa)	*68.9*	*[66]*
	Density, ρ (kg/m^3)	*2700*	*[66]*
	Poisson's ratio, ν	*0.33*	*[66]*
Solid Aluminium	*Young's Modulus, E* (GPa)	*71.5*	*Found experimentally*
	Density, ρ (kg/m^3)	*2709.7*	*Found experimentally*
	Poisson's ratio, ν	*0.33*	*[66]*
Brass tube	*Young's Modulus, E* (GPa)	*115*	*[66]*
	Density, ρ (kg/m^3)	*8750*	*[66]*
	Poisson's ratio, ν	*0.3*	*[66]*
Teflon	*Young's Modulus, E* (GPa)	*0.46*	*[66]*
	Density, ρ (kg/m^3)	*2160*	*[66]*
	Poisson's ratio, ν	*0.46*	*[66]*
Rubber	*Stress vs. Strain data*	*Table A.1*	*SHPB test data*
	Density, ρ (kg/m^3)	*1200*	*Found experimentally*
	Poisson's ratio, ν	*0.495*	*[60]*

Table 6.2 – Table of material properties used in the finite element model

6.4.1 Construction of the rubber material model

A hyperelastic material is an ideally elastic material which possesses isotropic (orientation of molecules is initially random) and nonlinear material properties. Hyperelasticity is valid for the modelling of elastomeric materials such as rubber, which demonstrates instantaneous elastic response up to large strains[60].

Hyperelastic materials derives from a strain energy potential, $U(\varepsilon)$. The strain energy potential relates the strain energy stored in the elastic material per unit volume (and therefore the stress-strain relationship) to the three strain components at that particular point in the material, disregarding factors such as the deformation history, heat dissipation and stress relaxation[60]. In order to employ any of the strain energy potentials available in ABAQUS, the relevant material constants or experimental test data need to be assigned to the particular strain energy potential model. Seeing that none of the material parameters are known, the stress-strain data obtained from the Split-Hopkinson Pressure Bar uniaxial compression tests performed on the rubber specimens are used to generate the rubber material model.

Essentially, the SHPB tests are reproduced in ABAQUS in order to validate the rubber material model which is eventually utilised. An axisymmetric finite element model of the rubber specimen is wedged between two rigid surfaces representing the magnesium pressure bar surfaces in contact with the front and rear surfaces of the specimen. The velocity applied to the top surface will produce the same rate of axial compression experienced by the specimen during the dynamic testing. Afterwards the stress-strain curves from the numerical analysis are compared to those obtained from the SHPB tests. The rubber material model is validated for strain rates of $1750s^{-1}$, $2200s^{-1}$ and $2500s^{-1}$.

ABAQUS is prompted to evaluate the experimental test data provided in order to determine the most favourable form(s) of strain energy potential to be used. The strain energy potentials revealed to be most suitable for the application include the Marlow, the Yeoh, the Mooney-Rivlin, the Ogden and the Polynomial form.

- The **Marlow** strain energy potential is given by[60]:

$$U = U_{dev}(\bar{I}_1) + U_{vol}(J_{el}) \qquad \text{Eq. 6.1}$$

The deviatoric part of the strain energy potential is defined by assigning either planar, uniaxial or equibiaxial material test data. The volumetric part is defined by assigning a Poisson's ratio to the material, by defining the volumetric test data, or by providing the lateral strains together with the planar, uniaxial or equibiaxial material test data.

- The **Mooney-Rivlin** form is defined by a polynomial strain energy function[60]:

$$U = C_{10}(\bar{I}_1 - 3) + C_{01}(\bar{I}_2 - 3) + \frac{1}{D_1}(J_{el} - 1)^2 \qquad \text{Eq. 6.2}$$

The initial shear modulus of the material is defined by $\mu_0 = 2(C_{10} + C_{01})$.

The bulk modulus of the material is defined by $K_0 = \frac{2}{D_1}$.

- The **polynomial** strain energy potential is given by[60]:

$$U = \sum_{i+j=1}^{N} C_{ij}(\bar{I}_1 - 3)^i(\bar{I}_2 - 3)^j + \sum_{i=1}^{N} \frac{1}{D_i}(J_{el} - 1)^{2i} \qquad \text{Eq. 6.3}$$

The initial shear modulus of the material is defined by $\mu_0 = 2(C_{10} + C_{01})$.

The bulk modulus of the material is defined by $K_0 = \frac{2}{D_1}$.

- The **Yeoh** form is a type of reduced polynomial strain energy potential[60]:

$$\begin{aligned} U = {} & C_{10}(\bar{I}_1 - 3) + C_{20}(\bar{I}_1 - 3)^2 + C_{30}(\bar{I}_1 - 3)^3 \\ & + \frac{1}{D_1}(J_{el} - 1)^2 + \frac{1}{D_2}(J_{el} - 1)^4 + \frac{1}{D_3}(J_{el} - 1)^6 \end{aligned} \qquad \text{Eq. 6.4}$$

The initial shear modulus of the material is defined by $\mu_0 = 2.C_{10}$.

The bulk modulus of the material is defined by $K_0 = \frac{2}{D_1}$.

- The form of the **Ogden** strain energy potential is defined by[60]:

$$U = \sum_{i=1}^{N} \frac{2\mu_i}{\alpha_i^2}(\bar{\lambda}_1^{\alpha_i} + \bar{\lambda}_2^{\alpha_i} + \bar{\lambda}_3^{\alpha_i} - 3) + \sum_{i=1}^{N} \frac{1}{D_i}(J_{el} - 1)^{2i} \qquad \text{Eq. 6.5}$$

The initial shear modulus of the material is defined by $\mu_0 = \sum_{i=1}^{N} \mu_i$.

The bulk modulus of the material is defined by $K_0 = \frac{2}{D_1}$.

The definitions of the symbols used in the formulation of the strain energy potential equations are listed below[60]:

U = strain energy per unit of reference volume

U_{dev} = deviatoric part of the strain energy potential

U_{vol} = volumetric part of the strain energy potential

$\bar{I}_1$ = first deviatoric strain invariant, which is defined as $\bar{I}_1 = \bar{\lambda}_1^2 + \bar{\lambda}_2^2 + \bar{\lambda}_3^2$

$\bar{I}_2$ = second deviatoric strain invariant, which is given by $\bar{I}_2 = \bar{\lambda}_1^{(-2)} + \bar{\lambda}_2^{(-2)} + \bar{\lambda}_3^{(-2)}$

$\bar{\lambda}_i$ = principle stretches, given by $\bar{\lambda}_i = J^{-1/3}.\lambda_i$

J = total volume ratio

J_{el} = elastic volume ratio, which relates the total volume ratio J to thermal volume ratio J_{th} by $J_{el} = \frac{J}{J_{th}}$, where $J_{th} = (1+\varepsilon^{th})^3$.

ε^{th} = linear thermal expansion strain

C_{10}, C_{01}, D_1 , μ_i and α_i = temperature dependent material parameters

N = material parameter

The five different strain energy potentials provided in the ABAQUS material package are employed in the rubber material model to be investigated and compared. Figure 6.12 displays the difference in behaviour of the rubber specimen under compression when the rubber material model incorporates each of the five strain energy potentials.

The red curve in Figure 6.12 depicts the true stress-strain data taken from the SHPB tests performed on the rubber specimens. The black curve in Figure 6.12 represents the trendline plotted through the experimental stress-strain curve. The stress-strain data taken from the trendline curve is input into the ABAQUS rubber material model with the intention of obtaining a similar stress-strain curve from the numerical analysis of the compression procedure.

It is observed from Figure 6.12 that employing the Mooney-Rivlin and Yeoh strain energy potentials in the rubber material model produces stress-strain curves that differ significantly from the experimental stress-strain curve, while the stress-strain data generated by employing

the Marlow, Ogden (with n=3) and polynomial (with n=2) strain energy potentials displays a closer relation to the experimental rubber material data.

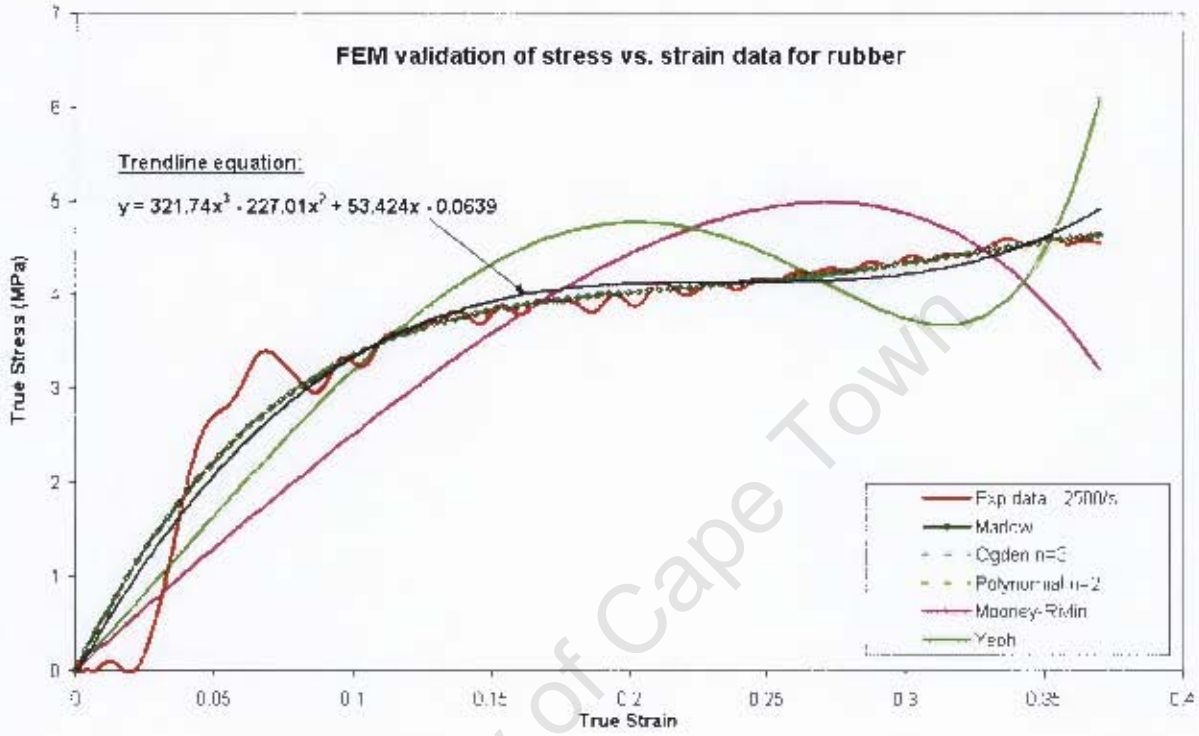

Figure 6.12 – Comparison of various rubber material models used in the numerical analysis

Thus far a Poisson's ratio of 0.495 is used while investigating the response provided by using the various strain energy potentials in the rubber material model. A Poisson's ratio of 0.495 is the upper limit suggested by the ABAQUS documentation manual. Although it is generally advised to use a lower Poisson's ratio in the region of 0.47, if the rubber material is highly confined between stiff metal surfaces and only a small surface area of the rubber is unconstrained, using a low Poisson's ration will generate inaccurate results[60]. However, according to the ABAQUS documentation manual, it is possible that in such a confined case where the rubber is subjected to high compression, using a high Poisson's ratio may also not provide accurate results[60]. As such, even though the validation of the compression stress-strain results given in Figure 6.12 is taken to be good, the stress results obtained during the simulations of the blast loading may not be accurate.

The effect of using a low (ν = 0.46) and high (ν = 0.495) Poisson's ratio in the rubber material model is investigated in Section 6.10.1.2.

6.5 INTERACTIONS BETWEEN PARTS IN THE ASSEMBLY

Frictional properties between the various materials need to be simulated to ensure correct interaction between the individual parts of the assembly. A "penalty" friction formulation is used to imitate the tangential behaviour of the materials and the frictional coefficients are given in Table 6.3. Pressure over-closure in the normal direction between all parts is simulated in ABAQUS by a "hard" contact function while allowing separation of the surfaces after contact. The "hard" contact formulation minimises the penetration of the nodes of the two surfaces in contact.

In the experimental model the rubber sole is glued onto the bottom surface of the metatarsals and the calcaneous, therefore a similar fixture has to be simulated in the numerical model. A "rough" friction formulation is assigned to simulate the tangential behaviour between the rubber and aluminium surfaces in contact, together with a "hard" contact function in the normal direction allowing no separation of the surfaces after contact. Combining these tangential and normal behaviour specifications ensures that no relative motion of the surfaces will occur.

Material 1	*Material 2*	*Tangential frictional coefficient*
Aluminium	*Aluminium*	*0.9*
Aluminium	*Steel*	*0.47*
Aluminium	*Brass*	*0.4*
Aluminium	*Teflon*	*0.1*
Steel	*Rubber*	*0.2*

Table 6.3 – Table listing friction coefficients between materials used in the foot model [67]

It is stated previously that the four holes for the four screws fixing the bottom hinge component to the foot is excluded from the numerical model, meaning the four screws are not modelled either. However, in the finite element model, the surfaces where the four holes are in the experimental model are identified in the top surface of the foot as well as the bottom surface of the bottom hinge component. A "tie" constraint is assigned to each of the surface pairs, which ties the nodes of the two selected surfaces. This procedure simulates the effect of having the foot and bottom part of the hinge fixed by four screws.

6.6 BOUNDARY CONDITIONS

Instead of constructing the entire horizontal ballistic pendulum, only the detonation plate and the Teflon alignment bushes are included in the finite element model of the test setup. In doing so, the runtime and size of the simulations are minimized. Although a simplified setup now represents the ballistic pendulum, the inherent behaviour of the pendulum is still maintained by assigning the correct boundary conditions.

Two sets of boundary conditions are employed in the numerical simulation of the blast event, as illustrated in Figure 6.13. Firstly, the Teflon bushes from the rig are encastred (allowing no translation or rotation of the bushes) in order to guide the movement of the tibia. Secondly, a displacement/rotation boundary condition is applied to the detonation plate, allowing translation only along the tibia axis and no rotation is permitted.

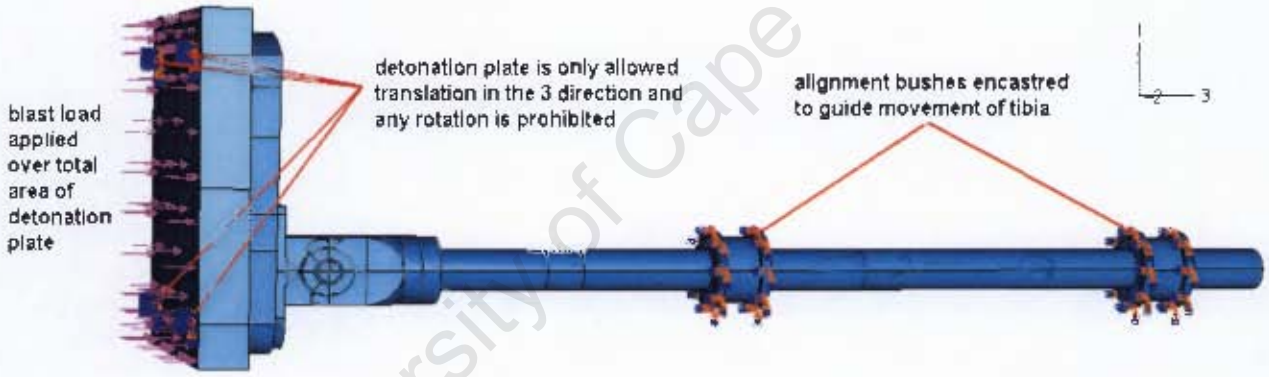

Figure 6.13 – Boundary conditions and load application

6.7 LOAD APPLICATION

The impact resulting from the detonation of the explosives is applied to the total area of the bottom surface of the detonation plate (as shown in Figure 6.13) in the form of a pressure pulse. The load is defined as a square pressure pulse (see Figure 6.14) which is applied exponentially over the bottom surface of the detonation plate. The duration over which the square pulse is applied is taken to be equal to the burn duration of the plastic explosives. The burn duration is calculated in Section 5.5.2 to be approximately 1.22μs.

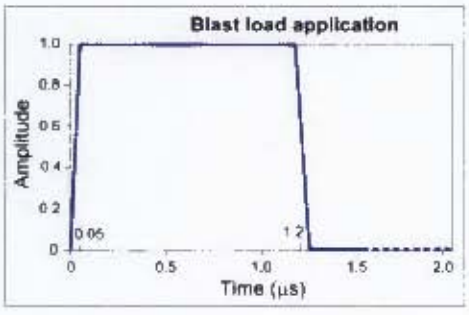

Figure 6.14 – Graph showing applied pressure vs. time

The peak pressure is applied in the centre of the plate which decays exponentially towards the edges of the detonation plate (explained in Figure 6.15). The peak pressure is calculated according to the magnitude of the impulse transmitted by the specific blast loading condition being simulated.

The load application is assigned by a user-defined subroutine written for each of the loading conditions. The peak pressure is assigned to act in the centre of the detonation plate for the blast loading applied in the centre of the foot model. The peak pressure of the decaying load is assigned to act at an offset which is axially in line with the calcaneous of the foot model for the blast loading applied at the heel.

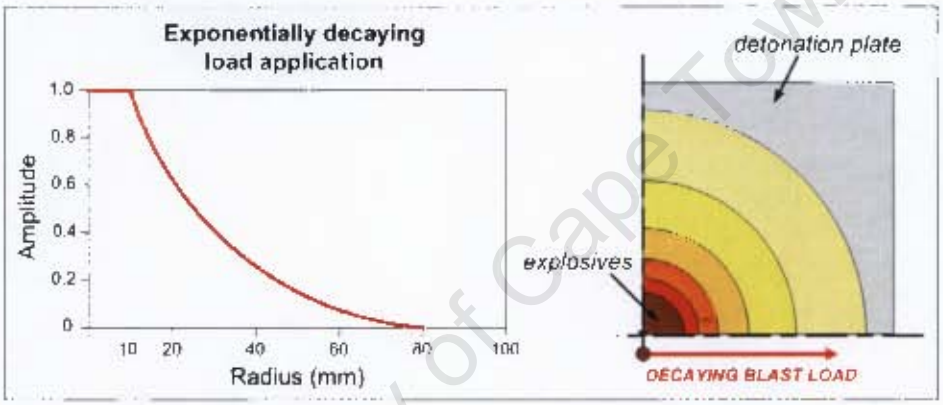

Figure 6.15 – Graph showing the exponentially decaying blast load

6.8 HISTORY OUTPUT

In order to compare the results obtained from the experimental blast tests to the results obtained from the finite element simulations, a consistent feature needs to be used. In the experimental test setup, a pair of strain gauges are placed 80mm above the base of the aluminium tube which records the strain experienced in that region of the tube. The strain signal recorded by the strain gauges during every blast test is then converted to provide the stress-time results. Hence it is decided to select elements in the numerical model of the aluminium tube which correspond to the position of the strain gauges in the experimental setup. The elements selected in the tube are hereon referred to as the "strain gauge" elements. In the course of the numerical simulation, the "strain gauge" elements are requested to record the stress experienced in them at each interval, therefore generating a stress signal which can be compared to the stress signal obtained from the experimental blast tests.

6.9 RESULTS FROM THE NUMERICAL SIMULATION OF BLAST LOADING PERFORMED, EXCLUDING THE RUBBER SOLE

This section of the report contains the stress-time results obtained from the finite element analyses performed to simulate the blast loading conditions where the rubber sole was not included in the test setup.

6.9.1 Blast loading in the centre of the foot model

The stress results obtained from the numerical analyses performed to simulate blast loading in the centre of the foot model are shown in Figure 6.16. The impulse applied to the centre of the detonation plate in the numerical simulation is taken from the experimental data (provided in Section 3.6.1) and relates to the detonation load as follows:

- 5+1g PE4 → 7.6Ns impulse
- 6+1g PE4 → 8.9Ns impulse
- 7+1g PE4 → 8.9Ns impulse

Simulation of the 5+1g explosives load applied to the centre of the detonation plate indicates a maximum stress of 26.23MPa to be experienced by the "strain gauge" elements in the tibia. The impulse used to simulate the detonation of both 6+1g and 7+1g explosives is roughly 1.2Ns higher than the impulse used to simulate the detonation of 5+1g explosives, which is clearly observed in the results given in Figure 6.16. The results show that a maximum stress of 30.50MPa and 31.25MPa is induced in the "strain gauge" elements for the 6+1g and 7+1g numerical simulation respectively.

It is noticed in Figure 6.16 that the finite element simulation produced multiple peaks in the compressive stress wave passing through the "strain gauge" elements. As briefly discussed in Section 5.6.3.1 pertaining the experimental results of blast loading in the centre without the rubber sole, the multiple peaks in the stress curve may be due to cyclic stress caused by the flexion of the foot during the blast event. This phenomenon is discussed in more detail in Section 7.2.1.2 of this thesis.

6.9.2 Blast loading at the heel of the foot model

Figure 6.17 presents the stress-time results retrieved from the finite element analyses performed to simulate blast loading of 5+1g PE4 at the heel of the foot model. The impulse applied axially in line with the heel of the numerical model of the foot surrogate is 7.8Ns. The maximum stress recorded in the "strain gauge" elements is seen in Figure 6.17 to be 39.36MPa.

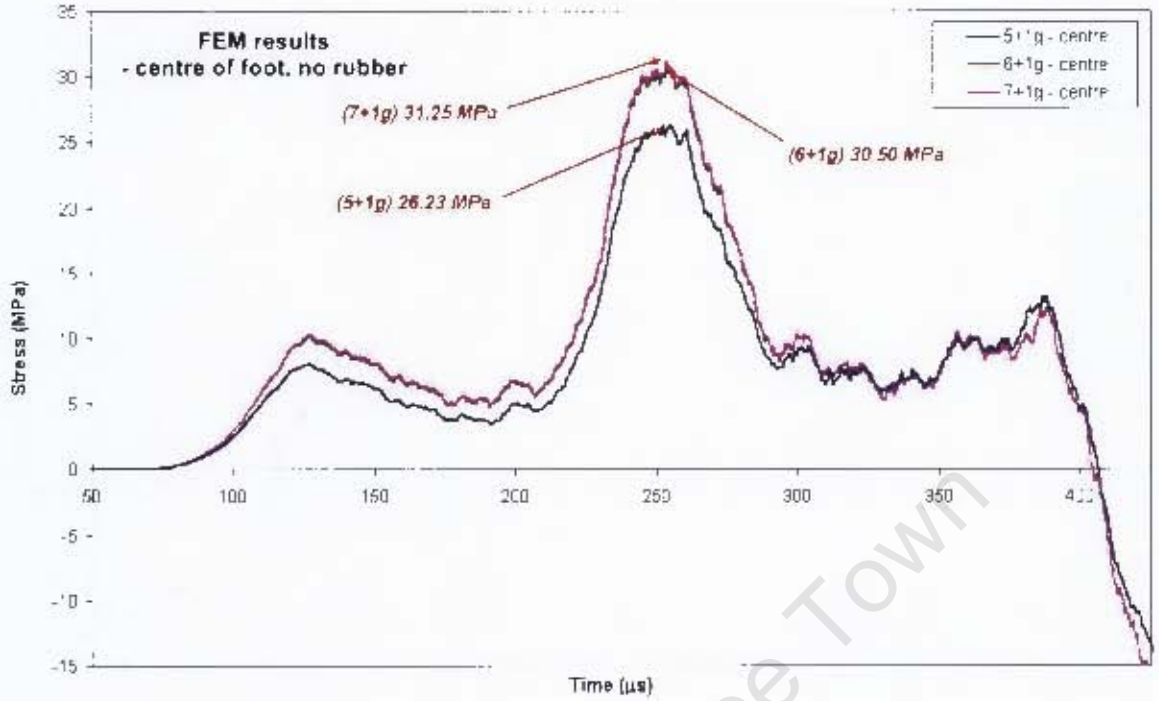

Figure 6.16 – Graph comparing FEM analyses results for blast loading in the centre of the foot, excluding the rubber sole

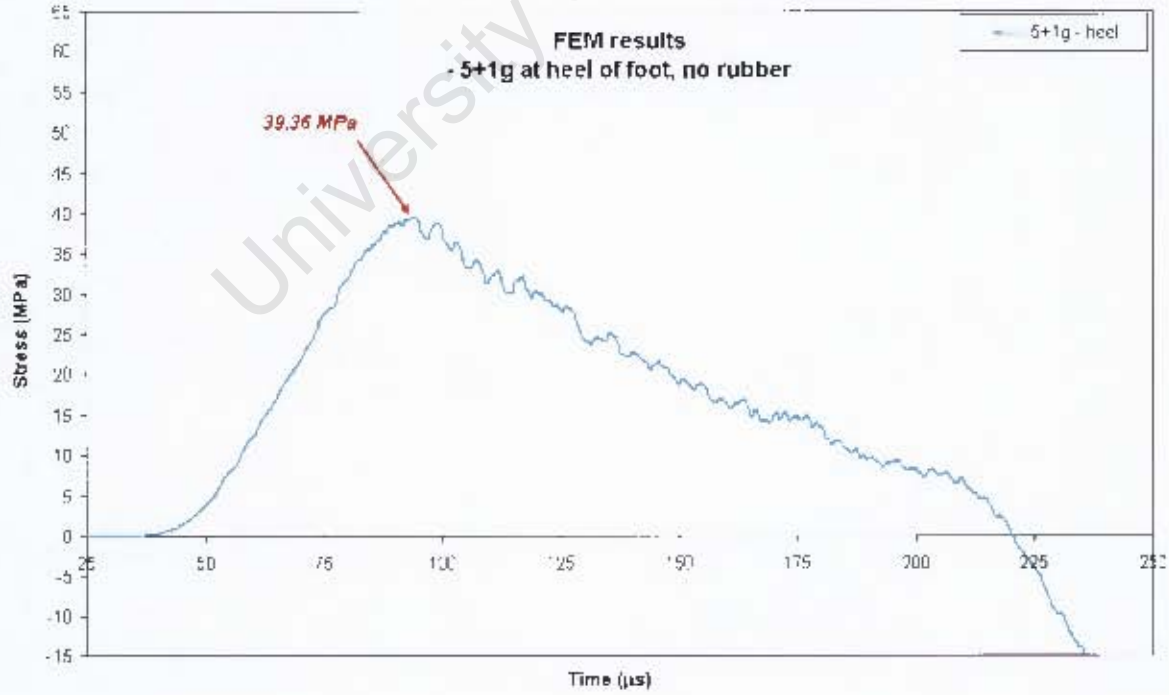

Figure 6.17 - Graph of the FEM analyses results for blast loading at the heel of the foot, excluding the rubber sole

6.10 RESULTS FROM THE NUMERICAL SIMULATION OF BLAST LOADING PERFORMED, INCLUDING THE RUBBER SOLE

This section of the report contains the stress-time results retrieved from the finite element simulations executed for the different blast loading conditions relevant to the blast tests performed where the rubber sole is included in the test setup. Firstly the aspects taken into account during the construction of the rubber material model and the effect of those parameters on the outcome of the finite element results are discussed. After the rubber material model is established, the eventual finite element results of the various blast loading conditions are examined.

6.10.1 Preparation of the rubber material model

It is concluded in Section 6.4.1 that the material characteristics resulting in the most favourable rubber material model includes using the determined density of 1200kg/m^3, a Poisson's ratio of 0.495 and employing the Ogden (n=3) or polynomial (n=2) strain energy potentials for a strain rate of 2500s^{-1}. As such, the rubber material model used to model the rubber sole is initially constructed by employing the main characteristics mentioned above. The results obtained by altering the parameters investigated in this part of the report are therefore all compared to the results obtained by using the rubber material model initially decided upon in Section 6.4.1.

6.10.1.1 Rubber sole configuration 1 vs. configuration 2

As explained in Section 6.2.6, the exact shape (viewed from the side) of the rubber sole used during the experimental blast tests is not defined, because the rubber sole is not shaped by any moulding or machining technique. Therefore, different shapes representing the rubber sole in the finite element model is initially tried out in order to examine the stress response provided by each of the models. The two models with most varying shape (shown in Figure 6.7 (a) & (b)) yielded the most varying stress-time results, which are presented in Figure 6.18. The numerical results obtained using these two different rubber sole configurations is compared to the experimental results obtained for the same loading condition in Figure 6.19.

From Figure 6.18 and Figure 6.19 it is clearly noticed that the final configuration leads to the optimum stress transmission, whereas the initial configuration of the rubber sole yielded negligible stress transmission.

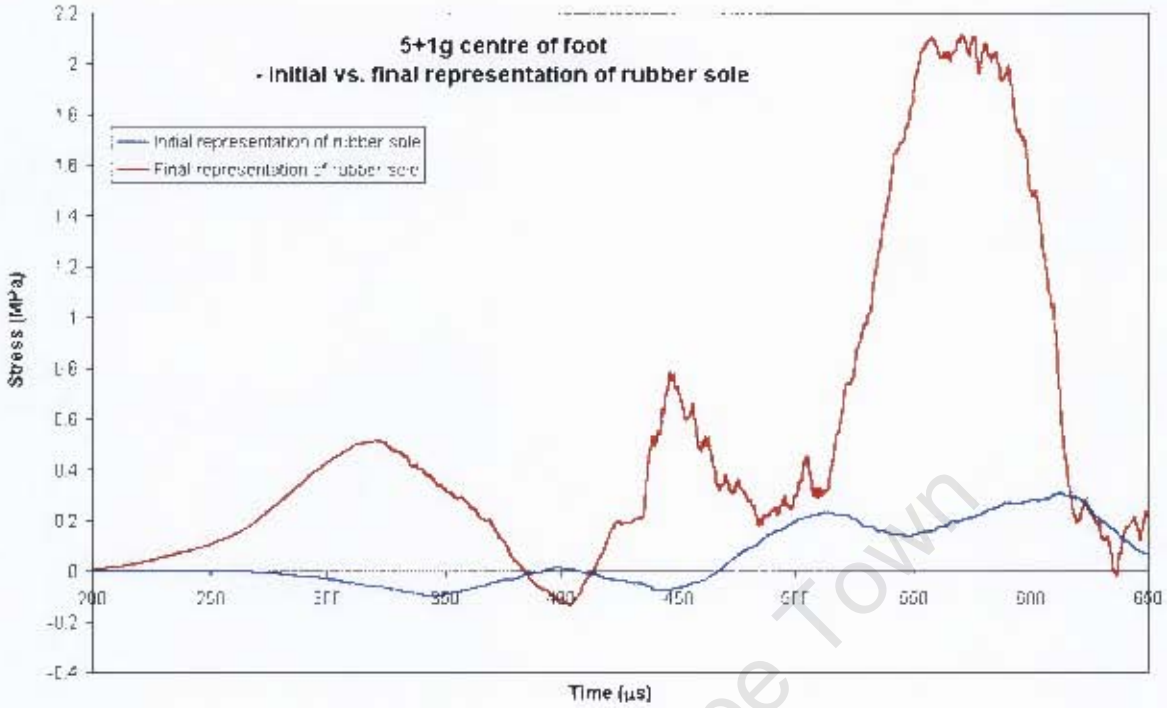

Figure 6.18 – Graph comparing the FEM results obtained for 5+1g explosive blast loading in the centre of the foot model, employing two different configurations of the rubber sole

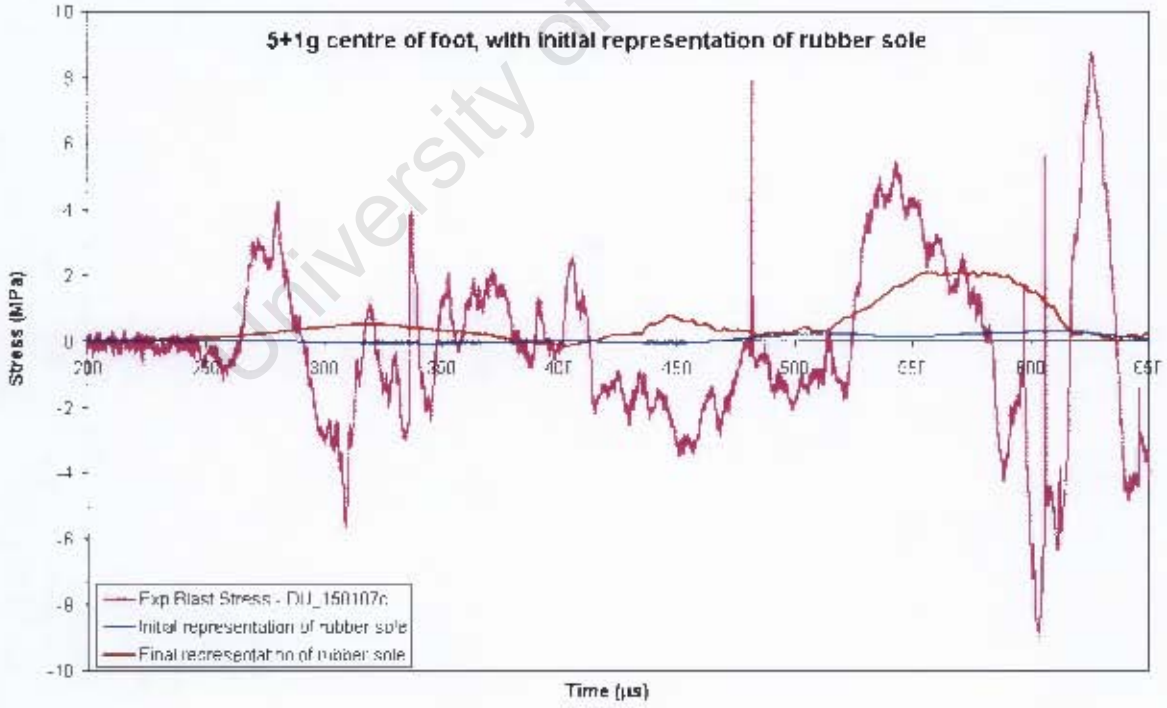

Figure 6.19 – Graph comparing the FEM results obtained when using the two rubber sole configurations to the experimental results obtained when detonating 5+1g explosives in the centre of the foot model

6.10.1.2 Effect of varying the Poisson's ratio of the rubber material model

Most solid rubber-like materials have very little compressibility compared to their shear flexibility, which implies that modelling the rubber as an incompressible material would lead to the most favourable results. However, in ABAQUS/Explicit if the rubber material is highly confined (as in this particular case), it is not possible to assume full incompressibility because the program has no means of forcing such a constraint at each material calculation point[60]. Therefore enough compressibility must be provided for the ABAQUS code to work, which may mean that the bulk behaviour of the rubber material is softer than that of the actual rubber material.

Solid rubber-like materials have Poisson's ratios varying between 0.490 and 0.497, but an upper limit of Poisson's ratio of 0.495 is suggested by the ABAQUS documentation, as the use of excessively small time increments is required[60]. It is unfortunately possible in the case where the rubber is in contact with stiff metal parts and has a small amount of free space, that using ABAQUS/Explicit will not yield accurate results[60].

It is observed from Figure 6.20 that providing more compressibility ($\nu = 0.46$) resulted in much less accurate results than when the suggested upper limit of $\nu = 0.495$ is used. However, even using such a high Poisson's ratio of 0.495 does not yield sufficient results to accurately reproduce the experimental results.

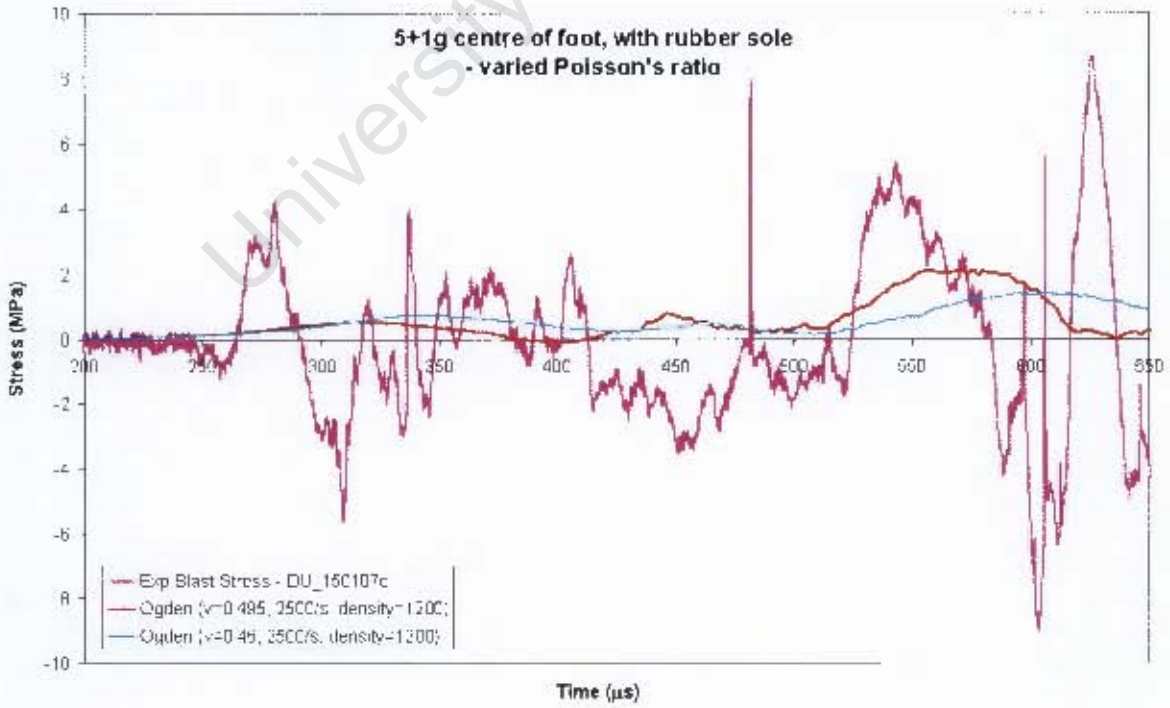

Figure 6.20 – Graph showing the effect of varying the Poisson's ratio of the rubber

6.10.1.3 Effect of employing various strain rate data in the rubber material model

The material characterisation of the rubber used in the experimental blast test setup is explained and discussed in Section 5.3.2 of this report. The material characterisation involved exposing the rubber specimens to a range of dynamic strain rates employing the compression Split-Hopkinson Pressure Bar. The strain rates analysed in Section 5.3.2 for the rubber specimen in compression are $1750s^{-1}$, $2200s^{-1}$ and $2500s^{-1}$.

It is initially assumed that employing the stress-strain data from the higher strain rate in the rubber material model would provide the most favourable finite element analysis results. However, it is decided to inspect the finite element results obtained by using stress-strain data from strain rates of $1750s^{-1}$, $2200s^{-1}$ and $2700s^{-1}$ as well, and the results are presented in Figure 6.21. Although stress-strain test data for a strain rate of $2700s^{-1}$ does not exist, the stress-strain test data obtained for the strain rates of $1750s^{-1}$, $2200s^{-1}$ and $2500s^{-1}$ was extrapolated in order to generate hypothetical stress-strain data for rubber subjected to a strain rate of $2700s^{-1}$.

The results in Figure 6.21 indicates that using the lower strain rate ($1750s^{-1}$) data results in a negligible amount of stress to be transmitted through the rubber layer, whereas using the higher strain rate (hypothetical $2700s^{-1}$) data yields the most appropriate stress transmission. Comparing the maximum stress recorded by the "strain gauge" elements, using a higher strain rate of $2700s^{-1}$ than the original $2500s^{-1}$ proves to provide the most favourable results when compared to the experimental stress results.

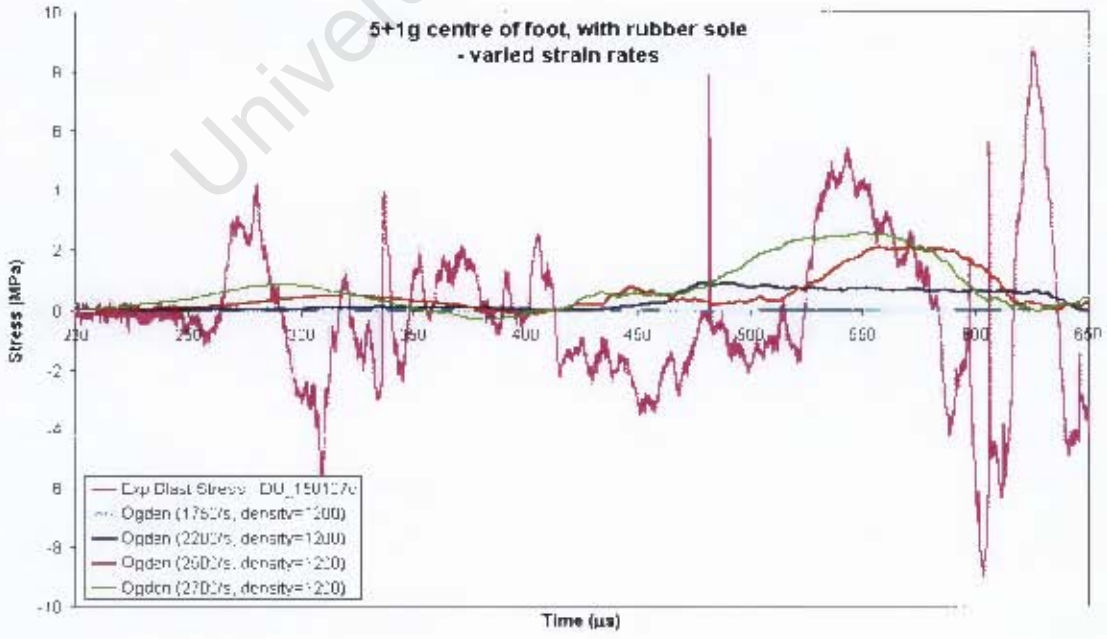

Figure 6.21 – Graph showing the effect of using different strain rate data in the rubber model

6.10.1.4 Employing different strain energy potentials in the construction of the rubber material model

As explained in Section 6.4.1 of this thesis, the hyperelastic behaviour of the rubber material is modelled by employing some form of strain energy potential. It is subsequently revealed the Ogden (with n=3) and the polynomial (with n=2) strain energy potentials to provide the optimum results in the finite element analyses. Each of the strain energy potentials discussed in Section 6.4.1 are employed in the rubber material model and the results are compared. The stress-time results obtained from the numerical analysis of blast loading applied in the centre of the foot is shown in Figure 6.22 and the results for blast loading applied axially in line with the heel is shown in Figure 6.23.

The results from the finite element simulations indicates that the Ogden (with n=3) and polynomial (with n=2) strain energy potentials yield the most favourable stress-time results. The results from the finite element simulations of the different impact loading conditions also indicate (as noticed in Section 6.4.1) that employing the Ogden (with n=3) and polynomial (with n=2) strain energy potentials arrive at essentially the same stress-time results.

Figure 6.22 shows that the numerical analyses for blast loading in the centre of the foot using the Ogden and polynomial functions do not accomplish the same maximum stresses as recorded during the experimental blast tests.

However, it is seen in Figure 6.23 that the numerical results for the maximum stress obtained during the analyses of blast loading applied at the heel of the foot employing the Ogden and polynomial functions shows very good correlation to the maximum stress recorded during the experimental blast tests. The results obtained by using the hypothetical stress-strain data of the $2700s^{-1}$ strain rate during the numerical analysis of blast loading applied at the heel is also included in Figure 6.23. The enhanced stress transmission through the rubber layer is observed in the quicker rise in the stress curve in order to reach the peak in the stress curve, as well as the higher maximum stress recorded by the "strain gauge" elements.

The difference in maximum stress experienced by the aluminium tube is discussed in more detail in Section 7.3.

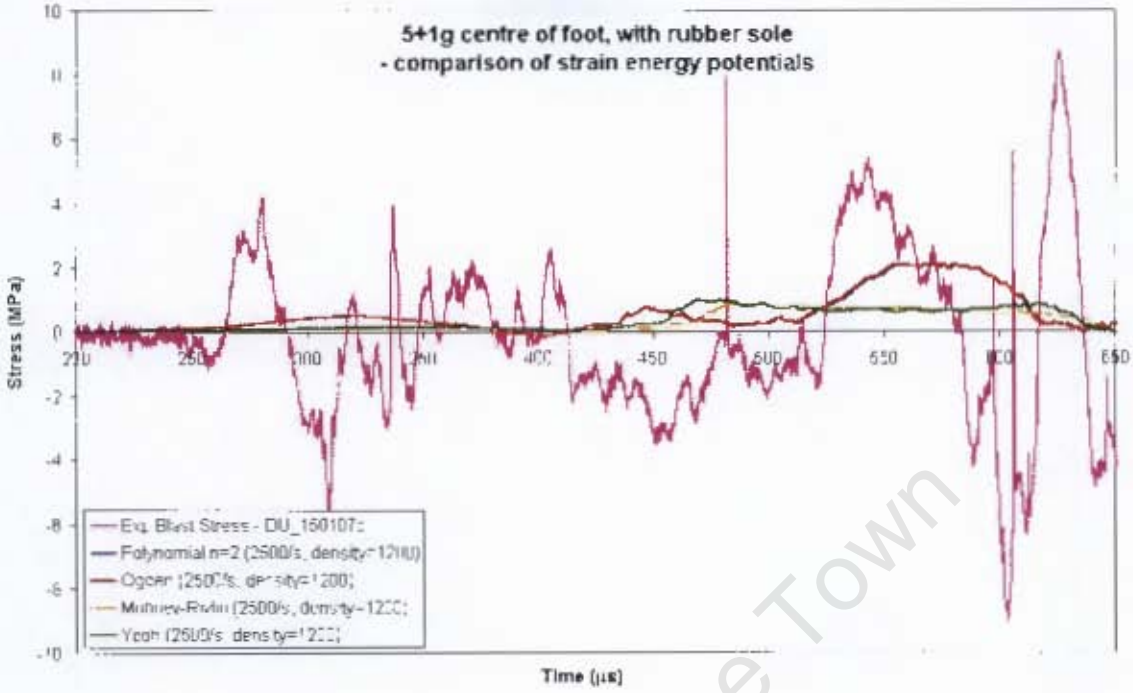

Figure 6.22 – Graph comparing the FEM results obtained for analysing 5+1g explosive blast loading in the centre of the foot model when using different strain energy potentials in the rubber material model

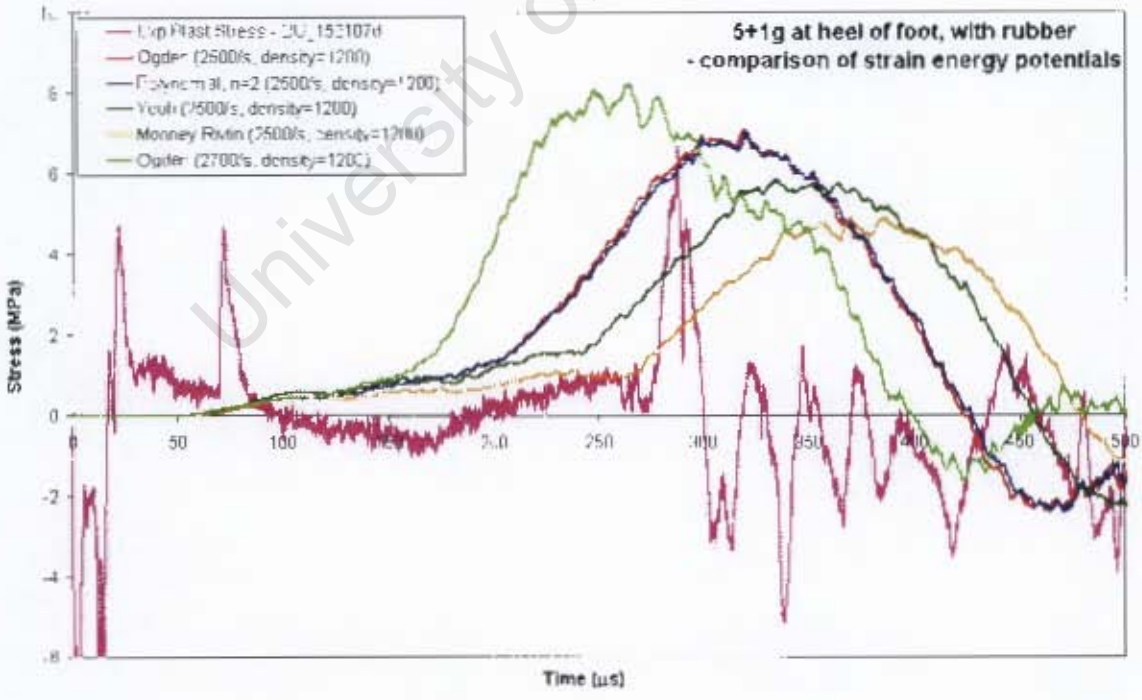

Figure 6.23 - Graph comparing the FEM results obtained for analysing 5+1g explosive blast loading at the heel of the foot model when using different strain energy potentials in the rubber material model

6.10.2Blast loading in the centre of the foot

The results obtained from the finite element analyses performed to simulate the blast loading in the centre of the foot with the rubber sole included in the test setup is presented in Figure 6.24. The various impulses applied to the detonation plate in the numerical model are once again taken from the experimental data provided in Section 3.6.1, and relate to the relevant explosive loading as follows:

- 5+1g PE4 → 7.5Ns impulse
- 6+1g PE4 → 8.7Ns impulse
- 7+1g PE4 → 9.1Ns impulse

The stress-time results shown in Figure 6.24 indicate the occurrence of two compressive stress waves passing through the "strain gauge" elements in short succession. The shape of the second compressive stress wave carries a distinct resemblance to the shape of the stress wave obtained during the numerical simulation of the blast loading in the centre of the foot model with the rubber sole excluded from the test setup. The origin of these two compressive stress waves is examined later in Section 7.3.1.2, and only the peak stress values are investigated for now.

During the first compressive stress wave passing through the "strain gauge" elements, a maximum stress of 0.51MPa, 0.46MPa and 0.44MPa is observed for blast loading using 5+1g, 6+1g and 7+1g explosives respectively.

The maximum stress which occurs during the second compressive stress wave passing through the "strain gauge" elements is recorded to be 2.11MPa, 2.31MPa and 2.49MPa for the blast loading using 5+1g, 6+1g and 7+1g explosives respectively.

6.10.3Blast loading at the heel of the foot model

Figure 6.25 presents the results obtained from the finite element analyses executed to simulate the blast loading applied in line with the heel of the foot mode with the rubber sole included in the test setup. The impulse applied in the numerical model to simulate the 5+1g PE4 detonating at the heel is taken to be 7.6Ns and 8.5Ns to simulate 7+1g PE4 detonating at the heel. The maximum stress experienced by the "strain gauge" elements in the tibia for blast loading using 5+1g explosives is observed to be 7.09MPa and 8.02MPa for blast loading using 7+1g explosives.

6.11 COMPARISON OF RESULTS FOR DIFFERENT BLAST LOADING POSITIONS

6.11.1 Simulation of blast loading performed excluding the rubber sole

The stress-time results obtained from the numerical simulations of blast loading in the centre of the foot model and blast loading at the heel of the foot model when the rubber sole is excluded, is compared in Figure 6.26. As blast loading at the heel is only performed using 5+1g explosives, the results with respect to impact loading position is only compared using the results relating to the 5+1g simulations. According to the finite element simulations, applying blast loading at the heel of the foot results in a 50% increase in stress recorded by the "strain gauge" elements selected in the lower region of the aluminium tube. The time delay in the onset of reaching the peak stress, which is noticed between the heel and centre blast loading, is observed to be approximately 150μs.

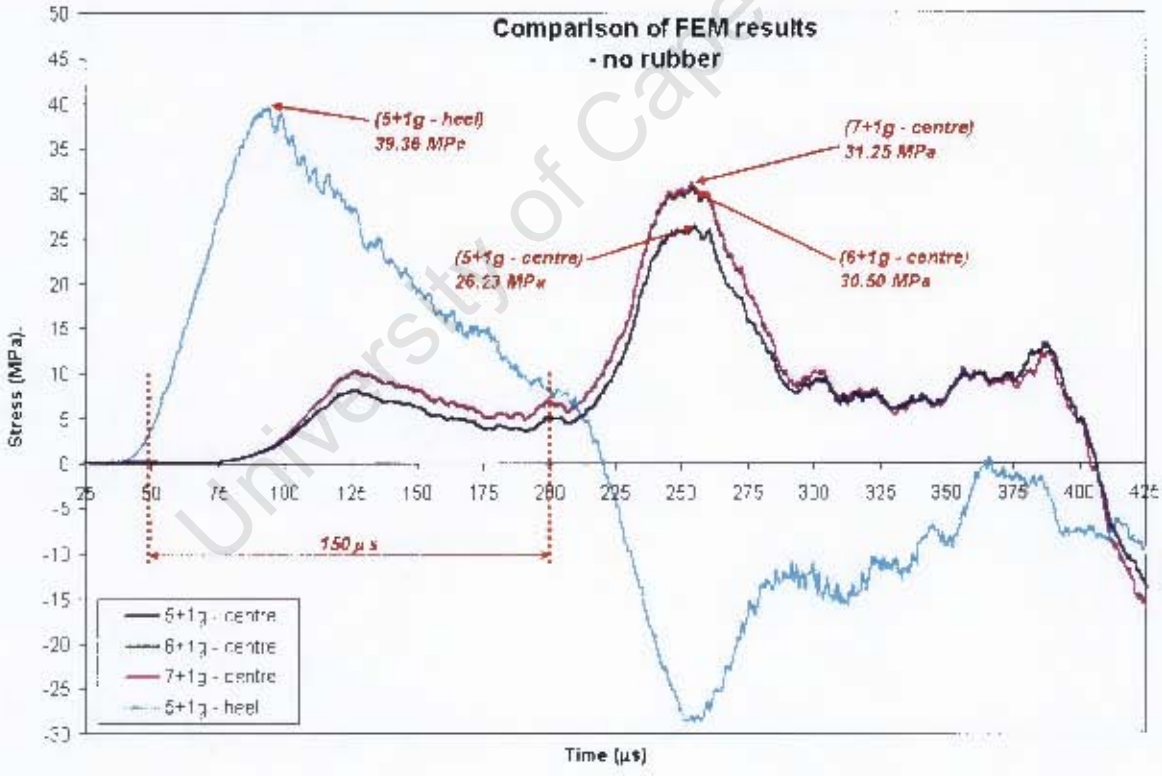

Figure 6.26 – Graph comparing the FEM results for blast loading in the centre and at the heel of the foot model, excluding the rubber sole

6.11.2 Simulation of blast loading performed including the rubber sole

A comparison of the results obtained from the finite element analyses performed to simulate the blast loading applied in the centre of the foot and at the heel of the foot when the rubber sole is included in the test setup, is presented in Figure 6.27. The numerical simulation stress-time results indicate that blast loading at the heel increases the maximum stress recorded by the "strain gauge" elements by 236% for the 5+1g explosive loading condition, and by 222% for the 7+1g loading condition. The percentage increase in stress is calculated by using the maximum stress value of the second peak occurring during the blast loading in the centre of the foot model.

The time delay is observed to be approximately 50μs between the onset of reaching the maximum stress for the heel blast and the onset of reaching the first compressive maximum stress for the centre blast. A time delay of roughly 300μs is observed to exist between the onset of reaching the maximum stress for the heel blast and the onset of reaching the second compressive peak stress for the centre blast loading condition.

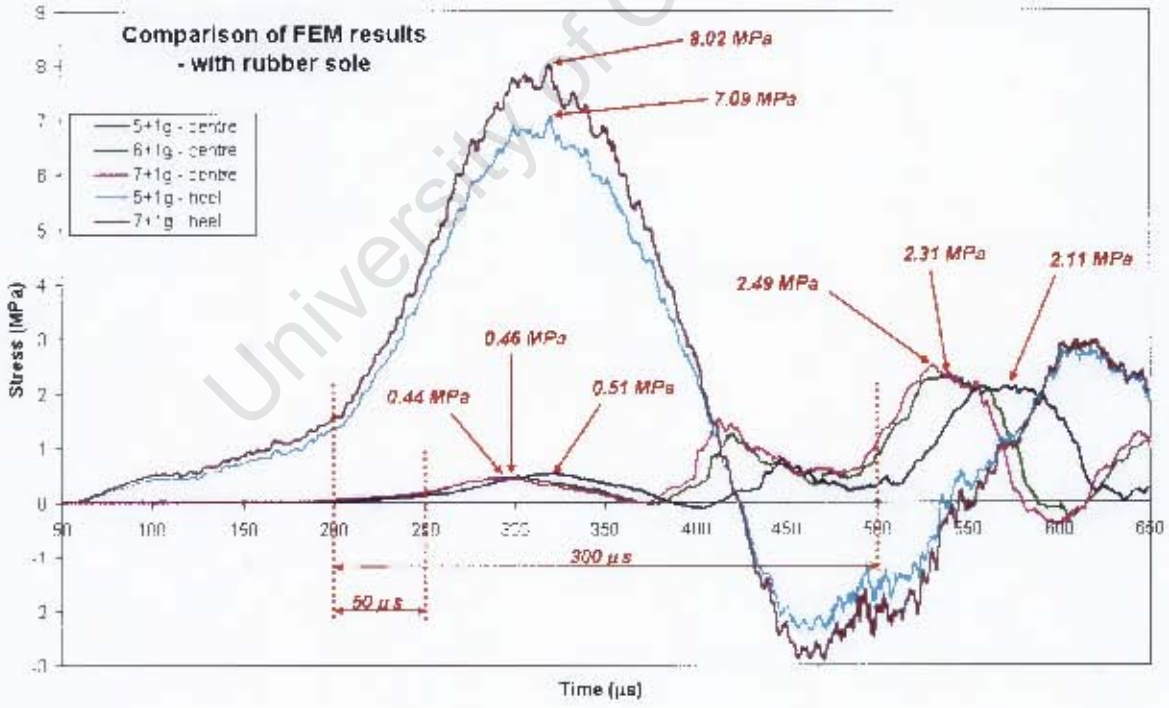

Figure 6.27 - Graph comparing the FEM results for blast loading in the centre and at the heel of the foot model, including the rubber sole

6.12 INVESTIGATING THE ATTENUATION EFFECT OF INCLUDING THE RUBBER SOLE

The attenuation provided by including the rubber sole in the finite element model is quantified in terms of the maximum stress experienced by the "strain gauge" elements selected in the lower region of the tibia tube. In the case of the loading conditions where the rubber sole is included, the maximum stress from the second compressive stress wave is used in the comparison. The time delay observed in the transmission of the stress wave during the blast loading applied in the centre of the foot model is also inspected.

6.12.1 Simulation of blast loading performed in the centre of the foot model

The series of results obtained from the finite element simulations of blast loading applied in the centre of the foot, excluding and including the rubber sole layer, is presented in Figure 6.28. Including the rubber sole in the finite element model of the test setup is seen to reduce the maximum stress experienced by the "strain gauge" elements by 91% for the blast loading simulated for 5+1g explosives. The results from the simulations of the 6+1g and 7+1g explosive blast loading shows that the maximum stress experienced in the lower region of the tibia is reduced by 92.4% and 92% respectively. It is also noticed from Figure 6.28 that the onset of reaching peak stress when the rubber sole is included in the test setup occurs approximately 290μs later than when the rubber sole is excluded from the test setup.

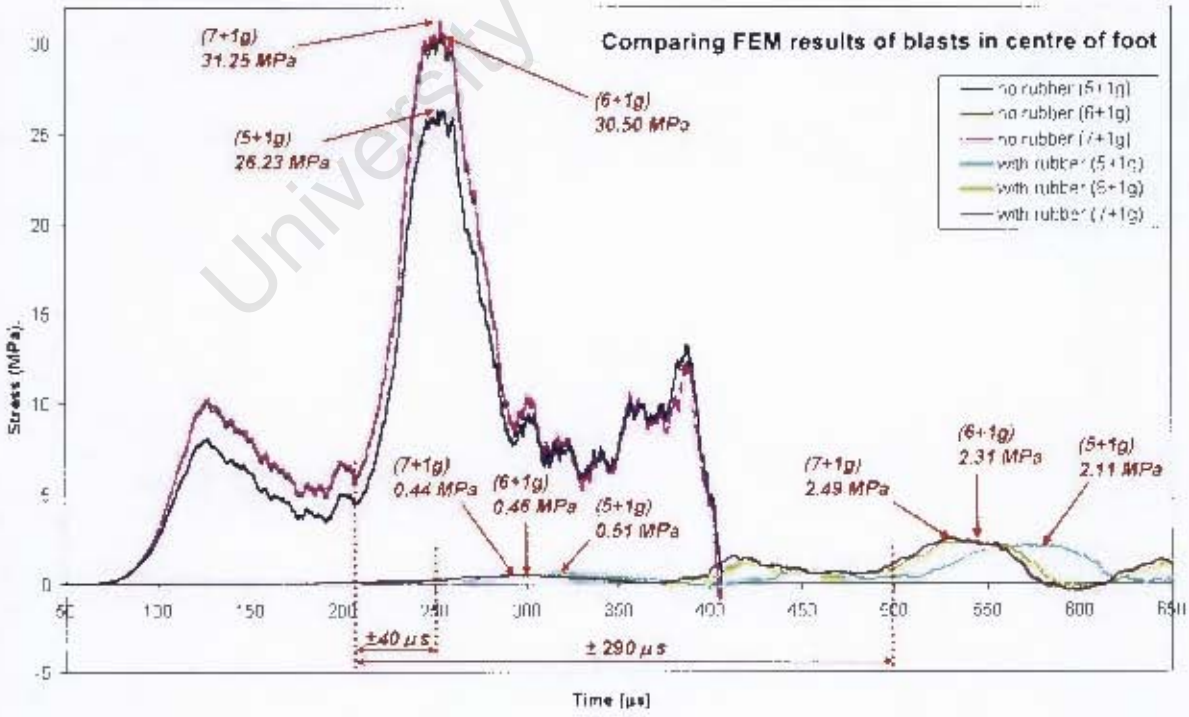

Figure 6.28 - Graph comparing FEM results when excluding and including the rubber sole for blast loading in the centre of the foot

6.12.2 Simulation of blast loading performed at the heel of the foot model

The stress-time results obtained from the finite element simulations of the blast loading applied axially in line with the calcaneous of the foot model, excluding and including the rubber sole, is provided in Figure 6.29. According to the results given in Figure 6.29, introducing the rubber sole layer in the test setup reduced the stress recorded by the "strain gauge" elements by 82% in the simulation of the blast loading performed using 5+1g explosives. It is observed that the onset of reaching the peak stress occurs roughly 160µs later in the case of the loading condition where the rubber sole is included in the test setup than when the rubber sole is excluded

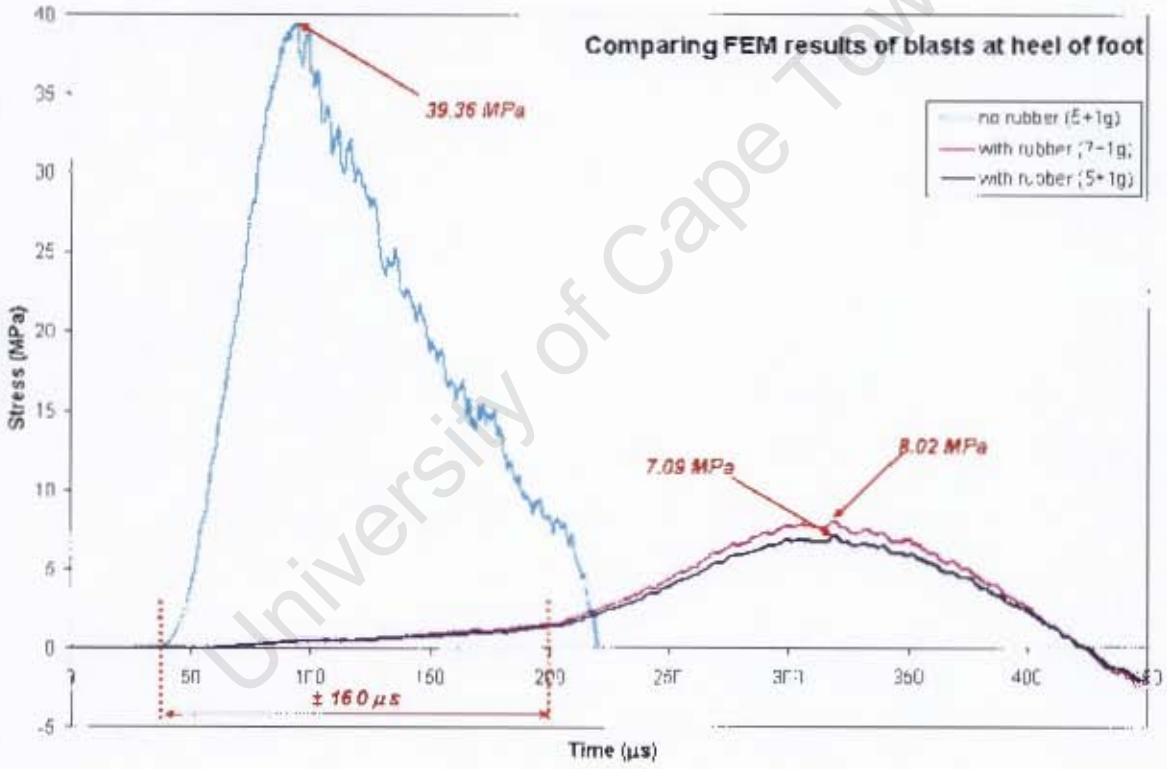

Figure 6.29 - Graph comparing FEM results when excluding and including the rubber sole for blast loading at the heel of the foot

Chapter 7 - Comparison and Discussion of Results

7.1 INTRODUCTION

This section of the dissertation contains the discussions pertaining to the major comparisons drawn while investigating the experimental and numerical results blast test results.

The discussion is divided into four main topics:

- Blast loading performed with the rubber sole excluded – The analytical, experimental and numerical results are compared. The phenomenon of the stress wave propagation along the components of the aluminium surrogate leg is examined. These two matters are discussed for blast loading applied in the centre of the foot and blast loading applied in line with the heel of the foot.
- Blast loading performed with the rubber sole included – The same procedure as mentioned above is followed for blast loading performed when the rubber sole is included in the test setup.
- Attenuation properties of the rubber sole – The reduction in the stress experienced by the aluminium tube and the time delay in the occurrence of the maximum stress in the tibia are examined and compared for blast loading applied in the centre of the foot and at the heel of the foot.
- Comparison with results from previous studies – In order to create a more comprehensive understanding of the results obtained during the blast tests, the results are compared to test results from previous studies where mechanical surrogate lower legs were used.

In essence, this section of the report is designed to set the milieu in which the concluding chapter is founded.

7.2 BLAST LOADING PERFORMED EXCLUDING THE RUBBER SOLE

7.2.1 Blast loading applied in the centre of the foot model

7.2.1.1 Comparing the analytical, experimental and numerical results

The stress-time results obtained during the analytical solution, the experimental blast tests and the numerical simulation of the blast loading of 5+1g PE4 in the centre of the foot model is compared in Figure 7.1. Although the stress curve of the analytical solution plots the stress values as the stress wave propagates through the interfaces of the foot model, the section of the curve from approximately 54μs to 250μs predicts the maximum average stress that can be expected to be transmitted along the tibia. As such, the analytical solution serves as tool to compare and verify the maximum stress recorded by the experimental blast tests and the numerical simulation.

The comparison of the experimental and numerical stress-time results retrieved for blast loading applied in the centre of the foot model using 6+1g PE4 and 7+1g PE4 is presented in Figure 7.2 and Figure 7.3 respectively.

Overall, the shape of the numerical stress-time curve compares well to the general shape of the experimental stress-time curves. In the results for the 5+1g blast, a significant correlation is observed between the numerical curve and the DU_110107a experimental curve, as all the peaks and valleys of the two curves coincide. The DU_090107c stress curve may possess a much smoother nature, but the time at which the maximum stresses are recorded in both the experimental and numerical results corresponds at approximately 250μs. In the results for the 6+1g and 7+1g blasts, the first and second peaks apparent in the numerical representation of the compressive stress curve is distinctly present in the experimental stress curve, although the experimental stress curve gradually slopes off after this point while the numerical curve shows a third peak to arise just before the end of the compressive stress wave.

It is also noticed from Figure 7.1, Figure 7.2 and Figure 7.3 that the experimental and numerical results show a consistency in the total time taken by the compressive stress wave to transmit along the foot model before returning to the strain gauges as a tensile stress wave. The compressive stress wave transmits in an average time span of 390μs.

The maximum stress recorded during every experimental blast test and numerical simulation performed of the centre blast loading is provided in Table 7.1. The percentage average standard deviation between the stress results is also calculated. It is evident from the results in Table 7.1 that the numerical simulations yields an excessive over-prediction of the

maximum stress recorded in the lower region of the aluminium tube. It should be noticed though that a 10.4% standard deviation in maximum stress exists between the two experimental blast test results, which in turn indicates the probability of a significant deviation to exist between the maximum stress values for the 6+1g and 7+1g load conditions. The percentage standard deviation in the maximum stress found during the analytical analysis, the experimental tests and the numerical simulation is calculated to be 18.3% for the 5+1g load condition.

The material properties for the mild steel and aluminium tube are taken from the manufacturer specifications, and the properties for the solid aluminium which the foot and ankle are machined from are experimentally determined. The only material properties of which the accuracy is uncertain are those assigned to the Teflon rig alignment bushes. However, the Teflon rig bushes mainly effect the translation of the tibia but not the amount of stress being transmitted in the tibia. As such, the over-predicted maximum stress values recorded by the "strain gauge" elements during the numerical simulation of the blast tests may be attributed to the following aspects:

- The interaction properties assigned in the finite element model may be inconsistent with the actual interaction occurring between the components of the foot model.
- Interaction of the base of the metatarsals and calcaneous with the detonation plate is important. Full contact between the bottom surfaces of the foot and the detonation plate is assumed in the finite element model, where full contact of these surfaces may not have existed in the experimental blast test setup. The foot model rests in a horizontal position in the horizontal ballistic pendulum. Therefore gravitational loading cannot be relied on in the experimental setup to ensure full contact between the base surfaces of the foot and the detonation plate. Employing a mechanism to keep the base in full contact with the detonation plate would however have impeded the free translation allowed to the foot model.

Blast load	***Analytical Stress*** (MPa)	***Experimental Stress*** (MPa)		***Numerical Stress*** (MPa)	***% standard deviation***
5+1g PE4	*18*	*16.5*	*20.3*	*26.23*	*18.3*
6+1g PE4	~	*20.3*		*30.50*	*20*
7+1g PE4	~	*22.3*		*31.25*	*16.8*

Table 7.1 – Table comparing maximum stress values retrieved from experimental and numerical results for blast loading applied in the centre of the foot, excluding the rubber

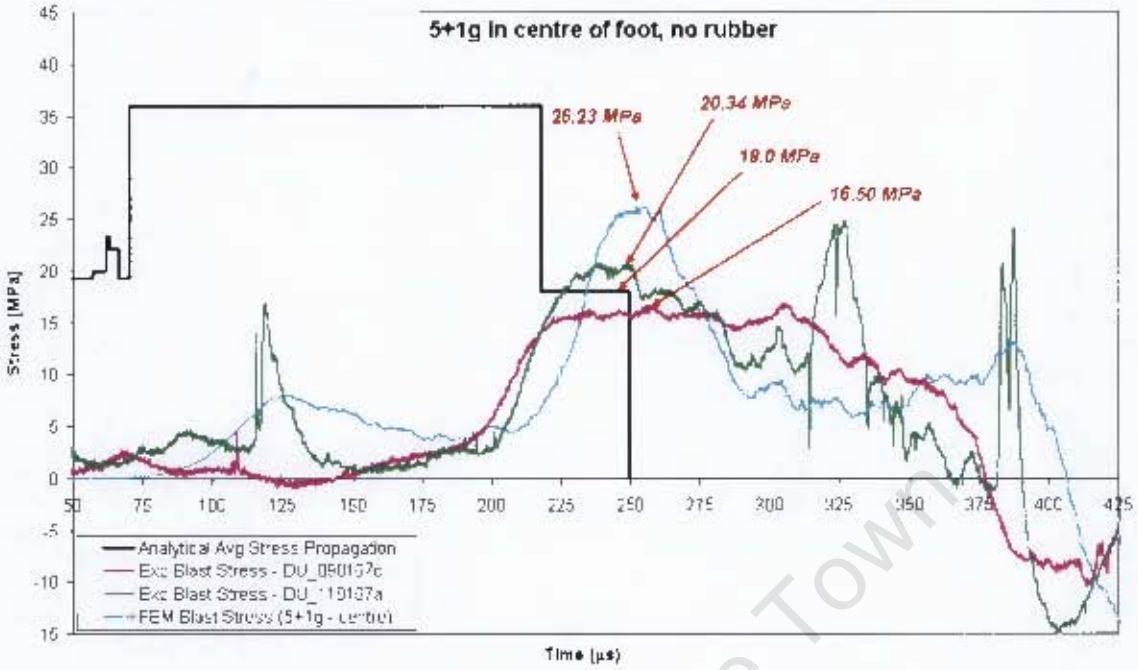

Figure 7.1 – Graph comparing the analytical, experimental and FEM results obtained for applying blast loading in the centre of the foot, excluding the rubber, using 5+1g explosives

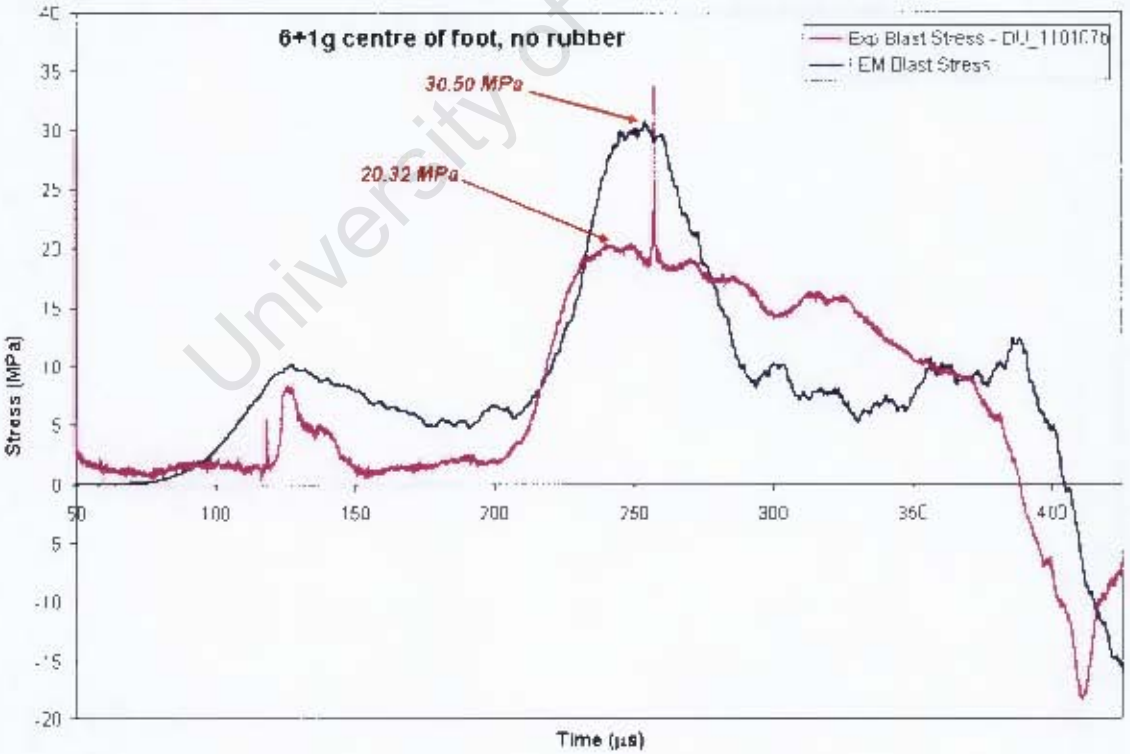

Figure 7.2 – Graph comparing the experimental and FEM results obtained for applying the blast load in the centre of the foot, excluding the rubber, using 6+1g explosives

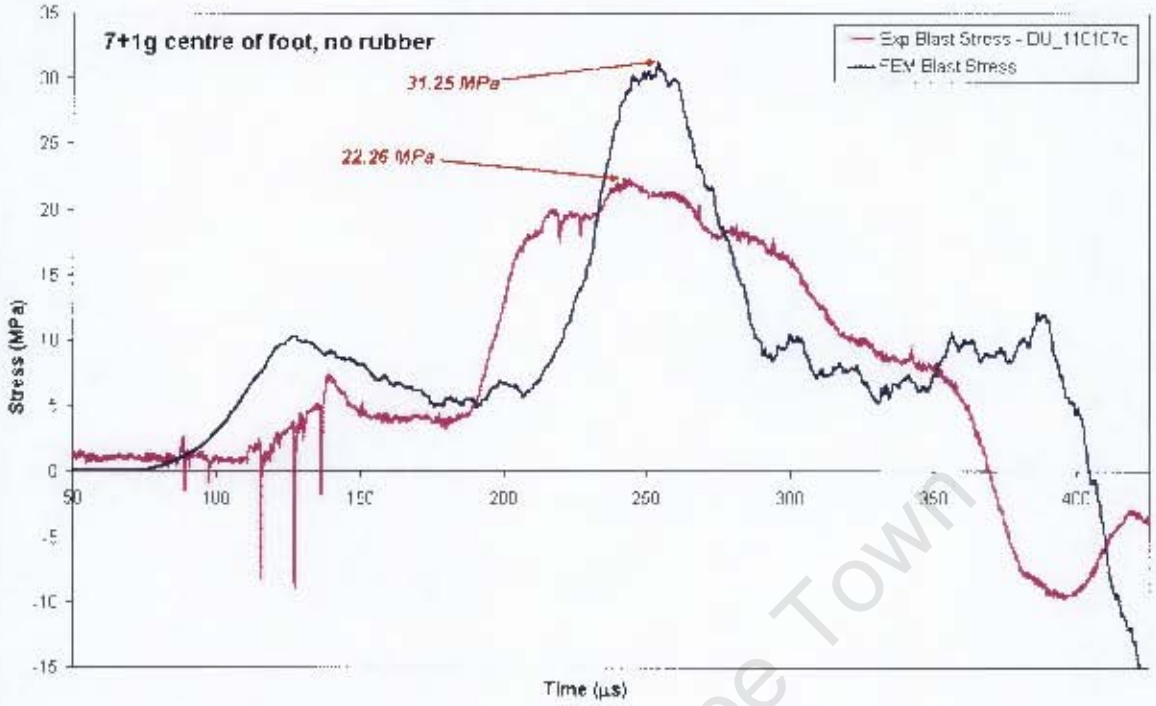

Figure 7.3 - Graph comparing the experimental and FEM results obtained for applying the blast load in the centre of the foot, excluding the rubber, using 7+1g explosives

7.2.1.2 Investigation of stress wave propagation through the foot model

According to the simplified analytical model of the blast load applied to the foot setup, the stress wave is expected to transmit through the foot and tibia and reflect back to the strain gauges in approximately 250µs. However, it is evident from the experimental and numerical results that the compressive stress wave transmits approximately 140µs longer. In an attempt to explain the extended time period as well as the multiple peaks present in the stress curve, it is decided to scrutinize the finite element simulation of the blast event.

Output files displaying the stress distribution in the finite element model are generated at specific intervals throughout the numerical simulation. Screen shots of a selection of the output files are presented in chronological order in Table 7.2 in order to illustrate the stress propagation through the foot model during the blast event. The stress output files corresponding to the main events in the stress curve (i.e. the peaks and the valleys of the stress curve) are then displayed on an enlarged version of the stress-time graph (Figure 7.5) in order to enhance visual understanding of the meaning of the stress-time graph.

From Table 7.2 and Figure 7.5 it is observed that the first peak in the stress curve relates to stress propagating via the calcaneous of the foot, the second peak relates to stress

propagating via the metatarsals of the foot and the third peak again relates to stress propagating via the calcaneous. As such, three main events are identified:

- Initially the stress wave caused by the detonation of the explosives in the centre of the detonation plate arrives at the same time at both the calcaneous and the metatarsal surfaces. However, the distance to the strain gauges on the tibia is shorter from the calcaneous than from the metatarsals. Although the stress wave starts to transmit from the metatarsals along the foot bridge, the upward motion of the calcaneous causes the metatarsals to be pushed down on the detonation plate.
- Forcing the metatarsals down on the detonation plate in turn causes a superimposed stress wave to be reflected back through the metatarsals. The magnified stress wave travels from the metatarsal surface along the foot bridge, through the ankle joint and rejoins the calcaneous stress wave in the tibia, inducing the maximum stress in the tibia.
- The stress wave now transmits back down through the ankle joint, but the portion of the stress wave travelling via the calcaneous reaches the detonation plate prior to the portion travelling via the metatarsals. The reflection of the stress wave through the calcaneous surface is deemed to cause the third peak in the stress curve.

Modifying the analytical model to simulate the events described above in a simplified manner yielded the results shown in Figure 7.4. The extended duration of the stress transmission is also explained hereby, as the occurrence of a second stress wave reflecting to the end of the tibia and back through the strain gauges is evident, which in turn would add an extra approximately 160µs to the transmission duration.

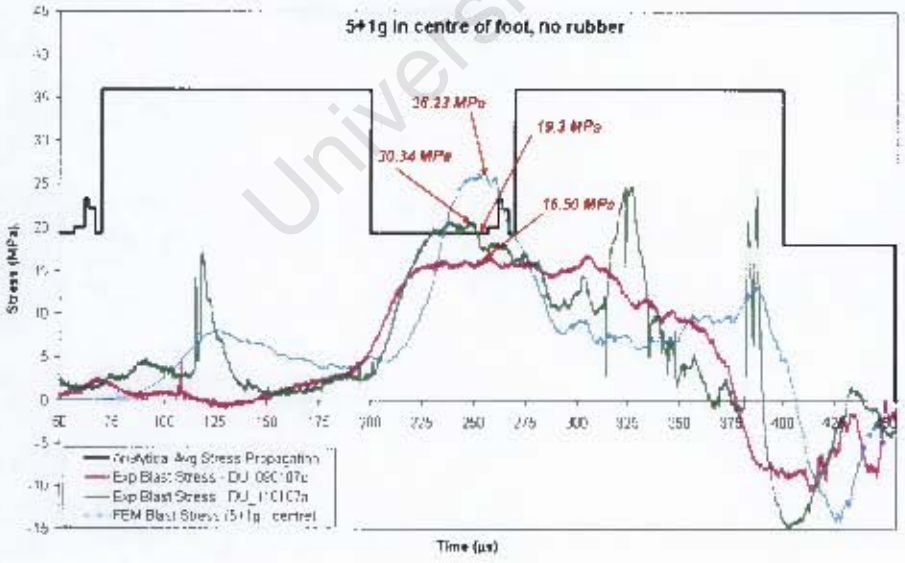

Figure 7.4 - Graph showing the comparison between the experimental, FEM and modified analytical results for the blast loading applied in the centre of the foot, excluding the rubber, using 5+1g explosives

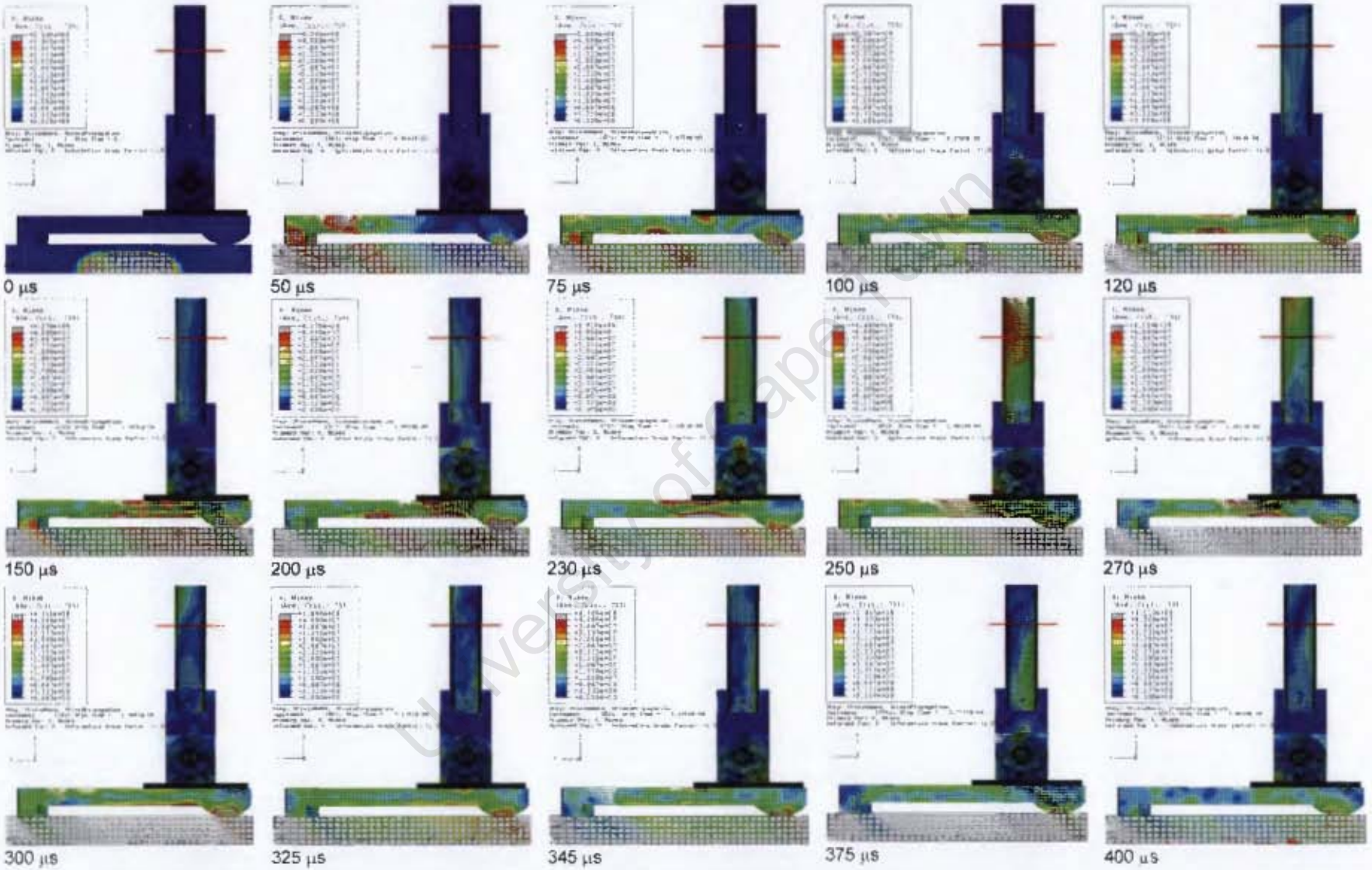

Table 7.2 – Table illustrating the stress propagation caused by a blast in the centre of the foot with the rubber sole excluded

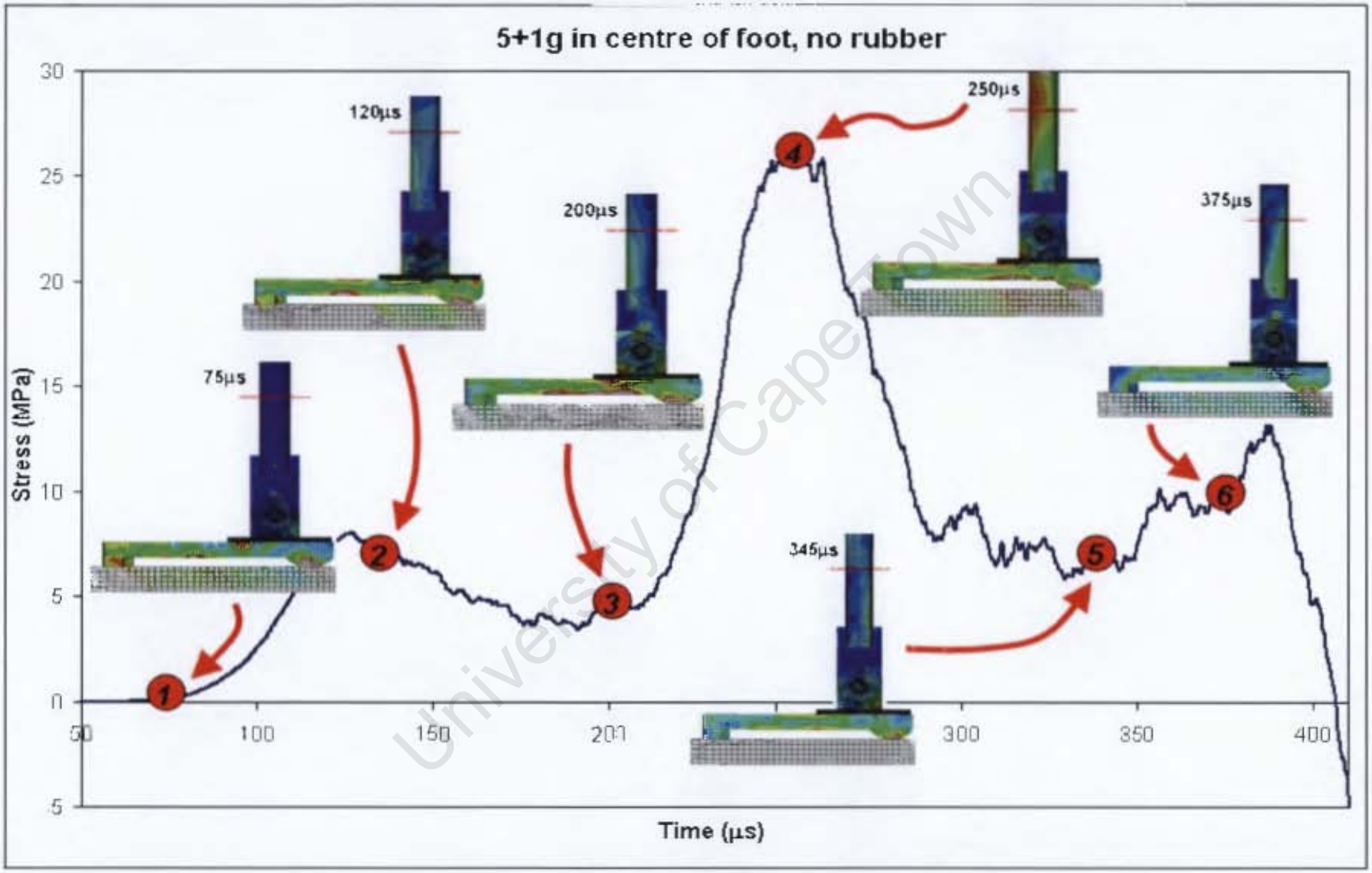

Figure 7.5 - Graphical representation of the stress propagation of the centre blast with the rubber sole excluded

7.2.2 Blast loading applied axially in line with the calcaneous of the foot model

7.2.2.1 Comparing the analytical, experimental and numerical results

The analytical, experimental and numerical stress-time results obtained for the blast loading of 5+1g PE4 positioned axially in line with the calcaneous of the foot model is compared in Figure 7.6. The results from the analytical stress propagation analysis is included to serve as an indication of the expected maximum stress to be experienced in the aluminium tube.

It is seen in Figure 7.6 that the results from the finite element simulation correlate well with the stress results obtained from the experimental blast tests. The shape of the experimental and numerical stress curves agrees well, with the maximum stresses in each curve occurring at essentially the same time (approximately 90μs). The duration of the compressive stress transmission through the foot complex and the tibia as observed for the experimental and numerical results also coincides, where the compressive stress wave changes into a tensile stress wave after approximately 225μs. The transmission duration of roughly 225μs is close to the expected duration of 265μs predicted by the analytical model.

The values of the maximum stress experienced by the aluminium tube during the blast event as recorded in the experimental blast tests and the numerical simulation are given in Table 7.3. The percentage standard deviation between the analytical, experimental and numerical stress results is calculated to be 12.7%. Once again it is noticed that the numerical simulation of the blast event yields a substantially over-predicted result for the maximum stress in the tube; however the percentage deviation between the analytical, experimental and numerical maximum stress is 6% lower than the percentage deviation observed for blast loading in the centre of the foot.

The over-prediction by the numerical simulation of the blast event can also be associated with the probable causes discussed previously in Section 7.2.1.1.

Blast load	***Analytical Stress*** (MPa)	***Experimental Stress*** (MPa)		***Numerical Stress*** (MPa)	***% standard deviation***
5+1g PE4	*36*	*27.7*	*32.7*	*39.36*	*12.7*

Table 7.3 - Table comparing maximum stress values retrieved from experimental and numerical results for blast loading applied at the heel of the foot, excluding the rubber

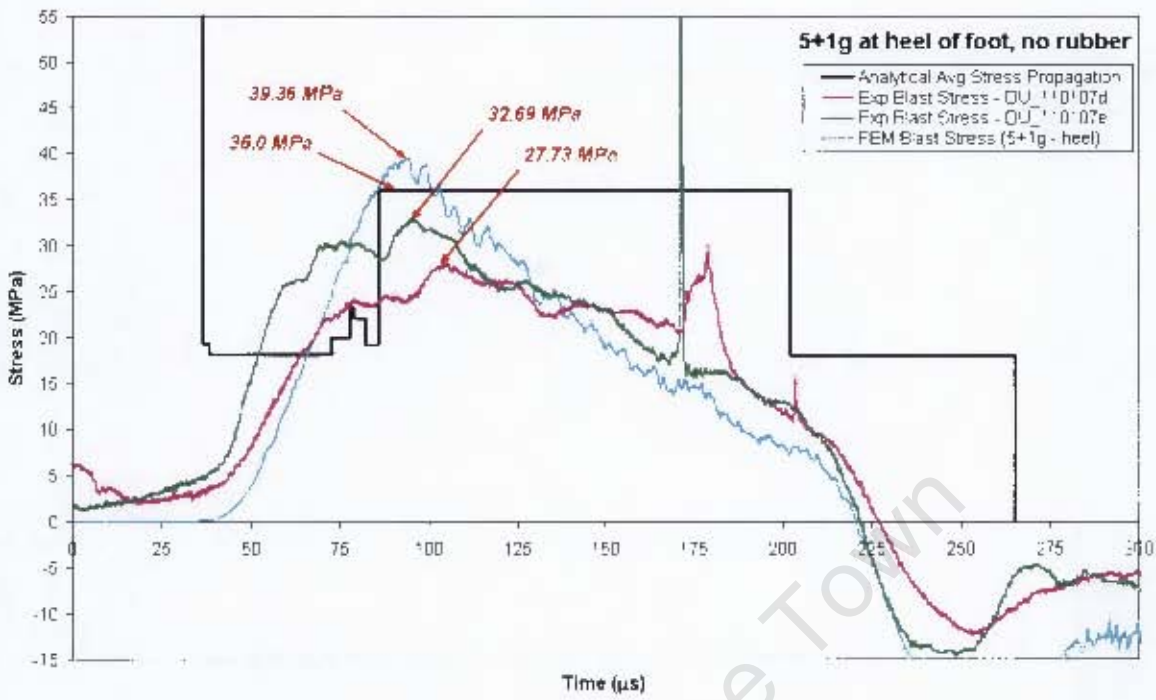

Figure 7.6 - Graph comparing the analytical, experimental and FEM results obtained for applying blast loading at the heel of the foot, excluding the rubber, using 5+1g explosives

7.2.2.2 Investigation of the stress wave propagation through the foot model

Applying a blast load axially in line with the heel of the foot induces a clearly defined and comprehensible stress curve. It is however still interesting to study the means of the stress wave propagation.

As shown in the analytical solution in Section 4.3.2, blast loading at the heel results in the stress wave to be mainly transmitted via the calcaneous region of the foot. The portion of the stress wave that transmits via the metatarsals joins the initial portion of the stress wave in the tibia, amplifying the stress in the tibia into attaining a peak value. This process is illustrated in Table 7.4 by means of a series of screen shots taken from the stress output files generated during the numerical simulation of the blast loading of 5+1g explosives positioned at the heel of the foot model. A selection of these screen shots that correspond to the initiation, rise, peak and decay of the stress wave propagation are also depicted in an enlarged version of the numerical stress curve (Figure 7.7).

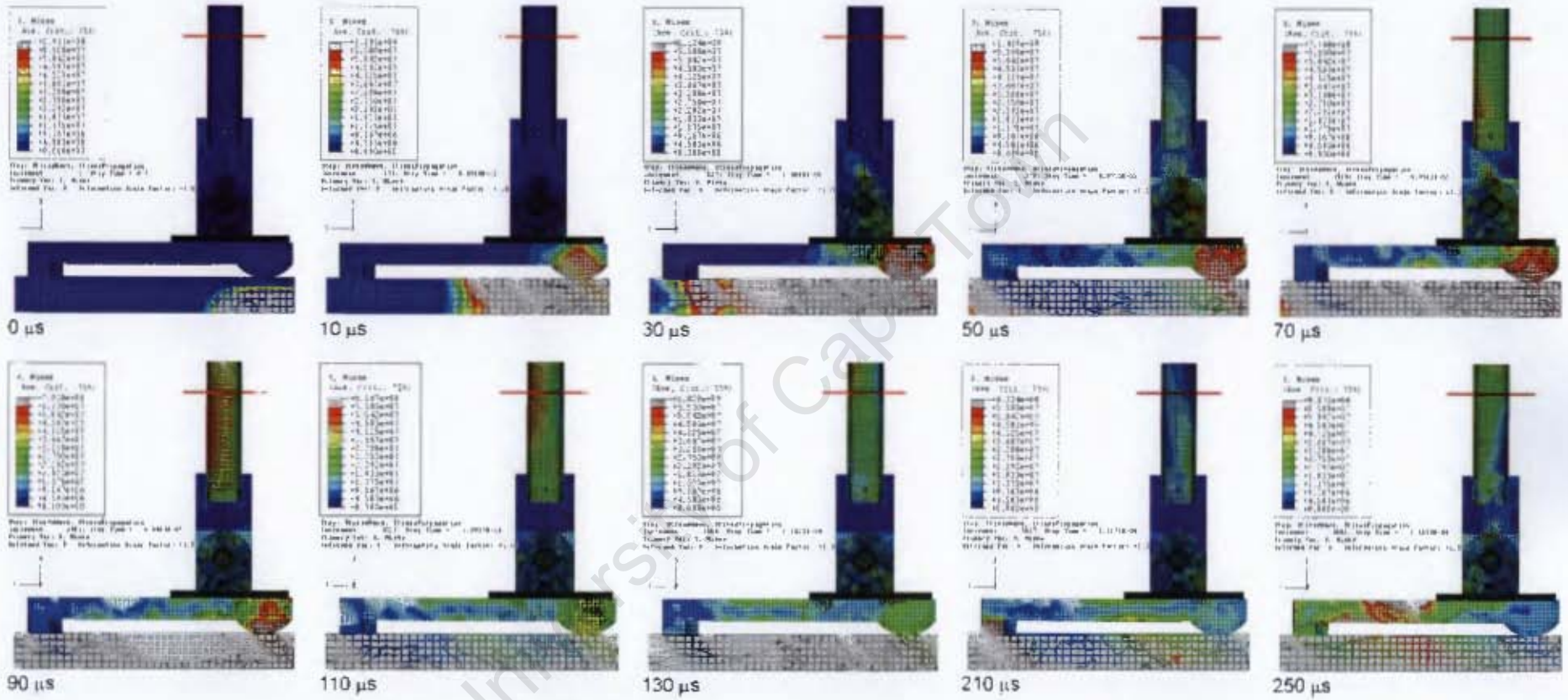

Table 7.4 - Stress propagation caused by a blast at the heel of the foot with the rubber sole excluded

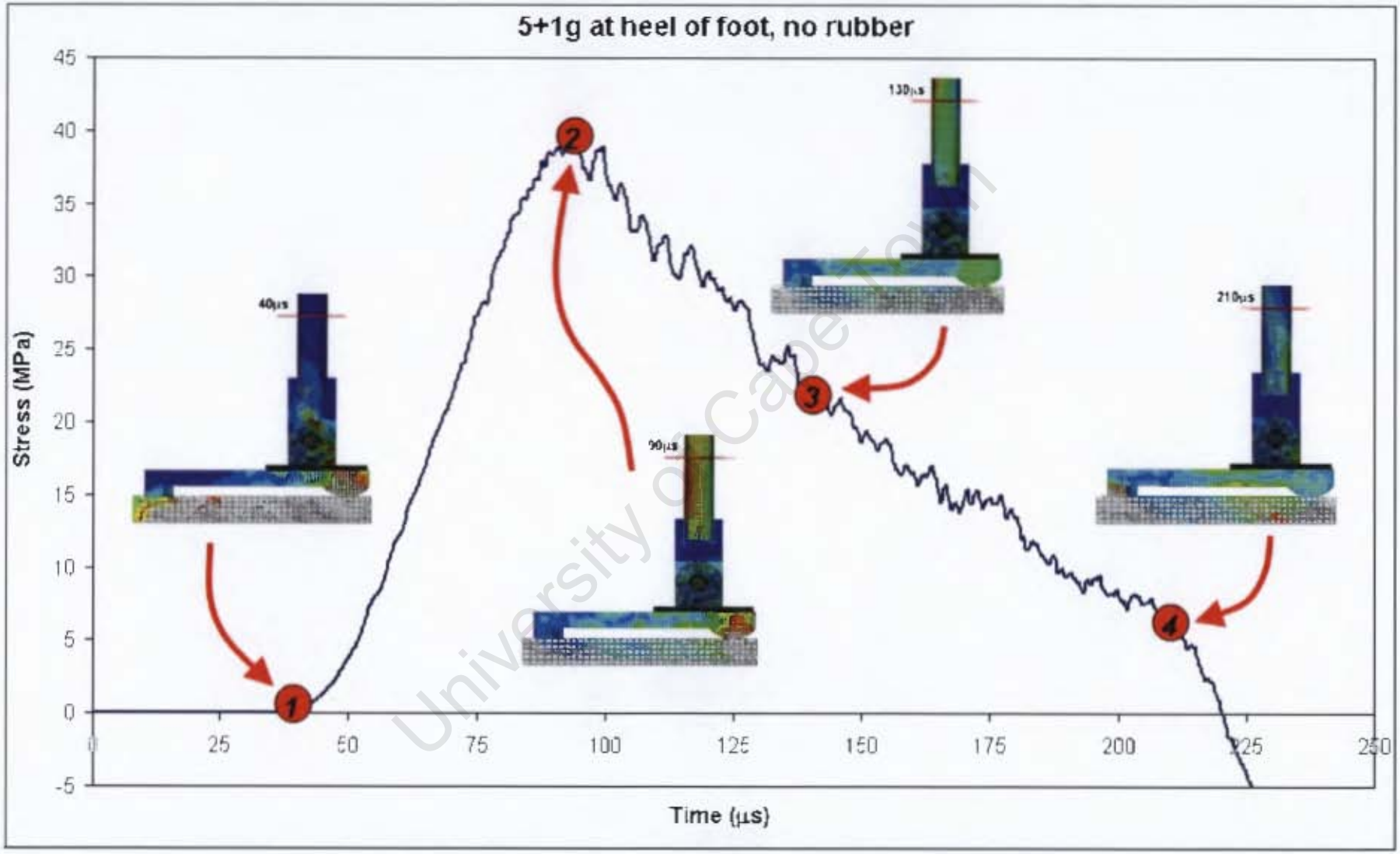

Figure 7.7 - Graphical representation of the stress propagation of the heel blast with the rubber sole excluded

7.3 BLAST LOADING PERFORMED INCLUDING THE RUBBER SOLE

7.3.1 Centre blast loading

7.3.1.1 Comparing the analytical, experimental and numerical results

The stress-time results obtained during the analytical solution, the experimental blast tests and the finite element simulation for blast loading of 5+1g explosives applied in the centre of the foot with the rubber sole included are compared in Figure 7.8. The analytical stress curve representing the stress propagation through the foot model is included to compare and verify the maximum stress values obtained from the experimental and numerical stress-time curves.

The comparison of the experimental and the numerical stress-time curves for the blast loading using 6+1g PE4 and 7+1g PE4 are presented in Figure 7.9 and Figure 7.10 respectively.

From the stress curves plotted in Figure 7.8, Figure 7.9 and Figure 7.10 it is evident that although the specific shape of the curves do not agree, the general trend of the stress curve generated during the numerical simulation follows a similar trend as displayed by the experimental stress curve. Also, the peaks of the initial and secondary compressive stress transmissions observed in the numerical stress curve coincide reasonably well with the two peaks observed in the experimental stress curve. The peak of the initial compressive stress wave occurs at approximately 310μs and the peak of the secondary compressive stress wave occurs at approximately 575μs.

The magnitude of the maximum stress values corresponding to the two compressive peaks retrieved from the experimental and numerical stress curves are compared in Table 7.5. The percentage by which the numerical results vary from the experimental results is also calculated for each blast load. The results provided in Table 7.5 indicates an excessive under-prediction supplied by the finite element analyses of the blast loading applied in the centre of the foot when the rubber sole is included in the test setup. Over-prediction is generally favourable when designing against failure; hence obtaining an under-prediction of up to 75% is discouraging.

In the previous section it is observed that results from the numerical simulations of the blast events yielded over-predicted maximum stress values, which means the major problem originates in the inclusion of the rubber sole in the numerical model. A range of difficulties related to the finite element modelling of the rubber sole exist, and all of them may have contributed to the atrocious results obtained from the numerical simulations of the blast

loading performed with the rubber sole included. The main problem areas related to the numerical modelling of the rubber sole are the following:

- Firstly, as discussed in Section 6.2.6, the exact geometry of the rubber boot sole is not defined. This in itself causes a big problem, as the area that is in contact with the detonation plate cannot be accurately defined in the finite element model. The amount of stress transmitted across each interface relies on the area ratio of the surfaces in contact. As such, the amount of stress transmitting across the surfaces of the rubber sole in contact with the detonation plate cannot be accurately modelled in the finite element model.
- The contact properties existing between the rubber surface and the mild steel and between the rubber surface and the aluminium surfaces are debatable.
- The compressive strain rate induced upon the rubber material during the blast event is not known, causing uncertainty as to which strain rate data should be used in the construction of the rubber material model. In this investigation, dynamic compression tests at strain rates up to $2500s^{-1}$ were performed on the rubber using the Split-Hopkinson Pressure Bar. Therefore the stress-strain data obtained from the $2500s^{-1}$ strain rate SHPB tests are used in the construction of the rubber material model.
- Only four strain energy potentials are investigated in the construction of the rubber material model, which lead to the conclusion that employing the Ogden (with n=3) or the polynomial (with n=2) strain energy potentials yields the optimum results. Although the other strain energy potentials available in the ABAQUS database seem unfavourable for the present application, it may prove useful to study their response as well as part of a more detailed project in the future.

	Initial peak compressive stress				***Secondary peak compressive stress***			
Blast load	***Analytical*** (MPa)	***Exp*** (MPa)	***FEM*** (MPa)	***% std. dev.***	***Analytical*** (MPa)	***Exp*** (MPa)	***FEM*** (MPa)	***% std. dev.***
5+1g PE4	*3.8*	*4.2*	*0.51*	*58.2*	*5.6*	*5.4*	*2.11*	*36.7*
6+1g PE4	~	*2.4*	*0.46*	*67.4*	~	*4.9*	*2.31*	*35.9*
7+1g PE4	~	*3.4*	*0.44*	*77.1*	~	*10*	*2.49*	*60.2*

Table 7.5 - Table comparing maximum stress values retrieved from experimental and numerical results for blast loading applied in the centre of the foot, including the rubber

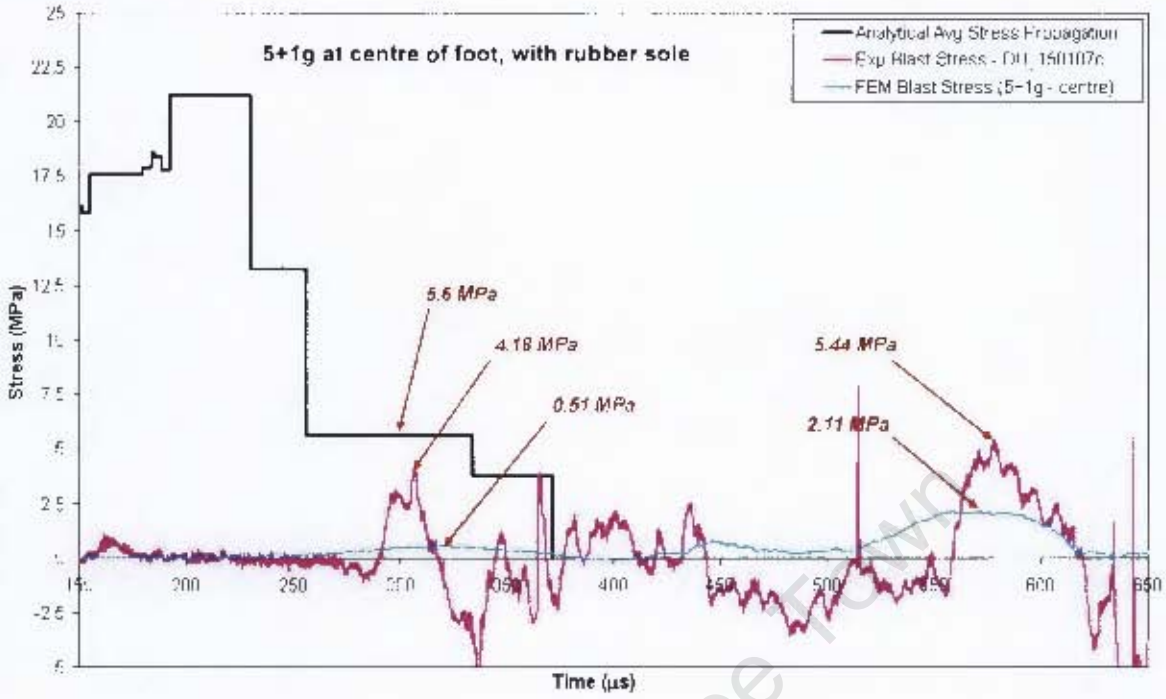

Figure 7.8 - Graph comparing the analytical, experimental and FEM results obtained for applying blast loading in the centre of the foot, including the rubber, using 5+1g explosives

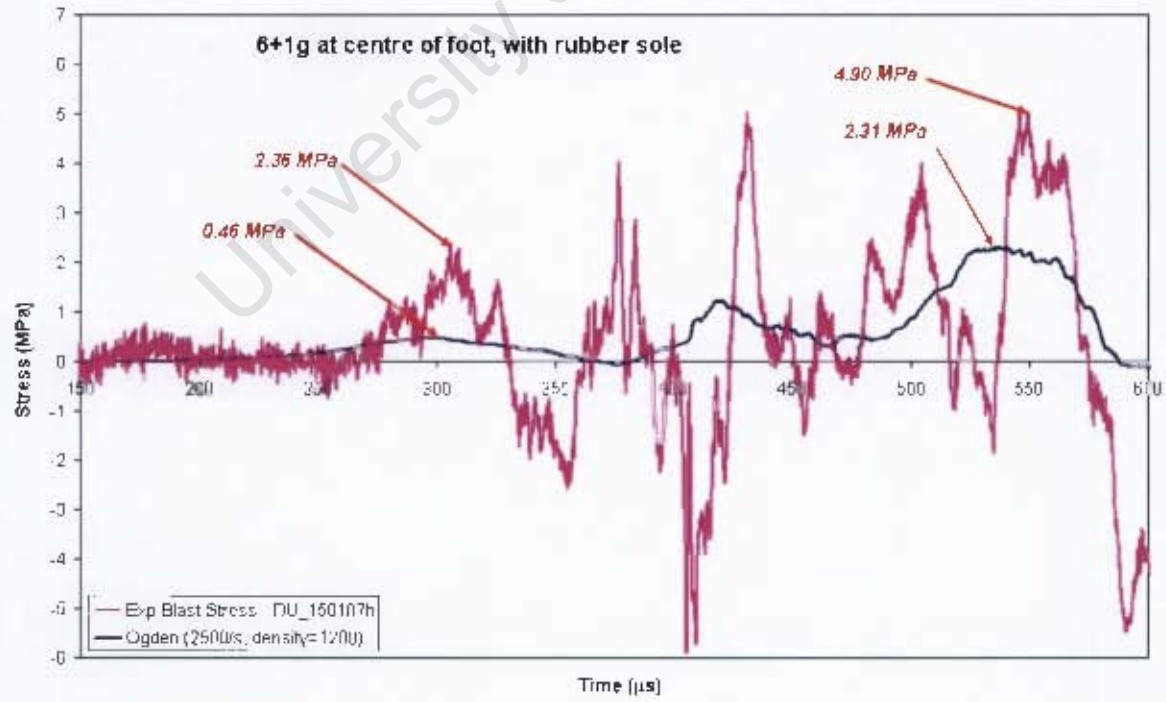

Figure 7.9 - Graph comparing the experimental and FEM results obtained for applying the blast load in the centre of the foot, including the rubber, using 6+1g explosives

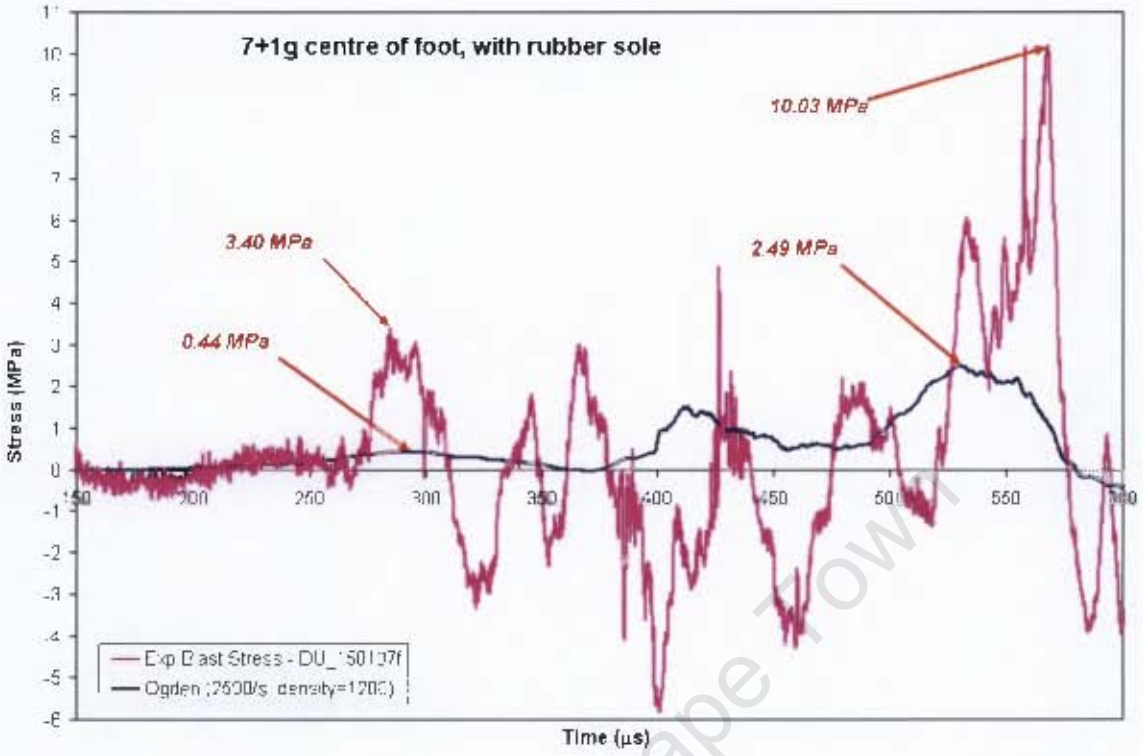

Figure 7.10 - Graph comparing the experimental and FEM results obtained for applying the blast load in the centre of the foot, excluding the rubber, using 7+1g explosives

7.3.1.2 Investigation of the stress wave propagation through the foot and rubber sole

The two compressive stress waves following one another in short succession calls for an explanation. In order to aid the investigation, the numerical simulation is once again scrutinised. Even though the stress results from the numerical simulations are not successful, the trend of the stress curve remains similar to that of the experimental stress curve, which means the reason or cause of the successive compressive stress waves can still be determined.

Fifteen screen shots from the stress output files generated during the finite element analysis are displayed in series in Table 7.6 in an attempt to depict the course of the stress propagation through the rubber sole, foot complex and tibia. Six of the screen shots are strategically selected and used in an enlarged version of the numerical stress curve in order to assist the reader visually in understanding the stress propagation (Figure 7.12).

- The first compressive stress curve originates from the stress wave travelling through the foot components as per usual, with only a small magnitude of stress propagating up and down the aluminium tube. It appears that the rubber layer acts as a dashpot,

damping the amount of stress being transmitted, and in turn sending a reflected wave back towards the detonation plate.

- The second compressive stress curve is initiated by two events occurring in the same time span. After the initial compressive stress wave returned past the strain gauges in the aluminium tube, the compressive stress wave becomes a tensile stress wave. However before the tensile stress wave could be transmitted in its totality, the energy absorbed by the rubber layer is now being dissipated with the rubber acting as a spring. The reflected wave from the initial compressive stress wave also starts to propagate forward through the foot components. These two events cause an enhanced compressive stress wave to be transmitted through the foot complex and tibia. It is noticed that the shape of the secondary enhanced compressive stress curve exhibits similarity to the shape of the compressive stress curve produced during the blast load applied in the centre of the foot with the rubber sole excluded from the test setup, implying that the stress wave follows the same propagation pattern which is expected.

A simplified analytical model is generated to attempt to model the events described above and the result is shown in Figure 7.11. A closer relationship between the maximum stress values from the analytical and experimental stress results is observed (also documented in Table 7.5).

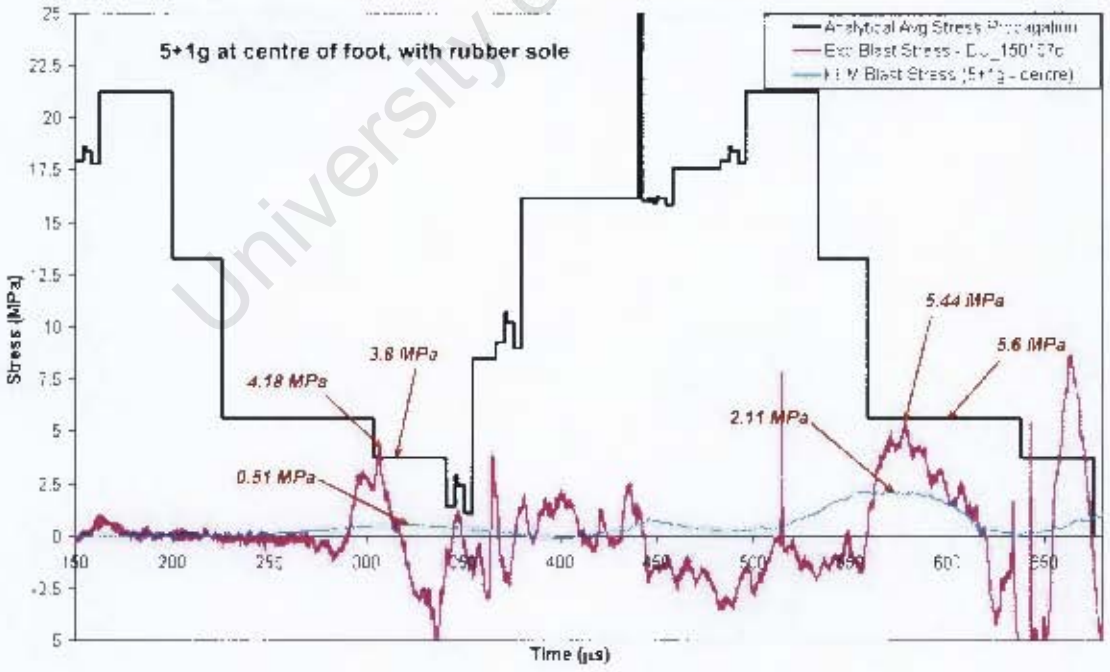

Figure 7.11 - Graph showing the comparison between the experimental, FEM and modified analytical results for the blast loading applied in the centre of the foot, including the rubber, using 5+1g explosives

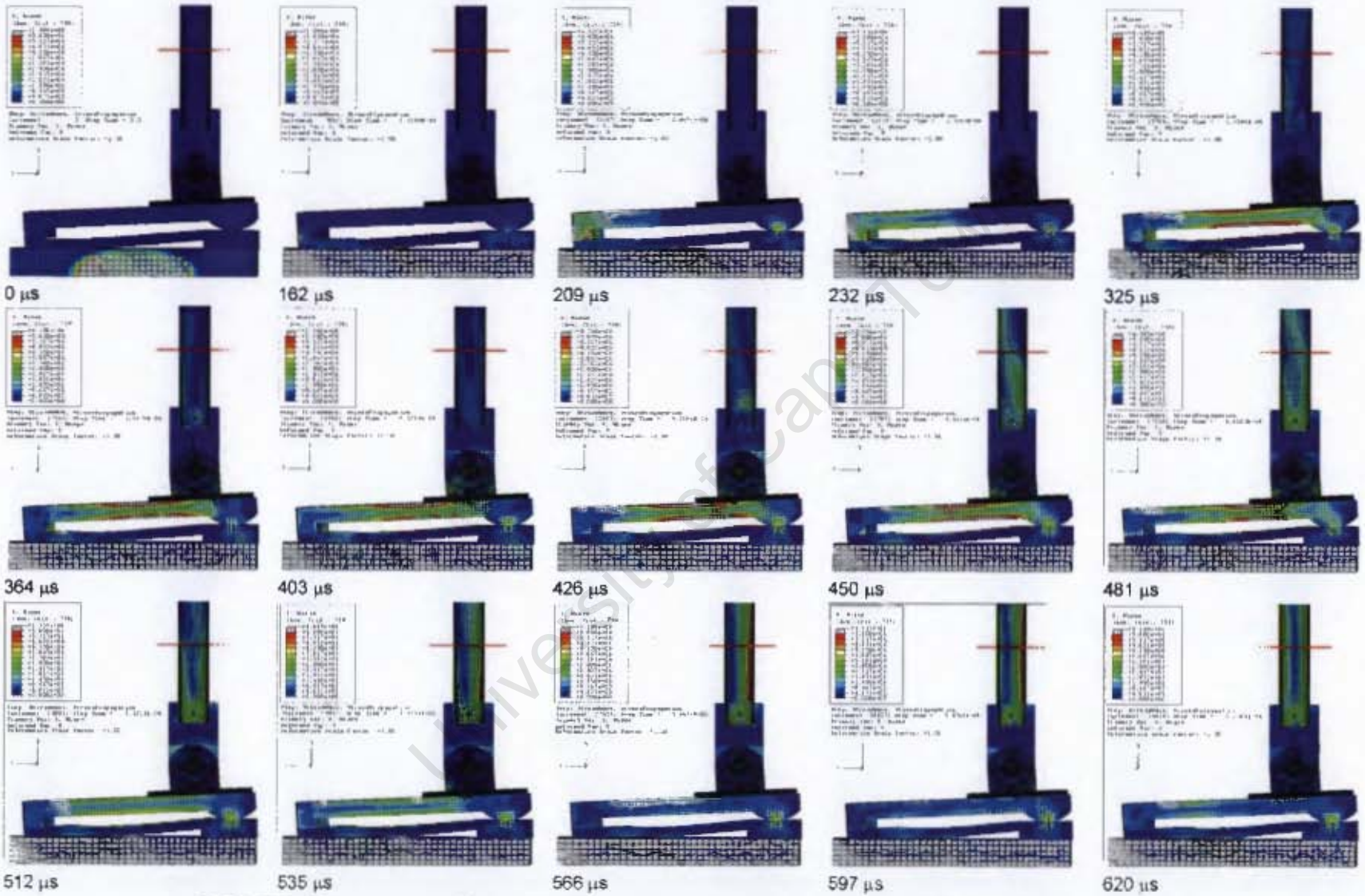

Table 7.8 - Stress propagation caused by a blast in the centre of the foot with the rubber sole included

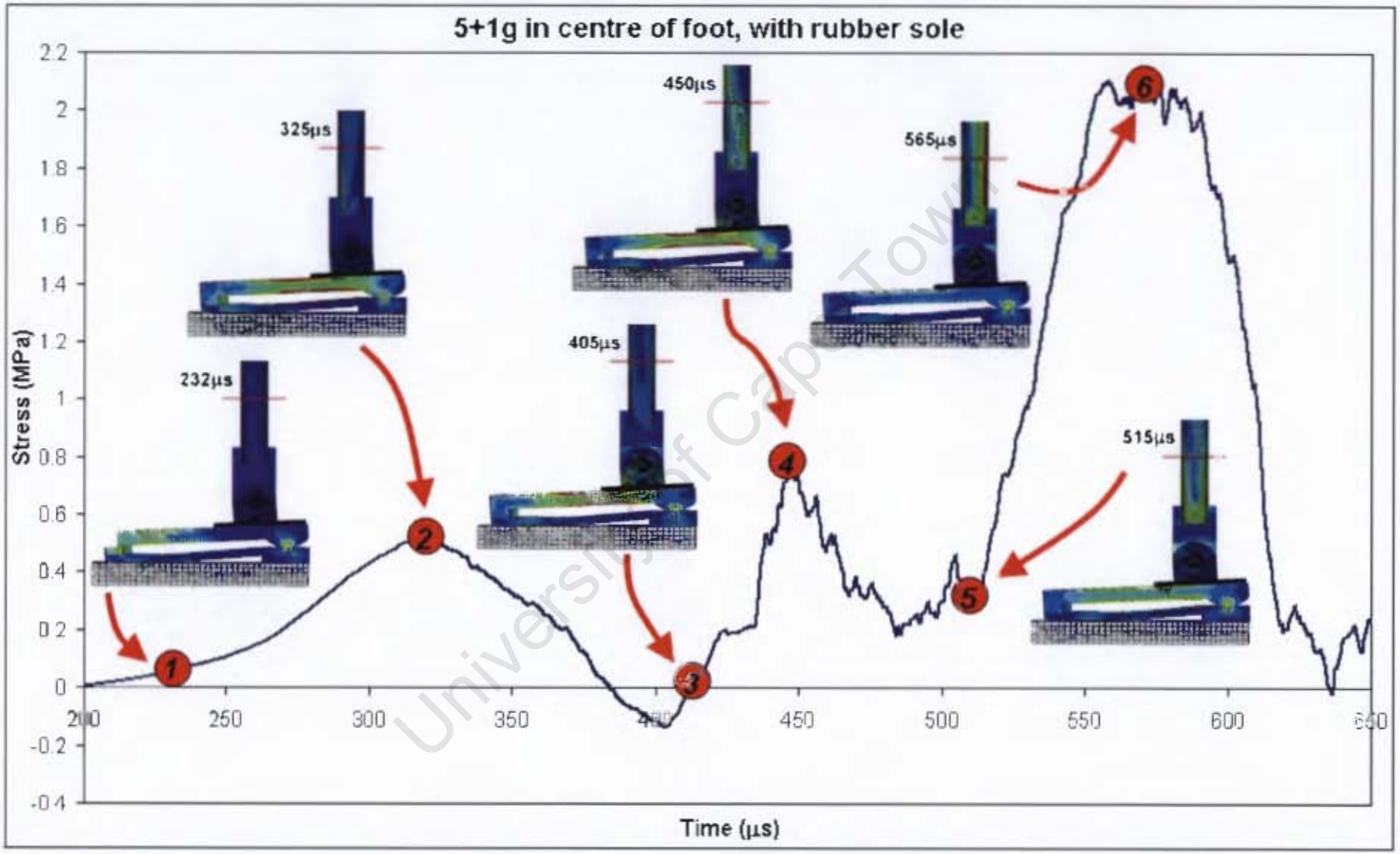

Figure 7.12 - Graphical representation of the stress propagation of the centre blast with the rubber sole included

7.3.2 Heel blast loading

7.3.2.1 Comparing the analytical, experimental and numerical results

Figure 7.13 contains the comparison of the stress-time results obtained in performing the analytical solution, the experimental blast test and the finite element simulation for blast loading using 5+1g PE4 positioned at the heel of the foot model with the rubber sole included in the test setup. Once again, the propagation of the stress through the foot components as produced by the analytical solution is included in Figure 7.13 to compare and verify the maximum stress values generated by the experimental tests and the numerical simulations.

The comparison of the experimental blast test and the numerical simulation performed for detonating 7+1g PE4 in line with the calcaneous of the foot model is provided in Figure 7.14.

As noted in the results of the blast loading applied in the centre of the foot model where the rubber sole is included, the shape of the numerical stress curve does not correlate well with the experimental stress curve. However, the general trend of the two stress curves essentially agrees when comparing the initiation of the stress increase, the stress peak and the stress decay. The time at which the maximum stress occurs in the experimental and numerical stress coincides at approximately 300μs.

The magnitude of the maximum stresses observed in the blast tests performed using 5+1g and 7+1g explosives are compared in Table 7.7. The percentage difference between the maximum stress experienced in the tibia during the experimental blast tests and the numerical simulations are also provided in Table 7.7. The analytical, experimental and numerical maximum stress results obtained for blast testing performed using 5+1g PE4 compares well, with a standard deviation of 9.7% existing between the values. Conversely, the deviation between the experimental and finite element simulation results for the blast test using 7+1g explosives is 35%. It must be noted though that the experimental maximum stress value for the 7+1g blast test is much lower than the experimental maximum stress value for the 5+1g blast test, which is not consistent as the higher explosive load should lead to a higher maximum induced stress.

Blast load	***Analytical Stress*** (MPa)	***Experimental Stress*** (MPa)	***Numerical Stress*** (MPa)	***% std.dev.***
5+1g PE4	*5.6*	*6.6*	*7.09*	*9.7*
7+1g PE4	~	*3.8*	*8.02*	*35.8*

Table 7.7 - Table comparing maximum stress values retrieved from experimental and numerical results for blast loading applied at the heel of the foot, including the rubber

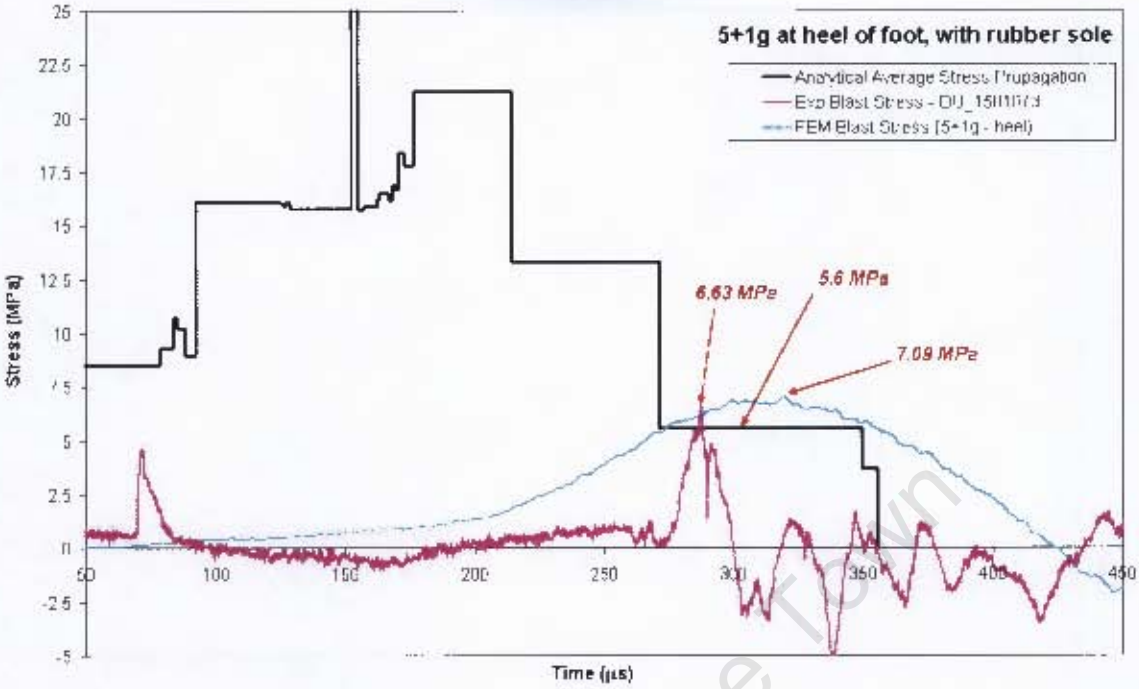

Figure 7.13 - Graph comparing the analytical, experimental and FEM results obtained for applying blast loading at the heel of the foot, including the rubber, using 5+1g explosives

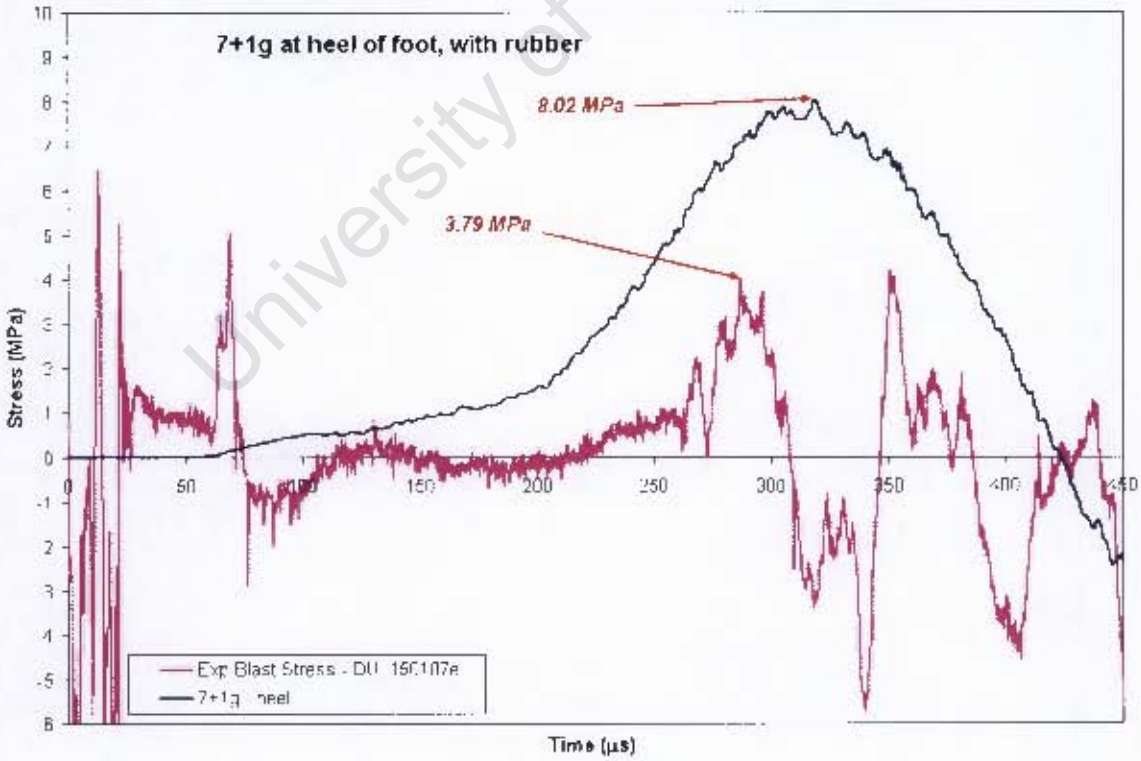

Figure 7.14 - Graph comparing the experimental and FEM results obtained for applying the blast load at the heel of the foot, including the rubber, using 7+1g explosives

Taking note of the good approximation of the maximum stress magnitude produced by the numerical simulations of the blast loading applied at the heel with the rubber sole included in the setup, implies that the problem in the simulations with the blast loading applied in the centre of the foot lies in the modelling of the toe section (and possibly the mid-section) of the rubber sole. This observation is consistent with the difficulties of modelling the rubber sole as discussed in Section 7.3.1.1. As the contact area for the toe section of the rubber sole is not precisely defined, the accuracy of modelling the stress propagation through the toe section is compromised.

7.3.2.2 Investigation of the stress wave propagation through the foot and rubber sole

Blast loading at the calcaneous of the foot model with the rubber sole included results in a stress curve of similar shape to the stress curve obtained for blast loading at the calcaneous with the rubber sole excluded from the test setup. This observation is expected, as the main portion of the stress wave travels via the calcaneous during heel blast loading conditions, whether a rubber sole is included or not.

The only difference in the stress curve when the rubber layer is included is the slow rise in stress until roughly 200μs. The duration of this plateau region in the stress curve is approximately 150μs, which corresponds to a single stress wave propagating along the foot components towards the end of the aluminium tube and back down the tibia towards the strain gauges. This observation compares well to the phenomenon of the initial compressive stress wave noticed when applying the blast load in the centre of the foot with the rubber sole included.

The slow rise in the stress curve can therefore be attributed to the compressive stress wave travelling along the foot components as per usual, with the rubber sole acting as a dashpot, damping the amount of stress being transmitted. The stress wave reflected back towards the detonation plate in this time then starts to propagate along the foot components. At the same time, the heel section of the rubber sole starts to dissipate the built-up energy, inducing an enhanced compressive stress wave to propagate along the aluminium tube and back down past the strain gauges.

The events discussed above is visually described as a series of screen shots taken from the stress output files generated during the numerical simulation of the blast loading applied at the heel of the foot model with the rubber sole included, using 5+1g PE4. Table 7.15 and Figure 7.16 contain a selection of the screen shots, demonstrating the stress propagation through the foot model during the blast event.

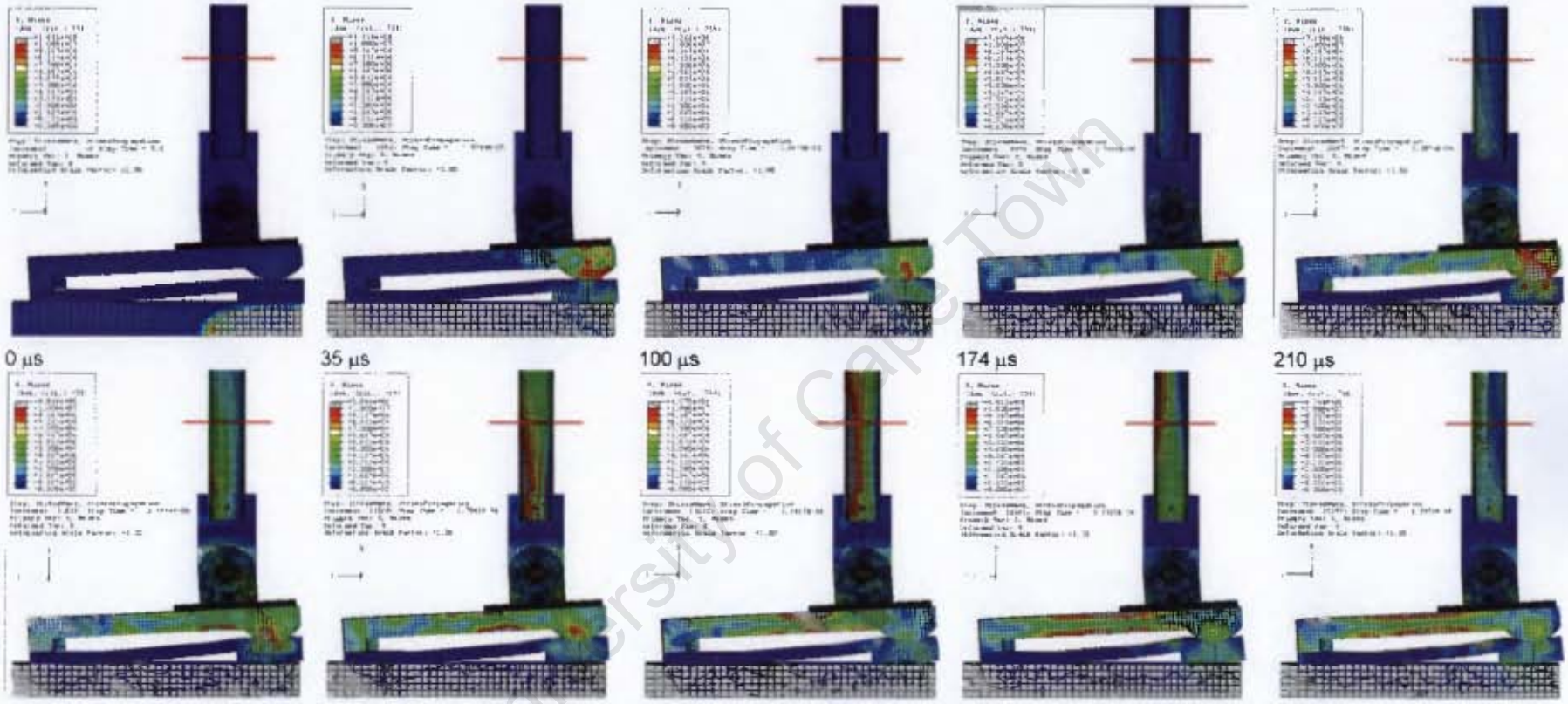

Figure 7.15 - Stress propagation caused by a blast at the heel of the foot with the rubber sole included

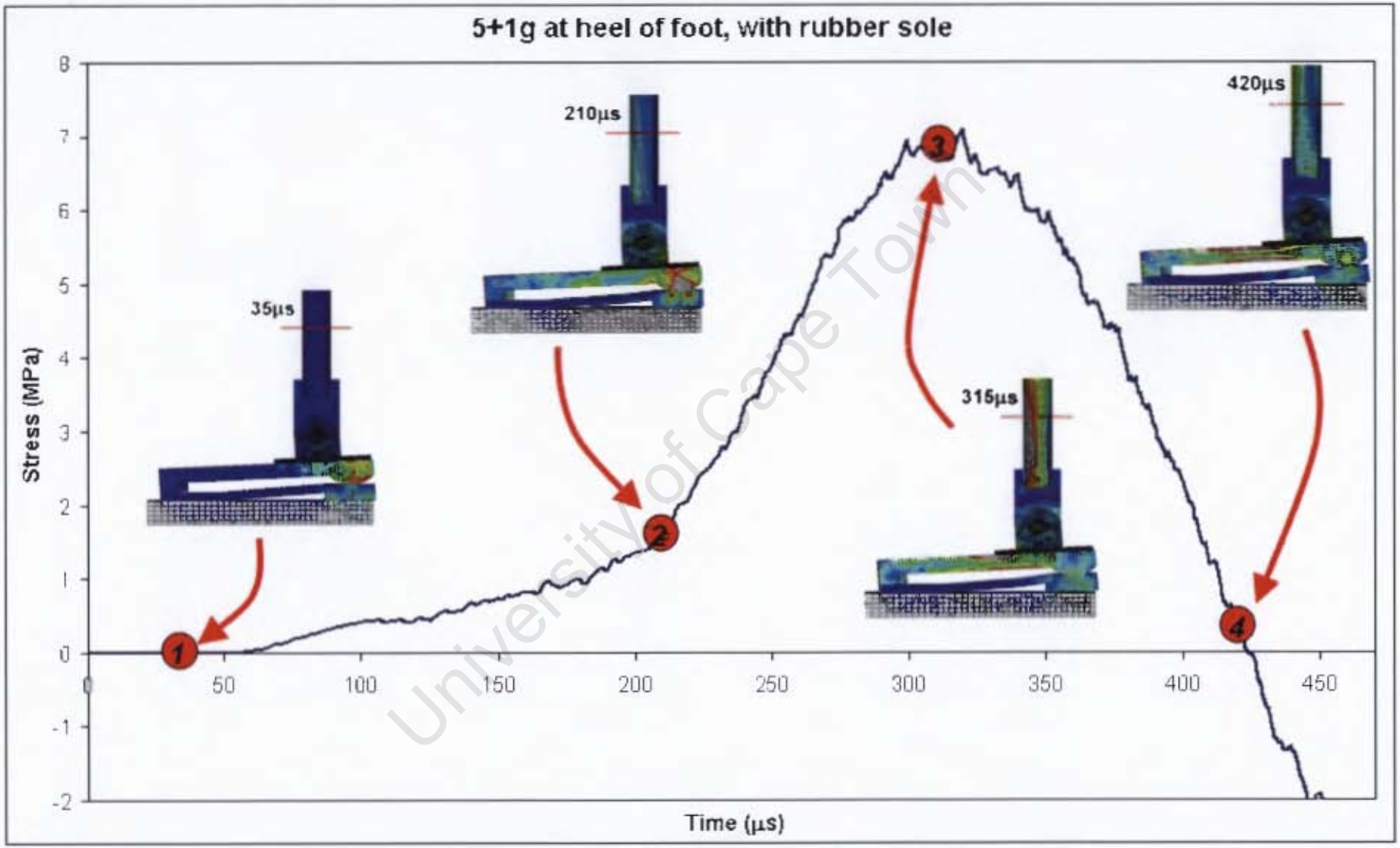

Figure 7.16 - Graphical representation of the stress propagation of the heel blast with the rubber sole included

7.4 COMPARING THE ATTENUATION PROPERTIES OF THE RUBBER SOLE OBSERVED DURING THE EXPERIMENTAL BLAST TESTS AND THE NUMERICAL SIMULATIONS

The rubber sole is employed in the blast test setup to serve as an attenuator to the blast loading applied to the foot model. The attenuation provided by the rubber layer is investigated in both the experimental blast tests and the finite element simulations. Section 5.6.5 of this report discusses the attenuation properties observed in performing the experimental blast tests and Section 6.12 discusses the attenuation provided by the rubber as observed in the numerical simulations of the various blast loading applications.

The attenuation characteristics of the rubber layer are observed in the form of stress reduction and a time delay in attaining maximum stress. For the experimental results, Figure 5.20 and Figure 5.21 demonstrates the attenuation provided by the rubber layer for blast loading applied in the centre and at the heel of foot respectively. The reduction in the stress experienced by the aluminium tube (given as a percentage) and the time delay in experiencing the maximum stress are documented in Table 7.8. It is observed that the 7+1g blast in the centre of the foot produced a 55% reduction in stress compared to the 68% and 76% noticed in the 5+1g and 6+1g blasts in the centre of the foot. Referring to Figure 5.20, it is noticed that the peak stress for the 7+1g blast is taken to be 10.03MPa. However, if it assumed that the 10MPa peak stress is actually caused by signal noise and the 6MPa peak stress occurring just prior to the 10MPa peak stress is used to calculate the stress reduction, a 73% attenuation of the maximum stress is observed, which is more consistent with the 5+1g and 6+1g attenuation results. In turn, the standard deviation between the experimental and numerical stress attenuation would decrease from 25.3% to 11.7%.

Table 7.8 is once again proof that the numerical simulations performed for the heel blasts provided more consistent and accurate results when compared to the numerical results obtained during the simulations of applying blast loading in the centre of the foot. Only a 3.8% deviation exists between the stress reduction observed during the experimental blast tests and the numerical simulations of the heel blast loading, whereas an average variation of 16.6% is noticed between the experimental and numerical attenuation results for blast loading performed in the centre of the foot model.

Loading condition	***Mass of PE4 used***	***Attenuation of stress experienced by tibia (%)***			***Time delay in onset of reaching maximum stress in tibia (μs)***		
		Exp.	FEM	Variation	Exp.	FEM	Variation
Centre of foot	5+1g	*68%*	*91%*	*14.8%*	*340μs*	*290μs*	*50μs*
	6+1g	*76%*	*92%*	*9.8%*			
	7+1g	*55%*	*92%*	*25.3%*			
Heel of foot	5+1g	*76%*	*82%*	*3.8%*	*170μs*	*160μs*	*10μs*

Table 7.8 – Table comparing the attenuation properties of including the rubber sole, as provided by the experimental blast tests and the FEM simulations

The improved accuracy of the numerical simulations of the heel blast loading applications is also noticed when comparing the time delay in attaining the maximum stress. A 50μs difference in the time delay is observed between the experimental and numerical results obtained for the blast loading applied in the centre of the foot, where a mere 10μs difference is observed between the experimental and numerical results for blast loading applied at the heel of the foot model.

7.5 COMPARING THE RESULTS FROM THE PRESENT INVESTIGATION TO RESULTS PROVIDED BY PREVIOUS STUDIES

In an attempt to put the results obtained during the present study in better perspective with respect to other similar studies, the peak stress results from this investigation are converted to force values and compared to the peak force results obtained during similar studies previously conducted (as described in Section 2.5 of this report). It is decided to view the results in terms of impact severity, as this will exhibit whether a trend exists in the amount of force experienced by the lower tibia during increasing axial impact loading.

The results published on the study performed by Bir et al.[8] in which the TROSS results were verified by using a horizontal impact rig are used in the current comparison, because the testing principle is similar to using the horizontal ballistic pendulum and force results over a relatively broad spectrum of impact severity is provided. The impact loading is rated as "low", "medium" and "high" severity impact (see Section 2.5.1.2), of which each impact severity is translated to a specific amount of impulse transferred during the impact to the surrogate lower leg. Seeing that both the Hybrid-III and Thor-Lx lower leg surrogates were used during the testing conducted by Bir et al.[8], the force results for both surrogate legs are included in the comparison.

Figure 7.17 shows the comparison between the peak force values obtained for the H-III surrogate leg, the Thor-Lx surrogate leg and the aluminium surrogate leg utilised in the experimental blast testing performed during the current investigation. It is noted that a peak force value for "high severity" testing of the H-III leg is not included, as the force experienced by the H-III leg exceeded the limit of the load cell used to record the force in the tibia of the H-III surrogate leg[8]. From the force values plotted in Figure 7.17 it is clear that the axial force experienced by the tibia in the both the H-III and Thor-Lx lower legs increases linearly as the severity of the impact is increased, as expected. Extending the lower portion of the trendlines indicates that the peak axial tibial force documented in the present study is consistent with the general trend.

Figure 7.18 compares the force values obtained when using the three different surrogate lower legs with an army combat boot fitted to the H-III and Thor-Lx lower legs and the rubber sole placed underneath the aluminium lower leg used in the current study. It is observed that the peak axial force in the tibia seems to increase logarithmically with increasing impact loading when a boot is included in the test setup. This logarithmic instead of a linear increase may be expected due to the hyperelastic nature of the rubber combined with the interaction of the remaining layers that the combat boot comprises of.

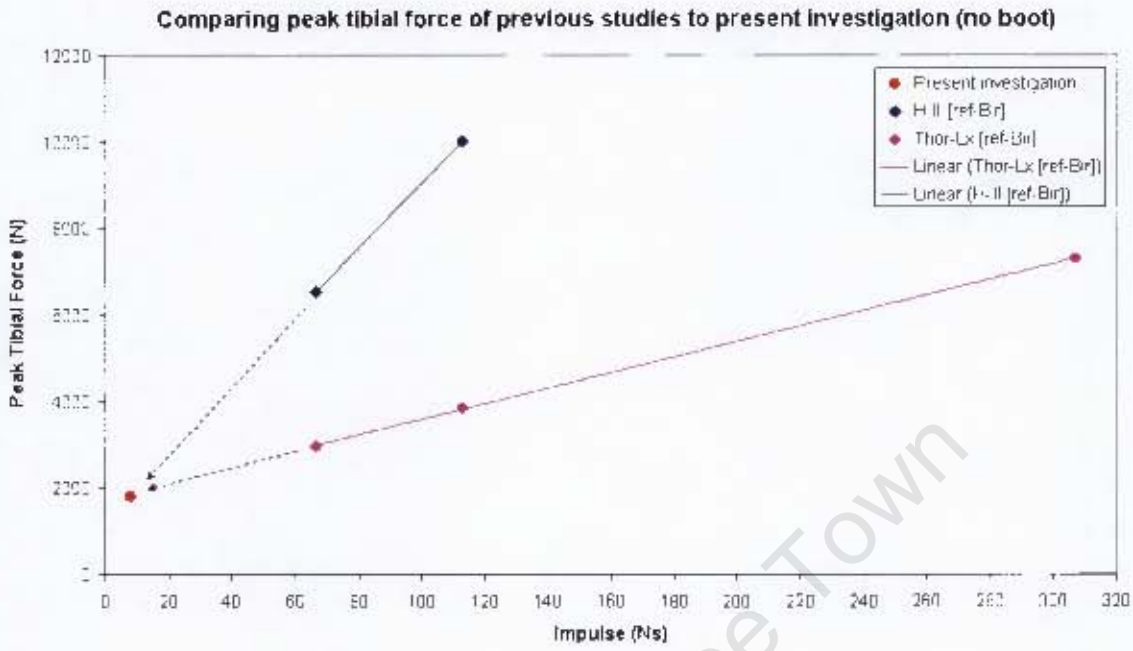

Figure 7.17- Graph comparing the peak tibial force recorded by the Hybrid-III and Thor-Lx surrogate lower legs (excluding the boot) to the peak force recorded during the present study (excluding the rubber sole)

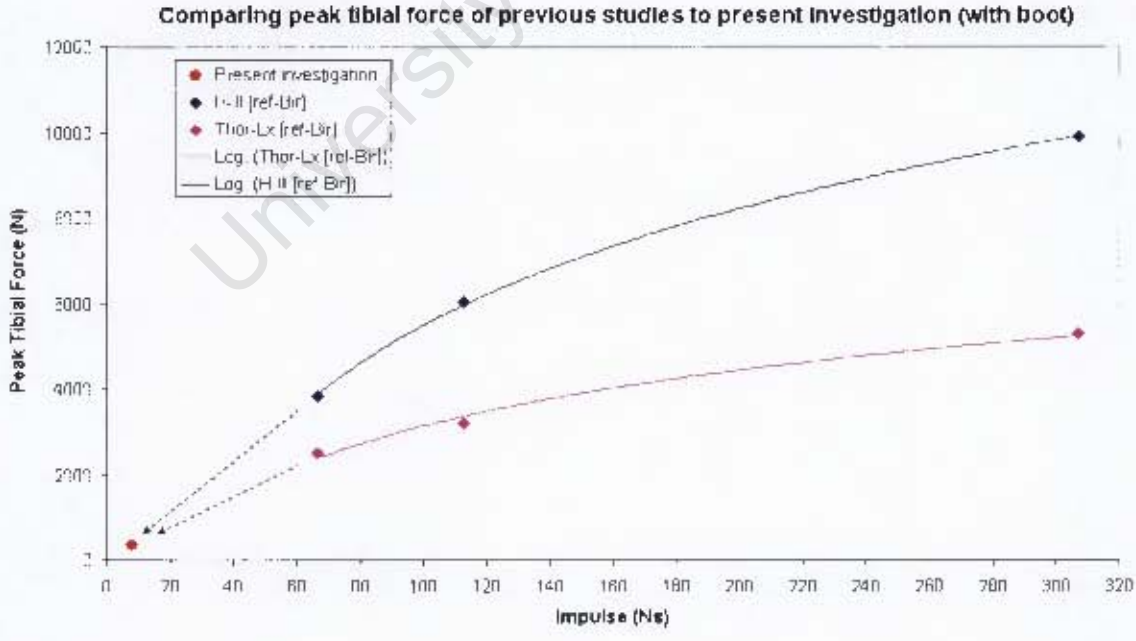

Figure 7.18 – Graph comparing the peak tibial force recorded by the Hybrid-III and Thor-Lx surrogate lower legs (including the boot) to the peak force recorded during the present study (including the rubber sole)

Chapter 8 - Conclusions

A series of blast tests using the horizontal ballistic pendulum was conducted, in which an aluminium surrogate lower leg was exposed to blast loading. The tests were divided into two categories, in which the first series of tests saw only the surrogate leg being impacted and the second series of tests included a layer of rubber to act as a boot sole. A finite element model of the surrogate leg and rig was created and simulations of the blast tests were executed. The results from these numerical simulations were compared and verified. As a result, the attenuation properties provided by the rubber layer during blast load could be examined. From the findings of this investigation, the following conclusions are made:

8.1 NON-INJURIOUS BLAST IMPACT TESTING

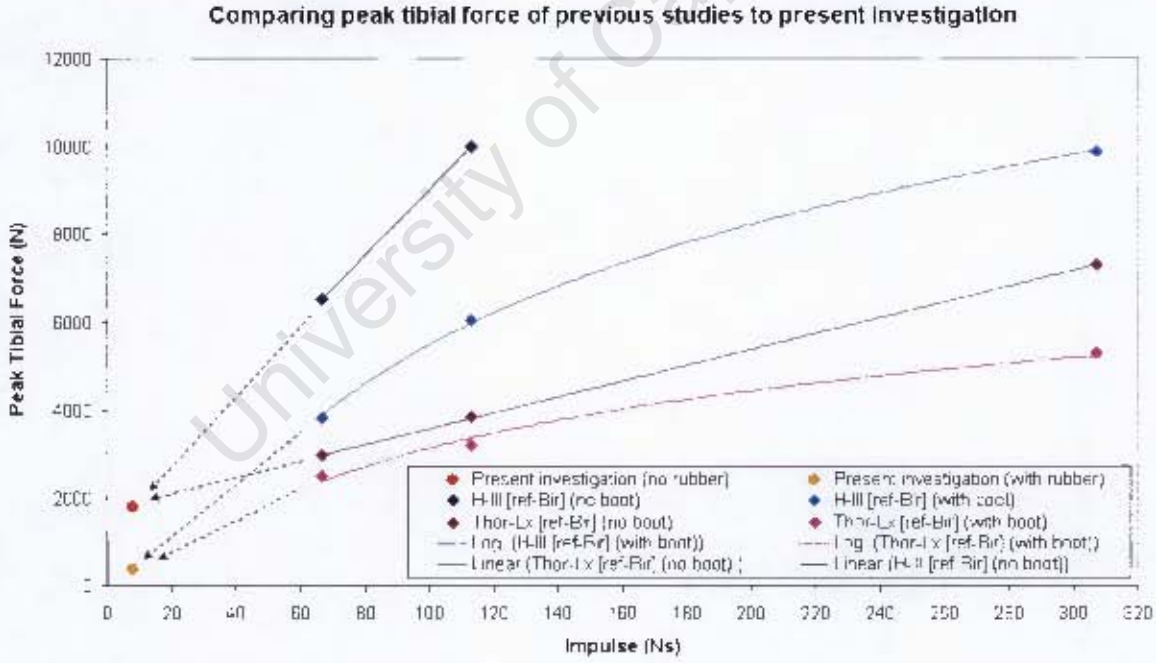

Figure 8.1 – Graph comparing the peak tibial force recorded by the Hybrid-III and Thor-Lx surrogate lower legs (excluding and including the boot) to the peak force recorded during the present study (excluding and including the rubber sole)

Referring to Figure 8.1, it is clearly shown that the blast testing performed in the present investigation is of a very low impact severity compared to impact tests conducted by other

researchers[8]. The peak force plotted to represent the peak force experienced by the aluminium surrogate leg is taken from the blast tests performed with the explosives positioned axially in line with the heel of the foot, seeing that the impact testing conducted by Bir et al[8] is also aligned axially with the heel of the H-III and Thor-Lx surrogate legs. Furthermore, the peak stress values recorded during the 5+1g blast tests are used, as blast testing without the rubber sole was not conducted with more than 5+1g explosives positioned at the heel. As was commented in Section 7.5, the results from the present investigation integrate well with the trends shown by the results taken from the tests performed by Bir et al.[8].

According to Table 2.6 provided in the Literature Review, the H-III and Thor-Lx surrogate legs are designed to experience a threshold of 8000N and 5600N respectively, which would indicate the probable occurrence of an AIS2+ injury. From Figure 8.1 it is evident that the peak axial force experienced by the tibia is below 2000N, indicating that minor injuries are expected in the lower leg.

8.2 *EFFECT OF POSITIONING OF THE EXPLOSIVE*

The differences in the stress wave travelling through the aluminium surrogate foot caused by varying the positioning of the explosives with respect to the foot is tabulated in Table 8.1.

	Explosive in centre of foot	***Explosive in line with heel of foot***
Magnitude of peak stress experienced in tibia	*When the rubber sole is excluded, the peak stress is roughly 39% lower than when the explosive is placed in line with the heel.* *When the rubber sole is included, the peak stress is roughly 18% lower than when the explosive is placed in line with the heel.*	*When the rubber sole is excluded, the peak stress is roughly 65% higher than when the explosive is placed in the centre of the foot.* *When the rubber sole is included, the peak stress is roughly 21% higher than when the explosive is placed in the centre of the foot.*
Time when peak stress is experienced in tibia	*When the rubber sole is excluded, the tibia experiences the peak stress approximately 80μs later than when the explosive is placed in the centre of the foot than when it is placed in line with the heel.* *When the rubber sole is included, the tibia experiences the peak stress approximately 275μs later than when the explosive is placed in the centre of the foot than when it is placed in line with the heel.*	
Number of peaks present in stress curve	*Two peaks are noticed in the stress curve, both when the rubber sole is excluded and included in the test setup.*	*Only one distinct peak is noticed in the stress curve, both when the rubber sole is excluded and included in the test setup.*

Table 8.1 – Table documenting the effects of varying the positioning of the explosives with respect to the surrogate foot in the blast test setup

8.3 ATTENUATION PROVIDED BY THE RUBBER LAYER

From the experimental blast test results it is noticed that the rubber layer provides two forms of attenuation to the blast stress. Including the rubber layer at the base of the surrogate foot caused a delay in the time at which the tibia experiences the peak stress, and as expected, the magnitude of the peak stress experienced by the tibia is significantly reduced. Referring to Figure 5.18 and Figure 5.19, a time delay of approximately 170μs up to 340μs is observed when the rubber sole is used in the test setup. The percentage amount of attenuation in the peak stress recorded in the tibia ranged from 54% up to 75% for blast impact with the explosives placed in the centre of the foot, and approximately 76% for blast impact with the explosives placed in line with the heel of the foot.

The attenuation provided by the standard army combat boot used in the impact testing of the Hybrid-III and Thor-Lx surrogate lower legs are calculated from the information published by Bir et al[8] to be:

- Hybrid-III surrogate leg[8]:
  - 41% (low severity impact)
  - 39% (medium severity impact)
- Thor-Lx surrogate leg[8]:
  - 15% (low severity impact)
  - 17% (medium severity impact)
  - 27% (high severity impact)

The amount of stress attenuation provided by wearing a standard army combat boot appears to vary to a large extent. However, the stress attenuation recorded when wearing the combat boot is significantly lower than the attenuation achieved in the present investigation by utilising only a rubber layer. This difference can be directly related to the following factor:

- The most obvious contributing factor is the fact that a combat boot constitutes layers of different material glued and nailed together to form a strong support for the foot. These layers include rubber for the outer sole, a spongy yet strong material layer making up the inner sole, a cardboard-like layer which is placed in between the outer and inner sole, a thin metal plate nailed to the heel to give shape to the base of the boot, and lastly hard set glue and nails holding the entire boot sole together. This arrangement is bound to transmit more of the stress wave than a layer of rubber, which would result in higher stress being experienced by the tibia and as such, lower stress attenuation is observed.

8.4 VALIDATION OF THE FINITE ELEMENT MODEL

The attempt to validate the experimental blast test results by creating a finite element model was partly successful. The finite element model constructed to simulate the aluminium surrogate leg without the rubber layer yielded essentially good results, as the shape of the stress curves and the magnitudes of the peak stresses for all the blast loading conditions correlated well with the experimental results.

However, the finite element model created to simulate the blast loading of the surrogate leg with the rubber sole included in the setup proved to be less successful. The same general trend in the shape of the stress curves could be observed, with the peaks coinciding at approximately the same time. The magnitudes of the peak stresses yielded by the numerical simulations for blast loading in the centre of the foot were greatly under predicted. In contrast, the magnitudes of the peak stresses given by the simulations of blast loading performed in line with the heel of the foot agreed reasonably well. This interesting observation leads to the conclusion that the numerical modelling of the front (metatarsal) portion of the rubber sole requires more detailed examination. It must however be remembered that the ABAQUS documentation manual on the modelling of rubber did warn that when the rubber layer is highly confined and/or subjected to high compression rates, accurate results may not be provided by the numerical simulation[60].

REFERENCES CITED

[1] Landmine action week. *Landmines and the Ottawa Treaty*. [Online]. Available: http://www.landmineaction.org [Cited 7 August 2007]

[2] *Banning anti-personnel mines: the Ottawa treaty explained*. ICRC publication, ref. 0702. [Online]. Available: http://www.icrc.org/WEB/ENG/siteeng0.nsf/htmlall/p0702?OpenDocument [Updated 1998, Cited 19 September 2007]

[3] *RTO-TR-HFM-089*. NATO Research and Technology Organisation. [Online]. Available: http://www.rta.nato.int/pubs/rdp.asp?RDP=RTO-TR_HFM-089 [Cited 12 August 2007]

[4] *Canadian Centre for Mine Action Technologies*. Defence Research and Development Canada. [Online]. Available: http://www.suffield.drdc-rddc.gc.ca/Facilities/CCMAT/index_e.html [Cited 31 January 2007]

[5] Chapter1 – Weapons Effects and Parachute Injuries, in *War Surgery*. [Online]. Available: http://www.usaisr.amedd.army.mil/ewsh/Chp1WeaponsEffects.pdf [Cited 27 February 2006]

[6] D. M. Bergeron, C. Chichester; *Protecting deminers from APLs: A review of U.S./Canada cooperation in R&D*. Journal of Mine Action, Issue 7.1, April, 2003. [Online]. Available: http://www.hdic.jmu.edu/journal/7.1/focus/bergeron/bergeron.htm [Cited 24 February 2006]

[7] M. S. Rountree, LTC R. M. Harris; *Countering the global landmine epidemic through basic science and research*. Journal of Mine Action, version 4.2, June, 2000. [Online] Available: http://maic.jmu.edu/Journal/4.2/Focus/GLE/global.htm [Cited 10 October 2006]

[8] C. Bir, A. Barbir, M. Wilhelm, M. van der Horst, F. Dosquet, G. Wolfe; *Validation of lower limb surrogates as injury assessment tools in floor impacts due to anti-vehicular landmines*. Proceedings of IRCOBI Conference, 279 – 288. Madrid (Spain), September 2006.

[9] Chang Nam Ahn, Han Il Bae, In Yeok Lee, Hyung Yun Choi; *The assessment of lower extremity injury using human FE model.* Hyundai Motor Company and Kia Motors Corporation. Euro-PAM, 2003.

[10] S. M. Kuppa, G. S. Klopp, J. R. Crandall, G. Hall, N Yoganandan, F. A. Pintar, R. H Eppinger, E. Sun, N. Khaewpong, M. Kleinberger; *Axial impact characteristics of dummy and cadaver lower limbs.* National Highway Traffic Safety Administration (United States), Paper Number 98-S7-O-10, pp. 1608 – 1617.

[11] Andrew Selth. *Landmines in Burma*, The Military Dimension. The Burma Project – Burma Debate. [Online]. Available: http://www.burmadebate.org/archives/winter00landmines.html [Cited 4 October 2006]

[12] D. M. Bergeron, G. G. Coley, M. S. Rountree, I. B. Anderson, R. M. Harris; *Assessment of foot protection against anti-personnel landmine blast using a frangible surrogate leg.* UXO Forum, 9 April – 12 April 2001.

[13] D. S. Cronin, K. Williams, C. R. (Dale) Bass, P. Magnan, F. Dosquet, D. M. Bergeron, J. L. M. J. van Bree; *Test methods for protective footwear against AP mine blast.* Proceedings of NATO Research and Technology Organisation Symposium. Equipment for Personal Protection MP-108. 2004.

[14] W. E. Baker; *Explosions in air.* Wilfred Baker Engineering (Second printing of 1973 edition). 1983.

[15] *Plastic explosive*. Wikipedia. [Online] Available: http://en.wikipedia.org/wiki/Plastic_explosive [Cited 13 August 2007]

[16] *Trinitrotoluene*. Wikipedia. [Online] Available: http://en.wikipedia.org/wiki/Trinitrotoluene [Cited 13 August 2007]

[17] Andy Smith; *Explosive content of mines.* [Online] Available: http://www.nolandmines.com/explosivesinmines.htm [Cited 13 June 2007]

[18] *RDX*. Wikipedia. [Online]. Available: http://en.wikipedia.org/wiki/RDX [Cited 13 August 2007]

[19] *C-4*. Wikipedia. [Online]. Available: http://en.wikipedia.org/wiki/C-4_(explosive) [Cited 13 August 2007]

[20] *Explosive material*. Wikipedia. [Online]. Available: http://en.wikipedia.org/wiki/Explosive [Cited 13 August 2007]

[21] *Structures to resist the effects of accidental explosions*, TM5-1300, NAVFAC P-397, AFR 88-22, 1990.

[22] The Steel construction institute, *The effects of simplification of the explosion pressure-time history*, British gas research and technology. OTI-92599(BRI), 1992.

[23] E. D. Esparza; *Blast measurement and equivalency for spherical charges at small scaled distances.* International Journal of Impact Engineering, Vol. 4 (1), pp 23 - 40, 1986.

[24] P. D. Smith, J. G. Hetherington; *Blast and ballistic loading of Structures*, Butterworth and Heinemann, 1994.

[25] *Landmines*. Global Security. [Online]. Available: http://www.globalsecurity.org/military/systems/munitions/landmines.htm [Cited 20 June 2007]

[26] N. Jacob, V. H. Balden, G. S. Langdon, S. Chung Kim Yuen, G. Nurick; *Literature research report: Flat bottom hull technology in landmine protected vehicles*. BISRU, University of Cape Town. May 2005.

[27] *Anti-personnel mine*. Wikipedia. [Online]. Available: http://en.wikipedia.org/wiki/Anti-personnel_mine [Cited 24 September 2006]

[28] *Mle 1951 AP blast mine*. Wikipedia. [Online]. Available: http://enwikipedia.org/wiki/Mle_1951_AP_blast_mine [Cited 13 August 2007]

[29] K. Bonsor; *How landmines work*. [Online]. Available: http://science.howstuffworks.com/landmine2.htm [Cited 14 August 2007]

[30] *Anti-tank mine*. Wikipedia. [Online]. Available: http://www.en.wikipedia.org/wiki/Anti-tank_mine [Cited 24 September 2006]

[31] *Shaped charge*. Wikipedia. [Online]. Available: http://en.wikipedia.org/wiki/Shaped_charge [Cited 17 October 2006]

[32] *Explosively formed penetrator*. Wikipedia. [Online]. Available: http://en.wikipedia.org/wiki/Explosively_Formed_Penetrator [Cited 17 October 2006]

[33] *TC/3.6 and TC/6 mines*. Wikipedia. [Online]. Available: http://en.wikipedia.org/wiki/TC/6_mine [Cited 13 June 2007]

[34] Dr. Nirain D'Souza. *A patient's guide to foot anatomy*. [Online]. Available: http://www.allaboutmydoc.com/surgeonweb/surgeonId.2729/clinicId.1432/theme.themeFoot [Cited 20 April 2006]

[35] Dr. Nirain D'Souza. *A patient's guide to ankle anatomy*. [Online]. Available: http://www.allaboutmydoc.com/surgeonweb/surgeonId.2729/clinicId.1432/theme.themeAnkle [Cited 20 April 2006]

[36] *Crash test dummy*. [Online]. Available: http://www.answers.com/topic/crash-test-dummy [Cited 19 October 2006]

[37] S. Kuppa, M. Haffner, R. Eppinger, J. Saunders; *Lower extremity response and trauma assessment using the Thor-Lx/HIIIr and the Denton leg in frontal offset vehicle crashes*. National Highway Traffic Safety Administration (USA), Paper number 456.

[38] *Thor-Lx, Full assembly*. Denton ATD. [Online]. Available: http://www.dentonatd.com [Cited 9 April 2006]

[39] J. Manseau, M. Keown; *Evaluation of the Complex Lower Leg (CLL) for its use in anti-vehicular mine testing applications.* Proceedings of IRCOBI Conference, Prague (Czech Republic), September 2005.

[40] D. Cronin; *Reducing the devastation.* Frontline – Canada, January/February 2005. [Online]. Available: http://www.frontline-canada.com [Cited 20 October 2006]

[41] E. Haug, Hyung-Yun Choi, S. Robin, M. Beaugonin; *Human models for crash and impact simulation, in Computational models for the human body*, Special volume of Handbook of Numerical Analysis, Volume 12, pp. 231 – 670.

[42] M. J. van der Horst, C. K. Simms, R. van Maasdam, P. J. C. Leerdam; *Occupant lower leg injury assessment in landmine detonations under a vehicle.* IUTAM proceedings. 2005.

[43] *Blast protective footwear.* [Online]. Available: http://www.firehouseinternational.com/usersite/search/searchitem.asp?id=14497 [Cited 24 October 2006]

[44] *Blast and Fragment Resistant Combat Boot.* [Online]. Available: http://www.bfrboots.com [Cited 4 October 2006]

[45] S. Islam, A. Makris, D. Bergeron; *The Spider Boot: An effective foot protection system against anti-personnel mine blasts.* Journal of Mine Action, version 4.2, June, 2000. [Online]. Available: http://maic.jmu.edu/Journal/4.2/Focus/SB/spiderboot.htm [Cited 24 October 2006]

[46] *Project 2 Overview – Develop common criteria for reporting injuries and fatalities.* Bureau of Transportation Statistics. [Online]. Available: http://www.bts.gov/publications/safety_in_numbers_conference_2002 [Cited 7 August 2007]

[47] J. Saunders, S. Kuppa; *Comparison of the responses and trauma assessment of the Thor-Lx/HIIIr and Hybrid III Denton legs in frontal offset vehicle crashes.* National Highway Traffic Safety Administration, SAE Government / Industry meeting, May 2002.

[48] G. N. Nurick, G. S. Langdon, Y. Chi, N. Jacob; *Behaviour of sandwich panels subjected to intense air blast – Part 1: Experiments.* Composite Structures (to appear 2008).

[49] J. E. Field, S. M. Walley, W.G. Proud, H. T. Goldrein, C. R. Siviour; *Review of experimental techniques for high rate deformation and shock studies.* International Journal of Impact Engineering,vol. 30, pp. 725 – 775, 2004.

[50] H. Kolsky; *An investigation of the mechanical properties of materials at very high rates of loading.* Proceedings of Royal Society London, 362, pp. 676 – 700, 1949.

[51] O. A. Shergold, N. A. Fleck, D. Radford; *The uniaxial stress versus strain response of pig skin and silicone rubber at low and high strain rates.* International Journal of Impact Engineering, vol. 32, pp. 1384 – 1402, 2006.

[52] L. M. Yang, V. P. W. Shim, C. T. Lim; *A visco-hyperelastic approach to modelling the behaviour of rubber.* International Journal of Impact Engineering, vol. 24, pp. 545 – 560, 2000.

[53] P. A. du Bois, S. Kolling, M. Koesters, T. Frank; *Material behaviour of polymers under impact loading.* International Journal of Impact Engineering, vol. 32, pp. 725 – 740, 2006.

[54] G. T. Gray III; Classic Split-Hopkinson Pressure Bar Testing, in *ASM Split-Hopkinson Pressure Bar Handbooks.*

[55] G. T. Gray III, W. R. Blumenthal; Split-Hopkinson Pressure Bar Testing of Soft Materials, in *ASM Split-Hopkinson Pressure Bar Handbooks.*

[56] T. Cloete; *Stress Wave Propagation in Uniform Bars.* Academic Notes. Department of Mechanical Engineering. University of Cape Town. 2007.

[57] F. North-Coombes; *Blast testing of aluminium foot model.* Undergraduate final year thesis. Department of Mechanical Engineering. University of Cape Town. 2005.

[58] A. L. Window and G. S. Hoister; *Strain Gauge Technology*, DA Information Services, p. 243, 1982.

[59] T. Cloete; *Linear Elasticity*. Course notes (MEC566Z). Department of Mechanical Engineering. University of Cape Town. 2005.

[60] *Hyperelastic behaviour*, ABAQUS Analysis User's Manual, ABAQUS Version 6.5 Documentation, © ABAQUS, Inc. 2004.

[61] *Fitting of hyperelastic and hyperfoam constants*, ABAQUS Theory Manual, ABAQUS Version 6.5 Documentation, © ABAQUS, Inc. 2004.

[62] *Speed of sound in various bulk media*. Hyperphysics. [Online]. Available: http://hyperphysics.phy-astr.gsu.edu/hbase/sound/souspe2.html [Cited 19 April 2007]

[63] ABAQUS, Inc., Rising Sun Mills, 166 Valley Street, Providence, R102909-2499, United States. Email: support@abaqus.com. Online: http://www.abaqus.com

[64] *Solid (continuum) elements*, ABAQUS Analysis User's Manual, ABAQUS Version 6.5 Documentation, © ABAQUS, Inc. 2004.

[65] *Assigning ABAQUS element types*, ABAQUS/CAE User's Manual, ABAQUS Version 6.5 Documentation, © ABAQUS, Inc. 2004.

[66] Material data obtained from Matweb. [Online]. Available: http://www.matweb.com

[67] *Friction Factors*. [Online]. Available: http://www.roymech.co.uk [Cited 28 March 2006]

APPENDICES TABLE OF CONTENTS

APPENDICES TABLE OF FIGURES

APPENDIX A

APPENDIX B

APPENDICES TABLE OF TABLES

Appendix A - Split-Hopkinson Pressure Bar Data

A.1 SHPB testing of rubber at 1750s^{-1} strain rate

Figure A.1 shows the stress curves (1-wave, 2-wave and average stress wave) obtained from analysing the data recorded during the SHPB testing of the rubber specimens at a strain rate of 1750/s. The 2-wave is seen to oscillate equally above and below the 1-wave up to a strain of 0.09, indicating that the stress at the front and rear surfaces attained a uniform stress state. After 0.09 strain the 2-wave is seen to diverge from and converge again to the 1-wave just before the rubber specimen surfaces loses contact with the surfaces of the pressure bar. Compression inducing an approximate strain of 0.28 is reached in the specimen before surface contact is lost. An essentially constant strain rate of 1750/s is achieved during the SHPB testing of the rubber specimen.

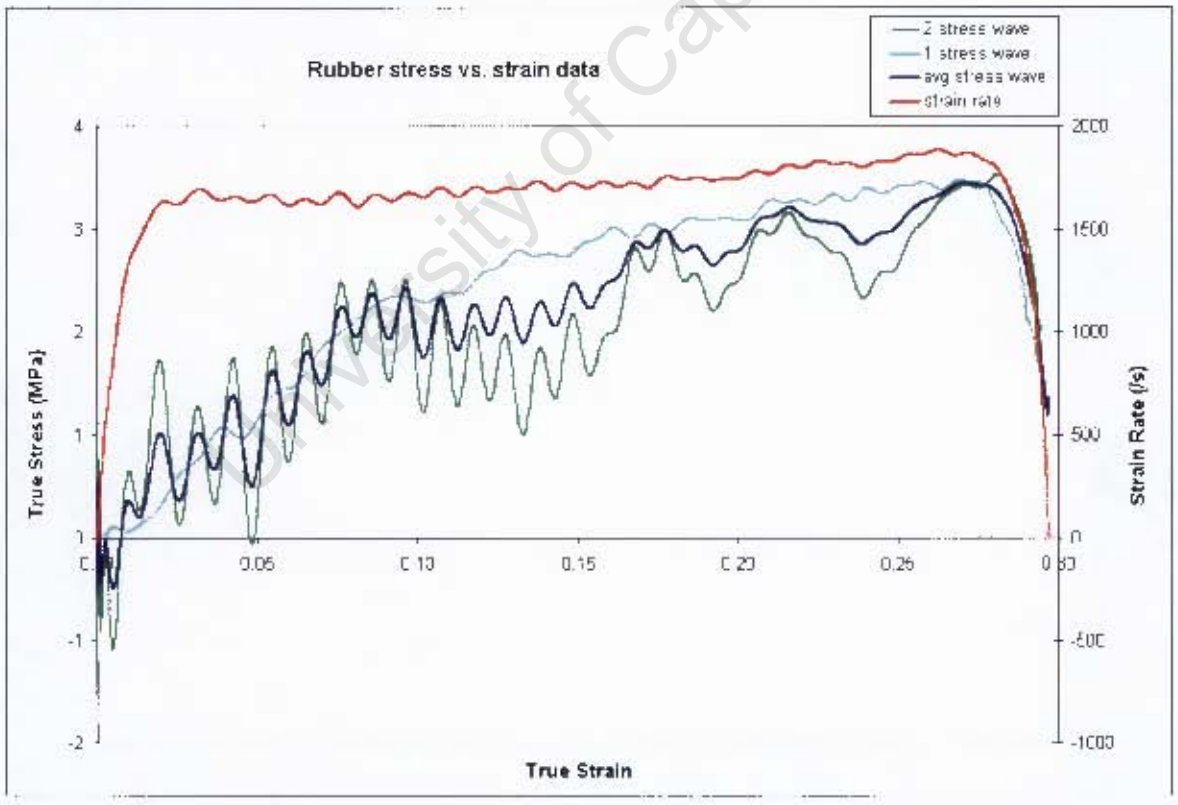

Figure A.1 - Graph displaying the 1-wave, 2-wave, average stress wave and the strain rate data as a function of strain, retrieved from SHPB testing of rubber specimens (length 3.5mm, diameter 19.5mm) performed at a strain rate of 1750/s

A.2 SHPB TESTING OF RUBBER AT 2200s^{-1} STRAIN RATE

Figure A.2 shows the stress curves (1-wave, 2-wave and average stress wave) obtained from analysing the data recorded during the SHPB testing of the rubber specimens at an approximate strain rate of 2200/s. The 2-wave is seen to oscillate equally above and below the 1-wave up to a strain of 0.075, indicating that the stress at the front and rear surfaces attained a uniform stress state. After 0.075 strain the 2-wave is seen to diverge from and converge again to the 1-wave just before the rubber specimen surfaces loses contact with the surfaces of the pressure bar. Compression inducing an approximate strain of 0.33 is reached in the specimen before surface contact is lost. The achieved strain rate increases slightly from 2000/s to 2400/s, however the strain rate shows a very small oscillating amplitude.

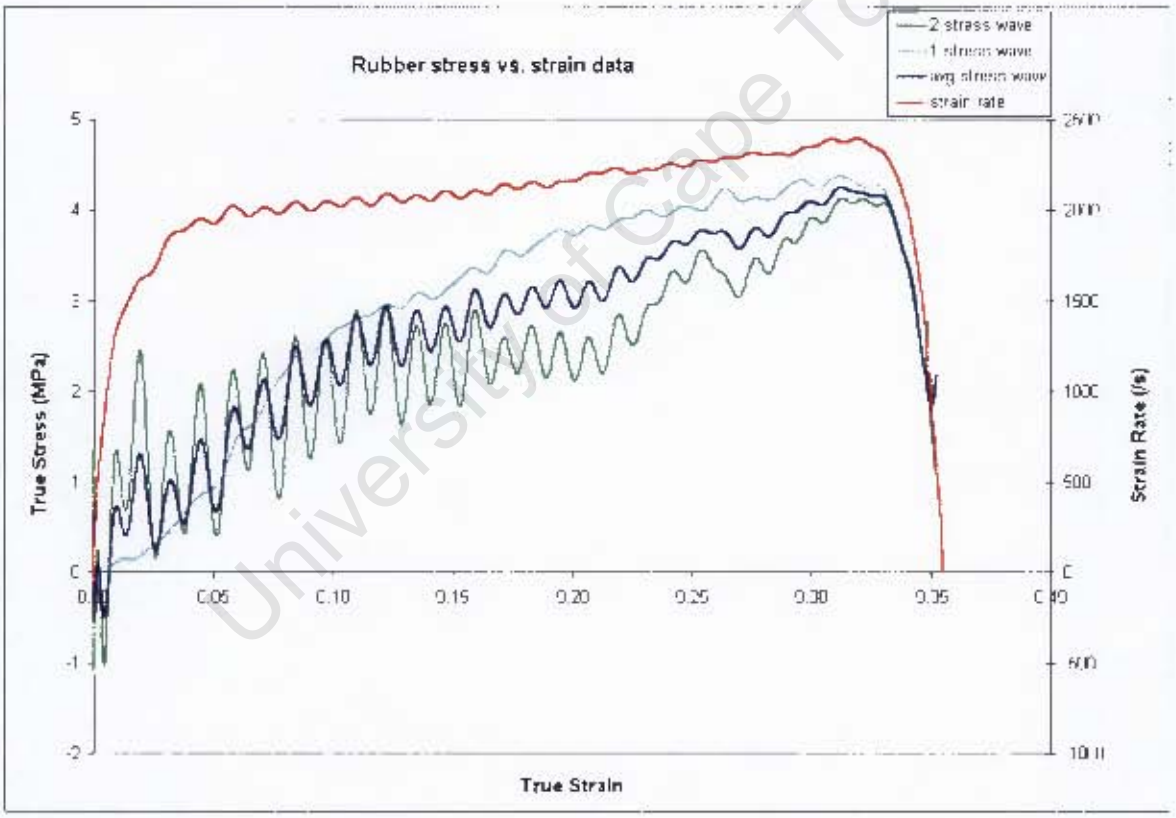

Figure A.2 - Graph displaying the 1-wave, 2-wave, average stress wave and the strain rate data as a function of strain, retrieved from SHPB testing of rubber specimens (length 3.5mm, diameter 19.5mm) performed at a strain rate of 2200/s

A.3 SHPB TESTING OF RUBBER AT 2500s^{-1} STRAIN RATE

Figure A.3 shows the stress curves (1-wave, 2-wave and average stress wave) obtained from analysing the data recorded during the SHPB testing of the rubber specimens at an approximate strain rate of 2500/s. The 2-wave is seen to oscillate equally above and below the 1-wave up to a strain of 0.16, indicating that the stress at the front and rear surfaces attained a uniform stress state. After 0.16 strain the 2-wave is seen to diverge from and converge again to the 1-wave just before the rubber specimen surfaces loses contact with the surfaces of the pressure bar. Compression inducing an approximate strain of 0.375 is reached in the specimen before surface contact is lost. The strain rate achieved during the SHPB testing increases steadily from 2100/s to 2900/s, although once again the amplitude at which the strain rate oscillates is very small.

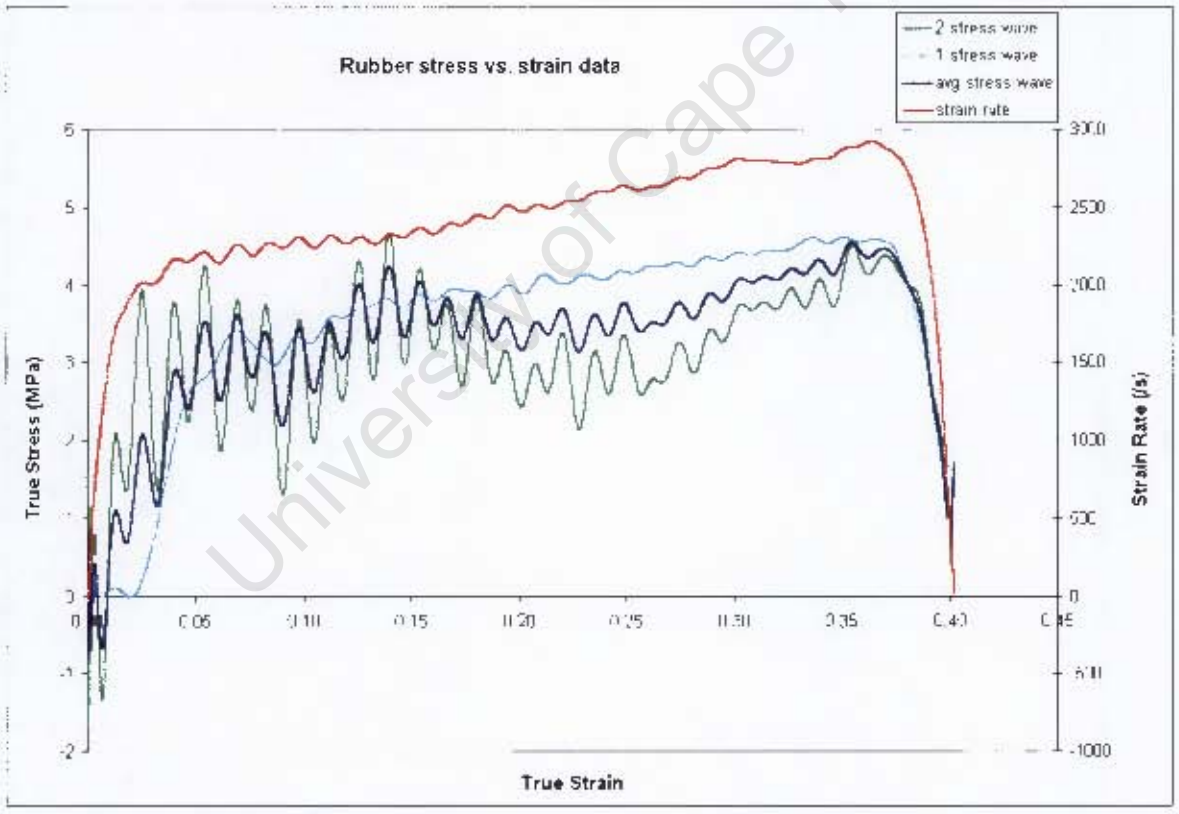

Figure A.3 - Graph displaying the 1-wave, 2-wave, average stress wave and the strain rate data as a function of strain, retrieved from SHPB testing of rubber specimens (length 3.5mm, diameter 19.5mm) performed at a strain rate of 2500/s

A.4 STRESS VS. STRAIN DATA (2500s^{-1} STRAIN RATE)

Table A.1 contains the stress vs. strain values taken from the curve fitted through the experimental stress vs. strain data taken from the SHPB testing performed on the rubber specimen at 2500/s strain rate. The stress-strain data from the fitted curve is employed in the rubber material model constructed in the finite element model of the rubber sole.

Strain	Stress (Pa)	Strain	Stress (Pa)	Strain	Stress (Pa)
0	0				
0.0037	214822	0.1258	3653540	0.2479	4150111
0.0074	420707	0.1295	3686529	0.2516	4161096
0.0111	617909	0.1332	3717275	0.2553	4172427
0.0148	806682	0.1369	3745914	0.259	4184122
0.0185	987272	0.1406	3772577	0.2627	4196197
0.0222	1159924	0.1443	3797392	0.2664	4208662
0.0259	1324880	0.148	3820483	0.2701	4221526
0.0296	1482377	0.1517	3841972	0.2738	4234791
0.0333	1632650	0.1554	3861975	0.2775	4248460
0.037	1775928	0.1591	3880606	0.2812	4262530
0.0407	1912438	0.1628	3897976	0.2849	4276993
0.0444	2042405	0.1665	3914192	0.2886	4291839
0.0481	2166048	0.1702	3929356	0.2923	4307056
0.0518	2283582	0.1739	3943568	0.296	4322627
0.0555	2395222	0.1776	3956925	0.2997	4338530
0.0592	2501177	0.1813	3969518	0.3034	4354741
0.0629	2601652	0.185	3981438	0.3071	4371234
0.0666	2696849	0.1887	3992769	0.3108	4387976
0.0703	2786967	0.1924	4003594	0.3145	4404934
0.074	2872201	0.1961	4013990	0.3182	4422068
0.0777	2952743	0.1998	4024034	0.3219	4439338
0.0814	3028781	0.2035	4033795	0.3256	4456697
0.0851	3100499	0.2072	4043343	0.3293	4474097
0.0888	3168078	0.2109	4052741	0.333	4491485
0.0925	3231697	0.2146	4062051	0.3367	4508806
0.0962	3291528	0.2183	4071328	0.3404	4526000
0.0999	3347742	0.222	4080628	0.3441	4543005
0.1036	3400507	0.2257	4090000	0.3478	4559752
0.1073	3449984	0.2294	4099491	0.3515	4576173
0.111	3496335	0.2331	4109144	0.3552	4592194
0.1147	3539715	0.2368	4118998	0.3589	4607738
0.1184	3580277	0.2405	4129089	0.3626	4622724
0.1221	3618170	0.2442	4139451	0.3663	4637067
				0.37	4650681

Table A.1 – Table of the fitted curve values of the stress vs. strain data retrieved from the SHPB testing of the rubber specimen at 2500/s strain rate

Appendix B - EXPERIMENTAL BLAST TEST DATA

The first two sections of Appendix B contain the graphs which portray the stress-time history recorded during the series of blast tests performed on the surrogate lower leg. The last two sections of Appendix B contains the test data noted down prior to and after conducting the blast tests. The test data comprises the ballistic pendulum characteristics as well as the initial velocity, impulse and force values calculated for each individual blast test.

B.1 RUBBER SOLE OMITTED FROM BLAST TEST SETUP

B.1.1 5+1g PE4 positioned in the centre of the foot model

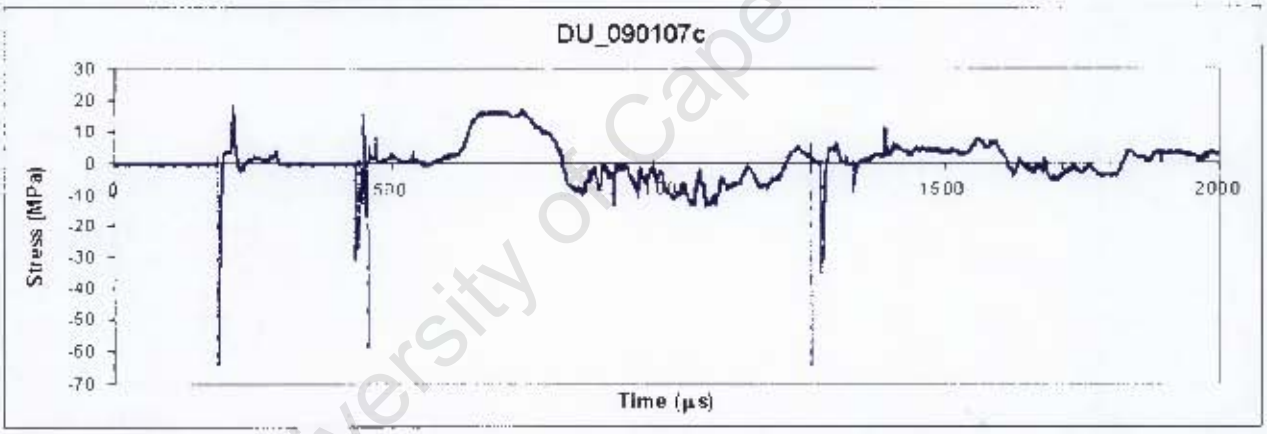

Figure B.1– Graph of stress vs. time history of blast test DU_090107c

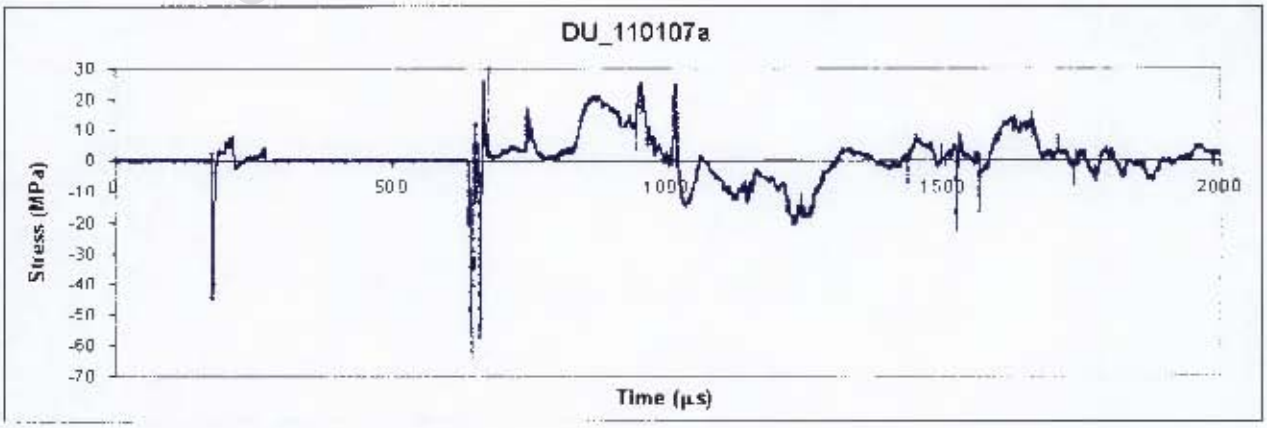

Figure B.2 - Graph of stress vs. time history of blast test DU_110107a

B.1.2 6+1g PE4 positioned in the centre of the foot model

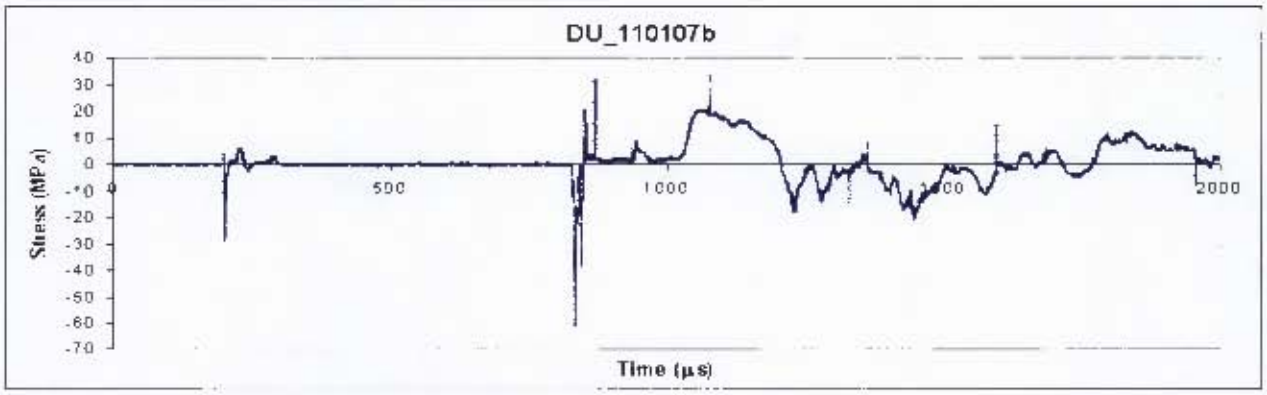

Figure B.3 - Graph of stress vs. time history of blast test DU_110107b

B.1.3 7+1g PE4 positioned in the centre of the foot model

Figure B.4 - Graph of stress vs. time history of blast test DU_110107c

B.1.4 5+1g PE4 positioned in line with the heel of the foot model

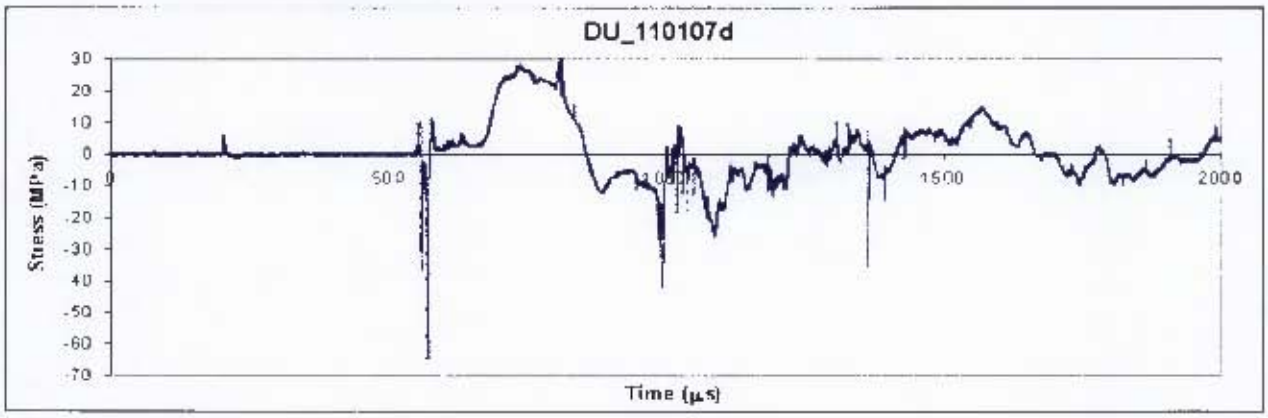

Figure B.5 - Graph of stress vs. time history of blast test DU_110107d

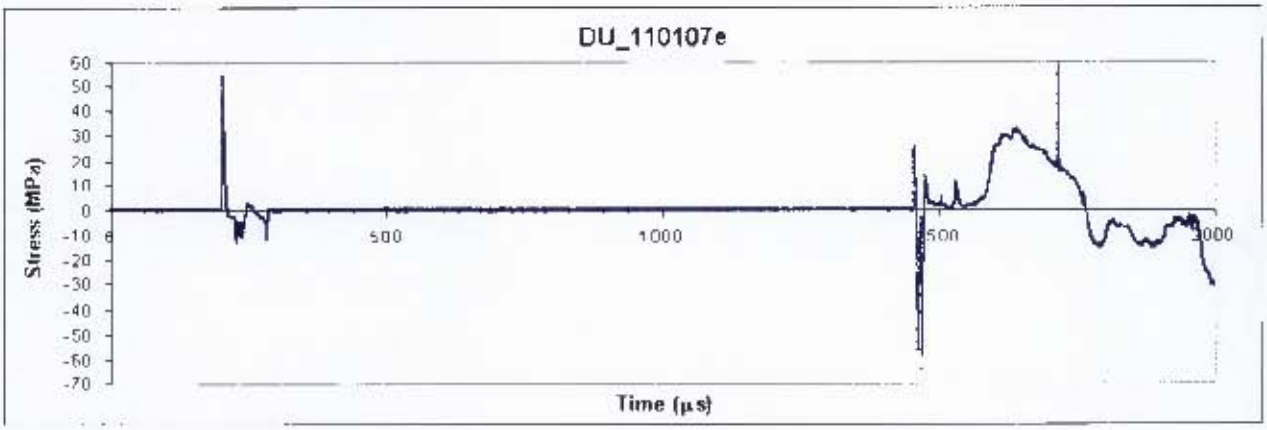

Figure B.6 - Graph of stress vs. time history of blast test DU_110107e

B.2 RUBBER SOLE INCLUDED IN THE BLAST TEST SETUP

B.2.1 5+1g PE4 positioned in the centre of the foot model

Figure B.7 - Graph of stress vs. time history of blast test DU_150107a

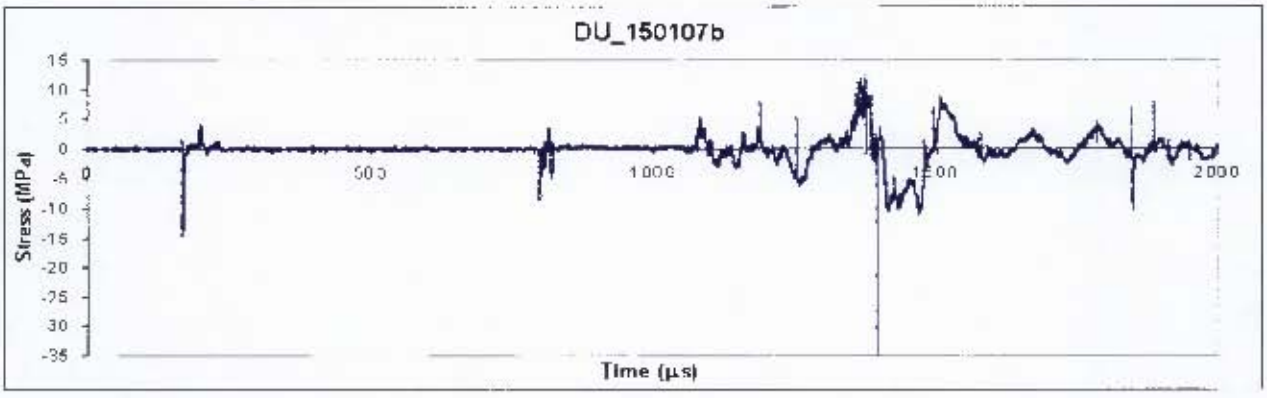

Figure B.8 - Graph of stress vs. time history of blast test DU_150107b

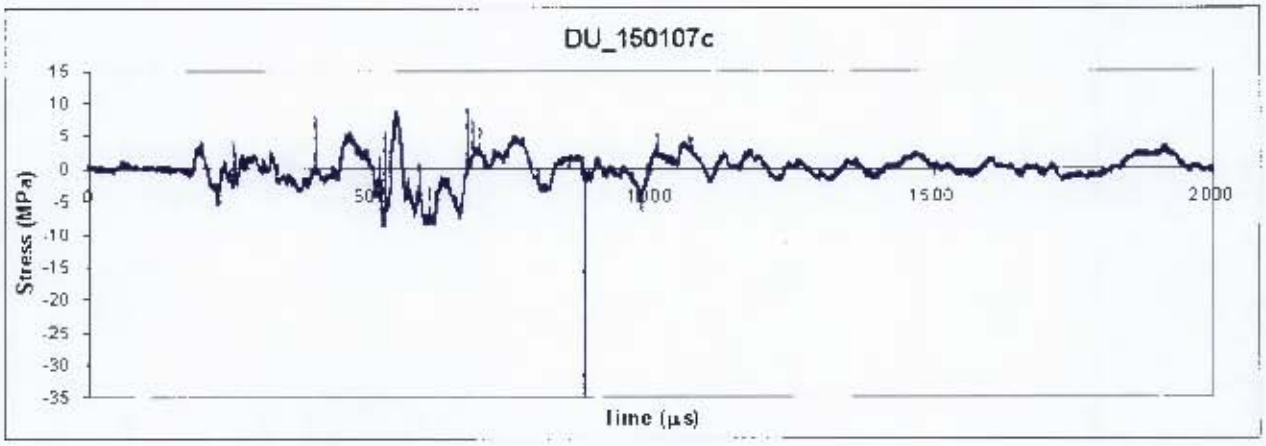

Figure B.9 - Graph of stress vs. time history of blast test DU_150107c

B.2.2 6+1g PE4 positioned in the centre of the foot model

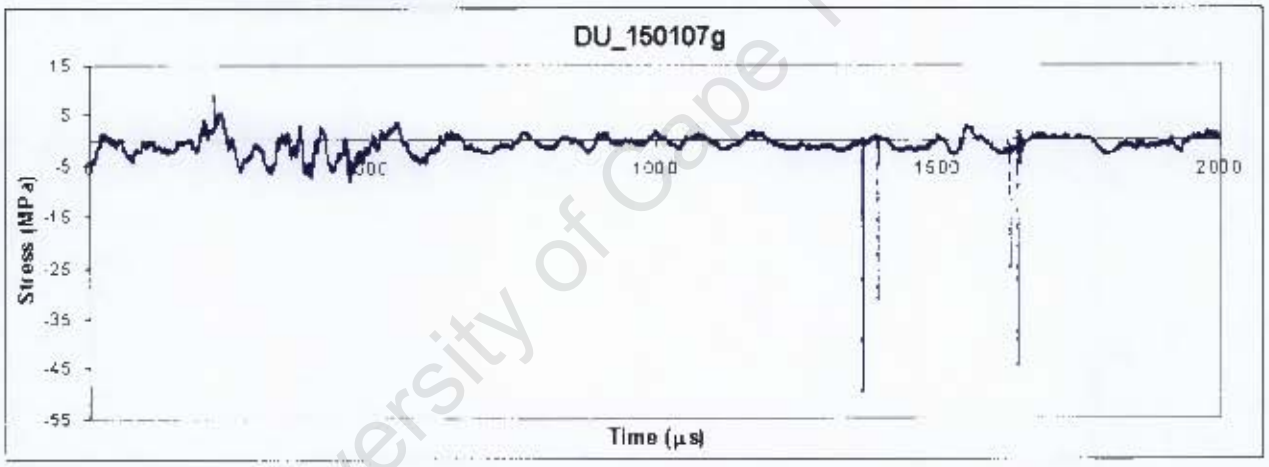

Figure B.10 - Graph of stress vs. time history of blast test DU_150107g

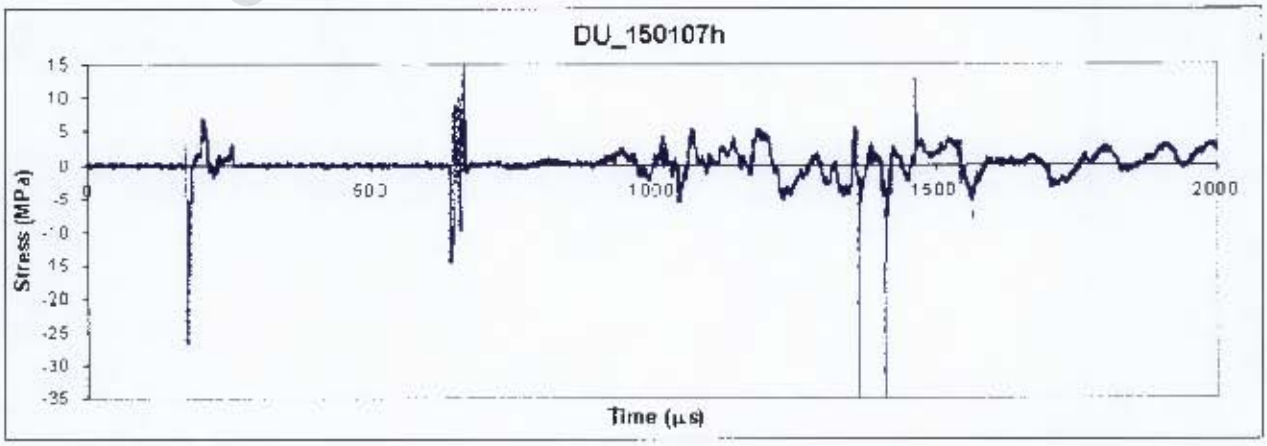

Figure B.11 - Graph of stress vs. time history of blast test DU_150107h

B.2.3 7+1g PE4 positioned in the centre of the foot model

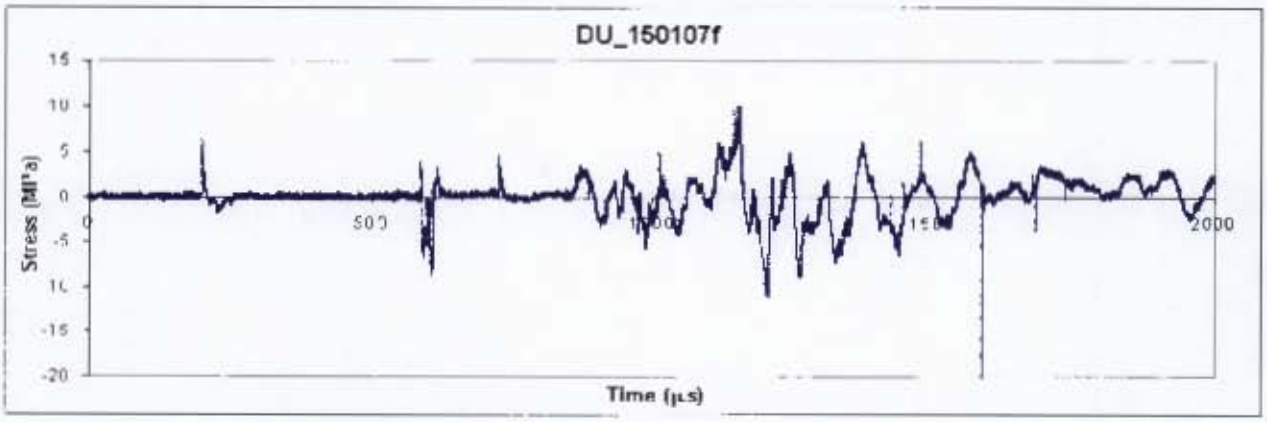

Figure B.12 - Graph of stress vs. time history of blast test DU_150107f

B.2.4 5+1g PE4 positioned in line with the heel of the foot model

Figure B.13 - Graph of stress vs. time history of blast test DU_150107d

B.2.5 7+1g PE4 positioned in line with the heel of the foot model

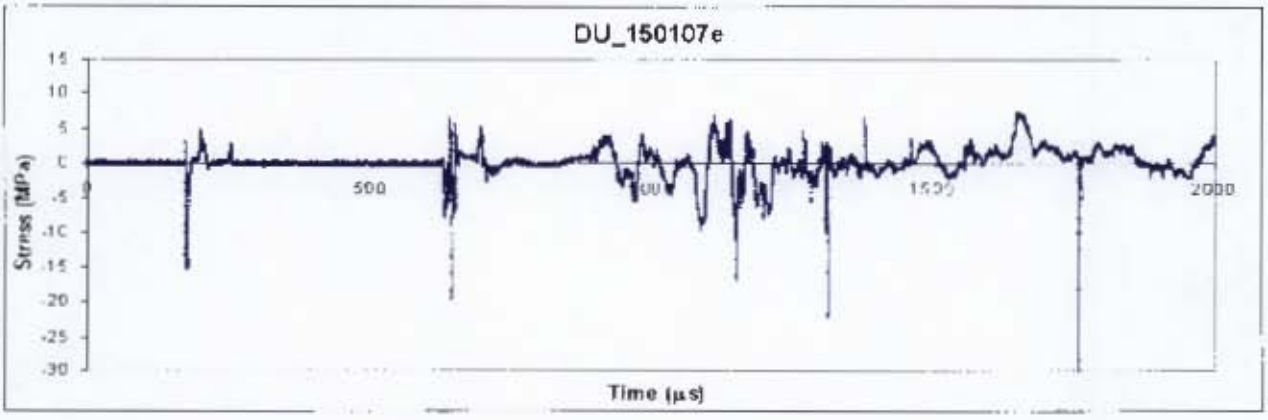

Figure B.14 - Graph of stress vs. time history of blast test DU_150107e

B.3 TEST DATA FOR BLAST TESTS PERFORMED EXCLUDING THE RUBBER SOLE

TEST DATA

Charge diameter = 0.02 m
Charge area = 0.000314159 m^2
Burn velocity = 7200 m/s

Test nr	1	2	3	4	5	6
Test name	DU_09010/c	DU_110107a	DU_110107b	DU_110107c	DU_11010/d	DU_11010/e
Definition	foot (centre)	foot (centre)	foot (centre)	foot (centre)	foot (heel)	foot (heel)
Charge mass (g)	5+1g	5+1g	6+1g	7+1g	5+1g	5+1g
	6	6	7	8	6	6
Period (s)	3.6	3.6	3.6	3.6	3.6	3.6
z (m)	0.19	0.19	0.19	0.19	0.19	0.19
a (m)	0.06	0.06	0.06	0.06	0.06	0.06
R	2.93	2.93	2.93	2.93	2.93	2.93
ΔT (μs)	1.38889E-06	1.38889E-06	1.38889E-06	1.38889E-06	1.38889E-06	1.38889E-06
Pendulum mass (kg)	71.5	71.5	71.5	71.5	71.5	71.5
ΔR (m)	0.0605	0.061	0.07	0.071	0.062	0.06
ΔL (m)	0.06	0.0595	0.069	0.07	0.062	0.058
X1 (m)	0.060709088	0.061212579	0.070280454	0.071288588	0.062219648	0.060205627
X2 (m)	0.059790912	0.059287421	0.068719546	0.069711412	0.061780352	0.057794373
β	0.008466519	0.017753077	0.012477807	0.012429017	0.003936363	0.022707999
V_n (m/s)	0.106767812	0.108556817	0.1240478	0.125821671	0.108979172	0.10724825
Impulse (Ns)	7.633898567	7.761812405	8.869417667	8.996249501	7.792010823	7.668249851
Force (MN)	5.496406968	5.588504932	6.38598072	6.477299641	5.610247792	5.521139892
Pressure (MPa)	17495.60676	17788.76369	20327.20796	20617.88511	17857.97336	17574.33411
x1 (m)	0.0605	0.061	0.07	0.071	0.062	0.06
d1 (m)	0.180271564					

Table B.1 – Table of blast test data for tests performed excluding the rubber sole

B.4 TEST DATA FOR BLAST TESTS PERFORMED INCLUDING THE RUBBER SOLE

TEST DATA

Charge diameter = 0.02 m
Charge area = 0.000314159 m^2
Burn velocity = 7200 m/s

Test nr	7	8	9	10	11	12	13	14
Test name	DU_150107a	DU_150107b	DU_150107c	DU_150107d	DU_150107e	DU_150107f	DU_150107g	DU_150107h
Definition	foot+rubber (centre)	foot+rubber (centre)	foot+rubber (centre)	foot+rubber (heel)	foot+rubber (heel)	foot+rubber (centre)	foot+rubber (centre)	foot+rubber (centre)
Charge mass (g)	5+1g	5+1g	5+1g	5+1g	7+1g	7+1g	6+1g	6+1g
	6	6	6	6	8	8	7	7
Period (s)	3.6	3.6	3.6	3.6	3.6	3.6	3.6	3.6
z (m)	0.19	0.19	0.19	0.19	0.19	0.19	0.19	0.19
a (m)	0.06	0.06	0.06	0.06	0.06	0.06	0.06	0.06
R	2.93	2.93	2.93	2.93	2.93	2.93	2.93	2.93
ΔT (μs)	1.38889E-06	1.38889E-06	1.38889E-06	1.38889E-06	1.38889E-06	1.38889E-06	1.38889E-06	1.38889E-06
Pendulum mass (kg)	71.5	71.5	71.5	71.5	71.5	71.5	71.5	71.5
ΔR (m)	0.0625	0.062	0.06	0.06	0.068	0.072	0.067	0.0675
ΔL (m)	0.0605	0.06	0.06	0.0585	0.0695	0.071	0.065	0.064
X1 (m)	0.062723227	0.062219648	0.060205627	0.060205627	0.068264542	0.072296841	0.067256764	0.067760638
X2 (m)	0.060276773	0.059780352	0.059794373	0.058294373	0.069235458	0.070703159	0.064743236	0.063739362
β	0.022102771	0.022218775	0.00380792	0.017922358	-0.007845913	0.012383441	0.021160205	0.033988433
V_0 (m/s)	0.111672172	0.110787168	0.105439377	0.106787317	0.118305751	0.127595966	0.119642126	0.121938191
Impulse (Ns)	7.984560276	7.921282507	7.53891549	7.635293138	8.458861194	9.123111598	8.554411996	8.71858063
Force (N)	5.748683399	5.703323405	5.428019153	5.497411059	6.090380059	6.568640351	6.159176637	6.277378053
Pressure (Pa)	18299.2642	18154.24224	17277.92159	17498.80289	19386.28184	20908.63162	19605.26814	19981.51494
x1 (m)	0.0625	0.062	0.06	0.06	0.068	0.072	0.067	0.0675
d1 (m)	0.180277564							

Table B.2 - Table of blast test data for tests performed including the rubber sole

Appendix C - MANUFACTURING DRAWINGS

The horizontal pendulum test rig used to conduct the blast testing is based on the standard design of test rigs previously used to perform testing in the BISRU blast laboratory. A new test rig frame was designed and manufactured to incorporate existing rig plates (number 3 in the Pendulum Rig assembly, drawing number PEND000AS) and Teflon bushes (numbers 14 and 15 in the Pendulum Rig assembly, drawing number PEND000AS). The silver steel alignment bars are guided by the Teflon bushes numbered 14 (drawing number PEND009) and the tibia of the surrogate leg is guided by the Teflon bushes numbered 15 (drawing number PEND010). The manufacturing drawings for the pendulum test rig are provided in drawings PEND001 to PEND013.

The assembled foot model is shown and labelled in assembly drawings FOOT000AS and FOOT001AS. The part drawings for the manufacturing of the surrogate foot, ankle and tibia are given in drawings FOOT001 to FOOT009.

Assembly drawing TESTRIG001 shows the Foot assembly placed in the Pendulum Rig as during the experimental test setup.

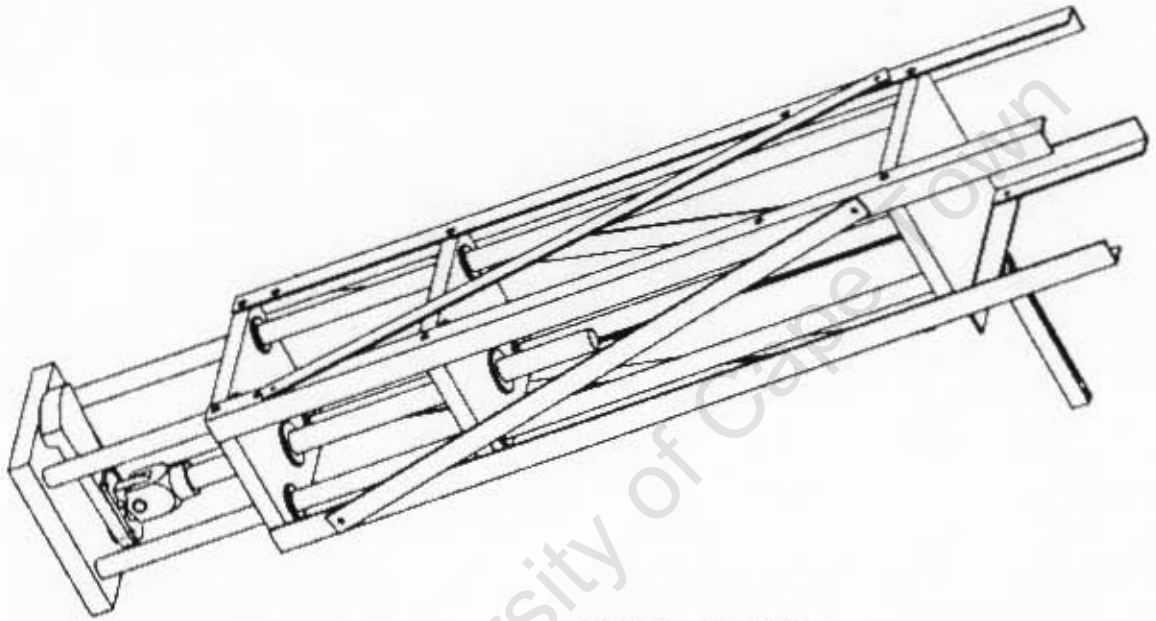

SCALE 0,150

2	PENDULUM_RIG	1	PENDDOCAS
1	FOOT_ASSEMBLY	1	FOOTDOCAS
Nr	Part name	Qty	Dwg number
SCALE 0,15	UNIVERSITY OF CAPE TOWN Department of Mechanical Engineering		
	Pendulum Test Setup		
25-09-06	D. Ungerer		TESTRIGDO1

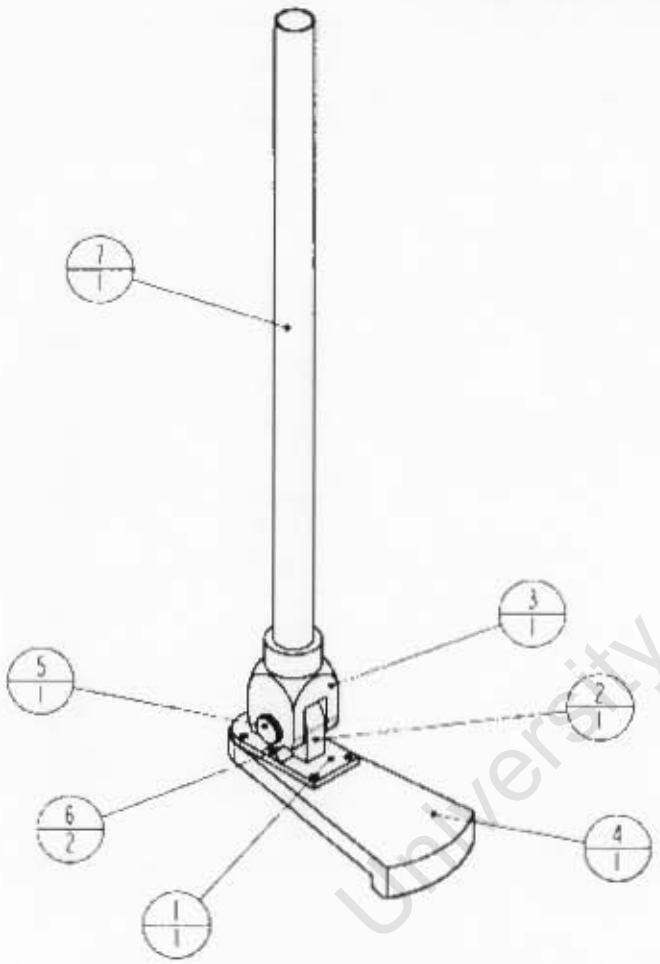

SCALE 0.250

10	TEFLON_SPACER	2	TEFLON
9	ANKLE_OUTER_BUSH	2	BRASS
8	ANKLE_INNER_BUSH	1	BRASS
7	TIBIA	1	6063 ALUMINIUM
6	STOPPER	2	6063 ALUMINIUM
5	PIN	1	6063 ALUMINIUM
4	FOOT	1	6063 ALUMINIUM
3	ANKLE_TOP_HINGE	1	6063 ALUMINIUM
2	ANKLE_BOTTOM_HINGE	1	6063 ALUMINIUM
1	ANKLE_BASE	1	6063 ALUMINIUM
No.	Part name	Qty.	Material

SCALE 0.25	UNIVERSITY OF CAPE TOWN Department of Mechanical Engineering	
	FOOT ASSEMBLY	
23-09-05	D. Ungerer	FOOT000AS

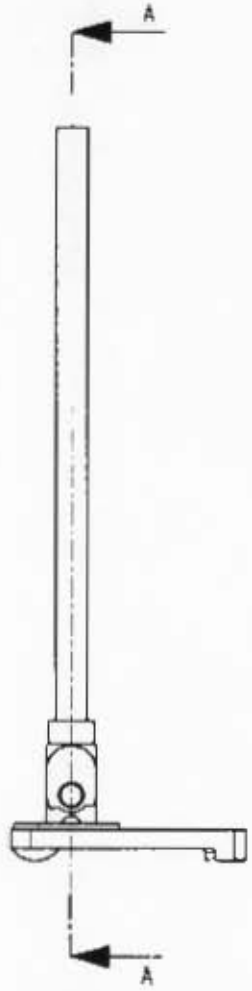

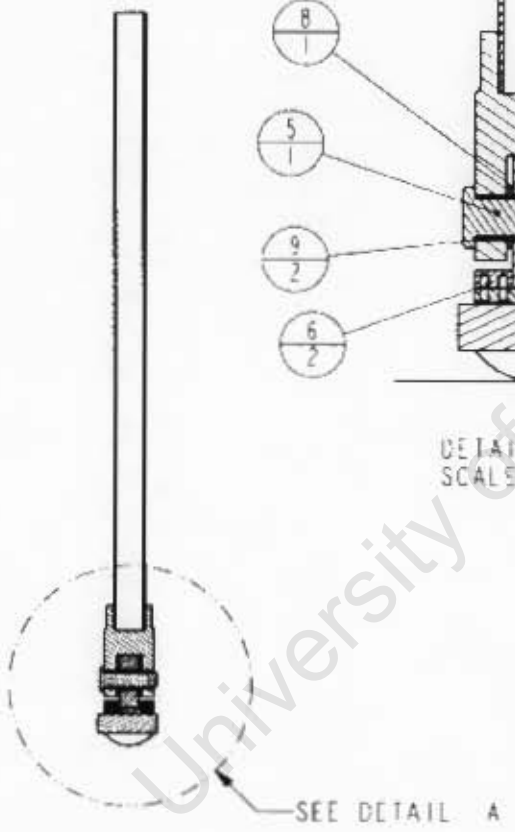

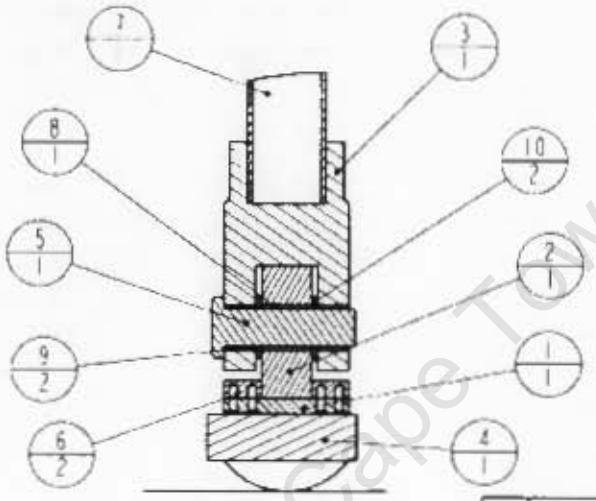

10	TEFLON_SPACER	2	TEFLON
9	ANKLE_OUTER_BUSH	2	BRASS
8	ANKLE_INNER_BUSH	1	BRASS
7	TIBIA	1	6063 ALUMINIUM
6	STOPPER	2	6063 ALUMINIUM
5	PIN	1	6063 ALUMINIUM
4	FOOT	1	6063 ALUMINIUM
3	ANKLE_TOP_HINGE	1	6063 ALUMINIUM
2	ANKLE_BOTTOM_HINGE	1	6063 ALUMINIUM
1	ANKLE_BASE	1	6063 ALUMINIUM
Nr	Part name	Qty	Material

SCALE 0.2	UNIVERSITY OF CAPE TOWN Department of Mechanical Engineering	
	FOOT ASSEMBLY	
20-09-06	D. Ungerer	FOOTOOIAS

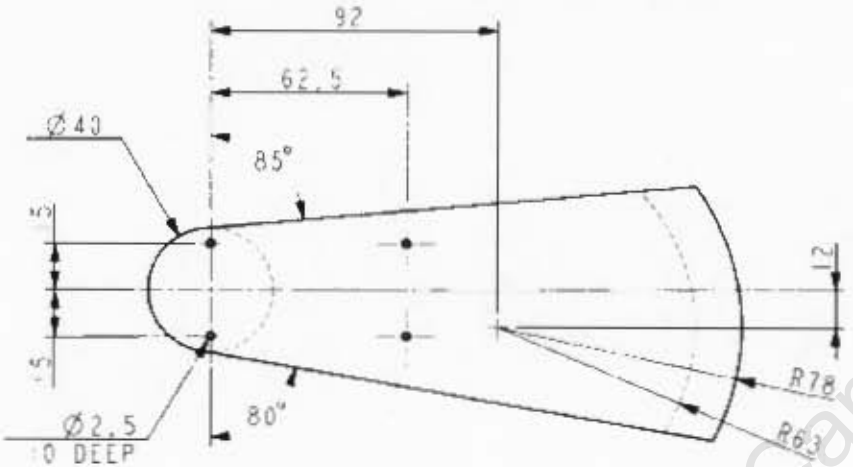

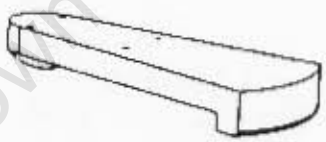

SCALE 0.300

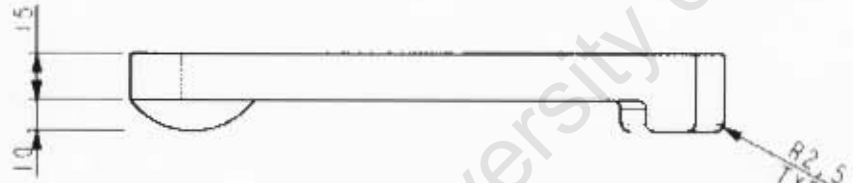

SCALE 0.500

4	6063 Aluminium	1	25MM AL PLATE
Nr	Material	Qty	Stock
SCALE 0.5	UNIVERSITY OF CAPE TOWN Department of Mechanical Engineering		
	Foot		
3-09-06	D Ungerer	FOOT001	

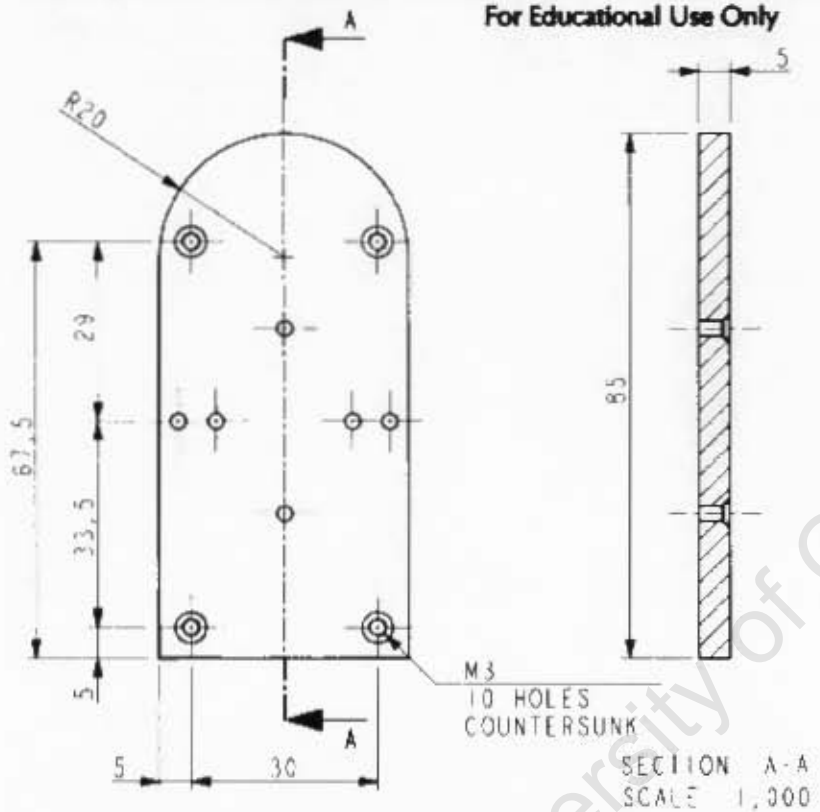

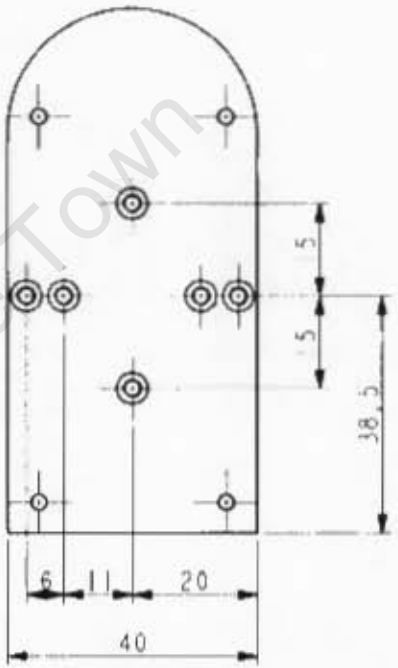

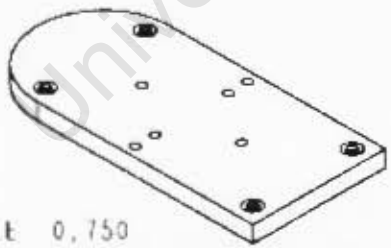

1	6063 Aluminium	1	6MM PLATE
Nr	Material	Qty	Stock
SCALE 1:2	UNIVERSITY OF CAPE TOWN Department of Mechanical Engineering		
	Ankle Base		
4-30-08	D. Ungerer		F001037

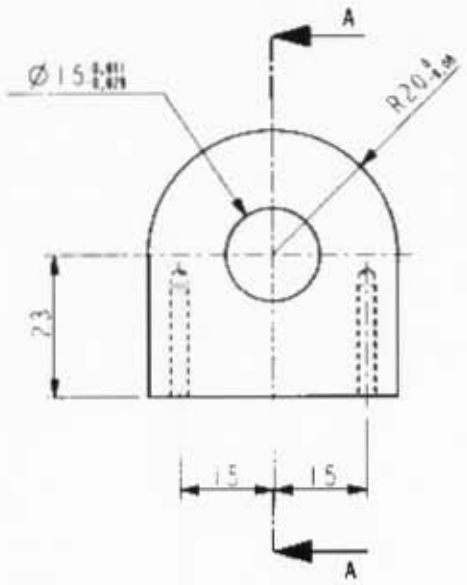

SECTION A-A
SCALE 1.000

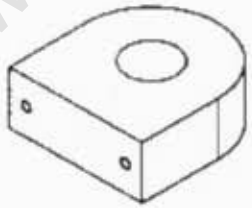

SCALE 0.750

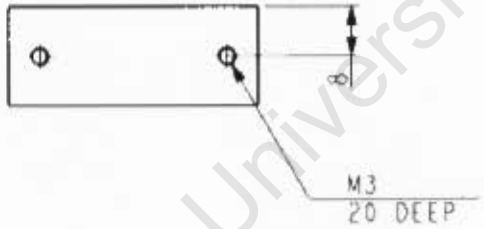

2	6063 Aluminium	1	20MM AL PLATE
Nr	Material	Qty	Stock
SCALE 1:0	UNIVERSITY OF CAPE TOWN Department of Mechanical Engineering		
	Ankle Bottom Hinge		
14-09-26	D. Ungerer		FOOT203

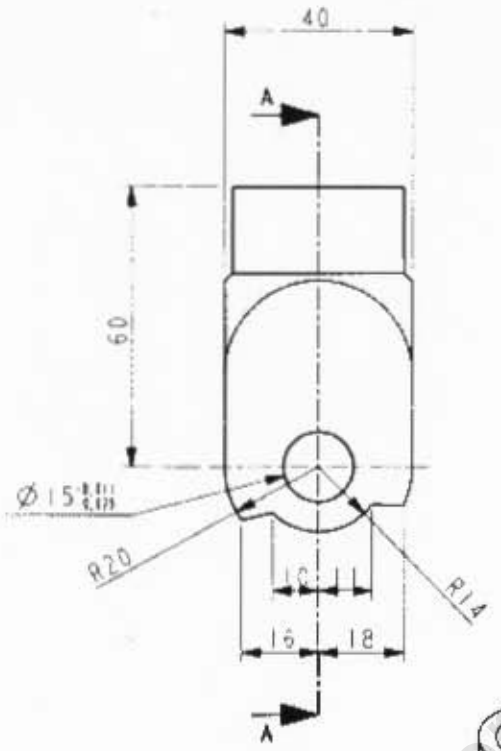

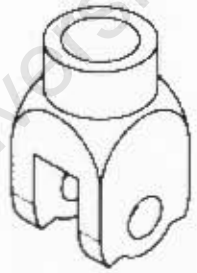

SCALE 0,500

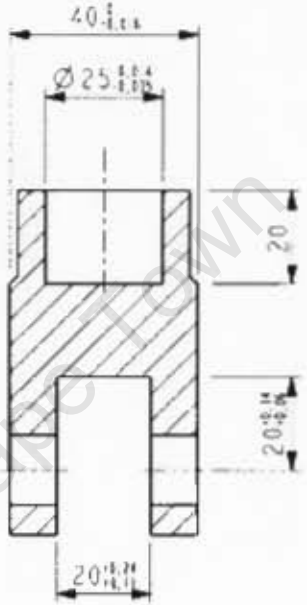

SECTION A-A
SCALE 0,750

3	6063 Aluminium	1	40x40 AL SQR BAR
No	Material	Qty	Stock
SCALE 0,75	UNIVERSITY OF CAPE TOWN Department of Mechanical Engineering		
	Ankle Top Hinge		
16-08-06	D. Ungerer		FOOT004

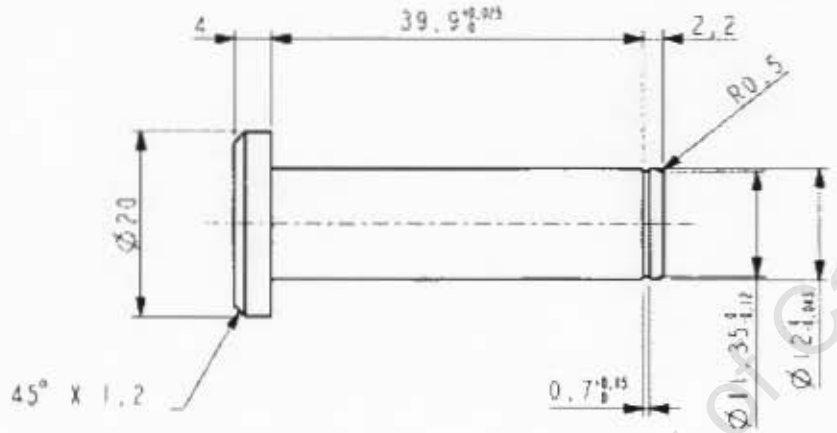

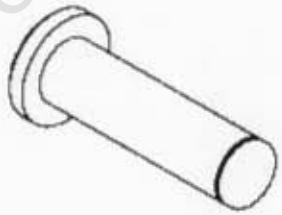

SCALE 1,000

5	6063 Aluminium	1	Ø20MM AL ROUND BAR
Nr	Material	Qty	Stock
SCALE 1:5	UNIVERSITY OF CAPE TOWN Department of Mechanical Engineering		
	Pin		
15 11 16	D Jagerer		FOOT005

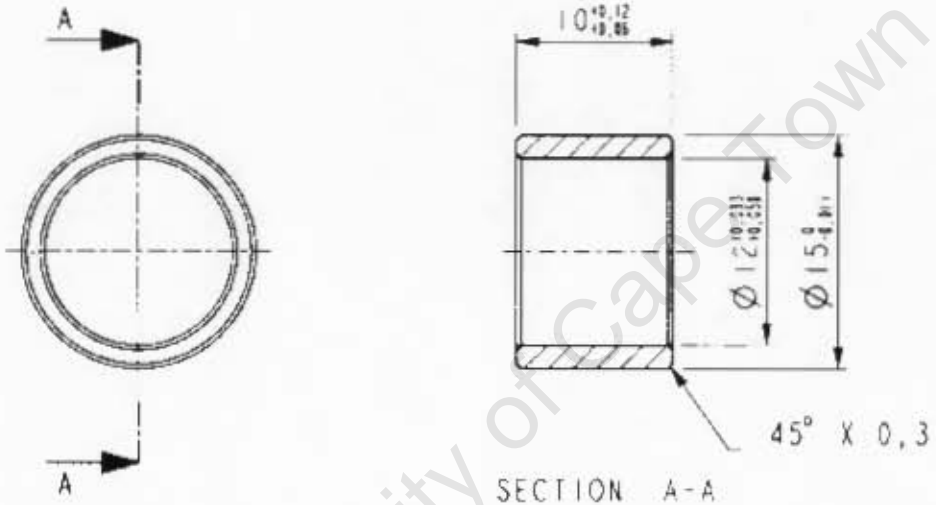

9	Brass	2	20MM OD ROUND BAR
Nr	Material	Qty	Stock
SCALE 2.5	UNIVERSITY OF CAPE TOWN Department of Mechanical Engineering		
	Ankle Hinge Outer Bush		
16-08-06	D. Ungerer	FOOT006	

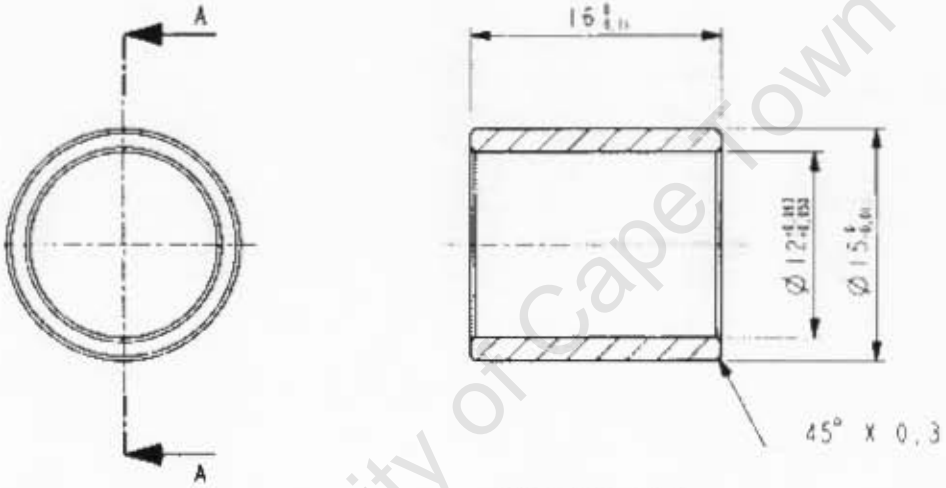

SECTION A-A
SCALE 2,500

8	Brass	1	20MM OD ROUND BAR
Nr	Material	Qty	Stock
SCALE 2 5	UNIVERSITY OF CAPE TOWN Department of Mechanical Engineering		
	Inner Ankle Hinge Bush		
16 20 06	D. Ungerer		1007007

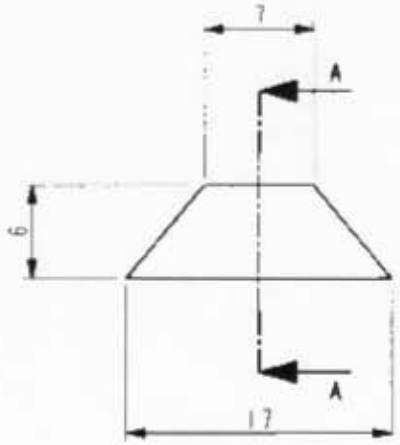

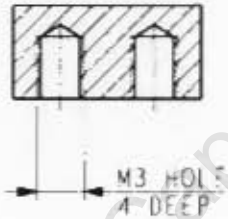

SECTION A-A
SCALE 2.500

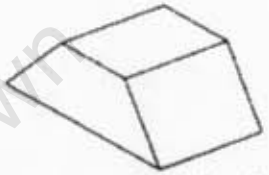

SCALE 2.000

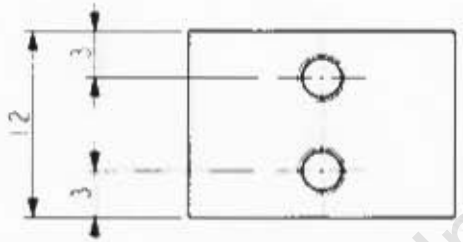

6	6063 Aluminium	2	6MM AL PLATE
Nr	Material	Qty	Stock
SCALE 2.5	UNIVERSITY OF CAPE TOWN Department of Mechanical Engineering		
	Stopper		
17-09-06	D Ungerer	FOOT008	

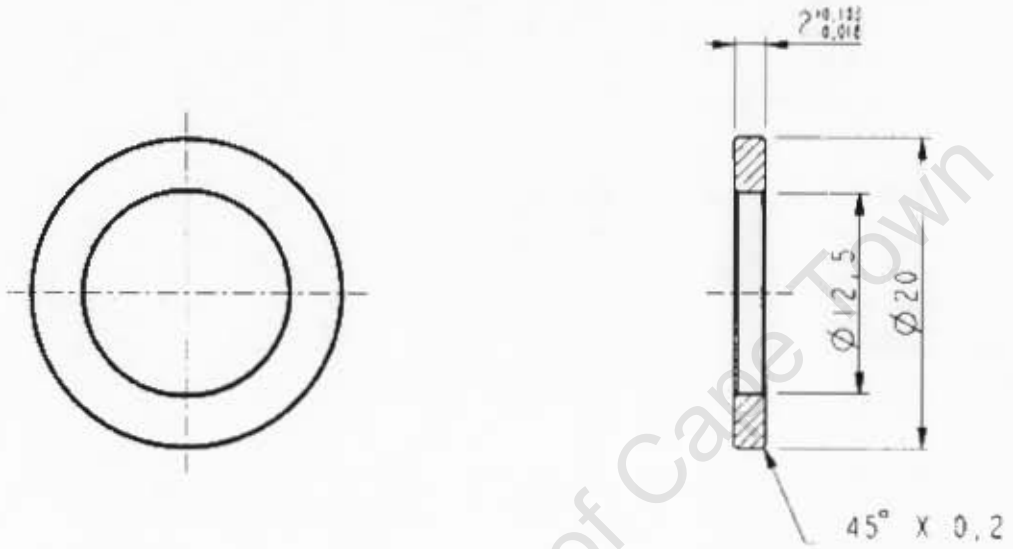

SECTION A-A
SCALE 2,500

IC	Teflon	2	20MM OD ROUND BAR
Nr	Material	Qty	Stock
SCALE 2,5	UNIVERSITY OF CAPE TOWN Department of Mechanical Engineering		
	Teflon Spacer		
16-09-06	D. Ungerer	FOOT009	

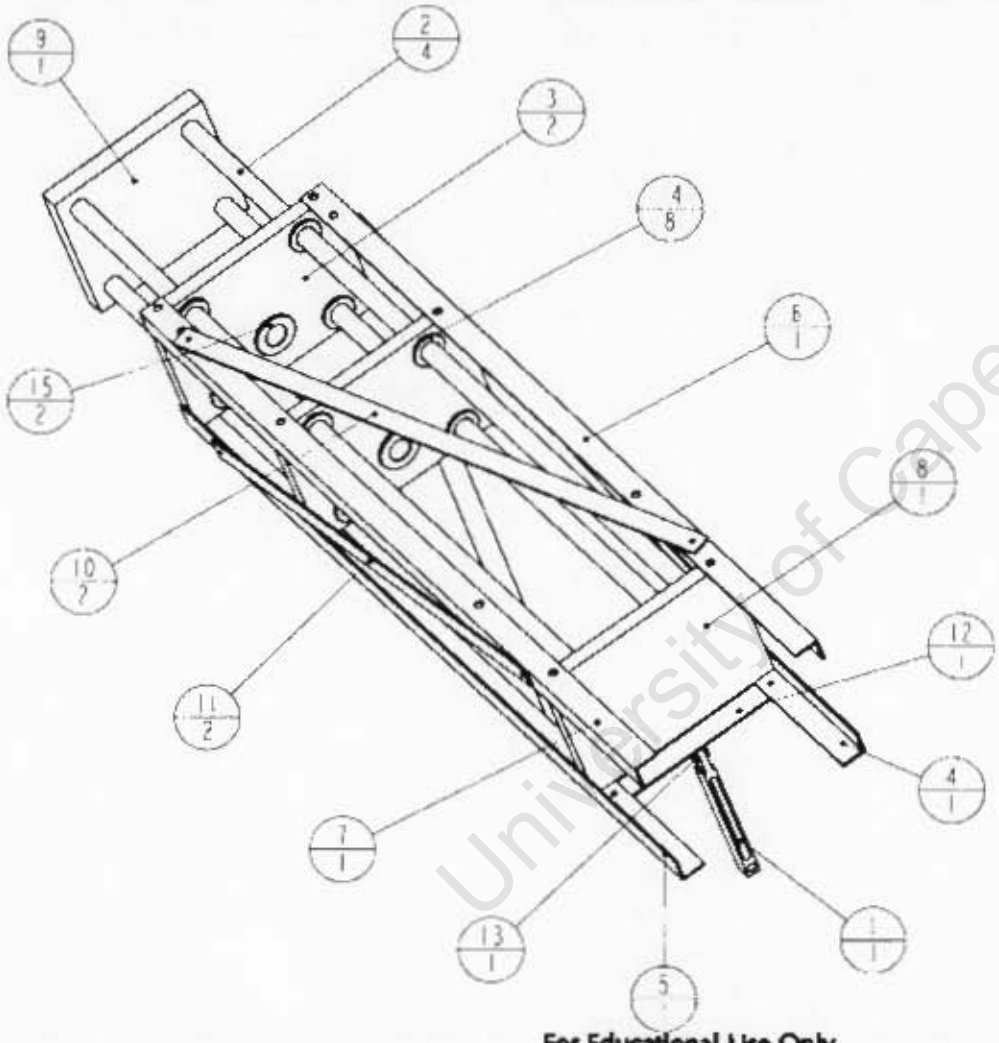

Nr	Part name	Qty	Material
15	TIBIA_RIG_BUSH	2	TEFLON
14	SS_BAR_BUSH	8	TEFLON
13	PEN_HINGE	1	STEEL
12	PEN_ATTACHMENT_BAR	1	STEEL
11	FLAT_CROSS_BAR_SIDE	2	STEEL
10	FLAT_CROSS_BAR	2	STEEL
9	DETONATION_PLATE	1	STEEL
8	BACK_PLATE	1	STEEL
7	ANGLE_BAR_TOPRIGHT	1	STEEL
6	ANGLE_BAR_TOPLEFT	1	STEEL
5	ANGLE_BAR_BOTTOMRIGHT	1	STEEL
4	ANGLE_BAR_BOTTOMLEFT	1	STEEL
3	RIG_PLATE	2	STAINLESS STEEL
2	SILVER_STEEL_BAR	4	SILVER STEEL
1	PEN	1	ALUMINIUM

SCALE 0.15	UNIVERSITY OF CAPE TOWN Department of Mechanical Engineering	
	PENDULUM RIG	
25-07-06	D. Ungerer	PEND000AS

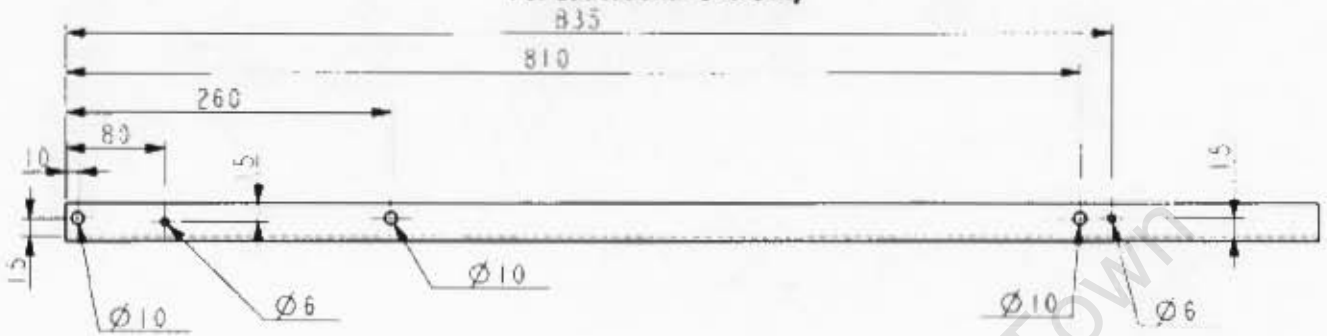

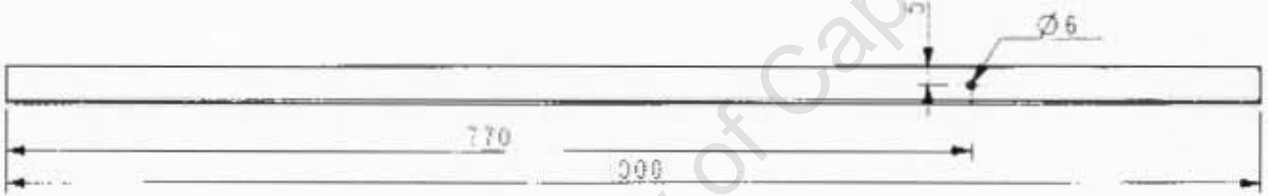

SCALE 0.100

1	Steel	1	40x40x3 ANGLE IRON
No	Material	Qty	Stock
SCALE 0.2	UNIVERSITY OF CAPE TOWN Department of Mechanical Engineering		
	Bottom Left Angle Bar		
01 07 06	D. Ungerer		PENDOO1

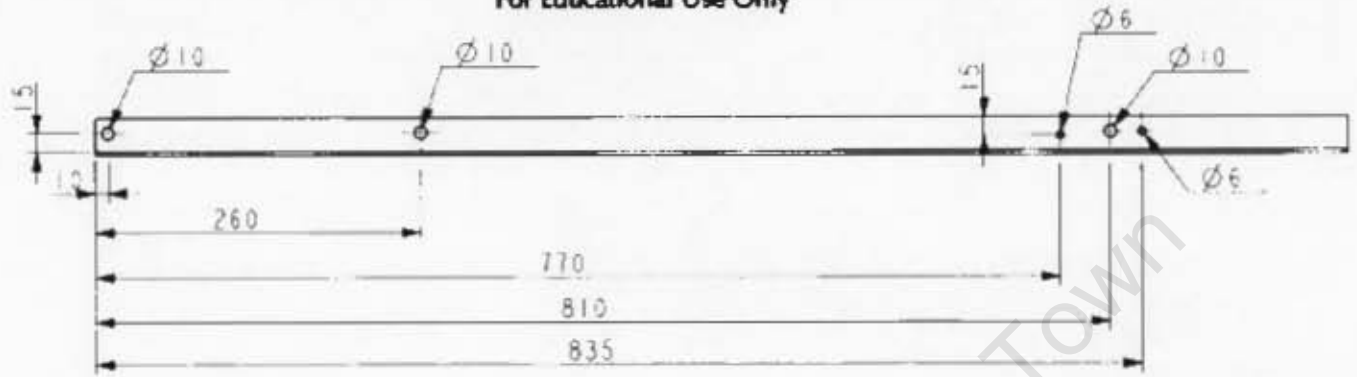

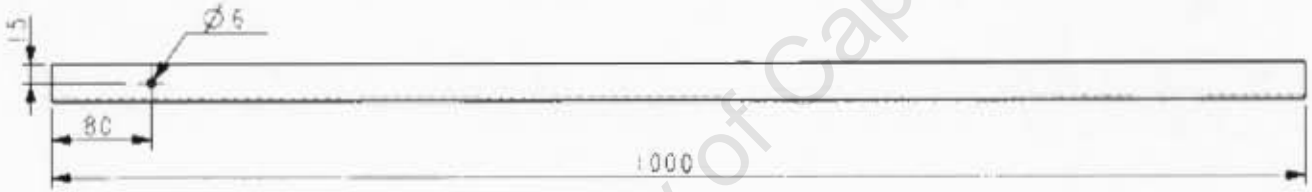

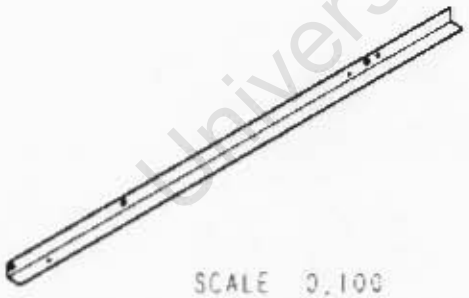

SCALE 0.100

2	Steel	1	40x40x3 ANGLE IRON
No	Material	Qty	Stock
SCALE 0.2	UNIVERSITY OF CAPE TOWN Department of Mechanical Engineering		
	Bottom Right Angle Bar		
01-07-06	D. Ungerer	PEN0002	

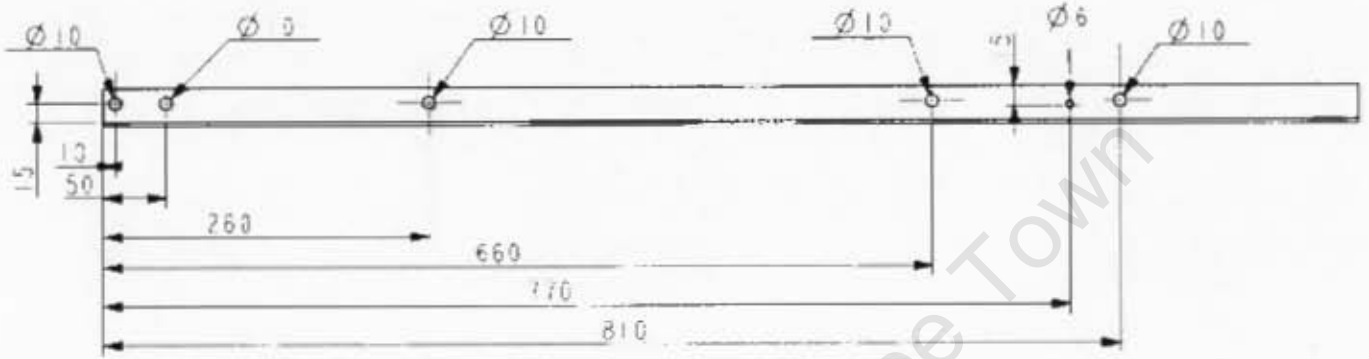

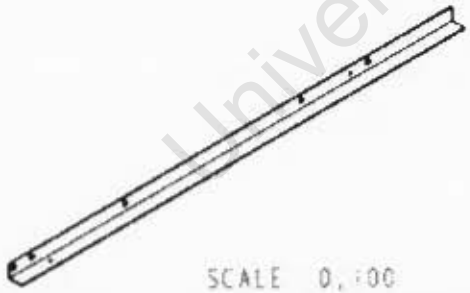

3	Steel	1	40x30x3 ANGLE IRON
Nr	Material	Qty	Stock
SCALE 0.2	UNIVERSITY OF CAPE TOWN Department of Mechanical Engineering		
	Top Left Angle Bar		
21-07-06	D. Ungerer	PEND003	

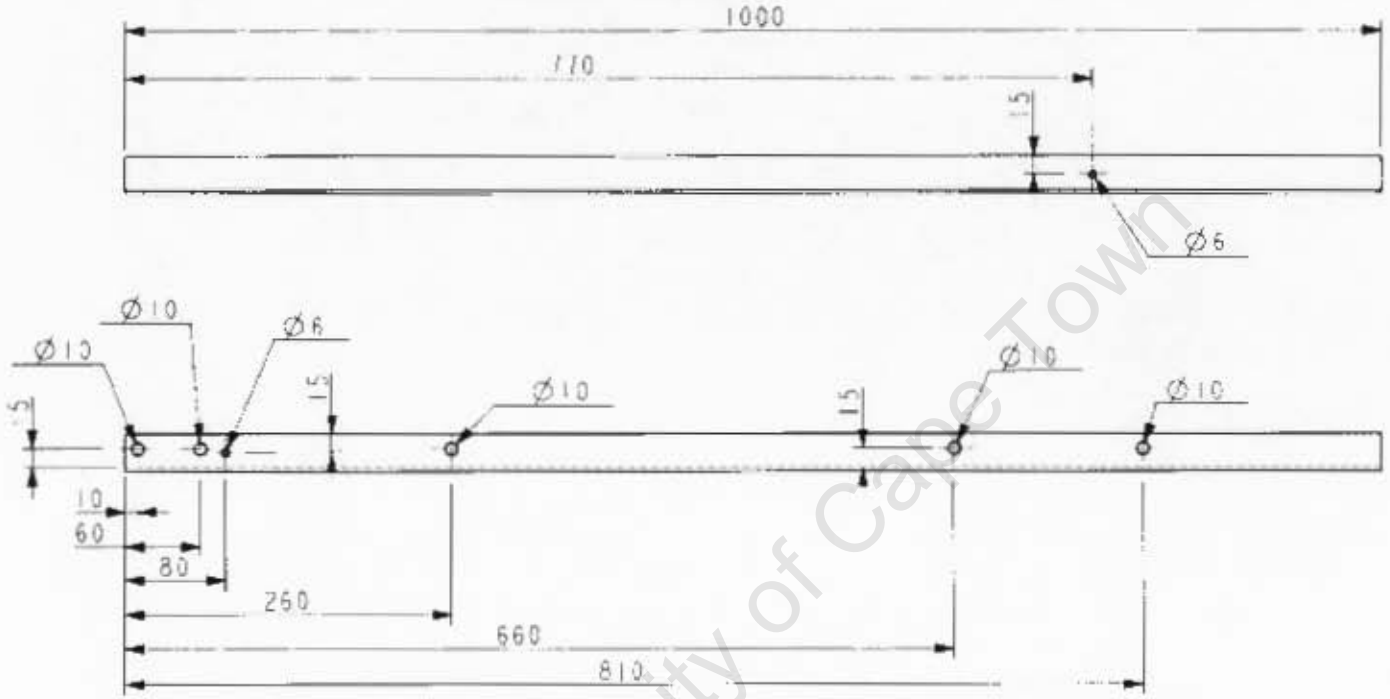

SCALE 0.100

4	Steel	1	40x40x3 ANGLE IRON
Nr	Material	Qty	Stock
SCALE 0.2	UNIVERSITY OF CAPE TOWN Department of Mechanical Engineering		
	Top Right Angle Bar		
0-07-06	D Ungerer		PEND034

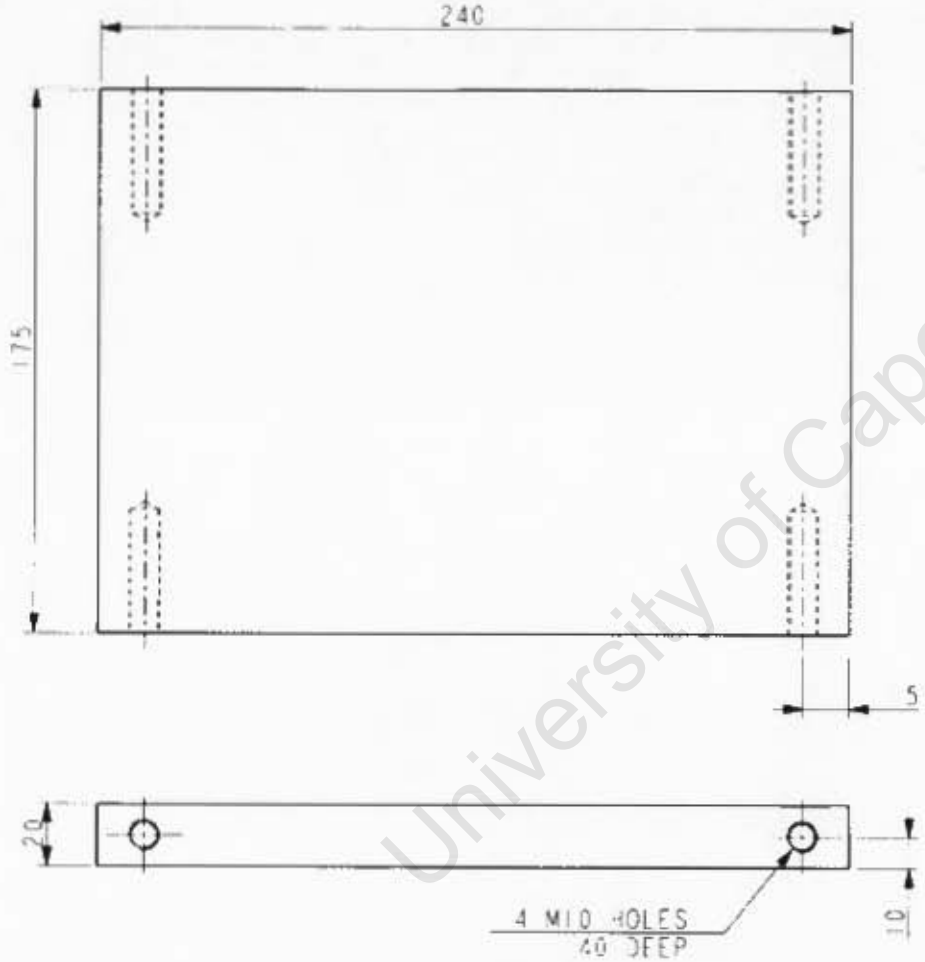

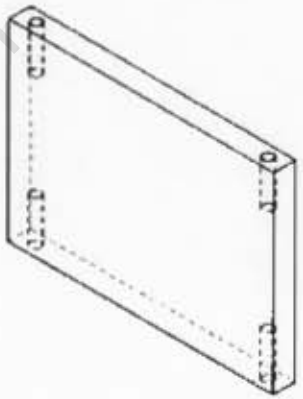

SCALE 0.250

5	Steel	1	20mm PLATE
Nr	Material	Qty	Stock
SCALE 0.5	UNIVERSITY OF CAPE TOWN Department of Mechanical Engineering		
	back Plate		
01 07 06	D.Ungerer	PTSDC05	

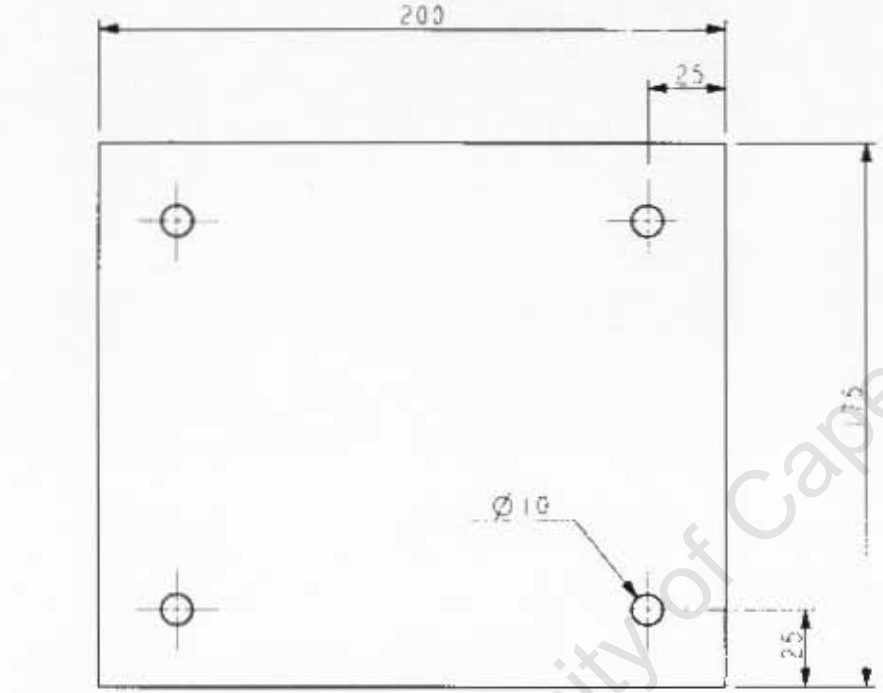

SCALE 0,500

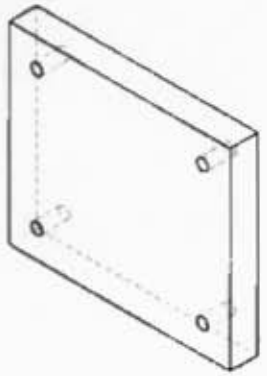

SCALE 0,250

6	Steel	1	25MM MILD STEEL PLATE
No	Material	Qty	Stock
SCALE 0.5	UNIVERSITY OF CAPE TOWN Department of Mechanical Engineering		
	Detonation Plate		
01-07-06	D. Ungerer	PEND005	

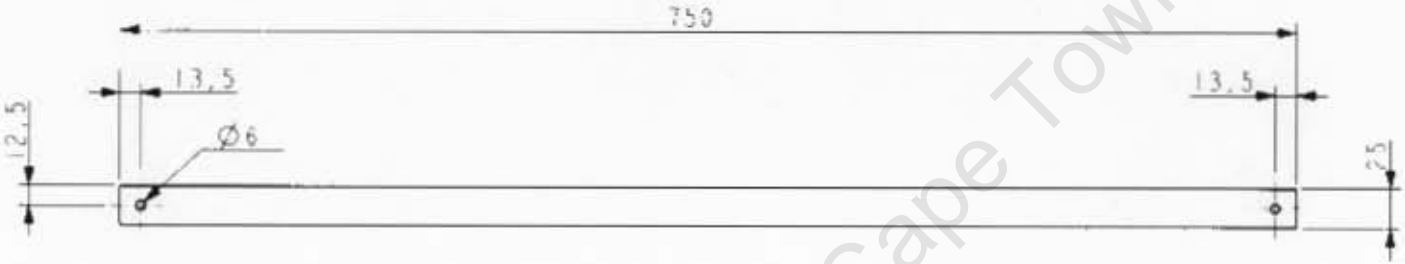

SCALE 0,250

1	Steel	2	3MM FLAT BAR
Nr	Material	Qty	Stock
SCALE 0 25	UNIVERSITY OF CAPE TOWN Department of Mechanical Engineering		
	Flat Cross Bar		
31-07-14	D Ungerer		PENDC07

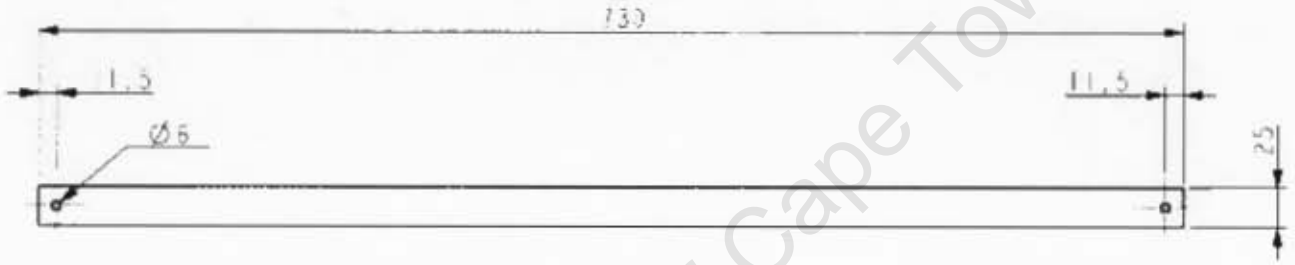

SCALE 0.250

8	Steel	2	3MM FLAT BAR
Nr	Materia	Qty	Stock
SCALE 0.25	UNIVERSITY OF CAPE TOWN Department of Mechanical Engineering		
	Flat Cross Bar - Sides		
01-07-06	D. Ungerer	PEN0008	

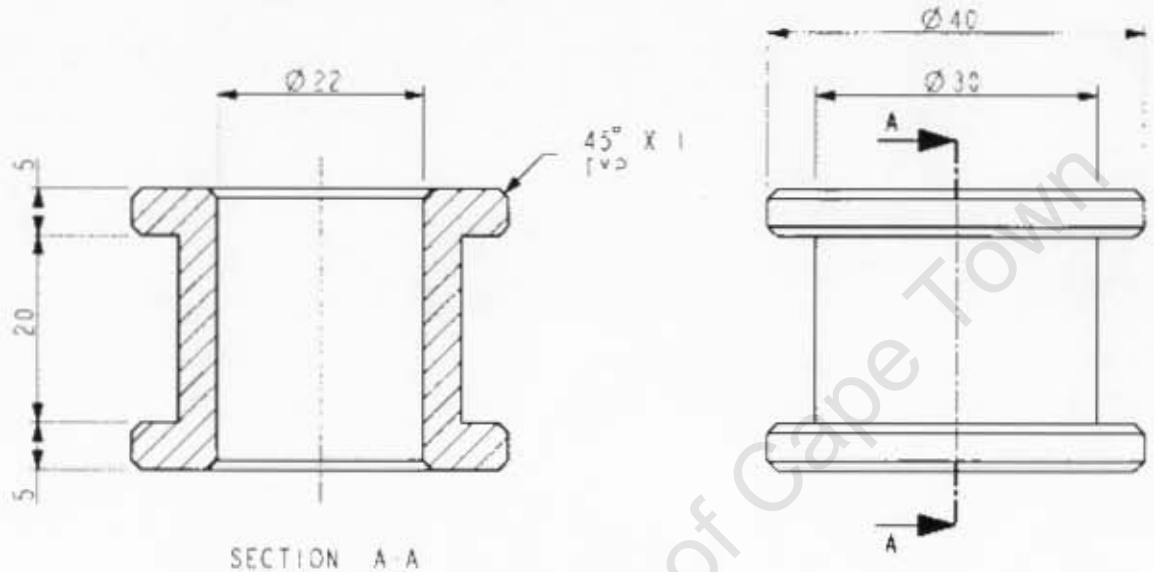

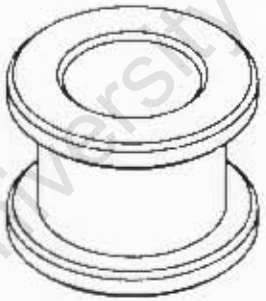

SCALE 1.000

13	Teflon	8	50MM ROUND BAR
Nr	Material	Qty	Stock
SCALE 1.5	UNIVERSITY OF CAPE TOWN Department of Mechanical Engineering		
	Hopkinson Bar Bush		
02-07-06	D. Ungerer	PEND009	

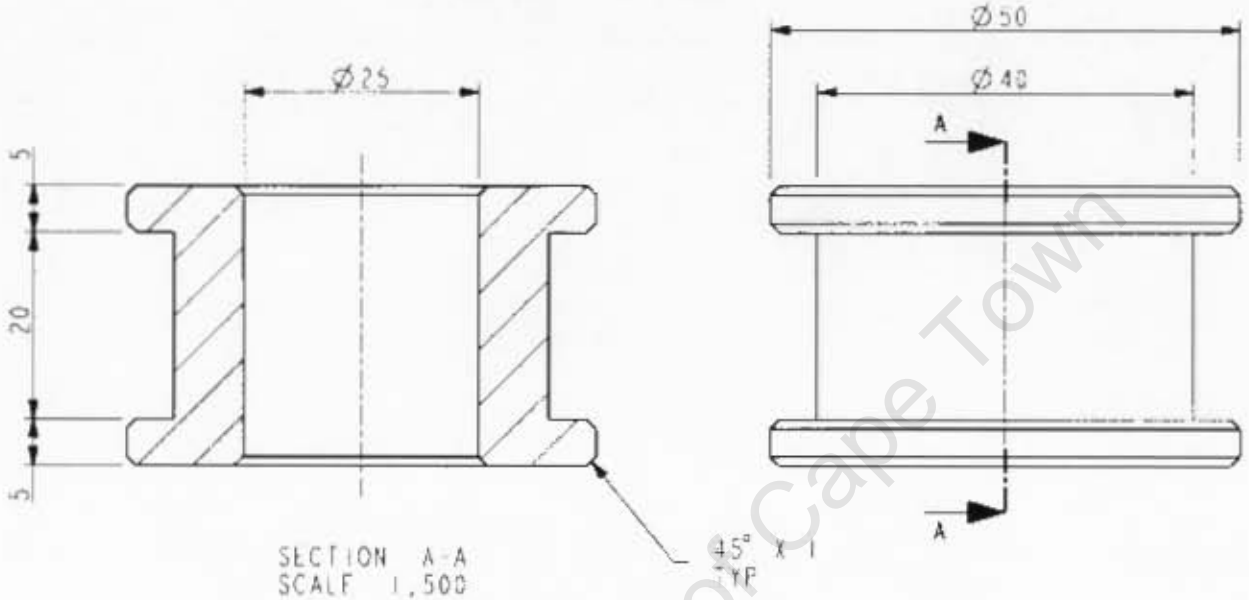

15	Teflon	2	50MM ROUND BAR
Nr	Material	Qty	Stock
SCALE 1:5	UNIVERSITY OF CAPE TOWN Department of Mechanical Engineering		
	Tibia Bush (Rig Plate)		
02-07-05	D. Ungerer		PEN3010

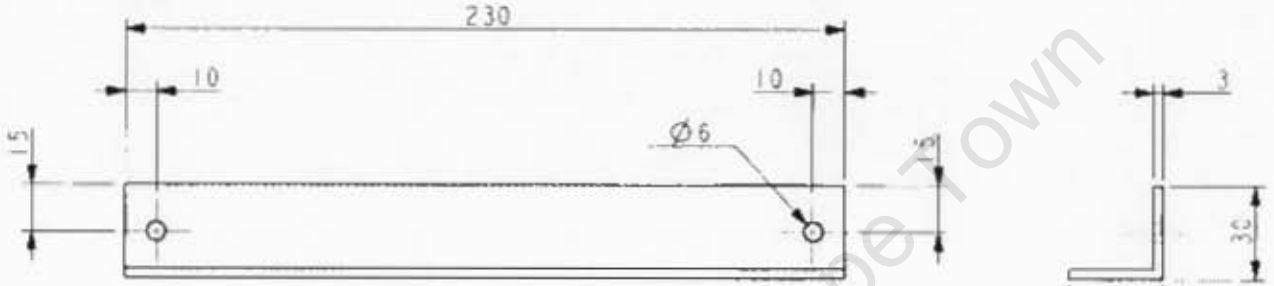

SCALE 0,500

SCALE 0,250

11	Steel	1	30x30x3MM ANGLE IRON
Nr	Material	Qty	Stock
SCALE 0,5	UNIVERSITY OF CAPE TOWN Department of Mechanical Engineering		
	Pen Attachment Bar		
02-07-06	D Ungerer	PEN0011	

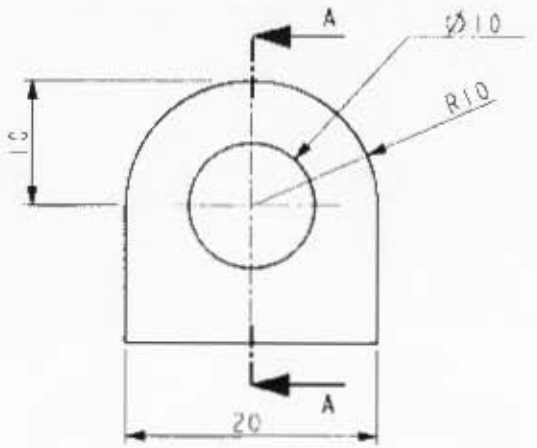

SCALE 2,000

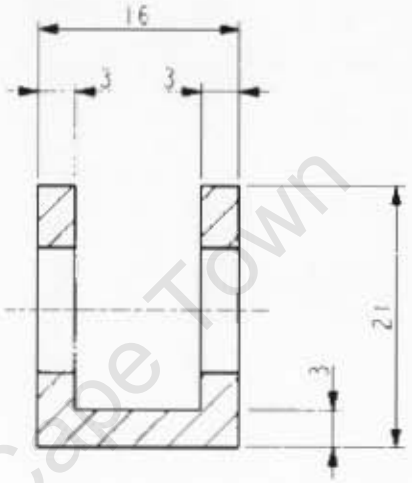

SECTION A-A

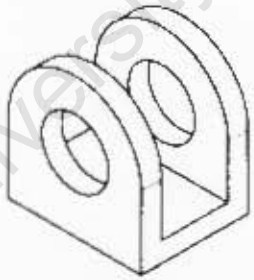

SCALE 1,500

14	Steel	1	20MM MILD STEEL PLATE
Nr	Material	Qty	Stock
SCALE 2:1	UNIVERSITY OF CAPE TOWN Department of Mechanical Engineering		
	Pen Hinge		
04-07-06	D Ungerer	PEN0012	

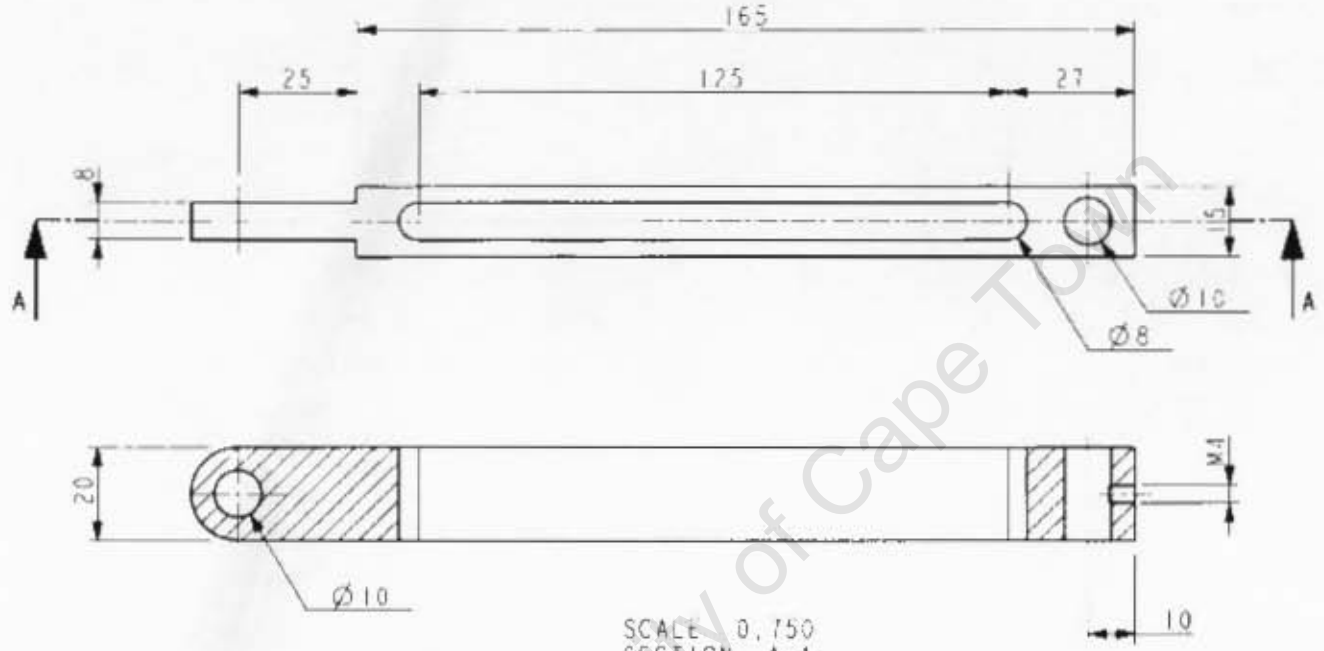

SCALE 0,250

10	Aluminium	1	20MM AL PLATE
Nr	Material	Qty	Stock
SCALE 0,75	UNIVERSITY OF CAPE TOWN Department of Mechanical Engineering		
	Rig Pen		
04-07-06	D. Ungerer		PEND013